

A Calorimetric Wire Detector for Measurement of Atomic Hydrogen Beams



JOHANNES GUTENBERG
UNIVERSITÄT MAINZ

Dissertation
zur Erlangung des Grades
„Doktor der Naturwissenschaften“
am Fachbereich Physik, Mathematik und Informatik
der Johannes Gutenberg-Universität
in Mainz
vorgelegt am 17. Oktober 2025

Christian Matthé

geboren in Mainz

License: This article is licensed under a Creative Commons Attribution 4.0 International License, which permits use, sharing, adaptation, distribution and reproduction in any medium or format, as long as you give appropriate credit to the original author(s) and the source, provide a link to the Creative Commons licence, and indicate if changes were made. The images or other third party material in this article are included in the article's Creative Commons licence, unless indicated otherwise in a credit line to the material. If material is not included in the article's Creative Commons licence and your intended use is not permitted by statutory regulation or exceeds the permitted use, you will need to obtain permission directly from the copyright holder. To view a copy of this licence, visit <http://creativecommons.org/licenses/by/4.0/>.

- 1. Berichtstatter und Betreuer: Prof. Dr. Sebastian Böser**
- 2. Berichtstatter: Prof. Dr. Randolf Pohl**

Abstract

The Project 8 collaboration aims to determine the absolute neutrino mass with a sensitivity of 40 meV by measuring the tritium decay spectrum. Project 8 will use atomic tritium confined in a magnetic trap to perform cyclotron radiation emission spectroscopy (CRES) on decay electrons produced directly in the trap and performing cyclotron motion in the same magnetic field.

Reaching the desired sensitivity will require the observation of a large number of tritium decays, since a tiny fraction ($\approx 10^{-13}$) of all decays produce an electron sufficiently close to the endpoint to be informative for the neutrino mass. Additionally, since molecular tritium sensitivity receives a large statistical penalty to energy resolution caused by the molecular final state distribution, atomic tritium must be used for the desired sensitivity.

Project 8 must develop an atomic tritium beamline capable of injecting $\gtrsim 10^{14}$ atoms/s into the CRES detection volume. Due to losses in cooling, injection, and trapping, we anticipate that this will require an atomic tritium source that initially produces an atom flux of $\gtrsim 10^{18}$ atoms/s. The development of such a source is currently underway, and a candidate, the Hydrogen Atomic Beam Source (HABS), is used for measurements presented in this thesis.

This thesis focuses on the development of a calorimetric wire detector capable of measuring the intensity and distribution of atomic hydrogen beams as required by Project 8. The detector uses a wire with a micrometer-scale diameter intersecting the beam on which a small fraction of the beam's hydrogen atoms recombine into molecules. The energy released heats the wire and produces a measurable change in its resistance.

We present measurements performed with such a detector to determine the distribution of hydrogen atoms across a beam produced by the test source, and present limits on the total flux of atoms that are produced by this source. We also present a theoretical description of the wire detector, including a simulation.

The results directly contributed to a better understanding of the HABS showing the utility of the calorimetric wire detector in further development of the atomic tritium beamline.

Contents

1	Introduction	1
2	Neutrino Mass Measurements	3
2.1	Neutrino oscillations	3
2.2	Neutrinoless double beta decay	5
2.3	Cosmology	6
2.4	Time of flight	7
2.5	Direct laboratory measurements	8
2.5.1	Choice of isotope	9
2.5.2	KATRIN	10
3	Project 8	13
3.1	CRES	13
3.2	Atomic Tritium	14
4	Mainz Atomic Test Stand (MATS)	17
4.1	Hydrogen Atomic Beam Source (HABS)	18
4.1.1	Capillary output distribution	21
4.1.2	Geometrically visible fraction of the capillary	23
5	Calorimetric Wire Detector	26
5.1	Signal: change in resistance	27
5.2	Simulation of the temperature distribution	29
5.3	Heat flow components	30
5.3.1	Recombination of hydrogen into molecules	31
5.3.2	Kinetic energy of beam gas	32
5.3.3	Blackbody radiation from the hot source	33
5.3.4	Electrical heating	35
5.3.5	Heat conduction	35
5.3.6	Radiative cooling	36
5.3.7	Free molecular heat transfer with residual background gas in the vacuum chamber	36
5.3.8	Radioactive heat from tritium decay	37
5.3.9	Representative example simulation	38
5.4	Consistency check	39
5.4.1	Length of simulated time	40
5.4.2	Length of wire segments	41
5.5	Design parameter studies	42
5.5.1	Wire length	43
5.5.2	Wire thickness	47
5.5.3	Alternate wire material platinum as a case study for the calorimetric efficiency of the detector	50
5.6	Wire sensitivity	54
6	Design Iterations	56
6.1	First realization (V1 Prototype)	56
6.2	V2 outside via mounting	57
6.3	V3 Multiple parallel wires	58
6.4	V4 Ceramic PCB	59

7	Beamless Wire detector measurements	62
7.1	Measuring zero current resistance	62
7.1.1	Method 1: Low power current offset	64
7.1.2	Method 2: high power extrapolation	66
7.1.3	Conclusion	69
7.2	Detection threshold	70
7.3	Calibration of resistance response to heating power	72
7.3.1	Correcting calibration for temperature distribution and resulting wire sensitivity	73
8	Beam measurements	75
8.1	Beam model	75
8.1.1	Beam gas heating model	76
8.2	Signal extraction	78
8.2.1	Primary signal extraction	78
8.2.2	Secondary signal extraction	80
8.3	Molecular beam shape scans	82
8.3.1	Secondary signal extraction for fully molecular beams	83
8.3.2	Molecular beam fit model	84
8.3.3	Accommodation coefficient and implications for absolute calibration	87
8.4	Atomic Beam shape scans	88
8.4.1	3-temperature-point method at 1scm	88
8.4.2	Systematic errors from temperature selection	92
8.4.3	Additional lower flows	94
8.5	Effective length over flow	96
8.6	Absolute atom count limits	97
9	Known issues and Suggestions	101
9.1	Suggested detector changes	101
9.1.1	Installation of an aperture	101
9.1.2	Increase detector travel range	102
9.2	Issues with flow switching	103
9.3	Suggestions elsewhere in the text	103
10	Conclusion	104
	Abbreviations	104
	References	106
A	Coordinate definitions	111
A.1	Coordinate transform to the wire plane	112
B	Primary extraction equilibration and systematics	114
B.1	Gas flow and pressure	114
B.2	Detector board temperature equilibration	116
B.2.1	Detector board temperature oscillations	116
B.2.2	Shorter 5 minute intervals at 1 sccm	118
B.2.3	Equivalent sample measurements at lower flows	120
B.3	Further Background temperature change mitigation strategies	123
B.3.1	Subtraction schemes	123
B.3.2	Deconvolution Subtraction	126

C	Extracted data for all flows	128
C.1	data	128
D	1-temperature-point method for beam analysis	130
D.1	Effective length	132
D.2	Absolute atom count limits based on the 1-T-P method	133
	Curriculum Vitae	136

1 Introduction

The work presented in this thesis is carried out in the context of development of an atomic tritium source for the Project 8 experiment [1], which aims to employ atomic tritium in combination with the novel technology of Cyclotron Radiation Emission Spectroscopy to achieve a neutrino mass sensitivity of $m_\beta < 40 \text{ meV}/c^2$. As an intermediate goal an atomic hydrogen source capable of producing on the order of 10^{19} atoms/s is being developed.

As part of this effort, detectors capable of monitoring the resulting intensity and distribution of an atomic hydrogen beam will be required. Traditionally, this could be achieved using a high resolution quadrupole mass spectrometer (QMS). However, situations are anticipated in which a QMS will not be ideal, in particular high magnetic fields and tight space constraints. To complement measurements with a QMS in such cases, a calorimetric wire detector, which measures the heat of atoms recombining into molecules, is being developed.

The concept of using such detectors for atomic hydrogen beams has previously been explored in literature [2–4] as well as in student thesis work performed by AG Pohl at JGU Mainz [5–7]. We use these as a starting point for work presented in this thesis. The primary component of the detector is a thin wire strung across the beam, such that it intercepts a small slice of the beam. A sizable fraction [8] of the atoms that hit the wire stick to its surface. On it, they can recombine into molecules, releasing 4.46 eV per molecule [9]. This causes a slight heating of the wire, which can be detected by measuring the corresponding increase in resistance.

An advantage of the wire calorimeter method is that, by using very thin wires, the detection of the beam can be accomplished without meaningfully disturbing the beam. This is useful for monitoring a beam that may be used for its primary purpose downstream of the detector. The wire detector can also be used in lower quality vacuum conditions than are required for mass spectrometry. This is desirable when scaling to more intense hydrogen beams without a commensurate scaling of pumping on the vacuum system, which cannot always be achieved. The Project 8 experiment will eventually employ strong magnetic fields [1], which will cause large issues for the sensitivity of a QMS [10] due to the free electrons and ions involved in its operation. It is expected that the wire detector should operate largely unaffected by magnetic fields, though this has not yet been shown experimentally. Finally, wire detectors can be built to be quite thin, such that they may be employed in confined spaces, where fitting a QMS might be challenging.

In this thesis we will show, that we have successfully used the wire detector to measure the relative intensity profile of an atomic hydrogen beam containing of order 10^{16} atoms/(cm²s), using a number of data-driven corrections to extract a small heating signal in a complex thermal environment. We have compared the measured profile with theoretical models of the source and found them to be in agreement.

We begin with an overview of the field of neutrino mass measurements in Section 2, which we follow up with a description of Project 8 and how it fits into this field in Section 3. In Section 4 we introduce the setup we use for all atomic hydrogen work in Mainz, including for measurements presented in this thesis. Section 5 provides a detailed overview of how the calorimetric wire detector works, including introducing a simulation thereof and how the insights we gain from this simulation guide the detector design we finally produce. Section 6 is a version history of the design iterations we went through during work on this thesis. In Section 7 we then present measurements performed with these detectors without the use of a hydrogen beam in order to understand its reaction to known heat sources. In Section 8 we follow this up with measurements characterizing

various hydrogen beams. Finally, in Section 9 we present suggestions for improvements that might be made to further improve the detector design and we conclude in Section 10.

2 Neutrino Mass Measurements

This work presented in this thesis was performed in the context of Project 8, an experiment to measure the neutrino mass. For the purpose of context, this section will give a brief introduction to the history, status and the scientific goals of the field of neutrino mass measurements. For a more comprehensive review, we recommend Formaggio et al. [11] and the ‘Neutrino Masses, Mixing, and Oscillations’ chapter of the Particle Data Book [12] on which the following summary is based.

Any discussion of the neutrino mass must start with the initial proposition of the existence of neutrino¹ by Pauli [13] in 1930. He suggested a neutral particle that is emitted along with the electron during beta decay of unstable nuclei. This is done as an attempt to explain why the electron is emitted with a continuous spectrum of kinetic energies, rather than being monoenergetic as would be required by energy and momentum conservation in a two-body decay involving only nucleus and electron. In the sentence immediately following the first mention of the neutrino, a first neutrino mass limit is also given as “in any case not larger than 0.01 times the proton mass”.

In almost a century since then, this upper limit of $\lesssim 10$ MeV has been pushed down by more than 7 orders of magnitude.

In the following subsections, we will briefly cover 5 different experimental ways to gather information on neutrino mass: neutrino oscillations, neutrinoless double beta decay, cosmological measurements, astrophysical neutrino time of flight, and finally “direct” mass measurements using beta decay electrons. We will see that the experiments which are indirectly informative on the neutrino mass would generally benefit greatly from having a direct neutrino mass measurement as a fixed input, rather than a fit parameter of the model.

2.1 Neutrino oscillations

Neutrino oscillations are a process by which neutrinos, which are generally produced in processes where their lepton flavor state - ν_e, ν_μ, ν_τ - is well defined, can change their flavor state during their propagation. Most critically for the question of the neutrino mass, this process requires that neutrinos must have a non-zero mass.

The 3 neutrino paradigm, the current best explanation to experimental results thus far, explains neutrino phenomenology as the result of the 3 flavor states, which are each a superposition of 3 mass eigenstates ν_1, ν_2, ν_3 with respective masses m_1, m_2, m_3 . The relationship between mass and flavor states can be described by:

$$\nu_\alpha = \sum_i U_{\alpha i} \nu_i, \quad (2.1)$$

where $i = 1, 2, 3$, $\alpha = e, \mu, \tau$ and $U_{\alpha i}$ elements of the 3×3 unitary leptonic mixing matrix, also referred to as the neutrino mixing matrix or the Pontecorvo–Maki–Nakagawa–Sakata (PMNS) matrix.

Neutrinos interact via the weak force according to their flavor state, and thus are produced and measured with defined flavor states. However, they propagate according to their mass states. Since the mass states have differing masses, they propagate with different speeds, leading to a changing mix of states depending on how far from a neutrino source a measurement is performed.

This paradigm was originally developed to explain primarily two puzzling observations: the solar and the atmospheric neutrino problems.

¹Pauli refers to it as the “neutron”, as the nucleon now known under that name had not yet been discovered.

The solar neutrino problem refers to a deficit of electron neutrinos observed in detectors on Earth, compared to the expected production rate in the Sun. Electron neutrinos are produced in the Sun during many of the nuclear fusion processes occurring in its core. Using a standard solar model (SSM) a prediction can be made for the flux of neutrinos expected from each of these processes [14]. The earliest measurements at the Homestake experiment [15] starting in the 1960s measured solar neutrino flux at only about 30% of the rate predicted. Similar measurements continued to be made, until the puzzle was ultimately resolved by measurements at the SNO and Super-Kamiokande experiments [16, 17]. These can be consistently explained under the assumption that neutrino oscillations shift the flavor population of solar neutrinos away from electron neutrinos to neutrino flavors which cannot be detected by these experiments, thereby leading to the undercount. Solar neutrino oscillations show that electron neutrinos are a superposition of at least 2 neutrino mass states with squared mass differences of order $\Delta m_{21}^2 \equiv m_2^2 - m_1^2 \approx 10^{-4} \text{eV}^2$.

The atmospheric neutrino problem refers to a similar deficit when measuring neutrinos originally produced in the muon neutrino flavor state in Earth's atmosphere. These neutrinos are produced in the decay chains of cosmic rays hitting Earth's atmosphere. The ratio of muon neutrino to electron neutrino production can be predicted, and when measured with detectors like Super-Kamiokande [18] it is found that after traveling through the Earth to the detector there are fewer than expected detections of muon neutrinos. Atmospheric neutrino oscillations show that muon neutrinos are also the superposition of at least 2 neutrino mass states but with different squared mass differences of order $\Delta m_{31}^2 \equiv m_3^2 - m_1^2 \approx 10^{-3} \text{eV}^2$.

Together with oscillation measurements of neutrinos produced in nuclear reactions and particle accelerators, these observations can be modeled with combined fits to result in a model of 3 mass eigenstates. According to the NuFit collaboration, the mass squared differences are [19]:

$$\Delta m_{21}^2 = 7.42_{-0.20}^{+0.21} \times 10^{-5} \text{ eV}^2 \quad (2.2)$$

$$\Delta m_{31}^2 = 2.517_{-0.028}^{+0.026} \times 10^{-3} \text{ eV}^2 \quad (\text{NMO}) \quad (2.3)$$

or

$$\Delta m_{32}^2 = -2.498_{-0.028}^{+0.028} \times 10^{-3} \text{ eV}^2 \quad (\text{IMO}) \quad (2.4)$$

As only squared mass differences can be measured with neutrino oscillations, we are left with an ambiguity of the ordering of the mass states. $m_1 < m_2 < m_3$ is known as the normal mass-ordering (NMO) while $m_3 < m_1 < m_2$ is known as the inverted mass-ordering (IMO). This is illustrated in Figure 2.1.

Observations of neutrino oscillations show that neutrinos have mass, that there are at least three mass states, and determine the differences in mass between these states. This is highly significant, since standard model of particle physics does not include a mechanism by which neutrinos gain mass [12]. Any explanation for the non-zero neutrino mass is necessarily new physics.

We are left with the question of the exact ordering of the mass states, as well as the absolute mass scale i.e. the mass of the lightest mass state. These are questions that may be accessible to other forms of experiments which are covered in the following sections.

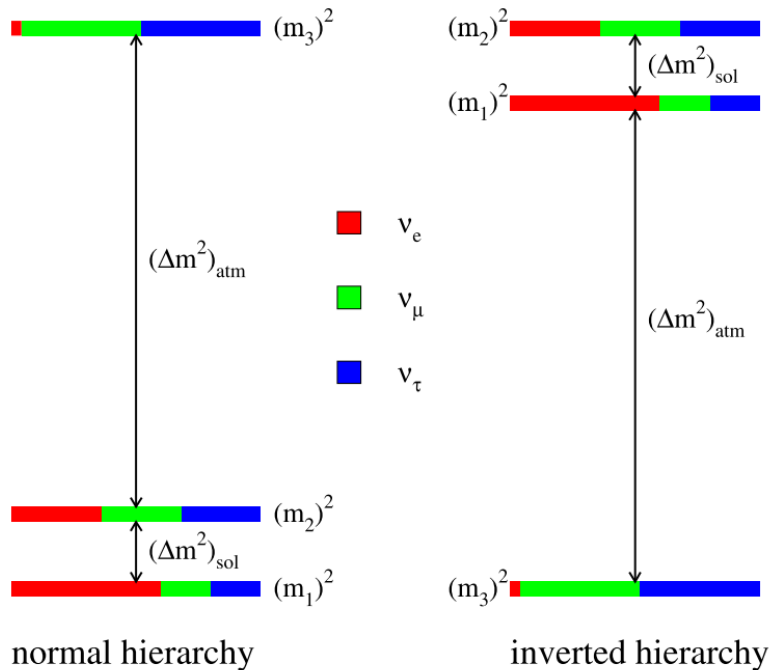


Figure 2.1: Cartoon of the two distinct neutrino mass hierarchies that fit nearly all of the current neutrino data, for fixed values of all mixing angles and mass-squared differences. The color coding (shading) indicates the fraction $|U_{\alpha i}|^2$ of each distinct flavor ν_α , $\alpha = e, \mu, \tau$ contained in each mass eigenstate ν_i , $i = 1, 2, 3$. For example, $|U_{e2}|^2$ is equal to the fraction of the $(m_2)^2$ “bar” that is painted red (shading labeled as “ ν_e ”). Source: [20]

2.2 Neutrinoless double beta decay

Neutrinoless double beta decay ($\nu 0\beta\beta$) is a hypothetical decay by which an atomic nucleus decays into one with 2 fewer neutrons and 2 more protons under the emission of 2 electrons following the form $(A, Z) \rightarrow (A, Z + 2) + 2e^-$. This decay is illustrated in Figure 2.2. The version of this decay that also includes the emission of 2 anti-electron neutrinos is standard model physics and has been observed, however the neutrinoless version requires the neutrino to be a Majorana particle. In this case the neutrino and antineutrino are both described by the same field. This allows for this decay to happen, and also introduces possible mechanisms for neutrino mass generation [12]. The potential discovery of the $\nu 0\beta\beta$ decay is therefore primarily an answer to the question of whether neutrinos are Dirac or Majorana particles [21].

The rate at which the decay occurs also provides information about $m_{\beta\beta}$, the effective Majorana mass of ν_e . In a minimal extension to the Standard Model, only adding Majorana neutrino mass terms for the 3 known mass states, the rate of the $\nu 0\beta\beta$ decay is proportional to $m_{\beta\beta}^2$ [21]. The relationship between $m_{\beta\beta}$ and the mass eigenstates is given by

$$\begin{aligned}
 m_{\beta\beta} &\equiv \left| \sum_i m_i U_{ei} \right| \\
 &\equiv \left| m_1 c_{12}^2 c_{13}^2 + m_2 s_{12}^2 c_{13}^2 e^{i\alpha_{21}} + m_3 s_{13}^2 e^{i(\alpha_{31} - \delta)} \right|, \quad (2.5)
 \end{aligned}$$

where $s_{ij} = \sin \theta_{ij}$, $c_{ij} = \cos \theta_{ij}$, θ_{ij} are the mixing angles of the PMNS matrix, δ the CP-violating phase, and α_{21}, α_{31} the two Majorana phases.

If the rate of such a decay can be measured, we can therefore gain information on

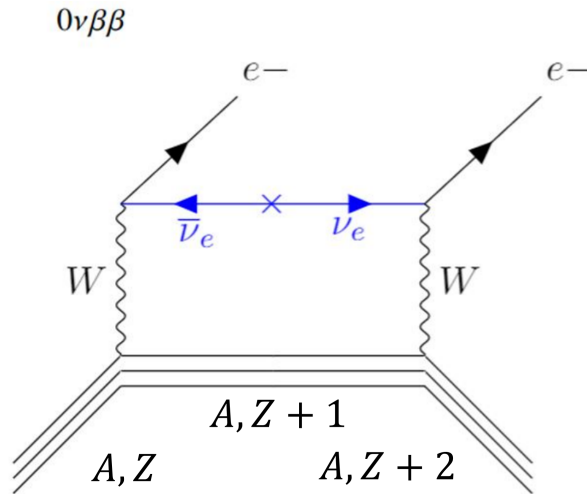


Figure 2.2: The Feynman diagram for neutrino-less double beta decay. Adapted from Source: [22]

the masses of the neutrino mass states when combined with additional information gathered from neutrino oscillations as described above. However, no $\nu 0\beta\beta$ decay has been measured to date. A non-discovery nevertheless sets an upper limit on the decay rate, and therefore $m_{\beta\beta}$ under the assumption that the neutrino is Majorana. The current best limits come from the measurement of the ^{136}Xe decay at KamLAND-Zen [23] with $m_{\beta\beta} < 28 - 122 \text{ meV}$.

The Majorana phases in Eq. 2.5 are in practice not measurable in any experiments that have been performed or conceived. The information on the neutrino mass from $\nu 0\beta\beta$ decay can only ever be incomplete. Conversely, given a previous direct measurement of the neutrino mass, the detection of the $\nu 0\beta\beta$ decay would not only determine the Majorana nature of the neutrino, but also allow for measuring the Majorana phase.

2.3 Cosmology

The Standard Model of Cosmology predicts the production of large numbers of thermal neutrinos during the expansion of the hot young universe following the Big Bang. These have steadily cooled with the expansion and it is predicted, that the temperature of relic neutrinos is of order $T_\nu^0 \sim 2 \times 10^{-4} \text{ eV}$ [11]. The energy density of neutrinos is expected to have a significant impact on the expansion history of the universe. In particular, due to neutrino oscillation measurements, we know that at least 2 of the 3 neutrino mass states are larger than T_ν^0 , and therefore they transitioned from ultra-relativistic to non-relativistic at some point in the expansion history of the universe. This is important since ultra-relativistic particle species contribute to the "radiation" density, while non-relativistic ones contribute to the "matter" density of the universe. These densities have differing effects on structure formation and expansion of the universe. Depending on precisely when this transition occurred and therefore depending on the neutrino mass this leaves imprints in the universe which can still be observed using cosmic microwave background (CMB) surveys and large scale structure surveys.

In principle cosmic surveys should be sensitive to the individual neutrino masses as every neutrino mass state should make the transition to non-relativistic at a different time. However, in practice (if all neutrino mass states are lighter than a few eV) the sensitivity of current and near future surveys is limited to measuring the sum of the neutrino masses labeled here as

$$\Sigma = \sum_i m_i. \quad (2.6)$$

Using information from neutrino oscillations, this can be expressed using the known mass-squared differences and the unknown lightest neutrino mass m_{least} :

$$\Sigma = m_{\text{least}} + \sqrt{\Delta m_{21}^2 + m_{\text{least}}^2} + \sqrt{\Delta m_{31}^2 + m_{\text{least}}^2} \quad (\text{NMO}) \quad (2.7)$$

or

$$\Sigma = m_{\text{least}} + \sqrt{-\Delta m_{32}^2 + m_{\text{least}}^2} + \sqrt{-\Delta m_{31}^2 + m_{\text{least}}^2} \quad (\text{IMO}) \quad (2.8)$$

The most recent publication of cosmological data using DESI+CMB data [24] reports $\Sigma < 0.072$ eV using their preferred model, but ranges upwards to up to $\Sigma < 0.195$ eV depending on the precise setup of the model used for fitting. From other neutrino mass measurements we can place additional limits. In case of normal (inverted) mass ordering, current oscillation data constrain $\Sigma > 0.0587$ eV ($\Sigma > 0.0992$ eV), while the direct mass measurement by the KATRIN [25] (see Section 2.5.2 constrains $\Sigma < 1.4$ in either case.

There is clearly sensitivity to the neutrino mass available in cosmological data, however extracting it is model dependent. A direct measurement of the neutrino mass would benefit these cosmology fits, as it could be used as an input rather than an output of these models. Reducing the number of free parameters would allow fitting parameters that are only accessible through cosmology such as the dark-energy equation of state and the Hubble parameter more accurately.

2.4 Time of flight

Neutrinos are produced by astrophysical sources such as supernova explosions. Since they are produced in a very short burst, and travel a very long distance, it is possible to gain information on the neutrino mass by measuring their arrival times. The travel time delay compared to a massless particle for a massive neutrino of mass m with energy $E \gg m$ at a distance D from the detector is

$$\Delta t(E, m) = D \left(\frac{m^2}{2E^2} \right) = 25.7 \text{ ms} \times \left(\frac{D}{50 \text{ kpc}} \right) \left(\frac{m}{\text{eV}} \right)^2 \left(\frac{10 \text{ MeV}}{E} \right)^2 \quad (2.9)$$

Even for observable supernovae, the time of origin t_0 would not be known with high enough precision to extract a neutrino mass directly. However, since the timing delay scales with neutrino energy would lead to a higher spread in neutrino arrival times than would be expected for a massless neutrino.

To date, the only event from which a sufficient number of neutrinos has been detected to perform this analysis was SN 1987 A, for which 25 neutrinos were detected. Analysis of this data puts a limit on the neutrino mass at 5.7 eV (95% c.l.) [26]. This value carries some level of model dependence, in this case on the model of the time distribution of neutrino emission from a core collapse supernova. Prior knowledge of the neutrino mass from other measurements would inversely allow for refining these models.

Given a future galactic supernova within $D \simeq 20$ kpc, existing and near-future neutrino detectors are expected to have neutrino mass sensitivities of $m > 1$ eV for JUNO [27] $m > 0.5$ eV for Hyper-Kamiokande [28].

2.5 Direct laboratory measurements

If a particle with a well-known initial state decays in a process involving a neutrino, the mass of the neutrino can be measured by very precisely measuring the energy and momentum of the other decay products. The mass of the neutrino can then be extracted using energy and momentum conservation. These kinematic measurements of the neutrino mass are called direct neutrino mass measurements, as they are for the most part model independent. In the following section we follow Formaggio et al. [11] to outline how such a measurement works.

The primary candidate for such measurements is the β -decay $(A, Z) \rightarrow (A, Z + 1) + e^- + \bar{\nu}_e$. Where the continuous nature of the β -decay spectrum suggested the existence of the neutrino in the first place, the precise shape of the energy spectrum of the electron around the endpoint contains information about the neutrino mass. The electron energy spectrum for a neutrino with 3 component mass states can be written as the sum the contributions of each state. The differential decay rate $d\Gamma$ per unit of electron energy dE is given by

$$\frac{d\Gamma}{dE} = \frac{G_F^2 |V_{ud}|^2}{2\pi^3} (G_V^2 + 3G_A^2) F(Z, \beta) \beta (E + m_e)^2 (E_0 - E) \times \sum_i |U_{ei}|^2 [(E_0 - E)^2 - m_i^2]^{1/2} \Theta(E_0 - E - m_i) \quad (2.10)$$

where G_F is the Fermi coupling constant, V_{ud} is an element of the CKM matrix, E (β) denotes the electron's kinetic energy (velocity), m_e is the electron mass, E_0 , the 'endpoint energy,' corresponds to the maximum kinetic energy in the absence of neutrino mass, m_i are the neutrino mass states, $F(Z, \beta)$ is the Fermi function, taking into account the Coulomb interaction of the outgoing electron in the final state, and $\Theta(E_0 - E - m_i)$ is the step function that ensures energy conservation. The vector and axial-vector matrix elements are $G_V = 1$ and $G_A = -1.2646(35)$ for tritium, respectively [29].

By contracting all the global constants as well as an approximation for the $F(Z, \beta)\beta(E + m_e)^2$ near $E = E_0 - m_i$ this equation can be simplified to the approximation

$$\frac{d\Gamma}{dE} \approx 3r_0(E_0 - E) \sum_i |U_{ei}|^2 [(E_0 - E)^2 - m_i^2]^{1/2} \Theta(E_0 - E - m_i) \quad (2.11)$$

where r_0 is a detected event rate in the last eV of the spectrum in the absence of a neutrino mass. It contains the information of the constants as well as the approximations for β , $E + m_e$ and $F(Z, \beta)$. For a full treatment see Section 4 of Formaggio et al. [11].

Finally, we can introduce the effective neutrino mass-squared in this decay process as

$$m_\beta^2 = \sum_{i=1}^3 |U_{ei}|^2 m_i^2 = m_1^2 + |U_{e2}|^2 \Delta m_{21}^2 + |U_{e3}|^2 \Delta m_{31}^2 \quad (2.12)$$

resulting in a final approximate differential decay rate of

$$\frac{d\Gamma}{dE} \approx 3r_0(E_0 - E) [(E_0 - E)^2 - m_\beta^2]^{1/2} \Theta(E_0 - E - m_\beta) \quad (2.13)$$

The effect of a non-zero m_β on the shape of the tritium beta decay spectrum can be seen in Figure 2.3. If the spectrum near the endpoint energy can be measured with sufficient precision, m_β^2 can be determined.

Since the matrix elements and mass squared differences are known from neutrino oscillations to better than 4% precision [19], the individual m_i can be calculated from Eq.(2.12) if m_β^2 is known.

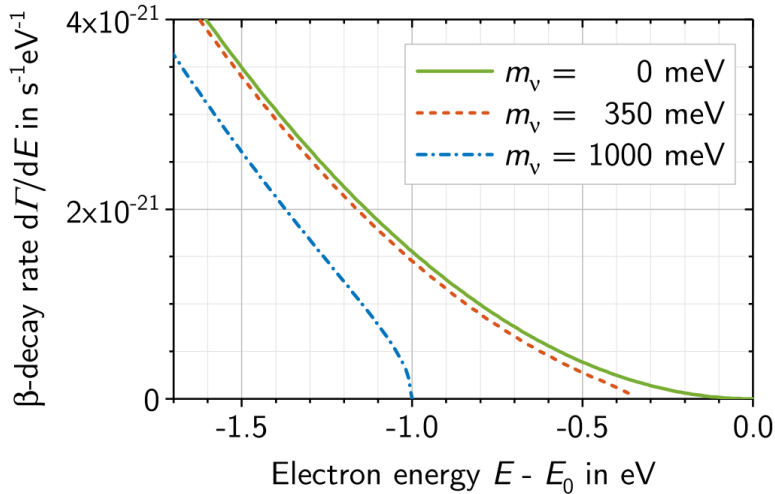


Figure 2.3: Beta spectrum of the decay of atomic tritium near the endpoint, as given by Eq. (2.13). In the figure, $m_\nu \equiv m_\beta$. Source: [30]

It should be noted, that since 2 of the mass states are non-zero, m_β is also non-zero even if the lightest mass state m_{least} were massless or unmeasurable small. Given the values from neutrino oscillations [19], the relation between m_{least} and m_β is

$$m_\beta^2 = m_{\text{least}}^2 + |U_{e2}|^2 \Delta m_{21}^2 + |U_{e3}|^2 \Delta m_{31}^2 \quad (2.14)$$

$$= m_{\text{least}}^2 + 7.74 \times 10^{-5} \text{ eV}^2, \quad (\text{NMO}) \quad (2.15)$$

or

$$m_\beta^2 = m_{\text{least}}^2 + |U_{e1}|^2 (-\Delta m_{21}^2 - \Delta m_{32}^2) + |U_{e2}|^2 (-\Delta m_{32}^2) \quad (2.16)$$

$$= m_{\text{least}}^2 + 2.47 \times 10^{-3} \text{ eV}^2, \quad (\text{IMO}) \quad (2.17)$$

In particular this means that for the inverted mass-ordering (IMO) $m_\beta \gtrsim 50 \text{ meV}$. An experiment capable of measuring m_β to better than this precision is guaranteed to either measure the neutrino mass, or rule out the IMO. This is the reason for the choice of target sensitivity of the Project 8 experiment (Section 3) just below this threshold.

2.5.1 Choice of isotope

As see in Figure 2.3, the relative effects of the neutrino mass on the differential decay rate are only significant for the region around the endpoint that is not very much larger than m_β . Therefore one important criterion for the selection of which isotope to use for measuring the beta decay spectrum is to maximize the rate of beta decay that produce electrons within a small region of this endpoint, say 1 eV for demonstration. This means we want to choose an isotope with a fairly short half life to produce the absolute event rate, and also with a low Q_A value, the mass difference between mother and daughter nuclide before and after the decay. A low Q_A means less total available energy, and therefore smaller spread of electron energies in the decay spectrum. This means a larger fraction of the decays happen close to the endpoint energy.

Table 1 shows how much of a few candidate isotopes is required to produce 1 decay event in the last eV of the spectrum per day. The tables shows that ${}^3\text{H}_2$, henceforth referred to in this work as (molecular) Tritium, yields by far the lowest required source mass per decay rate near the endpoint. This is of course not the only requirement,

Isotope	Spin-Parity	Half-life y	Specific activity Bq/g	Q_A eV	Branching ratio	Last eV	Source mass g
$^3\text{H}_2$	$1/2^+ \rightarrow 1/2^+$	12.3	3.6×10^{14}	18591	0.57	2.9×10^{-13}	2.0×10^{-7}
^{115}In	$9/2^+ \rightarrow 3/2^+$	4.4×10^{14}	0.26	147	1.2×10^{-6}	5.0×10^{-7}	7.5×10^7
^{135}Cs	$7/2^+ \rightarrow 1/2^-$	1.5×10^6	6.8×10^7	440	$(0.04-16) \times 10^{-6}$	2.2×10^{-8}	0.4 - 217
^{187}Re	$5/2^+ \rightarrow 1/2^-$	4.3×10^{10}	1.6×10^3	2470	1.0	1.2×10^{-10}	57
^{163}Ho	$7/2^- \rightarrow 5/2^-$	4750	1.8×10^{10}	2858		$\sim 10^{-12}$	$\sim 1.0 \times 10^{-5}$

Table 1: Candidate isotopes for direct neutrino mass measurements. The last column shows the source mass required to produce 1 event per day in the last eV of the spectrum. Q_A is the atomic mass difference. Source: [11]

however on the whole tritium based experiments have thus far turned out to produce the most competitive direct limits on the neutrino mass. One advantage of molecular tritium in this regard, is that it is a very simple molecule, which makes modeling so called final state effects of the molecule produced after the decay comparatively simple, though certainly not trivial [31], to model and account for. Pushing beyond the current best neutrino mass limits will nevertheless require moving from molecular tritium to atomic tritium to further simplify the final state effects. This is discussed in the following Section on KATRIN and Project 8.

See Formaggio et al. [11] for more detail on neutrino mass investigations performed with each of these isotopes, and their relative advantages.

2.5.2 KATRIN

The lowest limits on the neutrino mass to date have been measured by the KATRIN experiment [25, 32] using molecular tritium. KATRIN uses a "windowless gaseous tritium source" in which the decay of molecular tritium occurs



The decay electrons are then guided by a magnetic field to the pre-spectrometer and finally the main spectrometer, both of which are Magnetic-Adiabatic Collimation — Electrostatic (MAC-E) filters. This filter type, illustrated in Figure 2.4, uses an electric and a magnetic field in tandem. Electrons are introduced to the spectrometer from a region of high magnetic field and zero electrical potential. They follow the magnetic field lines, as these are spread out into a region of weakest magnetic field in the analysis plane of the spectrometer. This adiabatic transition collimates the electrons momentum in the forward direction in relation to the spectrometer. At the analysis plane, the electric potential is also maximal. The size of this maximum potential determines the minimum kinetic energy an electron must have to cross over to ultimately reach the detector plane. The MAC-E filter therefore acts as an integral filter allowing all electrons above a certain kinetic energy to be counted. By adjusting the threshold potential in steps, and measuring the integral flux of electrons at each, the beta spectrum can be reconstructed point by point.

The KATRIN collaboration has produced the most precise measurement of the neutrino mass-squared to date [25] at $m_\beta^2 = -0.14_{-0.15}^{+0.13} \text{ eV}^2$ resulting in an upper limit for the neutrino mass of $m_\beta < 0.45 \text{ eV}$ (90% c.l.). KATRIN's main spectrometer measures 23 m long and 10 m in diameter, making it likely the final iteration of the MAC-E filter as any further scaling of sensitivity would require an even larger size, which is deemed prohibitive.

A second limiting factor on KATRIN'S sensitivity is the final state distribution (FSD) of the produced HeT^+ molecule. Since KATRIN observes the decay of molecular tritium

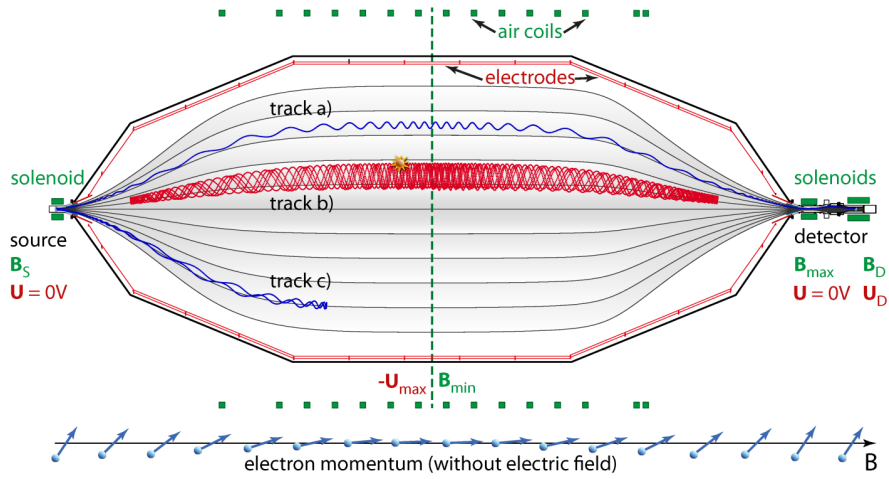


Figure 2.4: The principle of a MAC-E-Filter. The grey shaded area marks the magnetic flux tube connecting the source with the detector. The dashed green line at the center indicates the “analyzing plane” of the MAC-E-Filter, where the magnetic field is at its minimum B_{\min} and the electrostatic potential barrier at its maximum ($-U_{\max}$). Electrons, originating from the source on the left, are magnetically guided against the electrostatic retarding field towards the detector. Track a) is the trajectory of an electron with enough kinetic energy to overcome the retarding potential (cyclotron radius not to scale). The electron following track c) has less energy and is reflected back to the source. Track b) belongs to a magnetically trapped electron that has been created inside the MAC-E-Filter, for instance by a radioactive decay. The arrows at the bottom indicate the direction of the momentum of an electron relative to the guiding magnetic field line. The inhomogeneous field transforms transverse momentum into longitudinal momentum and back. Source: [33]

(Eq. (2.18), the Endpoint has to be corrected for the difference in binding energy of mother and daughter molecules

$$E_0 = Q_A - b_0 + b_{(f)0} - E_{\text{recoil}}, \quad (2.19)$$

where b_0 is the binding energy of the initial molecular state, $b_{(f)0}$ is the binding energy of the final molecular state, and E_{recoil} is the recoil energy imparted to the molecule.

This final state of the HeT^+ molecule can absorb a range of energies which effectively smears out the beta decay spectrum by the width of the distribution plotted in red in Figure 2.5. Calculating this distribution with enough precision to allow for sub eV resolutions on the neutrino mass is very difficult, but it is now possible to do precisely enough such that it is no longer the dominant systematic error [31]. However the broadening imparted by the FSD still results in a major statistical penalty, making it much more difficult to push below a few hundred meV neutrino masses.

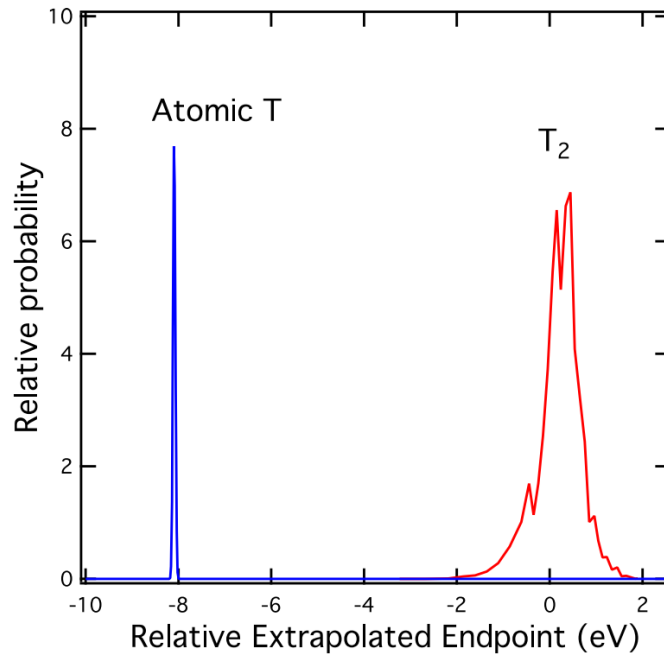


Figure 2.5: The ground-state manifold of molecular tritium compared to the ground state of atomic tritium. The ground-state Q-values differ by 8.29 eV. Because of recoil effects, the ground-state extrapolated endpoint values ($\Delta_{00} - m_e$ in [34]) differ by 9.99 eV, but the molecular rotational and vibrational excitations that broaden the molecular peak make the endpoint energy for the atomic decay effectively about 8 eV smaller than the molecule. Translational Doppler broadening corresponding to a temperature of 1 K is included in the atomic line. Source: Graphic from [11], the molecular line is from [35].

The limits imposed on neutrino mass sensitivity by the size restriction on further scaling of the MAC-E filter, as well as the sensitivity penalties imposed by the final state distribution warrant a change in technology for pushing below 100 meV sensitivity to m_β . The next section will present an experimental approach to surpassing these limitations.

3 Project 8

In this section we will introduce Project 8 [1], the neutrino mass experiment for which this thesis work was done. Project 8 aims to reach a sensitivity to m_β of 40 meV, with the goal of either determining the neutrino mass if it is larger than that or else determining that the neutrino masses are normally ordered.

Like previous direct neutrino mass experiments, Project 8 will measure the beta decay of tritium around the endpoint. Reaching the target sensitivity will require substantial improvements over the current state of the experiment KATRIN, discussed in Section 2.5.2. This is to be accomplished primarily with a switch in spectroscopy technique to cyclotron radiation emission spectroscopy (CRES) and from molecular tritium to atomic tritium.

3.1 CRES

The CRES technique is described and demonstrated in [36]. A gas source decays in a magnetic field emitting electrons which then experience centripetal acceleration around the B-field lines such that they perform cyclotron motion. This results in the coherent emission of radiation at the cyclotron frequency f :

$$2\pi f = \frac{2\pi f_0}{\gamma} = \frac{eB}{m_e + E/c^2} \quad (3.1)$$

where γ is the Lorentz factor, e is the elementary charge, m_e is the mass of the electron, c is the speed of light, and E is the kinetic energy of the electron. The zero-energy (non-relativistic) limit electron cyclotron frequency is a fundamental constant [12],

$$f_0 = 27.992489872(8)\text{GHz T}^{-1}. \quad (3.2)$$

Due to the energy dependence of the cyclotron frequency, we can measure the frequency to calculate the electron's kinetic energy from it. A sample CRES event is shown in Figure 3.1. The event begins abruptly and then chirps to higher frequency (lower energy) as it radiates away energy. The starting frequency represents the initial kinetic energy and is therefore the observable we are looking to measure. There are a series of frequency hops caused by discrete scattering events on residual gas that carry away some of the energy. Over the time frame shown in the figure, the electron travels about 60 km. A magnetic trap is required to keep the electrons in the sensitive volume of the CRES detector long enough to measure the starting frequency accurately.

The chief advantages of CRES are the high precision that is possible due to performing a non-destructive frequency-domain measurement, the extremely low background and the fact that tritium is transparent to the microwave frequency of the signal. The latter means that the radioactive source gas can be located inside of the CRES detector itself. This means that unlike a MAC-E filter there is no need for electron transport to the detector, and therefore no inherent limit on source column density as an electron does not have to travel long distances through the source without scattering. This means unlike a MAC-E filter, a CRES experiment will not have the same limitations on source size and therefore event rate as implied by the source to detector scaling relationship discussed in Section 2.5.2.

A CRES detector is also a differential spectrometer. It can measure the entire (or at least large sections of the) spectrum at once since every electron is sorted by frequency. This removes the "time expansion" penalty to measurement time required for filter-based spectrometry such as with a MAC-E filter [11], which must measure multiple times,

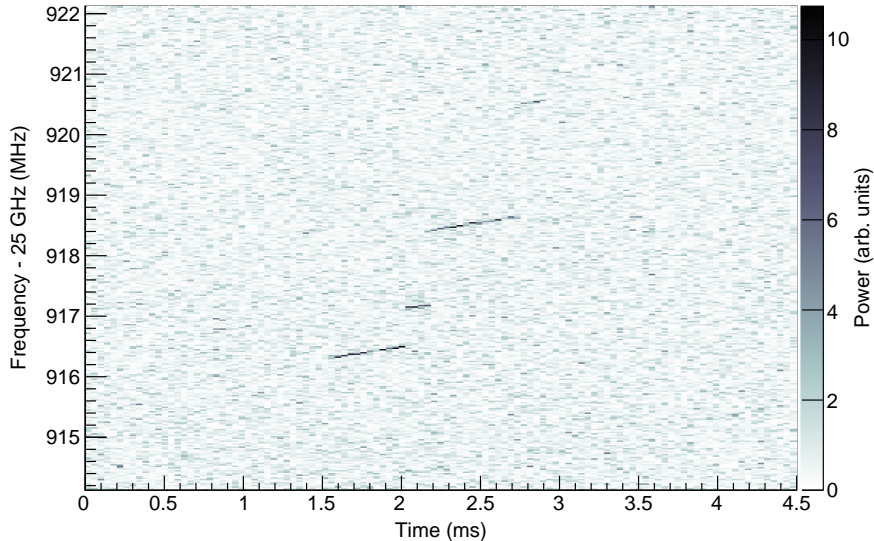


Figure 3.1: A single tritium beta-decay electron recorded with the CRES technique. An electron is created by ${}^3\text{H}_2$ decay near the lower left corner and forms a track that slopes upward due to radiation loss. The discontinuities from track to track are caused by the electron scattering inelastically from the residual tritium gas. The most probable jump size corresponds to about 14 eV. Eventually the electron scatters out of the trap and is lost. Source: [1]

setting the filter at a different energy threshold each time to build up the measured spectrum.

Extremely low backgrounds can be achieved with CRES. There are 2 distinguishable sources of background: physics background and false triggers. Physics backgrounds occur when an electron other than from tritium decay becomes trapped. To be mistaken for a real event it must have similar kinetic energy and a trappable momentum nearly perpendicular to the magnetic field. Beta decay gas contaminants are negligible in the vacuum environment, while decays on the walls of the vacuum chamber would return to the walls immediately due to the high magnetic field. This leaves only electrons created by cosmic rays as possible physical backgrounds which has been calculated at only about 0.01 events/(y eV m³).

False trigger backgrounds occur when random fluctuations in neighboring pixels of a spectrogram like in Figure 3.1 happen to appear like a real event track. This false trigger probability can be made arbitrarily small by increasing the threshold of integrated power along the spectrogram track [1]. This comes at the cost of detection efficiency for short but real tracks.

3.2 Atomic Tritium

The second major change Project 8 aims to make to improve neutrino mass sensitivity is a move from using molecular tritium to atomic tritium. As previously discussed in Section 2.5.2 and illustrated in Figure 2.5 the use of molecular tritium results in a difficult but treatable systematic error as well as an unavoidable statistical penalty. Part of the energy of the decay is absorbed by rotovibrational states of the daughter molecule which results in a few eV wide range of possible available kinetic energy for the electron which is to be measured. This results in an effective smearing out of the endpoint which can only be recovered with both very accurate knowledge of the FSD and significant, potentially

prohibitive, additional statistics.

Since the molecular state ${}^3\text{H}_2$ is energetically favored, atomic tritium must first be produced and then kept from recombining into molecules. Project 8 plans to use a magneto-gravitational trap to accomplish three goals at once: the decay electrons will be trapped by the magnetic field as required for CRES, the tritium atoms will be trapped by the combination of magnetic and gravitational fields, and finally hydrogen molecules will not be trapped because they do not have the required magnetic moment.

Trapping the atoms without contact to physical surfaces is required because free atoms of hydrogen recombine rapidly into molecules on surfaces. Recombination in gas-gas interactions is negligible at pressures below 10^{-5} mbar, since it is a three-body process due to momentum conservation requirements. A CRES apparatus must be operated at such low pressures in any case [1].

Not trapping T_2 is also very important, because the decay of tritium molecules would be a background on the atomic tritium endpoint. As can be seen in Figure 2.5 the endpoint energy of molecular tritium is actually higher than for atomic tritium. This is because the molecular end state $({}^3\text{HeT})^+ + e^-$ is a more tightly bound system than the atomic end state (for two tritium atoms one of which decays) $(\text{T} + {}^3\text{He}^+ + e^-)$. The additional chemical energy made available by the bound state produced by the molecular decay shifts the endpoint energy by a few eV compared to the atomic endpoint [37]. This means that a comparatively frequent decay of molecular decay at 8 eV from the endpoint produces electrons of the same energy as the relatively more infrequent and much more interesting decay of atomic tritium within 1 eV of its endpoint energy. This leads to a requirement of a very strict upper limit of the density ratios of T and T_2 of $n(\text{T}_2)/n(\text{T}) \lesssim 10^{-4}$ [1] in the trap.

The initial production of atomic tritium does not have to be quite this efficient, since the plan is to use magnetic guides to inject T into the trap. Molecules would not be guided by magnetic fields and therefore effectively filtered out.

Nevertheless the production of the required atomic tritium and its cooling to trappable temperatures is a significant challenge. The current baseline plan for atomic tritium production and cooling is illustrated in Figure 3.2. Atoms are initially produced by thermal dissociator, or "cracker", in which a sizable fraction of molecules is split into atoms. Atoms are then cooled by contact with an accommodator surface operated at ≈ 160 K; the temperature at which the recombination rate into molecules on aluminum is at a minimum. Further surface contact cooling is to be performed on a liquid helium cooled nozzle at ≈ 10 K. Due to the high recombination rates the design must minimize the average number of bounces per atom to perform this cooling with acceptable losses. Any further cooling must be performed with contactless methods for which we envision a magnetic evaporative cooling beamline (MECB) [38].

To achieve the anticipated trap density requirements we foresee requiring an initial flow of atoms from the source of $\gtrsim 10^{18}$ atoms/s, such that after taking into account the losses during cooling we can an injection of $\approx 10^{14}$ atoms/s into the trap at trappable temperatures of a few mK.²

²Hamish Robertson, atomic trap calculator

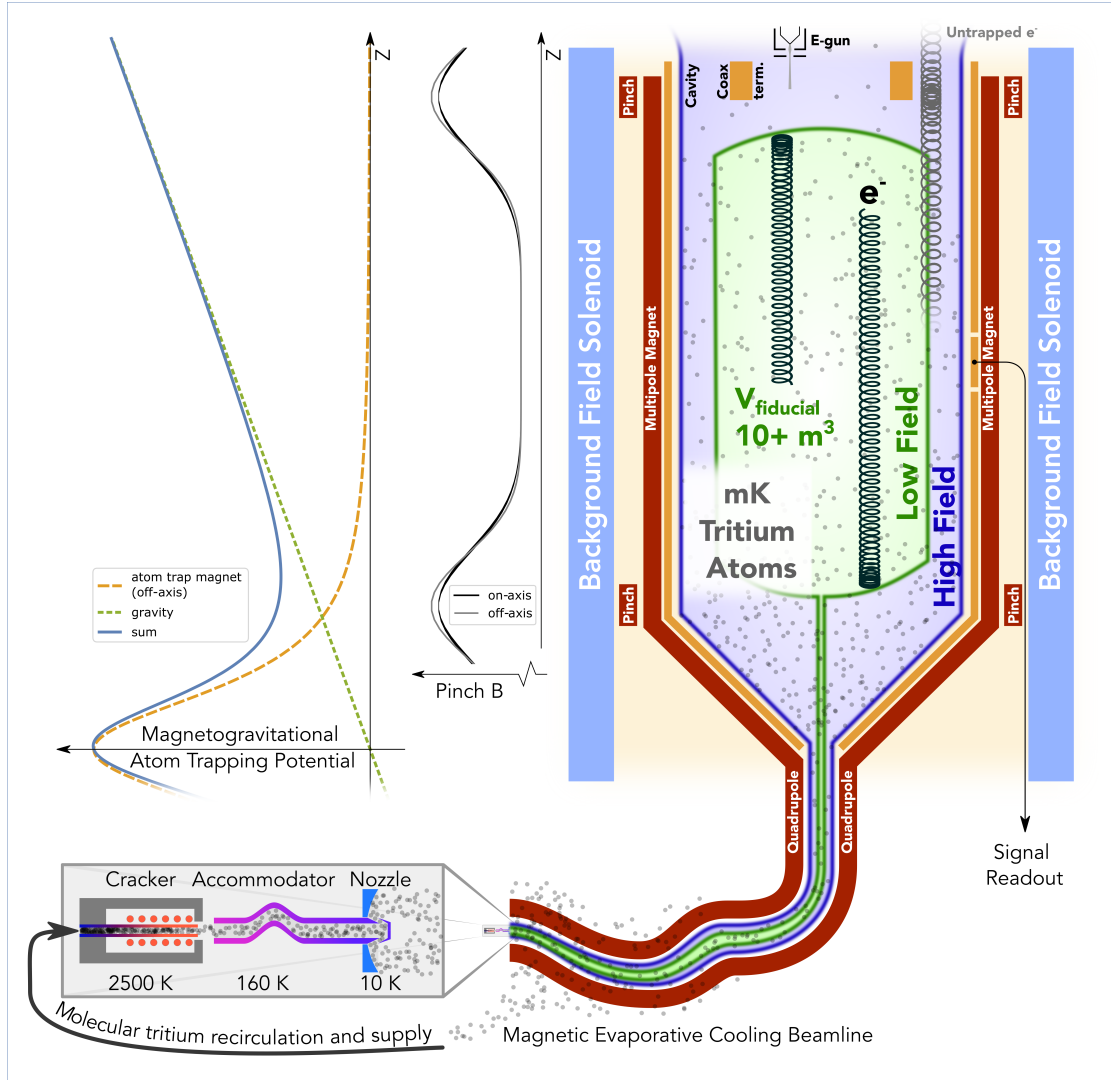


Figure 3.2: Sketch of the atomic tritium beamline as currently envisioned. T_2 molecules start in the bottom left of the image where they are injected into a thermal dissociator or "cracker" that produces T atoms which then pass through multiple cooling stages. At a temperature of a few mK they can then be injected into a magneto-gravitational trap displayed in the anticipated upright position at the right of the image. In this trap T can decay releasing electrons that are also trapped in the magnetic field and can then be measured with the CRES technique. A plot of the trapping potential is shown on the top left hand side. Graphic by Alec Lindman.

4 Mainz Atomic Test Stand (MATS)

To meet the requirements for atomic tritium production multiple parallel efforts are underway as part of Project 8. One effort is the Mainz Atomic Test Setup (MATS) which is a setup designed to test sources of atomic hydrogen for suitability to Project 8's needs. For the duration of the work presented in this thesis the, MATS was employed to characterize a thermal dissociation source option called the "Hydrogen Atomic Beam Source (HABS)", which is described in more detail in Section 4.1.

The MATS is operated using molecular hydrogen (with the option of using deuterium) rather than tritium for all tests presented in this thesis. Due to the substantial challenges of working with radioactive gasses, Project 8 follows the approach of developing components of the final beamline using regular hydrogen first whenever possible to minimize the additional cost and time burden of tritium handling. Follow up tests to ensure that lessons learned during development also work with tritium are planned afterwards e.g. in the KAMATE collaboration between JGU Mainz and TLK in Karlsruhe.

A picture of the MATS along with a highly simplified schematic is shown in Figure 4.1. The MATS is a stack of vacuum chambers connected by small openings called skimmers through which the hydrogen beam passes. All chambers are separately connected to vacuum pumps. While there are a large number of parts required to make this system function, as well as a number of secondary instruments (e.g. pressure gauges) in this setup, for now we will only discuss the main instruments depicted in the schematic and their function in the context of this thesis.

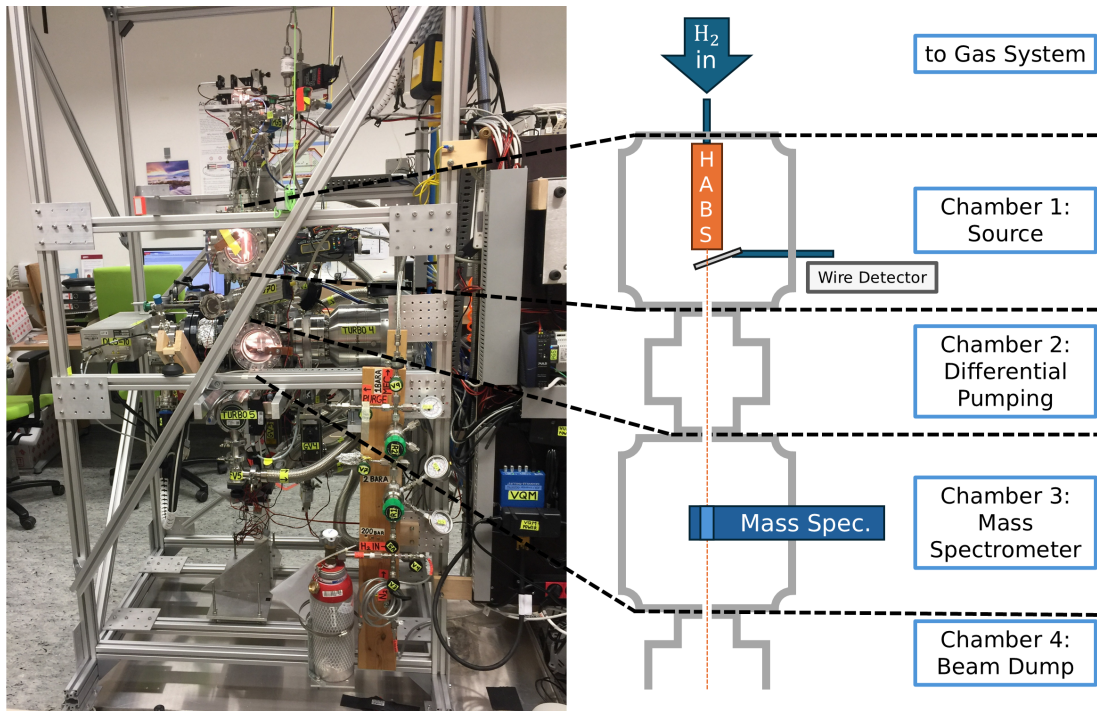


Figure 4.1: On the right we show a schematic view of the MATS vacuum chamber layout. The dashed lines to a picture of the setup on the left show where these sections line up with the real setup. Work presented in this thesis is primarily carried out in Chamber 1, which contains the wire detector mounted on a translatable stage for scanning through the beam. Photo on the left by A. Lindman.

The topmost chamber contains the Hydrogen Atomic Beam Source (HABS) and is therefore called the source chamber. Molecular hydrogen is passed from the gas system

into the top of the HABS. Depending on the temperature the HABS is heated to, a portion of the gas is dissociated into atoms and emitted from the bottom end of the source mixed with the remaining molecular hydrogen. Unless otherwise indicated, the calorimetric wire detector which is the subject of this thesis is located in the source chamber, as indicated by the schematic. This puts it as close as possible to the source, maximizing signal, and enables the detector to be translated underneath the source, to map the beam shape.

Chamber 2 is a differential pumping section. Its purpose is to allow for a larger pressure difference between the source chamber above and the mass spectrometer chamber below. The source chamber is necessarily at a comparatively high pressure, when gas is supplied to it via the source. Effusion of this gas through the bottom skimmer means the chamber below is exposed to a fraction of this gas load raising its pressure as well. By including the differential pumping section, which essentially repeats this effusion process at a lower pressure, only a much smaller fraction of this gas ends up in the mass spectrometer chamber.

The size of the skimmers between the chambers increases from the topmost skimmer between chambers 1 and 2 such that all geometric lines of sight through the topmost skimmers will end up in the beam dump without hitting other surfaces. This is meant to ensure that the primary beam is not scattered in the mass spectrometer region, which would significantly raise the pressure in that chamber.

This arrangement is optimized to achieve a very low background pressure ($\sim 10^{-10}$ mbar) in the mass spectrometer chamber even when a significant amount ($\sim 1 \times 10^{18}$ molecules/s) of hydrogen is introduced to the system through the source. This maximizes the signal-to-background ratio when measuring the beam with the mass spectrometer, which would also measure any background pressure of hydrogen in its chamber.

For most of the measurements performed with the wire detector presented in this thesis, the arrangement of chambers below is not very important. They are introduced here because the optimizations made for the mass spectrometer will influence design decisions made during this thesis and because references to measurements made with the mass spectrometer will occasionally be made.

4.1 Hydrogen Atomic Beam Source (HABS)

For the results presented here, we use a commercially available “Hydrogen Atomic Beam Source” (HABS)³. This is a thermal hydrogen dissociator manufactured by *MBE Komponenten GmbH* that produces atomic hydrogen by passing a flow of molecular hydrogen through a tungsten capillary that is heated to around 2200 K [39]. An annotated model showing the inner workings of the HABS is shown in Figure 4.2.

A simplified diagram of the gas system is shown in Figure 4.3. The hydrogen flow through the source is controlled by a mass flow controller⁴ in the range of 0.002 – 20 standard cubic centimeters per minute⁵ (sccm). Before entering the source, the gas flows through a purifier⁶ which removes any water, oxygen or hydrocarbon contaminants. This purifier takes a few seconds at high flows and up to few hours at very low flows, to be saturated with hydrogen to the point, that the same amount of hydrogen that enters it from the mass flow controller side exits downstream. We therefore employ a pneumatically operated valve just after the purifier, which we switch on and off in time with the mass flow controller, in order to keep the purifier at a given desired pressure that

³<https://www.mbe-komponenten.de/gas-sources/habs/>

⁴Alicat Model: MCE-20SCCM-D-DB15K

⁵1 sccm = 4.48×10^{17} molecules/s

⁶Entegris GateKeeper MC1-904F

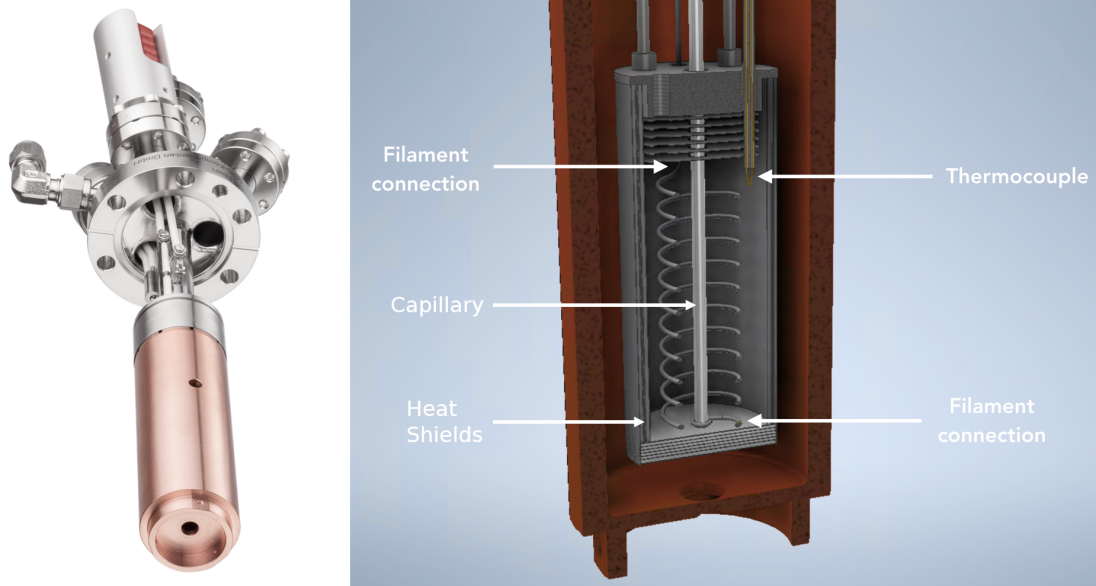


Figure 4.2: An image of the HABS attached to its vacuum flange on the left. On the right is a cutaway of a 3D model showing the internal parts. Gas is pumped through the capillary, which is heated by passing a current through a heating filament in close proximity. The thermocouple can be used to monitor the source temperature. Image by MBE Komponenten, CAD model adapted from A. Lindman.

corresponds to the steady state flow set on the mass flow controller. This is necessary to allow fast switching of gas flows below 10 sccm when using the purifier. This is described in more detail in Appendix B.

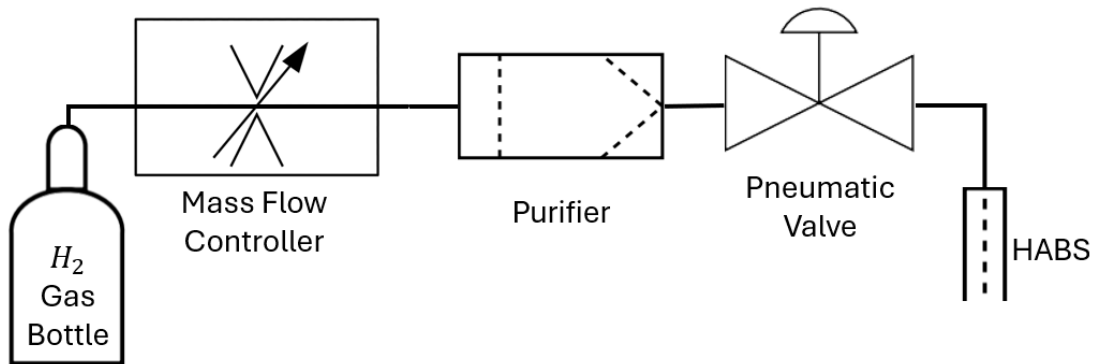


Figure 4.3: Simplified gas flow diagram showing only components relevant to wire detector operations. Gas flows from the gas bottle through a mass flow controller which is used to set the flow of hydrogen into the setup. The purifier removes impurities from the gas flow. The Pneumatic valve is used in synchronization with the mass flow controller, to isolate the purifier in the state required for steady state flow as set by the flow controller. The purifier otherwise acts as a capacitor which first needs to be saturated with hydrogen before it passes an equal amount of gas as it receives from the flow controller.

For the primary results presented here, the HABS capillary is located 35 mm above the wire detector. At typical settings of a flow of 1 sccm of H₂ at 2200 K, the source produces a beam intensity of order 10^{16} atoms/cm²s [39]. In the ideal case where all atoms landing on the detector recombine, releasing 4.46 eV per molecule, this corresponds to a heat load of about 7 mW/cm². In the case of the detector wire that will be discussed

in Section 5 with a length of 20 mm and diameter of $5\ \mu\text{m}$ this corresponds to at most $7\ \mu\text{W}$ of heating along the length of the wire.

Hydrogen is emitted from the HABS as a diverging beam, with an initially undetermined fraction of dissociation [40]. Since the wire is not a point detector, it always integrates a portion of the beam along its length. The change in beam intensity along this length must be modeled.

We derive the HABS beam output intensity distribution j_{HABS} based on a theoretical model [41] modified by the setup geometry. As it will be defined, j_{HABS} is the probability density per unit angle [1/sr] of finding a particle which leaves the HABS capillary at a certain angle from the capillary axis downstream of the copper cooling shroud covering the HABS.

Figure 4.4 illustrates the geometry of the HABS. The capillary forms an initial beam which is then modified, when parts of it are obscured by the copper shroud. We call the fraction of the capillary which is visible under a viewing angle θ relative to the capillary axis $g_{\text{visible}}(\theta)$ (see Section 4.1.2). This functions as a geometric correction factor to the initial output intensity distribution of the capillary $j_{\text{norm}}(\theta; l_{\text{eff}})$ (see Section 4.1.1) such that

$$j_{\text{HABS}}(\theta; l_{\text{eff}}) = j_{\text{norm}}(\theta; l_{\text{eff}}) \cdot g_{\text{visible}}(\theta). \quad (4.1)$$

This does include an implicit assumption that gas exiting the capillary has a uniform density across the exit plane. This may not be exactly true, and Monte Carlo simulations indicate this may change the effective g factor by a few percent, depending on the actual gas density distribution. Absent a fully-fledged model for the gas density distribution in the exit plane of the capillary, for the purposes of this thesis, we will assume it to be a uniform distribution, such that every point in the capillary exit plane emits gas with equal intensity.

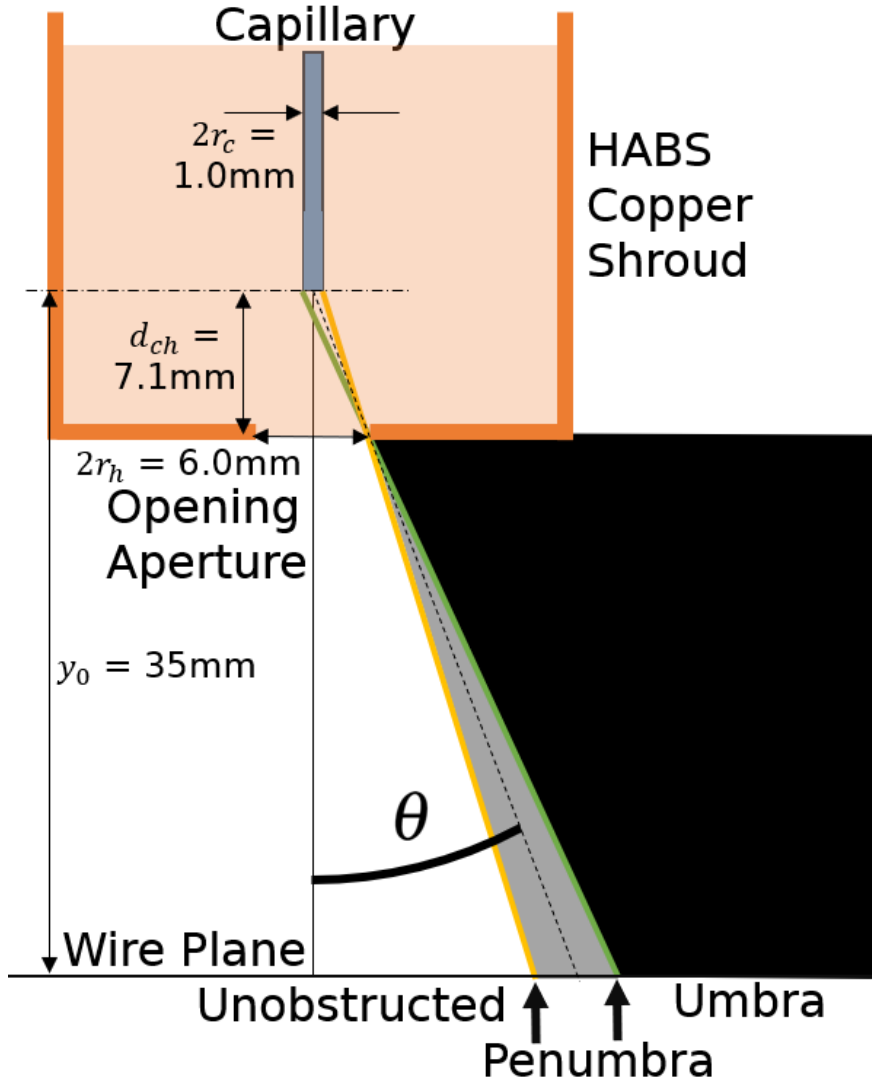


Figure 4.4: A sketch of the geometry of the HABS copper shroud, which partially and then fully obscures the capillary from which the hydrogen beam originates. The inside edge of the penumbra is located at 19.4° and the outside edge at 26.2° . Beyond the outside edge no portion of the beam is expected to be visible (umbra). The angle θ is always measured between the capillary axis and a line drawn from the center of the capillary at its front face. Additional clarification on the coordinate definitions is available in Appendix A.

4.1.1 Capillary output distribution

As described in the following text, we construct the output distribution from the capillary $j_{\text{norm}}(\theta; l_{\text{eff}})$ such that it is a normalized probability density function. Normalization is useful, since the total flow of molecular hydrogen through the source capillary is known and controlled by a mass flow controller.

We start from the theoretical model of beam intensity from a cylindrical capillary, which is adopted from literature and denoted with j . Refer to Tschersich et. al. [41] for a comprehensive explanation. j is a function with a single dimensionless shape parameter called the effective length, l_{eff} , which describes the effective ratio of length to diameter of the capillary. l_{eff} differs from the physical aspect ratio of the capillary if gas flow through the capillary is large enough, such that the flow cannot be approximated as transparent molecular flow along the entire length. All gas flows used in our study are large enough

that l_{eff} is much shorter than the physical length of the capillary.

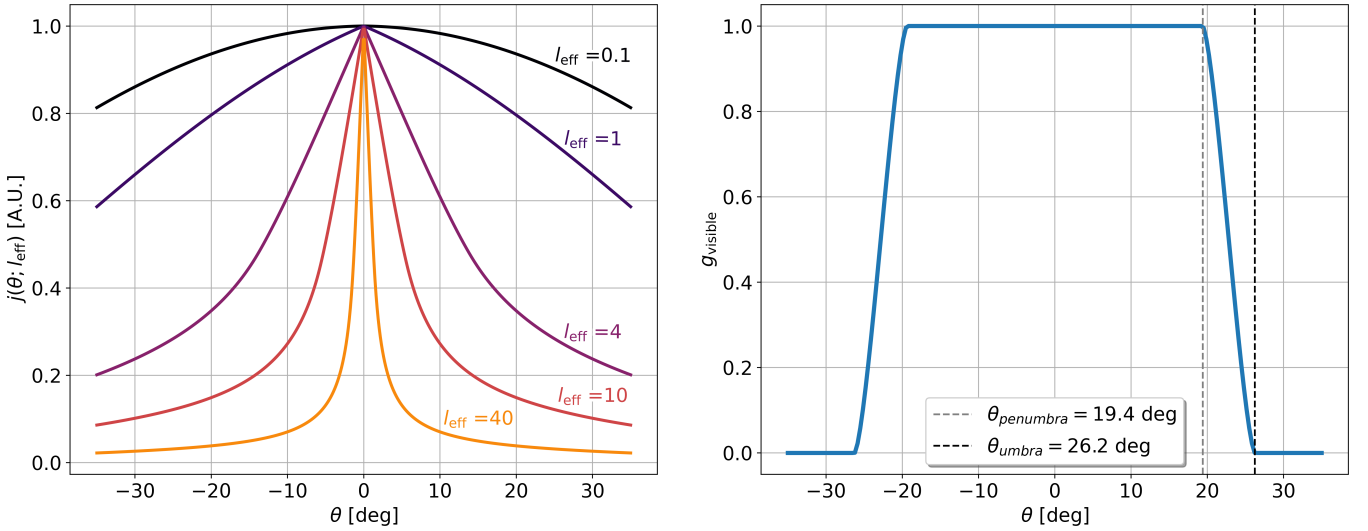
The beam model j is given by

$$\begin{aligned} j(\theta) &= j_d(\theta) + j_w(\theta) \\ \text{with } j_d(\theta) &= \cos(\theta) \cdot U(\beta) \\ \text{and } j_w(\theta) &= \frac{4}{3\pi} \left(1 - \frac{1}{2l_{\text{eff}}+1}\right) \frac{1}{l_{\text{eff}}} \frac{\cos(\theta)^2}{\sin(\theta)} (1 - V(\beta)) \\ &\quad + \left(1 - \frac{1}{2l_{\text{eff}}+1}\right) \cos(\theta)(1 - U(\beta)), \end{aligned} \quad (4.2)$$

$$\text{where } \begin{cases} U(\beta) = (2\beta - \sin(\beta))/\pi \\ V(\beta) = \sin(\beta)^3 \\ U(\beta) = V(\beta) = 0 \end{cases} \quad \begin{cases} \theta < \arctan(1/l_{\text{eff}}) \\ \text{otherwise} \end{cases} \quad (4.3)$$

$$\text{and } \beta(\theta) = \arccos(l_{\text{eff}} \cdot \tan(\theta)). \quad (4.4)$$

Here j_d is the formed by the gas which passes through the tube *directly* without wall interactions after the flow becomes molecular, whereas j_w is the gas which is rescattered from the *walls* of the capillary before exiting. V and U are auxiliary functions which we do not interpret physically.



(a) The relative output intensity j as a function of angle from the capillary axis θ . j converges to the Lambert cosine law for small l_{eff} , equivalent to a zero length aperture. For large l_{eff} it becomes a more centrally focused beam.

(b) The fraction of the capillary opening that is visible to an observer (in this case the wire) from the angle θ . At high angles the copper shroud surrounding the HABS capillary obscures the opening, first partially and then entirely, leading to reduced hydrogen flux at those angles.

Figure 4.5: The two beam shaping components of $j_{\text{HABS}}(\theta; l_{\text{eff}})$ are plotted as a function of the viewing angle θ . On the left we show the shape of the beam as it exits the source capillary, and on the right the multiplicative geometric modification function g_{visible} that is caused by the exit aperture of the HABS shroud.

Figure 4.5 shows how j and g_{visible} evolve with angle. j falls off to reduced intensities as the angle increases, decreasing more sharply for larger l_{eff} . g_{visible} acts as a window function with a smooth transition from fully visible at small angles, to partially shadowed, to fully obstructed at larger angles.

We normalize the intensity profile j by the integral over the emittance hemisphere

$$j_{\text{norm}}(\theta; l_{\text{eff}}) = \frac{j(\theta; l_{\text{eff}})}{\int_0^{\pi/2} \int_0^{2\pi} j(\theta, l_{\text{eff}}) \sin \theta d\theta d\varphi}. \quad (4.5)$$

It should be noted here that since j is also a function of the effective length l_{eff} the normalization integral has to be recalculated for every l_{eff} . The normalization as described here results in the integral of j_{norm} over the hemisphere being equal to one.

$$\int_0^{\frac{\pi}{2}} \int_0^{2\pi} j_{\text{norm}}(\theta; l_{\text{eff}}) \sin \theta d\theta d\varphi = 1. \quad (4.6)$$

Normalized this way, j_{norm} can be treated as a probability density function for the emission of any single gas particle.

After multiplication with $g_{\text{visible}}(\theta)$, $j_{\text{HABS}}(\theta; l_{\text{eff}})$ is of course no longer normalized to 1. This is the intended behavior, as we can measure how many particles flow through the capillary, but we cannot directly measure how many make it out of the copper shroud.

4.1.2 Geometrically visible fraction of the capillary

In this section we discuss the windowing effect of the cutout in the HABS shroud on the beam as pictured in Figure 4.4. Depending on the viewing angle θ a different fraction of the capillary is visible from below, which we call g_{visible} . This fraction is relevant for the beam intensity on the wire, as only the portions of the capillary occluded by the HABS shroud do not contribute, which leads to a sharp drop in beam intensity within the penumbra of the shroud. The resulting window function $g_{\text{visible}}(\theta)$ is relevant for calculating the heating power due to the beam on the wire detector, which will be used in fits in Section 8.

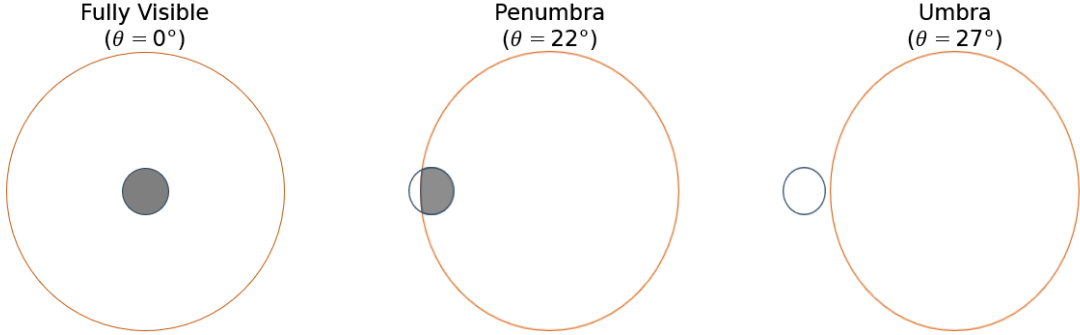


Figure 4.6: Illustrated view of the capillary when looking up at the HABS from the wire detector when it is placed in the center, the penumbra and the umbra of the HABS shroud. The shaded area of the smaller circle represents the region of the capillary end surface that is visible from the wire. The exact size and shape of this region depends on the viewing angle θ at which the capillary is located relative to the wire.

We define

$$g_{\text{visible}}(\theta) = \frac{A_{\text{visible}}(\theta)}{A_{\text{capillary}}}, \quad (4.7)$$

where $A_{\text{capillary}}$ is the area of the capillary end face and A_{visible} is the portion of that area which is visible from a viewing angle θ as illustrated in figure 4.4. Figure 4.6 shows that when seen from below, this problem turns into a calculation of the intersection of the circles formed by the capillary and the opening in the HABS shroud. Calculating the area of the intersection when accurately taking perspective and the resulting change from circles to ellipses in the projection into account is quite complicated. Instead we will make approximations to keep the problem analytically solvable since the resulting equation will be called many times during the fitting routines it will be used for.

We will simplify the problem by assuming that any deviation away from a circular projection is small, since we always expect to be fully in the umbra for $\theta > 30^\circ$. We will also approximate the arc section formed by the HABS shroud as a straight terminator moving across the circle formed by the capillary. This is only a small deviation, since the much larger HABS only has a small curvature over the width of the capillary as can be seen in Figure 4.6. We accept the few percent level inaccuracy introduced by these approximations.

The geometric approximation to a straight terminator passing over a circle, illustrated in Figure 4.7, allows us to calculate A_{visible} as the integral over a circle equation such that

$$A_{\text{visible}} = 2 \int_{z_1}^{z_0} dz \sqrt{r_c^2 - z^2} \quad (4.8)$$

where r_c is the inner radius of the capillary. Which has the analytical solution of

$$A_{\text{visible}} = r_c^2 \left[\frac{z}{r_c} \sqrt{1 - \left(\frac{z}{r_c}\right)^2} + \arcsin\left(\frac{z}{r_c}\right) \right]_{z_1}^{z_0}. \quad (4.9)$$

Since we always choose $z_0 = r_c$ to be on the edge of the capillary circle we can calculate A_{visible} as a function of only z_1

$$A_{\text{visible}}(z_1) = r_c^2 \left(\frac{\pi}{2} - \frac{z_1}{r_c} \sqrt{1 - \left(\frac{z_1}{r_c}\right)^2} - \arcsin\left(\frac{z_1}{r_c}\right) \right). \quad (4.10)$$

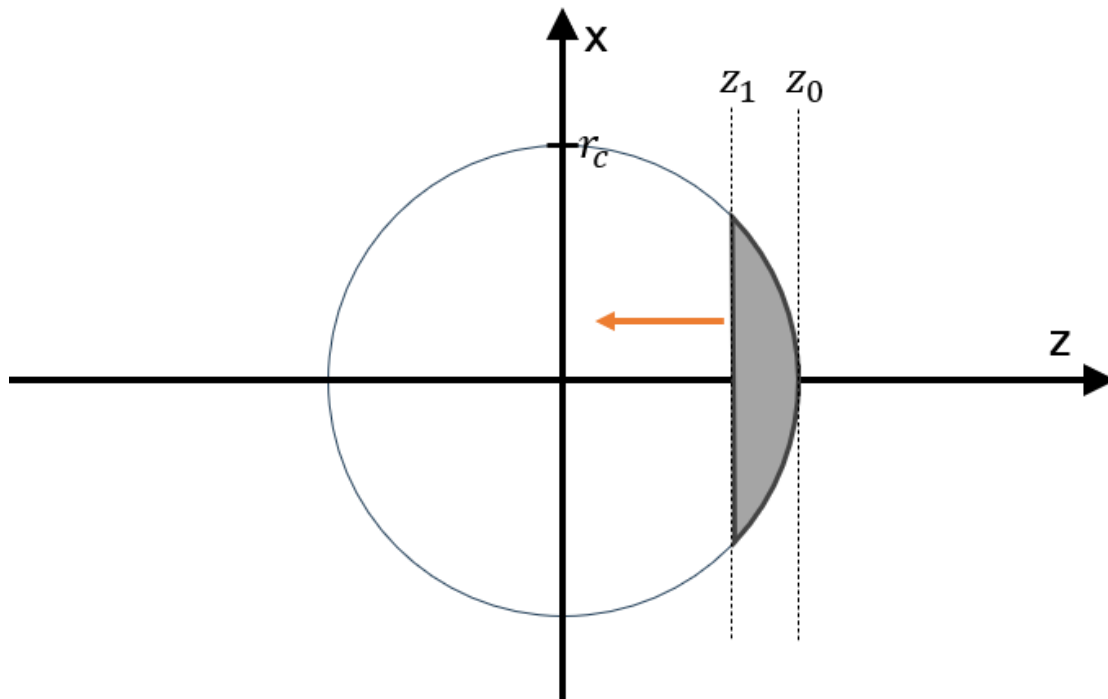


Figure 4.7: Illustration of the integration of A_{visible} . The capillary circle is integrated along a straight terminator as a simplification for the ellipsoidal arc shaped shadow cast by the circular HABS shroud opening.

We can then write z_1 as a function of the viewing angle θ_1 under which the HABS shroud occludes the capillary up to z_1

$$z_1 = r_h - d_{\text{ch}} \cdot \tan(\theta_1), \quad (4.11)$$

where r_h is the radius of the opening in the HABS shroud, and d_{ch} is the distance between the HABS opening and the capillary, as illustrated in Figure 4.4. And thus we can solve $A_{\text{visible}}(\theta)$ for any viewing angle θ within the penumbra. The final piecewise function for g_{visible} under any viewing angle is then.

$$g_{\text{visible}}(\theta) = \begin{cases} 1 & \text{if } \theta < \theta_{\text{penumbra}} \\ \frac{A_{\text{visible}}(z_1(\theta))}{\pi r_c^2} & \text{if } \theta_{\text{penumbra}} \leq \theta \leq \theta_{\text{umbra}} \\ 0 & \text{if } \theta > \theta_{\text{umbra}} \end{cases} \quad (4.12)$$

with $\theta_{\text{penumbra}} = \arctan\left(\frac{r_h - r_c}{d_{\text{ch}}}\right)$ and $\theta_{\text{umbra}} = \arctan\left(\frac{r_h + r_c}{d_{\text{ch}}}\right)$. The resulting function for $d_{\text{ch}} = 7.1$ mm, $r_h = 3.0$ mm, and $r_c = 0.5$ mm is plotted in Figure 4.5b.

While these size and position values can of course be measured in principle, in practice they have not been measured to the precision implied here. This means it is sometimes necessary to treat them as free model parameters when fitting data measured with the wire detector. Since d_{ch} is the least precisely known, and since these parameters can have highly correlated effects on fits, we generally only fit d_{ch} as a single additional geometry parameter. See Section 8.3 for more details.

More generally, any misalignment of the capillary and the HABS shroud, either in angle or position, would change the calculation presented above. In our simplified approach we have assumed that both the capillary and shroud openings are perfectly centered on each other and have no tilt with respect to each other, such that we can define the y-axis as running through the centerline of the capillary and the shroud opening. The real assembly may subtly deviate from this simplification, but we do not quantify that effect in this thesis.

5 Calorimetric Wire Detector

In this section we will discuss the development of the calorimetric wire detector. We will introduce formulae to describe our understanding of heat flow along the wire, use these for simulation of the detector and illustrate the design iterations we went through.

The operating principle of the detector is the detection of the heat released by the recombination of atomic H back into H₂ on the surface of a thin wire. This calorimeter wire is strung across the beam, such that it intercepts a small slice of the beam. A sizable fraction (in the tens of percent depending on the surface) [8] of the atoms that hit the wire stick to its surface, where they can recombine into molecules, releasing 4.46 eV per molecule [9]. A portion of this energy is absorbed by the wire causing a slight heating, which can be detected by measuring the corresponding increase in resistance. Such detectors for atomic hydrogen beams have been previously discussed in literature [3, 4].

For reference during the ensuing descriptions, the final result of development work in this thesis is the wire detector depicted in Figure 5.1, which consists of a 5 μm thick gold-coated tungsten wire, that is strung across a 20 mm wide gap. On each side of the gap, the wire is mounted on the aluminum nitride printed circuit board (PCB) by soldering it to copper traces leading to the readout electronics. The thickness of the wire was chosen to be the thinnest that could be readily procured and assembled into the detector. A thinner wire has higher base resistance as well as a lower heat conductivity such that, for a given heating power, temperature changes to the wire and resulting resistance changes are maximized. For the same reason a longer wire to further increase the aspect ratio of the detector is preferable. The length of the wire used here was chosen to fit within the space available in the vacuum chamber and to pass through a CF40 vacuum flange.

The wire resistance is measured by applying a constant current to the wire and recording the voltage drop over the wire with a digital multimeter. The wires typically have a room temperature resistance of $\approx 65 \Omega$ rising to as much as 100Ω during operation.

The detector PCB is mounted on a z-translator stage⁷, such that the wire can be scanned across the hydrogen beam. About 31 mm of travel is available within the confines of the vacuum chamber. This travel covers roughly -15° in one direction and $+30^\circ$ of the beam in the other direction of the capillary axis, as seen from the wire's location. Approximately 25% of particles emitted from the capillary are in this region, and the beam intensity drops to $\approx 40\%$ of its maximum intensity at 20° off-center for a beam produced by a typical flow of 1 sccm⁸. Due to an aperture, the beam is cut off beyond 26° allowing for measurements with the wire fully outside of the beam. The details of the hydrogen beam source are described in Section 4.1.

In the following subsections we will discuss the various effects that must be accounted for when doing calorimetry using a resistive wire. We will introduce these effects in the context of a finite-element thermal model of the wire which illustrates the scaling of various heat fluxes on the temperature - and by extension resistance - of the wire. Simulated design studies based on this model informed our decisions when building the wire calorimeter and will be presented later in this section. The simulation is realized as Python code available on GitHub⁹.

⁷McAllister Bellows-sealed Linear Translator (CF 40)

⁸1 sccm $\approx 4.48 \times 10^{17}$ molecules/s

⁹https://github.com/christianmatthe/wire_detector

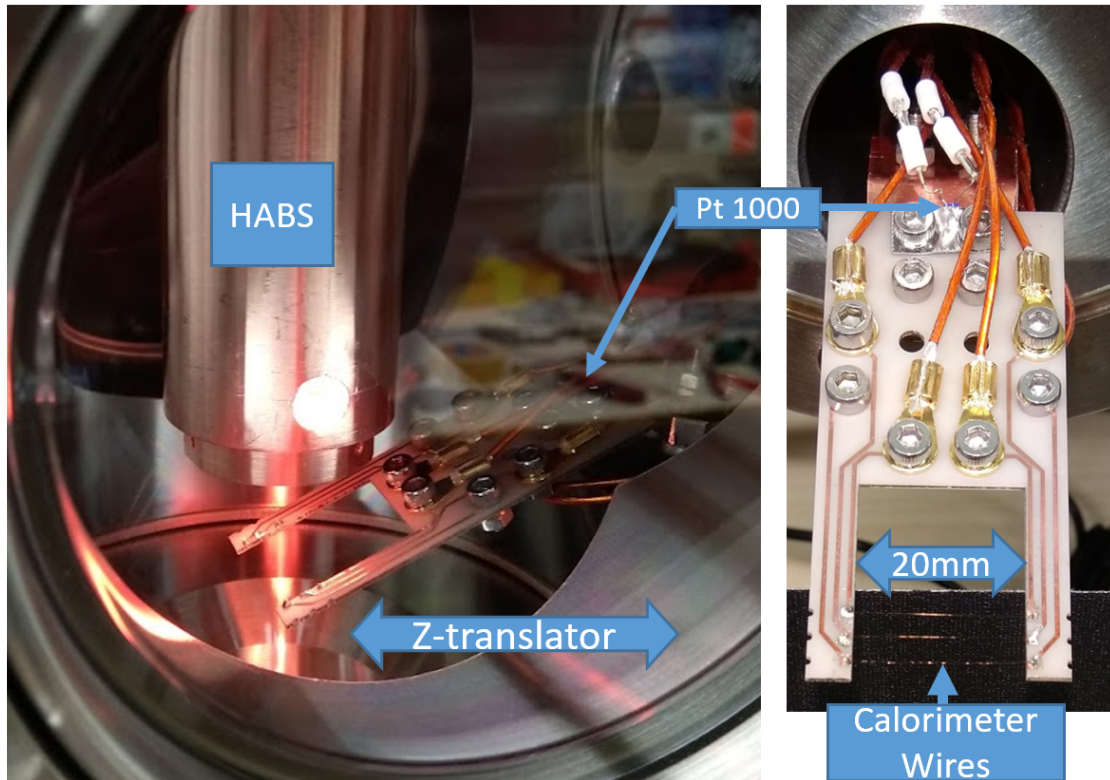


Figure 5.1: On the left is a view into the vacuum chamber containing both the hydrogen atomic beam source (HABS) and the wire detector. The HABS can be seen to be glowing as it does when operated at high temperatures. The z-axis, along which the wire detector can be moved, is indicated. A frontal view of the wire detector is shown on the right. Three wires are attached to the detector board for redundancy. The rearmost wire is used for all the data presented in this thesis. A Pt1000 temperature sensor is clamped to the back of the detector board for monitoring its temperature.

5.1 Signal: change in resistance

The direct measurable of the wire detector are the current I that flows through the wire and the voltage drop V over the wire. Using these the resistance $R = V/I$ can be determined. The wire resistance depends on its temperature, which forms the basis of the calorimetric measurement. In linear approximation, for an arbitrary temperature distribution $T(x)$ along a cylindrical wire the total wire resistance is

$$R = \int_{\text{wire}} \frac{\rho_R}{A_{\text{cs}}} (1 + a \cdot (T(x) - T_{\text{ref}})) dx \quad (5.1)$$

with ρ_R the specific resistance, A_{cs} the cross sectional area and a the temperature coefficient of resistivity, and T_{ref} is the reference temperature at which the quoted or measured value of ρ_R and a are valid.

To simulate behavior of the wire resistance we therefore need to calculate the temperature distribution along the wire. This distribution is only analytically solvable if one makes simplifying assumptions, requiring that heating effects be linear in temperature. Most obviously this means approximating thermal radiation ($\propto T^4$) with a Taylor expansion to first order. Studies of calorimetric wire detectors based on analytical modeling are available in literature [3]. While good approximations can be made for small temperature changes < 50 K we nevertheless opt for finite-element methods to gain more flexibility.

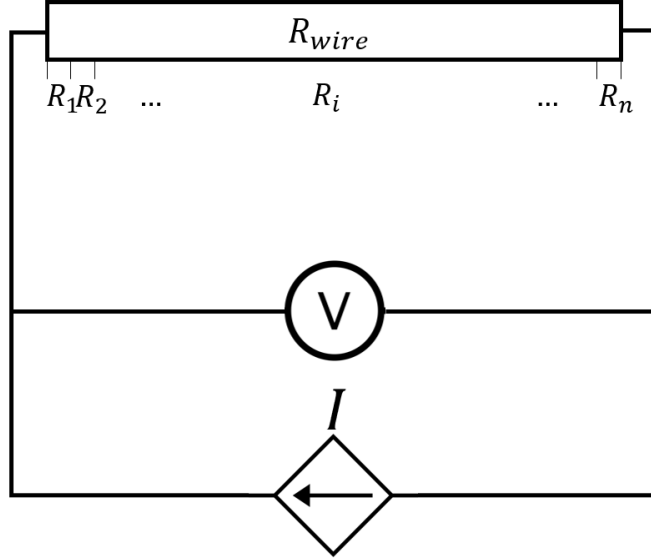


Figure 5.2: Basic electrical design of the wire detector. The main functional piece is the calorimeter wire strung across a gap in the detector board. The voltage drop V over the wire is measured while a current I is applied to the wire. This allows a measurement of the wires resistance R_{wire} . It is important to point out, that the wire is an extended resistor, which is indicated into the arbitrary division into n wire segments. A change in temperature at any point along the wire changes the local resistance R_i .

Approximated for a finite number of elements n_{seg} the integral in Eq. (5.1) becomes

$$R = \sum_i^{n_{seg}} R_i = \sum_i^{n_{seg}} \frac{\rho R \cdot l_{seg}}{A_{cs}} (1 + a \cdot (T_i - T_{ref})) \quad (5.2)$$

where R_i and T_i are the resistance and temperature of segment i and l_{seg} is the length of the segments. This basic electrical approximation we adopt for simulation is illustrated in Figure 5.2.

The raw signal of any measurement is then the change in resistance ΔR between initial equilibrium and final equilibrium after a change in heat input to the wire.

$$\Delta R = R(T_{final}(x)) - R(T_{initial}(x)) \quad (5.3)$$

As an illustration, the simulated change in temperature profile along the wire is shown in Figure 5.3. This example shows the wire responding to a heat source in form of a 1 mA current flowing through the wire, which causes Joule heating ($P = I^2 R$). In this example, the temperature along the wire increases by up to 30°C , which in turn results in an increase of resistance of about $5.3\ \Omega$ or a 10% change.

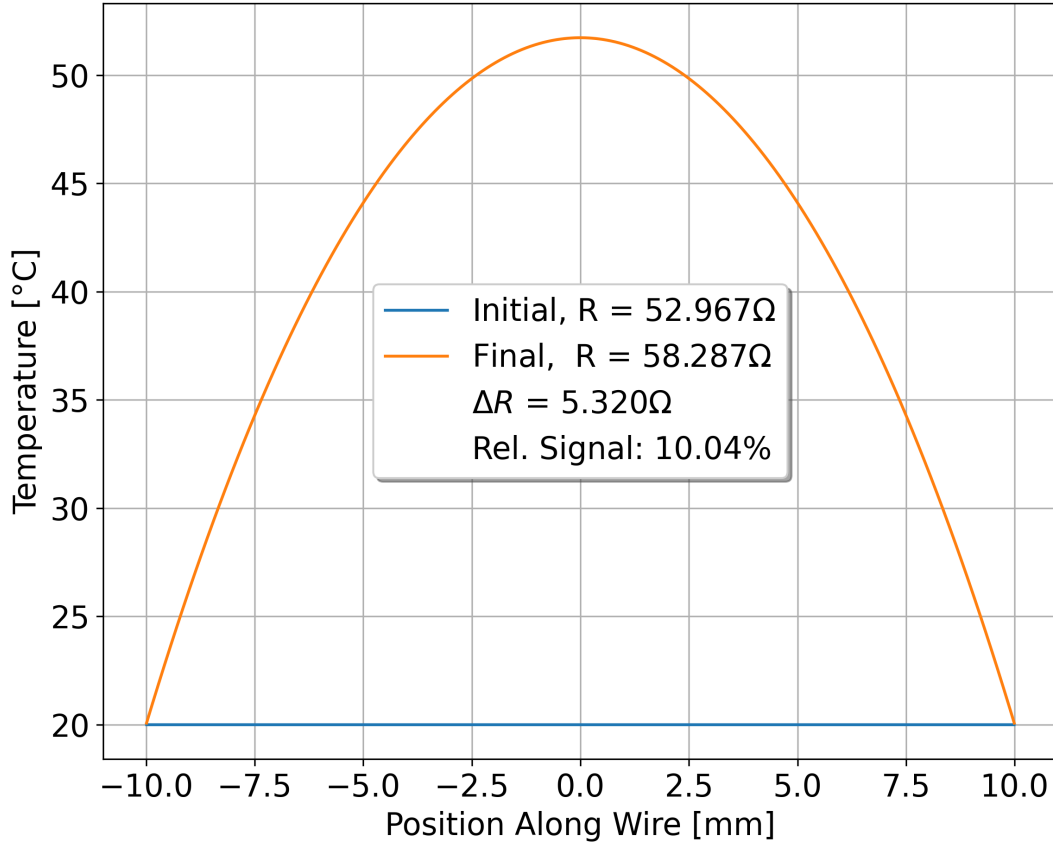


Figure 5.3: Simulated temperature profile along the wire for an “Initial” wire at 20 °C and a “Final” equilibrium after simulating a current of 1 mA through the wire. The resistance of the wire in initial and final states is indicated as well as the absolute and relative change in resistance.

5.2 Simulation of the temperature distribution

For our simulation we discretize the spatial dimension along the wire into wire segments of length l_{seg} and time into steps of length Δt . For every segment of the wire we can calculate the change in temperature ΔT in response to an input of net heat ΔQ starting from the definition of the heat capacity

$$C = \lim_{\Delta T \rightarrow 0} \frac{\Delta Q}{\Delta T}. \quad (5.4)$$

Therefore for sufficiently fine timesteps such that ΔT is small for every wire segment we can calculate the change in temperature

$$\Delta T = \frac{\Delta Q}{C} \quad (5.5)$$

for a cylindrical wire segment with the heat capacity

$$C_{\text{seg}} = A_{\text{cs}} \cdot l_{\text{seg}} \cdot \rho \cdot c, \quad (5.6)$$

where ρ is the density of the wire material, A_{cs} is the area of the circular cross section of the wire, and c is the specific heat capacity of the material.

For calculating the net heat input ΔQ on a wire segment we define the quantity f_{net} , the net *rate of heat flow per unit length of wire*, henceforth called just *heat flow*. ($[f] = \frac{[\text{Power}]}{[\text{Length}]}$ is a power density along the long axis of the wire):

$$f_{\text{net}} = \frac{\Delta Q}{l_{\text{seg}} \cdot \Delta t}, \quad (5.7)$$

which is independent of the simulation step size parameters l_{seg} and Δt . Solving for ΔQ we obtain

$$\Delta Q = f_{\text{net}} \cdot l_{\text{seg}} \cdot \Delta t \quad (5.8)$$

and substituting ΔQ and C_{seg} into Eq. (5.5) yields

$$\begin{aligned} \Delta T &= \frac{f_{\text{net}} \cdot l_{\text{seg}} \cdot \Delta t}{A_{\text{cs}} \cdot l_{\text{seg}} \cdot \rho \cdot c} \\ &= \frac{f_{\text{net}} \cdot \Delta t}{\rho \cdot A_{\text{cs}} \cdot c}, \end{aligned} \quad (5.9)$$

which allows us to calculate the change in temperature of a wire segment in one time step in response to an f_{net} of our choosing. For normal operations, the simulation is run for a number of steps such that ΔT converges to ≈ 0 for all wire segments, i.e. until thermal equilibrium is reached.

The decisions on what to include in the calculation of f_{net} is the main challenge in creating a useful simulation. For work presented in this thesis we define f_{net} as the sum of multiple heat flow components:

$$\begin{aligned} f_{\text{net}} &= f_{\text{rec}} + f_{\text{el}} + f_{\text{beam_gas}} + f_{\text{bb}} \\ &\quad - f_{\text{rad}} - f_{\text{conduction}} - f_{\text{bkgd_gas}}, \end{aligned} \quad (5.10)$$

where f_{rec} is heating due to the recombination of hydrogen atoms on the surface of the wire and is the component we aim to measure, f_{el} is ohmic heating due to electrical current, f_{rad} is due to radiation (emission from the wire and absorption from the surrounding chamber), $f_{\text{conduction}}$ is due to thermal conduction along and out of the wire, $f_{\text{beam_gas}}$ is due to the kinetic energy of atoms and molecules in the beam, f_{bb} is due to the blackbody radiation from the hot and glowing HABS, and $f_{\text{bkgd_gas}}$ is due to interactions with the background gas in the chamber. The equations describing each individual component can be found in Section 5.3.

Integrating any of these heat flows f_j over the length of the wire yields

$$P_j = \int_{\text{wire}} f_j(x) dx \approx \sum_i^{n_{\text{seg}}} f_j(x_i) \cdot l_{\text{seg}}, \quad (5.11)$$

the total heating (cooling) power due to this source (sink).

P_{rec} contains information about the amount of atomic hydrogen that is in the measured beam and how it is distributed. It is therefore the component of interest for this thesis. The procedure for extracting it from the raw signal is detailed in Section 8.2.

5.3 Heat flow components

This section is a glossary of equations used in the simulation of the wire detector. All quantities f_j are power densities (power per unit length of wire [W/m]) due to various effects that impact the wire.

5.3.1 Recombination of hydrogen into molecules

The detection of heating due to the recombination of atomic hydrogen into molecules is the primary purpose of the wire calorimeter. For modeling its contribution f_{rec} we need to calculate

$$f_{\text{rec}} = \frac{d^2 N_{\text{at}}}{dt dx} \cdot E_{\text{eff}} \quad (5.12)$$

where $\frac{d^2 N_{\text{at}}}{dt dx}$ is the rate ((particles/s)/m) at which atoms hit the wire per unit length and E_{eff} the effective average energy of recombination per atom that hits the wire.

We calculate E_{eff} as the product of the energy released per recombination E_{rec} and the calorimetric efficiency of the wire surface for recombination η_{rec} :

$$E_{\text{eff}} = \eta_{\text{rec}} \cdot \frac{E_{\text{rec}}}{2}, \quad (5.13)$$

where the recombination energy $E_{\text{rec}} \approx 4.46\text{eV}$ is divided by 2 since 2 atoms are required per recombination reaction. The calorimetric efficiency for recombination of atoms on a given surface is the fraction of the total available chemical energy in form of the difference in binding energy between atomic and molecular hydrogen that ultimately heats up the wire. This fraction which we will call η_{rec} can be divided into multiplicative factors describing substeps of the process. One possible factorization is

$$\eta_{\text{rec}} = \alpha_H \cdot \gamma_S \cdot \beta_{\text{rec}} \quad (5.14)$$

where α_H is the likelihood of an atom that hits the surface to stick to it, γ_S is the likelihood of an atom adhered to the surface to recombine into H_2 , and β_{rec} is the fraction of the recombination energy that is deposited into the wire (rather than being carried away by the H_2). For our purposes, this factorization is of largely academic nature, since we have no way of measuring these parameters individually in the setup presented in this thesis. However the factorization is useful for comparison of figures presented in literature. A discussion of the relevant sources ([42], [43], [44]) will occur in Section 5.5.3 where we discuss the potential effects of the choice of wire material. In short we ultimately conclude, that η_{rec} is poorly constrained by literature e.g. following Melin et al. [43] for a platinum surface $\eta_{\text{rec}} = 0.009_{-0.006}^{+0.009}$, while Livshits et al. [44] suggest the possibility of η_{rec} as high as 0.25 for an appropriately treated platinum surface.

As a result, wherever we are forced to make a choice, such as for this simulation, we simply choose to set $\eta_{\text{rec}} = 1$. In practice η_{rec} simply becomes part of a fit parameter summarizing multiple unknowns later (see Section 8.1), and therefore a precise choice is not required for most results we present.

Setting $\eta_{\text{rec}} = 1$ overestimates the expected signal of the wire detector. In the analysis of real beams choosing the factor 1 minimizes the atom flux required to explain the recombination heating signal that is measured. An atom flux measurement derived from $\eta_{\text{rec}} = 1$ is therefore a conservative limit on the number of atoms produced by the source. This is desirable because producing a large number of atoms is a requirement for the goals of the Project 8 collaboration, and underestimating the atom count will make lead us in the direction of developing a more capable source, rather than settling on one that may produce an inadequate number of hydrogen atoms.

The second component of Equation (5.12), $\frac{d^2 N_{\text{at}}}{dt dx}$ can be calculated from the flux density J [particles/m²s] of atoms in the beam at the wire surface, which in simulation we can of course set arbitrarily. In practice we calculate it either from a hypothetical "top hat" shaped flat circular beam of uniform flux density, or from j_{HABS} a realistic

beam model for a thin capillary defined in Section 4.1. For calculating the atom flux per unit wire length we must simply integrate over a slice of the wire in z -direction (i.e. over the width of the wire for a single x -position):

$$\frac{d^2 N_{\text{at}}}{dt dx} = \int_{\text{wire}} dz J(x, z, y) \quad (5.15)$$

which for a beam of uniform density $J(x, z, y) = J_0$ is simply

$$\frac{d^2 N_{\text{at}}}{dt dx} = \int_{\text{wire}} dz J(x, z, y) = J_0 \cdot d_{\text{wire}} \quad (5.16)$$

where d_{wire} is the diameter of the wire.

For a realistic beam model for our source $J_{\text{HABS}} = \Phi_{\text{at}} \cdot j_{\text{HABS}}$, where Φ_{at} is the total flow of atoms in the beam ([atoms/second]), we obtain instead

$$\frac{d^2 N_{\text{at}}}{dt dx} = \int_{\text{wire}} dz J(x, z, y) = \Phi_{\text{at}} \cdot j_{\text{HABS}}(\theta_i; l_{\text{eff}}) \cdot \frac{\cos^3(\theta_i)}{y_0^2} \cdot d_{\text{wire}}, \quad (5.17)$$

where $\frac{\cos^3(\theta)}{y_0^2}$ results from the coordinate transform when converting j_{HABS} which is defined in spherical coordinates as a probability density per steradian [1/sr] to a probability density over the cartesian coordinates of the wire [1/m²] (see Appendix A for details). y_0 is the distance from the source capillary end-face to the wire and the angular position θ_i is the the angular position of the wire segment with respect to the source capillary axis.

We therefore ultimately end up with

$$f_{\text{rec}} = j_{\text{HABS}}(\theta(i); l_{\text{eff}}) \frac{\cos^3(\theta(i))}{y_0^2} \cdot \Phi_{\text{at}} \cdot d_{\text{wire}} \cdot \eta_{\text{rec}} \cdot \frac{E_{\text{rec}}}{2} \quad (5.18)$$

for our recombination heat flow using our source model.

And for a uniform atomic beam of intensity J_0 we obtain

$$f_{\text{rec,uniform}} = J_0 \cdot d_{\text{wire}} \cdot \eta_{\text{rec}} \cdot \frac{E_{\text{rec}}}{2}. \quad (5.19)$$

5.3.2 Kinetic energy of beam gas

In addition to the heat load due to recombination, a given hydrogen atom or molecule which hits the wire also delivers a portion of its thermal kinetic energy. Since the source and therefore the beam is operated at temperatures upwards of 2000 K, this contribution can be substantial.

For a beam of mixed atomic and molecular composition we must add the contribution of each component

$$f_{\text{beam_gas}} = f_{\text{at}} + f_{\text{mol}}. \quad (5.20)$$

For each of the components we can use the same approach as in Eq. (5.12) for the recombination heat flow such that

$$f_{\text{at/mol}} = \frac{d^2 N_{\text{at/mol}}}{dt dx} \cdot E_{\text{eff,kin}_{\text{at/mol}}}, \quad (5.21)$$

only now we must consider the effective average transfer of kinetic energy per particle $E_{\text{eff,kin}_{\text{at/mol}}}$. This we can calculate as

$$E_{\text{eff,kin}_{\text{at/mol}}} = \alpha_{E_{\text{at/mol}}} \cdot \left(C_{V_{\text{at/mol}}}(T_{\text{at/mol}}) \cdot T_{\text{at/mol}} - C_{V_{\text{at/mol}}}(T_i) \cdot T_i \right) \quad (5.22)$$

where $C_{V_{\text{at/mol}}}$ ¹⁰ is the heat capacity per particle of atomic and molecular hydrogen respectively as a function of the temperature of the gas $T_{\text{at/mol}}$, and T_i is the temperature of the wire segment i at position x_i . By selecting the appropriate subscript _{at/mol} this equation yields the intensity of the atomic or molecular beam gas heating component. α_E is the energy accommodation coefficient of the gas on the wire and describes the average fraction of the available kinetic energy which is passed on to the wire, defined by

$$\alpha_E = \frac{E_i - E_r}{E_i - E_w}, \quad (5.23)$$

where E_i is the average energy of the incident particles, E_r is the average energy of the reflected particles, and E_w is the energy a gas particle carries away if it desorbs in thermal equilibrium with the wire surface.

This is a surface dependent parameter which is initially unknown and set to 1 in the simulations presented in this thesis. In Section 8.3.2 we will discuss methods for determining this value from data for a purely molecular beam.

Following the same procedure for calculating the number of particle hits on the wire as in the previous section, Eq. (5.21) yields

$$f_{\text{at/mol}} = j_{\text{HABS}}(\theta(i); l_{\text{eff}}) \frac{\cos^3(\theta(i))}{y_0^2} \cdot \Phi_{\text{at}} \cdot d_{\text{wire}} \cdot \alpha_{E_{\text{at/mol}}} \cdot \left(C_{V_{\text{at/mol}}}(T_{\text{at/mol}}) \cdot T_{\text{at/mol}} - C_{V_{\text{at/mol}}}(T_i) \cdot T_i \right) \quad (5.24)$$

for the HABS beam model and

$$f_{\text{at/mol}} = J_{\text{at/mol}} \cdot d_{\text{wire}} \cdot \alpha_{E_{\text{at/mol}}} \cdot \left(C_{V_{\text{at/mol}}}(T_{\text{at/mol}}) \cdot T_{\text{at/mol}} - C_{V_{\text{at/mol}}}(T_i) \cdot T_i \right) \quad (5.25)$$

for a uniform beam of flux density $J_{\text{at/mol}}$.

For the simulation we generally assume the temperature of the gas $T_{\text{at/mol}}$ to be equal to the source temperature, though these can be simulated as separate parameters. For a source temperature of ≈ 2000 K the kinetic energy of a hydrogen atom is approximately one tenth of its chemical potential energy $E_{\text{rec}}/2$. Therefore, for a pure atomic hydrogen beam $f_{\text{beam_gas}} \approx f_{\text{rec}}/10$. However for a mixed beam with less than 10% atom content, $f_{\text{beam_gas}}$ can be the larger of the two.

The effects of $f_{\text{beam_gas}}$ will be explored with measured data in Section 8.

5.3.3 Blackbody radiation from the hot source

So long as the wire detector is in direct line of sight of the hot parts of the HABS such as the source capillary itself, it will receive a heat load due to thermal blackbody radiation emitted from the source. The exact contribution of this effect is difficult to model, since in principle it would require exact geometrical descriptions and temperature maps for

¹⁰NIST $C_{V,\text{H}_2}(T)$: <https://webbook.nist.gov/cgi/cbook.cgi?ID=C1333740&Type=JANAFG&Table=on#JANAFG>, $C_{V,\text{H}}(T)$: <https://webbook.nist.gov/cgi/cbook.cgi?ID=C12385136&Mask=1>

all parts of the setup which are within line of sight of the wire and have a different temperature. We contend ourselves with only including contributions from the hottest (and therefore most intensely radiating) parts of the source directly to the wire.

We start by calculating the power radiated from the hot portions of the source. Using the Stefan-Boltzmann law the radiant excitation from a *gray body* is

$$M = \varepsilon \cdot \sigma \cdot T^4 \quad (5.26)$$

where ε is the gray body emittance, σ is the Stefan-Boltzmann constant and T is the temperature of the gray body.

Simplifying the geometry substantially, we model the HABS as just a hot circle of area A_{HABS} when seen from the wire below, which emits with intensity $M = \varepsilon_{\text{HABS}} \cdot \sigma \cdot T_{\text{HABS}}^4$ from every point. At the wire, a distance of y_0 from the HABS, this intensity is diluted by the surface area of the sphere formed around the emitting surface with radius y_0 , such that at the location of the wire every point of the glowing surface A_{HABS} causes an irradiance E_e per emitter area of

$$\frac{dE_e(y_0)}{dA} = M/(4\pi y_0^2) = \varepsilon_{\text{HABS}} \cdot \sigma \cdot T_{\text{HABS}}^4/(4\pi y_0^2). \quad (5.27)$$

Integrating over A_{HABS} while disregarding for simplicity that every point in A_{HABS} is at a slightly different distance to a point on the wire, we get

$$E_e(y_0) = \int_{A_{\text{HABS}}} \frac{dE_e(y_0)}{dA} dA \approx \varepsilon_{\text{HABS}} \cdot \sigma \cdot T_{\text{HABS}}^4 \frac{A_{\text{HABS}}}{(4\pi y_0^2)} \quad (5.28)$$

which is the radiant exposure ([W/m²]) at the wire surface due to the glowing HABS.

From here we just have to multiply with the wire diameter and the wires absorptivity. Using the simplification of treating the wire as a gray body with constant absorptivity, we can use Kirchoffs law of thermal radiation, which states that for such a body the absorptivity α_λ is equal to the emissivity ε_λ . We can therefore multiply with the wires own emissivity ε instead to obtain the heat flow due to blackbody radiation from the glowing source

$$f_{\text{bb}} = \varepsilon \cdot \varepsilon_{\text{HABS}} \cdot \sigma \cdot T_{\text{HABS}}^4 \cdot \frac{A_{\text{HABS}}}{4\pi r_{\text{HABS}}^2} \cdot d_{\text{wire}}. \quad (5.29)$$

This is a deliberate oversimplification of the source geometry and its thermal output. For any meaningful improvement thermal models of the source itself would be required. For our simulations we simply set A_{HABS} to be the size of the opening of the HABS shroud at uniform temperature T_{HABS} . The emissivities are also free parameters and are initially set to 1 just to get a sense of scale.

In practice, blackbody radiation from the source is often the dominant source of heat on the wire when the source is hot. However, if the source temperature is well stabilized, f_{bb} is constant and so its effect can be eliminated by other means for data extraction. See Section 8.2 for more details on how we deal with this contribution on real data.

Additional secondary effects, such as the source radiation heating other parts of the wire holding structure or heating of the chamber itself are not modeled in the simulation. We justify this on the grounds, that due to their larger size, the ceramic PCB and the stainless steel holding structure have thermal conductance and heat capacities multiple orders of magnitude higher than the wire itself.

5.3.4 Electrical heating

For measuring the resistance of the wire, as well as for use as a calibration heat source, we apply currents to the wire. Due to Joule heating this causes an additional heat load on the wire of

$$P_{\text{el}} = I^2 R, \quad (5.30)$$

where I is the current and R is the resistance of the wire. We can express the distribution of this heat for a wire with discrete elements as

$$f_{\text{el}} = I^2 \cdot R_i(T_i)/l_{\text{seg}} \quad (5.31)$$

where $R_i(T_i) = (\rho \cdot l_{\text{seg}}/A_{\text{cs}}) \cdot (1 + a) \cdot (T_i - T_{\text{ref}})$ is the resistance of the segment i , and l_{seg} is the length of the segment. ρ is the specific resistance, A_{cs} denotes the cross-sectional area of the wire and a is the temperature coefficient of resistivity. T_i is the temperature of segment i and T_{ref} is the reference temperature at which ρ is quoted.

Because I can be freely adjusted both in simulation as well as the real experiment the effect size of f_{el} can vary widely, but it is in practice often one of the largest heat sources.

5.3.5 Heat conduction

The main mechanism by which heat is distributed in the wire is heat conduction. Due the simplified construction of our simulation we can calculate this using the one dimensional version of the Fourier's law

$$q_x = -k \frac{dT}{dx}, \quad (5.32)$$

where q_x is the local heat flux density ($[\text{W}/\text{m}^2]$) in the x direction, k is the materials heat conductivity and $\frac{dT}{dx}$ is the gradient of temperature along the wire.

We choose all our gradient conventions such that a positive heat flux is heat that flows *out* of a given wire segment. This is keeping with Equation (5.10) where conduction is typed as a heat loss mechanism due to the negative sign. Of course a segment with warmer neighbors will still receive net heating, which will be a negative $f_{\text{conduction}_i}$.

For discrete wire segments that are $\Delta x = l_{\text{seg}}$ apart this equation yields a conductive heat flow between two adjacent segments from segment i to segment $i - 1$

$$q_{i \rightarrow (i-1)} = -k \frac{(T_{i-1} - T_i)}{l_{\text{seg}}}, \quad (5.33)$$

where T_i is the Temperature of wire segment i . Since any wire segment has two neighbors, the net heat flux density on the wire segment is

$$q_{\text{net}_i} = q_{i \rightarrow (i-1)} + q_{i \rightarrow (i+1)} = -k \cdot \frac{(T_{i-1} - T_i) + (T_{i+1} - T_i)}{l_{\text{seg}}}. \quad (5.34)$$

To once again obtain a linear heat flow density we multiply with the wire cross section A_{cs} and then divide by the segment length l_{seg} yielding

$$f_{\text{conduction}_i} = q_{\text{net}_i} \cdot \frac{A_{\text{cs}}}{l_{\text{seg}}} = -k(T_i) \cdot \frac{(T_{i-1} - T_i) + (T_{i+1} - T_i)}{l} \cdot \frac{A_{\text{cs}}}{l_{\text{seg}}}, \quad (5.35)$$

where we also allow for a temperature dependent heat conductivity $k(T_i)$ ¹¹.

¹¹For our main material of interest, Tungsten, we calculate $k(T)$ by interpolating data found here: https://www.efunda.com/materials/elements/TC_Table.cfm?Element_ID=W.

For terminal wire segments at either end, the same equation is used. Except that, for indices outside of the range of the wire itself we let the wire detector board act as an infinite heat bath at $T_0 = T_{n_{seg}+1} = T_{\text{board}}$. We generally set $T_{\text{board}} = 20^\circ\text{C}$ as an approximation of the chamber temperature.

5.3.6 Radiative cooling

Whenever the wire is warmer than the surrounding vacuum chamber it loses heat to radiation. Here we once again start from the gray body Stefan-Boltzmann law (Eq. (5.26)), which we multiply with the circumference of the wire to get the linear heat flow density

$$f_{\text{rad,loss}} = \pi \cdot d_{\text{wire}} \cdot M = \pi \cdot d_{\text{wire}} \cdot \sigma \cdot \varepsilon \cdot T_i^4, \quad (5.36)$$

where d_{wire} is the diameter of the wire, σ is the Stephan-Boltzmann-constant and ε is the emissivity of the wire surface.

If we want the net heat flow due to radiation on the wire surface, we must subtract out background thermal radiation from the vacuum chamber. If we simplify to treating the vacuum chamber as a blackbody radiator at temperature T_{chamber} we can calculate the net radiative losses as

$$f_{\text{rad}} = \pi \cdot d_{\text{wire}} \cdot \sigma \cdot \varepsilon \cdot (T_i^4 - T_{\text{chamber}}^4), \quad (5.37)$$

where now the wire does not keep losing energy if it is in thermal equilibrium the vacuum chamber.

The emissivity ε of the wire surface is generally not precisely known from literature, and the value therefore would have to be tuned using a calibration scheme if accuracy was desired. As default it is generally set to $\varepsilon = 0.2$ as a rough approximation of unpolished gold.

5.3.7 Free molecular heat transfer with residual background gas in the vacuum chamber

While the wire detector generally operates in very low pressure environments, there can nevertheless be non-negligible heat loss to the residual gas in the source chamber. The exact pressure varies with the amount of flow through the source and the strength of the pumping. In our setup even at maximum flow (20 sccm) pressure in the source chamber is no more than 5×10^{-4} mbar, which equates to a mean free path for hydrogen of ≈ 20 cm, larger than the internal dimensions of the source chamber (roughly a cube with 15 cm side length). This means that residual pressures are comfortably in the free molecular flow regime for any lower flows.

We therefore use an equation for the free molecular heat transfer¹² to model the heat transferred between the wire and the vacuum chamber by the gas in the chamber. The heat flux density ($[\text{W}/\text{m}^2]$) at the surface of the wire is given by

$$q(x) = G \cdot p \cdot F_a \cdot F_{\text{wire-chamber}} \cdot (T_{\text{chamber}} - T(x)) \quad (5.38)$$

where G is the "G factor" that will be calculated below, p is the absolute pressure in the source chamber, F_a is the accommodation coefficient *factor*, $F_{\text{wire-chamber}}$ is the view factor from surface of the wire to surface of the chamber, T_{chamber} is the temperature of the chamber and T is the temperature of the wire at position x .

¹²based on <https://tfaws.nasa.gov/TFAWS07/Proceedings/TFAWS07-1013.pdf>

The accommodation coefficient *factor* is given by

$$F_a = 1 / \left(\frac{1}{\alpha_{E_{\text{wire}}}} + \frac{A_{\text{wire}}}{A_{\text{chamber}}} \cdot \left[\frac{1}{\alpha_{E_{\text{chamber}}}} - 1 \right] \right). \quad (5.39)$$

where the α_E 's are the accommodation coefficients for the respective surface and the A 's are the areas of the respective surfaces. Since $A_{\text{wire}} \ll A_{\text{chamber}}$ this reduces to

$$F_a = \alpha_{E_{\text{wire}}} \quad (5.40)$$

in our case.

We can also reduce the view factor to $F_{\text{wire-chamber}} = 1$ since the wire is fully enclosed by the chamber (and the hot parts in the field of view are separately accounted for by f_{bb}).

Finally the G factor is given by

$$\frac{\gamma + 1}{\gamma - 1} \cdot \sqrt{\frac{k_B}{8\pi \cdot m \cdot T_{\text{chamber}}}} \quad (5.41)$$

where $\gamma = \frac{C_p}{C_v}$ is the ratio of the specific heats, k_B is the Boltzmann constant and m is the mass of the hydrogen molecule.

Applying all this to Eq. (5.38) we obtain

$$q(x) = p \cdot \alpha_{E_{\text{wire}}} \cdot \frac{\gamma + 1}{\sqrt{8\pi(\gamma - 1)}} \sqrt{\frac{k_B (T(x) - T_{\text{chamber}})^2}{m T_{\text{chamber}}}}, \quad (5.42)$$

which we have to multiply with the wire circumference $\pi \cdot d_{\text{wire}}$ to obtain

$$f_{\text{bkgd_gas}} = \pi d_{\text{wire}} \cdot p \cdot \alpha_{E_{\text{wire}}} \cdot \frac{\gamma + 1}{\sqrt{8\pi(\gamma - 1)}} \sqrt{\frac{k_B (T_i - T_{\text{chamber}})^2}{m T_{\text{chamber}}}} \quad (5.43)$$

$$\approx 3 \sqrt{\frac{\pi}{2}} d_{\text{wire}} \cdot p \cdot \alpha_{E_{\text{wire}}} \sqrt{\frac{k_B (T_i - T_{\text{chamber}})^2}{m T_{\text{chamber}}}}, \quad (5.44)$$

where the second line results from applying the standard diatomic approximation of $\gamma = 7/5$ which is appropriate for hydrogen at $T \approx 300\text{K}$ and is therefore used for all our simulations presented in this work.

It should be noted, that the simplifications we made effectively amount to treating background gas in the chamber as having the temperature of the chamber whenever it hits the wire. The only exception is the direct line of sight beam treated separately as $f_{\text{beam_gas}}$. This assumes gas injected into the chamber by the beam accommodates quickly to the chambers temperature, such that back scattering effects are negligible.

The model for $f_{\text{bkgd_gas}}$ retains one free parameter α_E which is in principle dependent on surface and gas properties as well as the temperature and is therefore not well known a priori and would need to be separately measured. For simulations presented in this work it is generally set to 1. This is the maximum physical value, and is therefore a pessimistic estimation of this nuisance heat flow.

5.3.8 Radioactive heat from tritium decay

With a tritium rather than a protium source we might additionally consider heating on the wire due to radioactive decay of adhered atoms. As no tritium experiments were

conducted for this thesis we can ignore this contribution going forward. Nevertheless we will present a brief order of magnitude estimate of the effect.

The total energy released in the radioactive decay of a collection of tritium atoms is

$$\begin{aligned} P_{\text{decay}} &= Q_A \cdot \frac{dN}{dt} \\ &= Q_A \cdot N \cdot \frac{\ln(2)}{t_{1/2}} \end{aligned} \quad (5.45)$$

where $Q_A \approx 18.6$ keV is the atomic mass difference of the tritium decay and $\frac{dN}{dt}$ is the decay rate for a number of tritium atoms N with half life $t_{1/2} = 12.33$ years.

In order to forego a lengthy and dubious attempt to estimate the number of tritium atoms that might adhere to the wire at any one time, for this estimate we will assume an approximate worst case of a saturation of the wire with one tritium atom per tungsten atom in the entire wire.

This number is easy to calculate

$$N_T = N_W = \pi \cdot \left(\frac{d_{\text{wire}}}{2} \right)^2 \cdot l_{\text{wire}} \cdot \frac{\rho_W}{m_W} \quad (5.46)$$

with $\rho_W = 19.3 \times 10^3$ kg/m³ the density of tungsten and $m_W = 183.84$ u the atomic mass of tungsten.

Substituting all these values into Eq. (5.45) we obtain $P_{\text{decay}} \approx 132$ nW. For comparison, we will later present measurements of heating due to recombination P_{rec} of approximately $1 \mu\text{W}$ for a real beam of intermediate intensity (1 sccm). Given that we have likely dramatically overestimated the number of tritium atoms that remain adhered to the wire we can be sure that decay heating would not overwhelm our signal. Using realistic values would likely make it a negligible source of heating. Since we do not use tritium during this thesis we can certainly safely neglect it moving forward in this work.

5.3.9 Representative example simulation

For a sense of the relative sizes of the effects impacting the wire temperature, we simulate a typical beam and show, in Figure 5.4, the heat flows described in the previous sections after equilibrium has been reached for typical settings for gas flow (1 sccm) and HABS temperature (2200 K). Most important to note is, that both the f_{el} and f_{bb} are significantly larger than the heat sources f_{rec} and $f_{\text{beam_gas}}$ caused by a typical beam. This means that both must be well stabilized to be able to see the beam signal among small fluctuations in larger effects.

Fluctuations in f_{el} are minimized by using a highly stable power supply ¹³, capable of stabilizing the 1 mA measurement current running across the wire to better than 10^{-5} relative fluctuations. To minimize fluctuations in f_{bb} the HABS is operated on a PID-controlled loop stabilizing the readout of an internal thermocouple in close proximity to the HABS capillary.

However, it has not been feasible to model all effects impacting the wire with sufficient precision to formulate a relationship for extracting beam heating power from wire resistance directly. In part this is due to the great number of material and surface properties that enter into the model, many of which are only available with insufficient precision. Even the ostensibly simple calculation of the wire's baseline resistance at room

¹³Keithley SourceMeter 2400

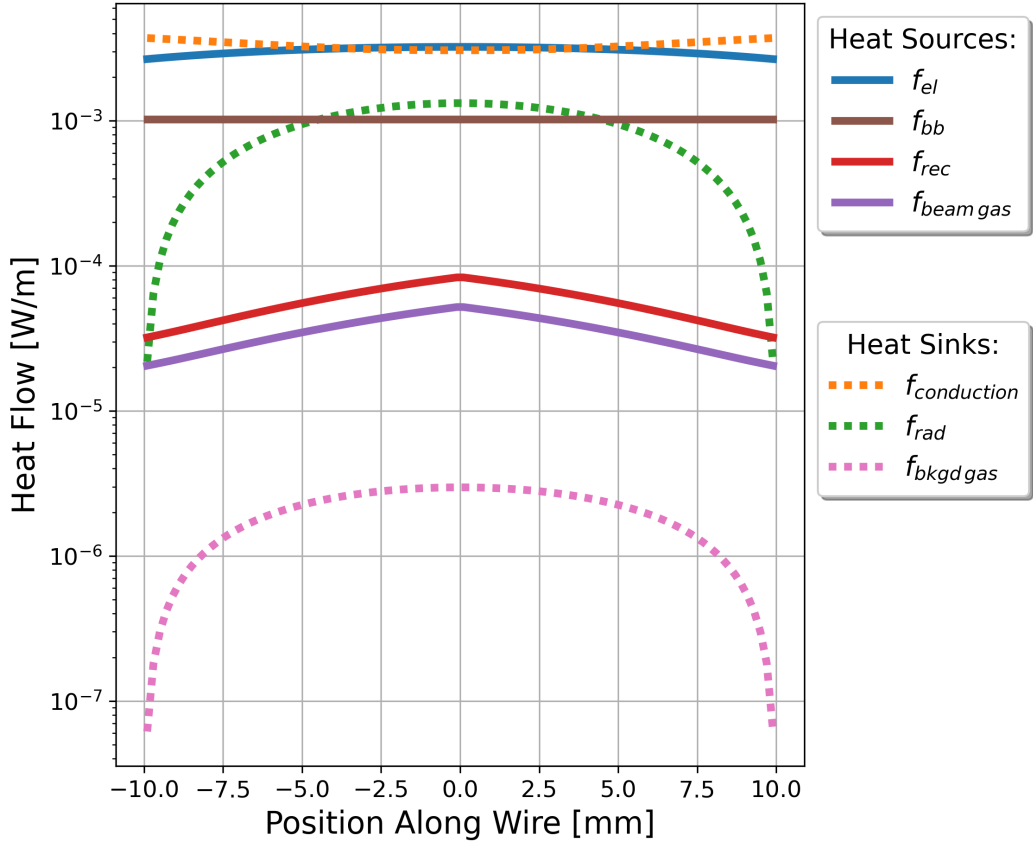


Figure 5.4: Comparison of the scale of the various simulated heat flow components at the time of equilibrium over the extent of the wire. Sources which transfer heat into the wire are plotted with solid lines, while sinks that remove heat from the wire are drawn in dashed lines. Note that the heat sinks are subtracted in Eq. (5.10), and therefore cancel out a heat source of equal size in this plot. The hydrogen beam selected for this simulation contains 1 sccm of molecular hydrogen at 2200 K with a 10% dissociation rate into hydrogen atoms. The beam width is chosen to be consistent with beams at this flow rate as will be measured later in this thesis.

temperature turns out to be problematic, because the manufacturer only guarantees the diameter of the wire to a 10% precision. This is further complicated because a gold-coated tungsten wire is used, where the exact impact of the coating on wire resistance is difficult to model with great confidence. Exact measurements of the sticking fractions and accommodation coefficients for $f_{\text{beam-gas}}$ and f_{rec} are very challenging to determine with sufficient precision [42]. Additionally, changes in chamber temperature not modeled here also cause changes in wire resistance larger than that of the expected signal.

Ultimately, this simulation is used to inform the design of the detector and the interpretation of the data but not to directly derive a beam signal from wire resistance. Instead an indirect extraction of the signal (Section 8.2) is used along with a calibration scheme (Section 7.3) for correlation of wire resistance to incident power measured.

5.4 Consistency check

In the interest of usability we aim to keep simulation runtime as short as possible. To this end the length of simulated time is kept as short as possible, and the resolution in time and wire length are kept as coarse as they can be without impacting simulation results.

In this section we will show, as a consistency check, that the simulation converges as these parameters are increased, and that the choice of simulated time, time step length and length of wire segments we choose for further use are produce results sufficiently close to the converged result.

5.4.1 Length of simulated time

We check the convergence of the simulation to a new equilibrium by tracking the resistance for every timestep of the same simulation as shown in Figure 5.3. In that example the wire is simulated for a total of 20 seconds. The evolution of the wire resistance in the first 10 seconds is shown in Figure 5.5. The wire monotonously approaches the new equilibrium state, with convergence to better than 1 part in 10^9 in total resistance change achieved within 10 seconds. The remaining resistance change ΔR forms a straight line on the log-linear plot, indicating an exponential equilibration process typical for thermal processes. The intersect times indicated in Figure 5.5 list the time to reach $1 - e^{-1} \approx 63\%$ and $1 - e^{-3} \approx 95\%$ equilibration. The required times therefore correspond to one and three times the equilibration time constant respectively. These yield a time constant of 0.475s and 0.474s respectively. The fact that these are compatible to within 2 parts per thousand shows that the exponential function describes the process reasonably well.

We conclude that the simulation converges, and that 10 seconds of simulated time is sufficient to reach equilibrium within the tolerance required.

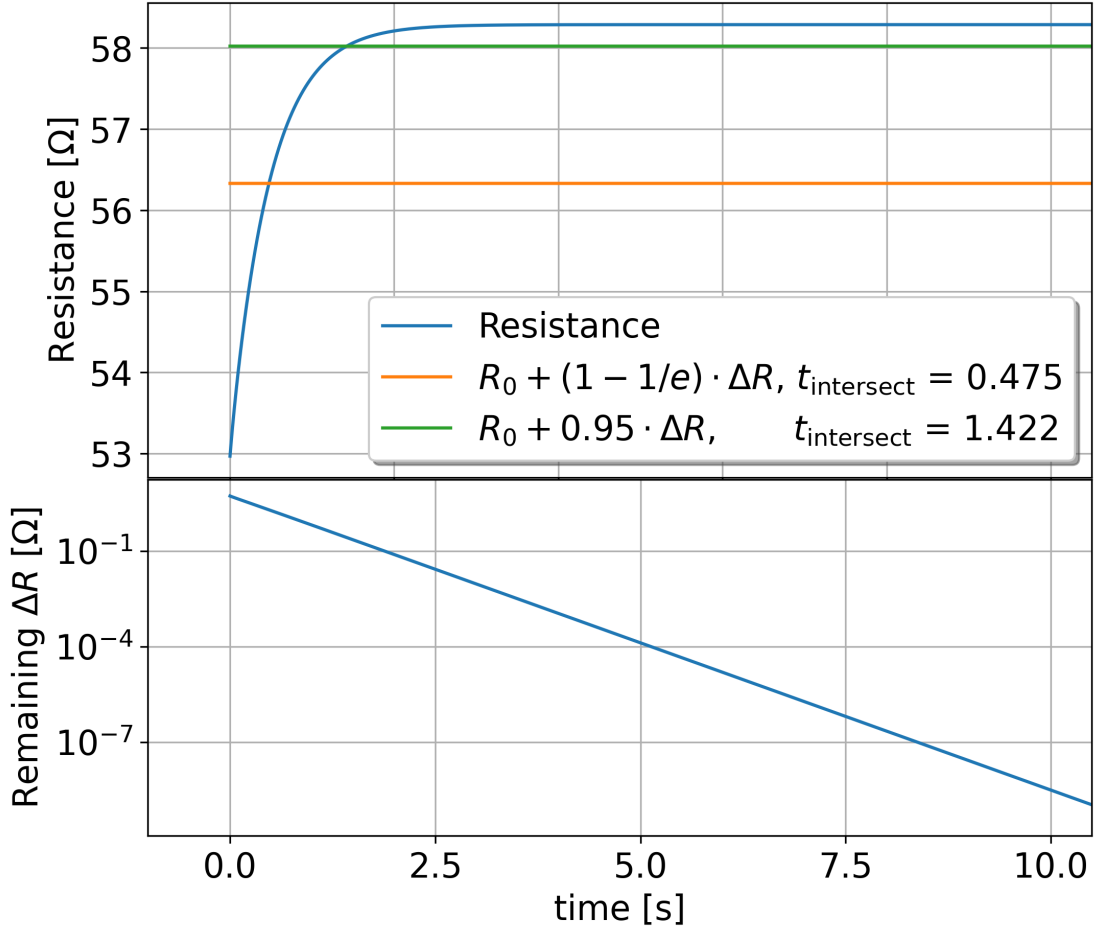


Figure 5.5: Resistance of the simulated wire over time after a 1 mA current is applied to tungsten wire 20 mm long and 5 μm in diameter. The $1 - e^{-1} \approx 63\%$ and $1 - e^{-3} \approx 95\%$ equilibration levels are indicated along with the time when they are reached. In the lower subplot the remaining resistance change to full equilibrium is plotted logarithmically.

5.4.2 Length of wire segments

We check that sufficient spacial resolution is used, by running the same simulation of a 20 mm log wire divided into progressively more and smaller segments. We calculate the resistance change ΔR for all these wires after a 1 mA current was applied for a simulated time of 20 s. We then calculate the difference in resistance change for a given segment length l_{seg} with the limit of ΔR for an infinitesimal l_{seg} .

$$\Delta R(l_{\text{seg}}) - \lim_{l_{\text{seg}} \rightarrow 0} \Delta R(l_{\text{seg}}) \quad (5.47)$$

As we cannot actually simulate infinitely many wire segments, we use a minimal segment length of $l_{\text{seg}} = 20\mu\text{m}$ as our approximate limit.

As Figure 5.6 shows, this approach is justified, as the deviation from the approximate limit shows a clear converging trend with lower l_{seg} . We plot a trend function scaling with l_{seg}^2 to illustrate that the deviation is well described by such a function and can therefore be expected to converge as l_{seg} approaches 0.

Running the simulation with smaller l_{seg} also requires the simulation to be run with smaller time step sizes, to keep it from crashing when some wire segments receive enough heat per time step to cause their temperature value to overflow. This means a larger

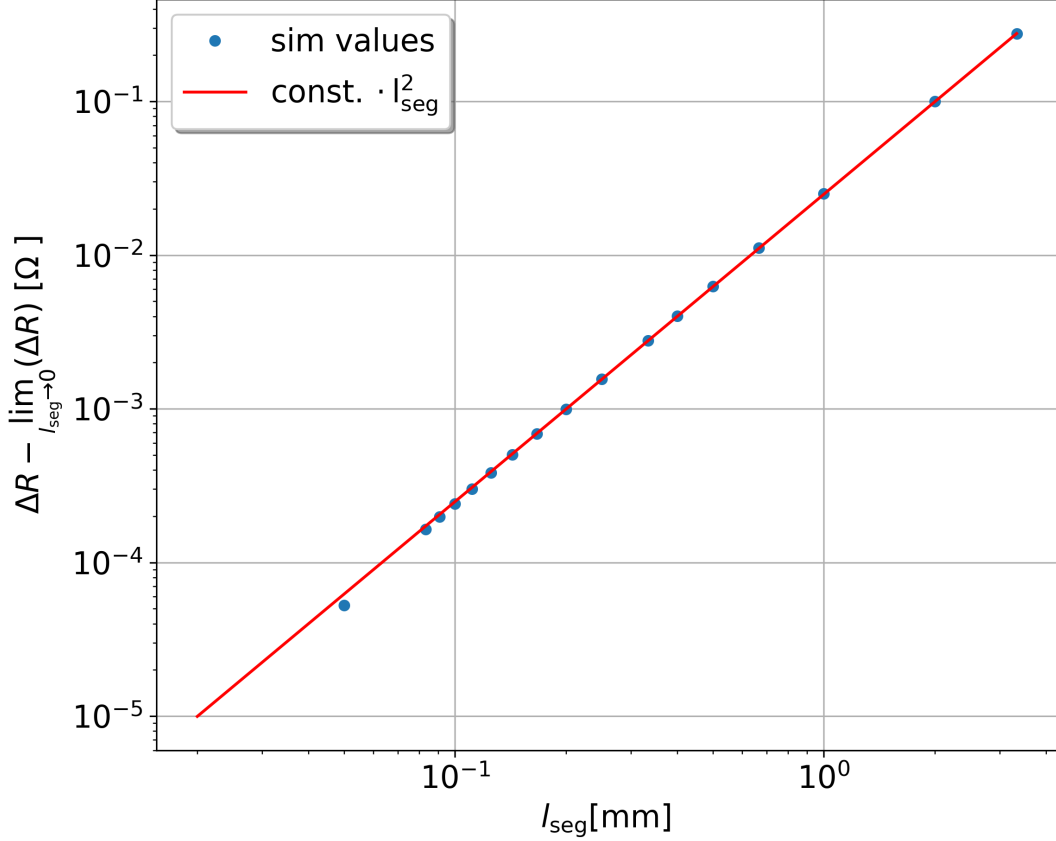


Figure 5.6: Deviation of ΔR from the converged value for infinitesimally small l_{seg} . The deviation increases with larger l_{seg} scaling approximately with the square of l_{seg} .

number of time steps must be calculated to reach the same total simulation time. In the case of 1000 wire segments of $l_{\text{seg}} = 20 \mu\text{m}$ each, this requires a time step size of less than $3 \mu\text{s}$ resulting in a total of 7.2 million steps run to reach the 20s simulation time target, which resulted in a runtime of 50 minutes on modest hardware.

The decision was therefore taken to run simulations presented in this work at one tenth of that spatial resolution, where runtime is reduced to essentially equivalent to simulation time at about 30s. As shown in Figure 5.6 a reduction in resolution to $l_{\text{seg}} = 200 \mu\text{m}$ incurs a penalty in accuracy of ΔR of a factor of less than 10^{-3} . This is deemed acceptable for the purposes for which we use the simulation in this work, and is required for making simulation time tractable for parameter searches.

Decreasing the time step size lower than required to prevent the simulation from crashing changes ΔR by no more than a factor of 10^{-9} and is therefore not done. For $l_{\text{seg}} = 200 \mu\text{m}$ the time step size is chosen at $250 \mu\text{s}$.

5.5 Design parameter studies

We can use the simulation to vary design parameters to optimize the performance of the wire detector while minimizing slow iterations of hardware. In the following sections we present parameter searches for optimal wire length, thickness, operating current and material.

5.5.1 Wire length

An unavoidable design choice is the length of the calorimeter wire. The dominating consideration is of course to build a detector that can actually be built and fits into the space available within setup where the measurement is to take place. Indeed, in all examples of the Design iterations presented in Section 6 the length of the wire is driven by the desire to fit the entire detector assembly through the 35 mm wide opening in a CF 40 vacuum flange.

To build a functioning detector it is also desirable to maximize the signal ΔR measurable for a given amount of heating power. As the absolute precision of most methods for Voltage, Current or resistance measurements scale with the size of the measured value, it is above all desirable to maximize the size of the relative signal $\Delta R/R_{\text{initial}}$. In particular for the multimeter we ultimately use for most of the measurements in this thesis the precision of a voltage measurement in the relevant 100 mV range is at best 30 ppm of the value + 30 ppm of the range¹⁴.

The length of the wire or more precisely the ratio of length to cross sectional area is important to the wire calorimeters performance, since any change in temperature on the wire is suppressed by thermal conduction along the wire. As specified in Eq. (5.35), the magnitude of heat conduction depends on the cross sectional area of the wire as well as the steepness of the temperature gradient. A longer wire can have shallower temperature gradients for the same change in wire temperature. We may therefore expect longer wires to be able to insulate heat deposited on them more effectively, leading to higher measurable resistance changes for the same input heat.

To get a numerical idea of the impact of wire length we simulate the effect of applying a set amount of power to a wire as a function of wire length. Figure 5.7 shows the simulated ΔR over a range of wire lengths when a $1 \mu\text{W}$ power is applied to the standard $5 \mu\text{m}$ thick tungsten wire. Two versions of the simulated results are displayed: One in which the entire heating power is applied to a single wire segment in the center and one in which the same power is evenly spread along the wire.

The signal ΔR initially rises steeply with wire length but the effect diminishes above a few centimeters of length for the chosen wire thickness. Centrally concentrated heating causes a larger change in wire resistance for the same heating power. This can be understood as the effect of thermal conduction along the wire, where heating applied close to the wire ends can more easily be conducted out of the wire, requiring a lower temperature change in the wire.

As previously mentioned, the larger initial resistance of a longer wire can mean that even a larger ΔR cannot necessarily be measured with higher resolution by a multimeter whose tolerance scales with size of the measured resistance. We therefore also present the relative signal $\Delta R/R_{\text{initial}}$ in Figure 5.8. This shows a maximum between 3 to 4 cm wire length. This maximum can move around depending on the exact parameters chosen for the simulated wire. The simulation presented here is set to be a good representation for the wires we will use for measurements presented later and $1 \mu\text{W}$ of heating is within the typical range of signals we actually measure. The wires we used for the detectors described in Section 6 are between 2 and 3 cm in length and therefore not far away from the maximum in relative signal.

The results change somewhat when we take a look at the case of wide beams, where the total energy received increases with wire length, since a larger area of wire is exposed to the beam. For illustration a hypothetical top hat shaped pure atomic H beam with

¹⁴We used a Keysight Truevolt 34461A, Datasheet: <https://www.keysight.com/us/en/assets/7018-03846/data-sheets/5991-1983.pdf>

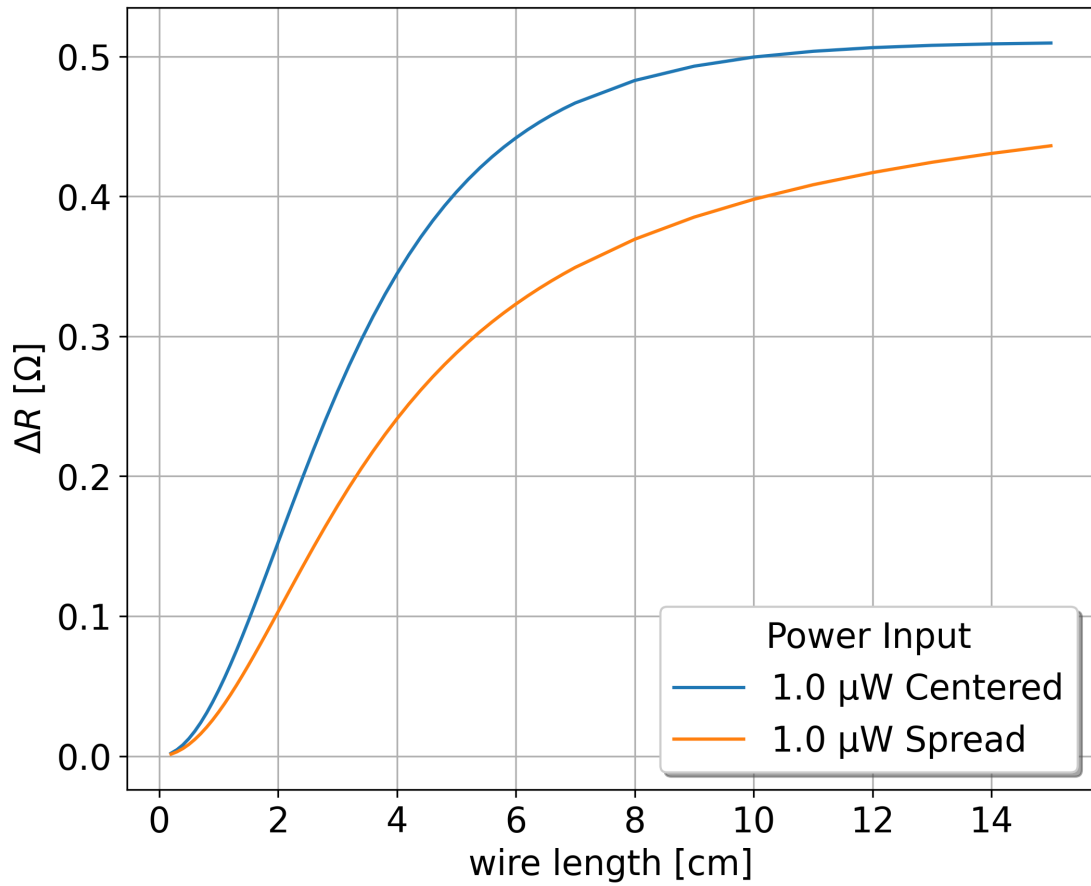


Figure 5.7: Resistance change ΔR in simulated wires before and after $1 \mu\text{W}$ is applied to them. In the blue simulation the power is applied entirely to the central wire segment. In the orange the same total power is spread evenly along the wire.

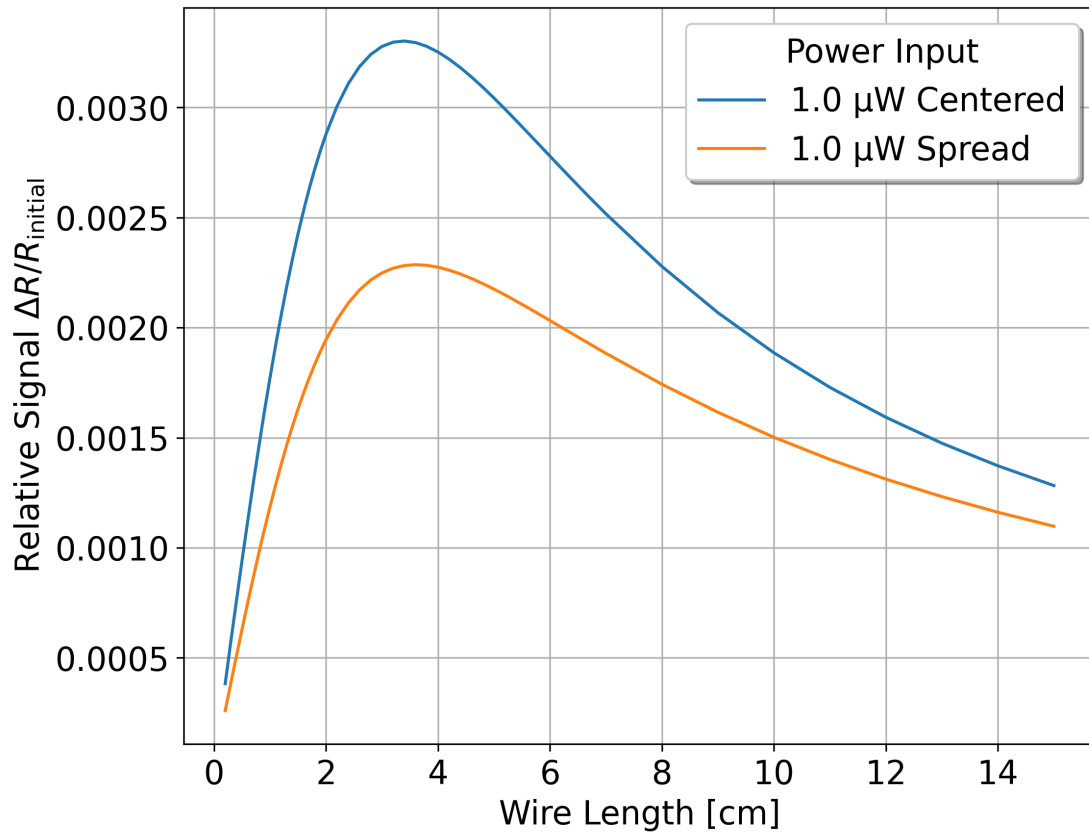


Figure 5.8: Simulated relative signal for a $1 \mu\text{W}$ heat load applied either centrally or spread over the wire. In either case there is a maximum below 4 cm of wire length.

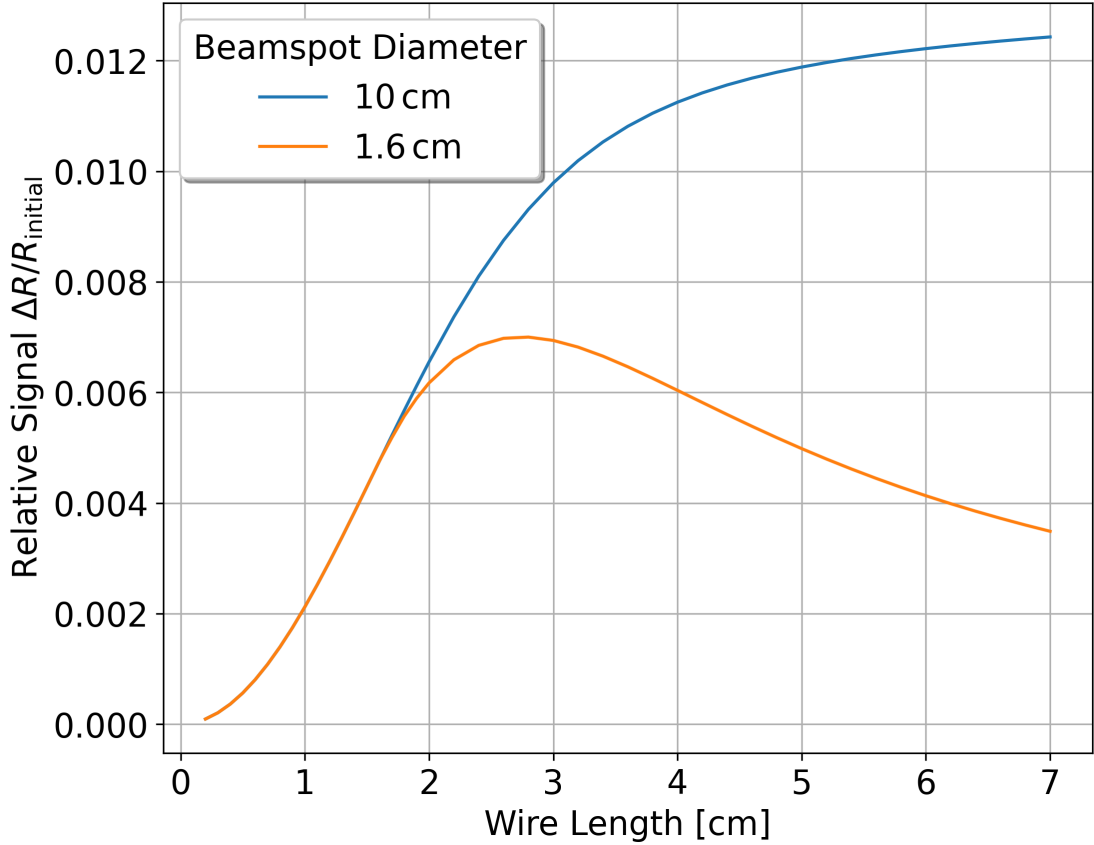


Figure 5.9: Simulated relative signal for wires illuminated with beams of uniform density of 10^{16} atoms/(cm²s). The 10 cm beam always fully illuminates the wire within the range presented and provides total power increasing linearly with wire length. The thinner 1.6 cm does not fully illuminate the wire, and delivers a constant total power to wires longer than the beam diameter.

a uniform density of 10^{16} atoms/(cm²s) inside the circular beamspot and 0 outside is simulated impinging on the wire. Figure 5.9 shows the resulting relative signal for 2 beams that differ only in width, one 10 cm in diameter and one 1.6 cm. As long as both beams fully illuminate the wire their effect is equivalent as expected. However as the wire becomes longer than the shorter beam is wide, parts of the wire are no longer receiving additional heating. For about another centimeter of wire length the relative signal continues to increase despite constant total heating, because the more centrally concentrated heating is more effective per unit power and the longer wire is better at insulating its center. This matches up with the same effects seen in Figure 5.8. In the simulated example, beyond 3 cm in length the wire heated by the "thin" 1.6 cm beam starts showing a decreasing relative signal with wire length, while the fully illuminated wire exhibits a monotonously increasing relative signal within the range of simulated wire lengths.

Even in this essentially best case scenario for a longer wire where every increase in length also increases power delivered linearly, the relative signal for the fully illuminated wire only increases very slowly above 4 cm of wire length.

The same relative signal analysis for a realistic scenario using f_{rec} as described by Equation (5.18) for HABS-like beams (Section 4.1) is shown in Figure 5.10. We select a beam of 1×10^{17} atoms/s and beam shape parameter $l_{\text{eff}} = 4$. This roughly corresponds to a beam that is created by passing 1 sccm of H₂ through the source with a dissociation

fraction of $\approx 10\%$. This is approximately the type of beam that is actually measured in Section 8.4.1. The centrally concentrated nature of the simulated HABS beam, means that it too produces a maximum in relative signal for relatively short wire lengths, in this case around 5 cm.

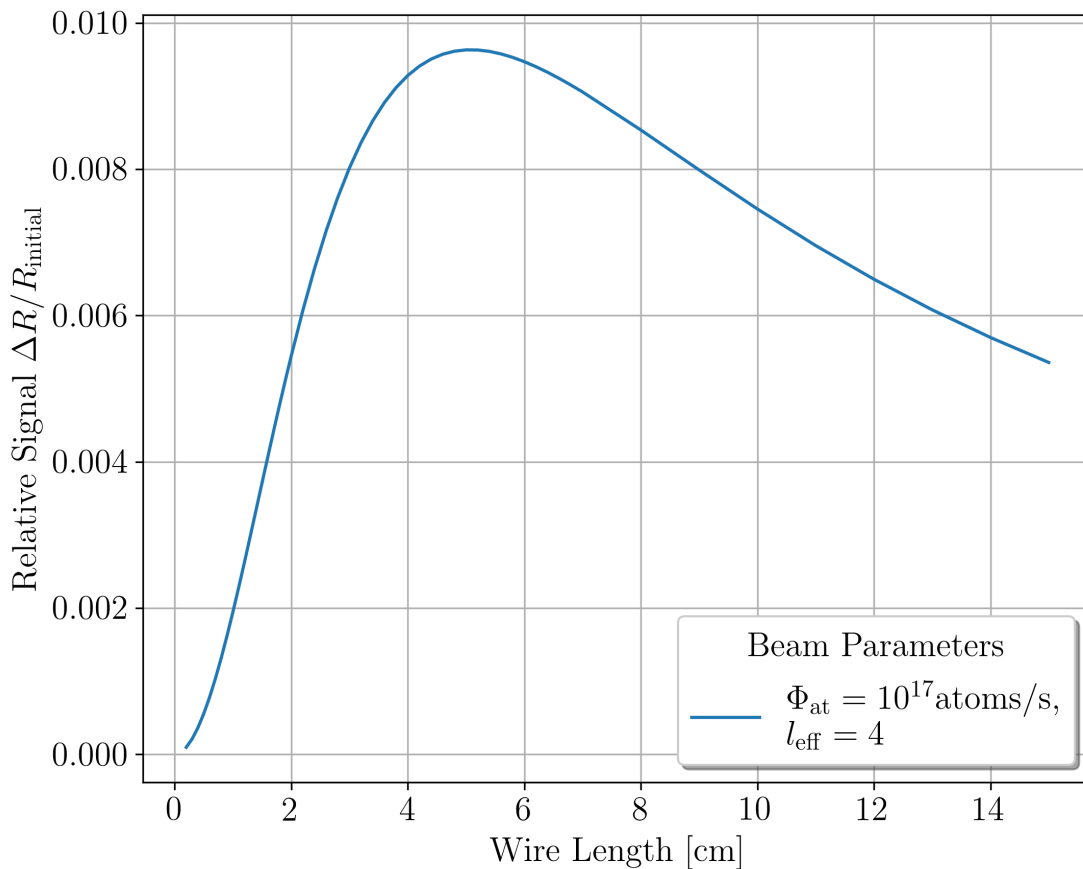


Figure 5.10: Simulated relative signal for wires illuminated with a realistic beam containing 1×10^{17} atoms/s. See Figure 4.5a for a reference of the beam shape with $l_{\text{eff}} = 4$. This beam approximates a real beam at a flow rate of 1 sccm of H_2 and $T_{\text{HABS}} = 2200$ K.

We can conclude, that the choices we made to keep the wire length between 2 to 3 cm due to space restrictions are also not too far off optimal wire lengths in terms of relative signal. Any shorter wires would start to suffer strong penalties in signal due to more efficient thermal conduction. Any gains of longer wires would be marginal, and unlikely to be worth the trade offs they would require for construction. We caution, that the values for optimal wire length may change when other wire parameters, are changed, especially for changes in wire thickness.

5.5.2 Wire thickness

To determine the effect of wire thickness on the resistance change signal, we simulate the effect of a constant density atomic hydrogen beam of various magnitudes on wires with varying wire diameters d_{wire} . The resulting relative signal for a beam with constant density of 10^{16} atoms/(cm^2s) over the entire wire is shown in Figure 5.11.

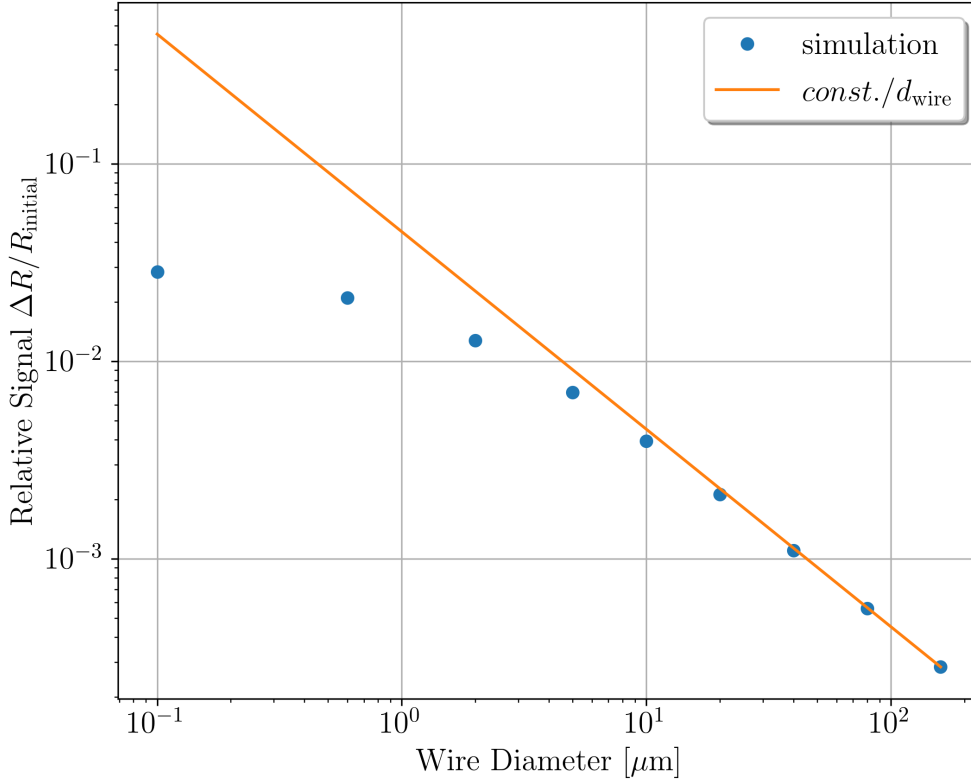


Figure 5.11: Relative Signal for a beam of uniform density of 10^{16} atoms/(cm^2s) for various wire diameters. A $\text{const.}/d_{\text{wire}}$ trend line is plotted to illustrate the behavior for large wire diameters, with the constant fitted to the largest diameter simulation. At small wire diameters the relative signal flattens out, indicating a diminishing return for further decreasing wire diameters below $10 \mu\text{m}$.

For large wire diameters ($\gtrsim 10 \mu\text{m}$), the heat transfer along the wire is dominated by thermal conduction (see f_{cond} Eq. (5.35)). This effect scales with the cross sectional area of the wire, and is therefore proportional to d_{wire}^2 . A thicker wire also receives more power from a uniform density beam, scaling with the wires projected area from the point of view of the wire (see f_{rec} Eq. (5.18)). This extra power compensates one of the factors of d_{wire} from the more efficient conductive heat transfer. The result is, that the temperature difference - and therefore the relative signal $\Delta R/R_{\text{initial}}$ - scales with $1/d_{\text{wire}}$ for large wire diameters, as indicated by the trend line plotted in Figure 5.11.

For small wire diameters ($\lesssim 10 \mu\text{m}$), Figure 5.11 shows that the scaling of relative signal with wire diameter begins to flatten out. For these very thin wires, the contribution of radiative cooling (see f_{rad} Eq. (5.37)) becomes significant and eventually dominant, even for small temperature changes. This is because f_{rad} scales only with the outside of the wire and therefore with the circumference of the wire, while f_{cond} scales with the cross sectional area. The circumference is of course proportional to d_{wire} . The quadratic scaling in d_{wire} means that as f_{cond} shrinks much more rapidly with smaller d_{wire} than the linearly scaling f_{rad} . Eventually, for very small wire diameters or very high temperatures, when f_{rad} becomes the dominant cooling mechanism, the relative signal remains constant with d_{wire} . Both the projected wire area, relevant for the power received from the uniform density beam, and the wires surface area, relevant for radiating away the heat, scale

equally with d_{wire} and they compensate each other. For a comparison of the effect sizes the simulated heat flows for a $0.6 \mu\text{m}$ and $10 \mu\text{m}$ are plotted in Figure 5.12.

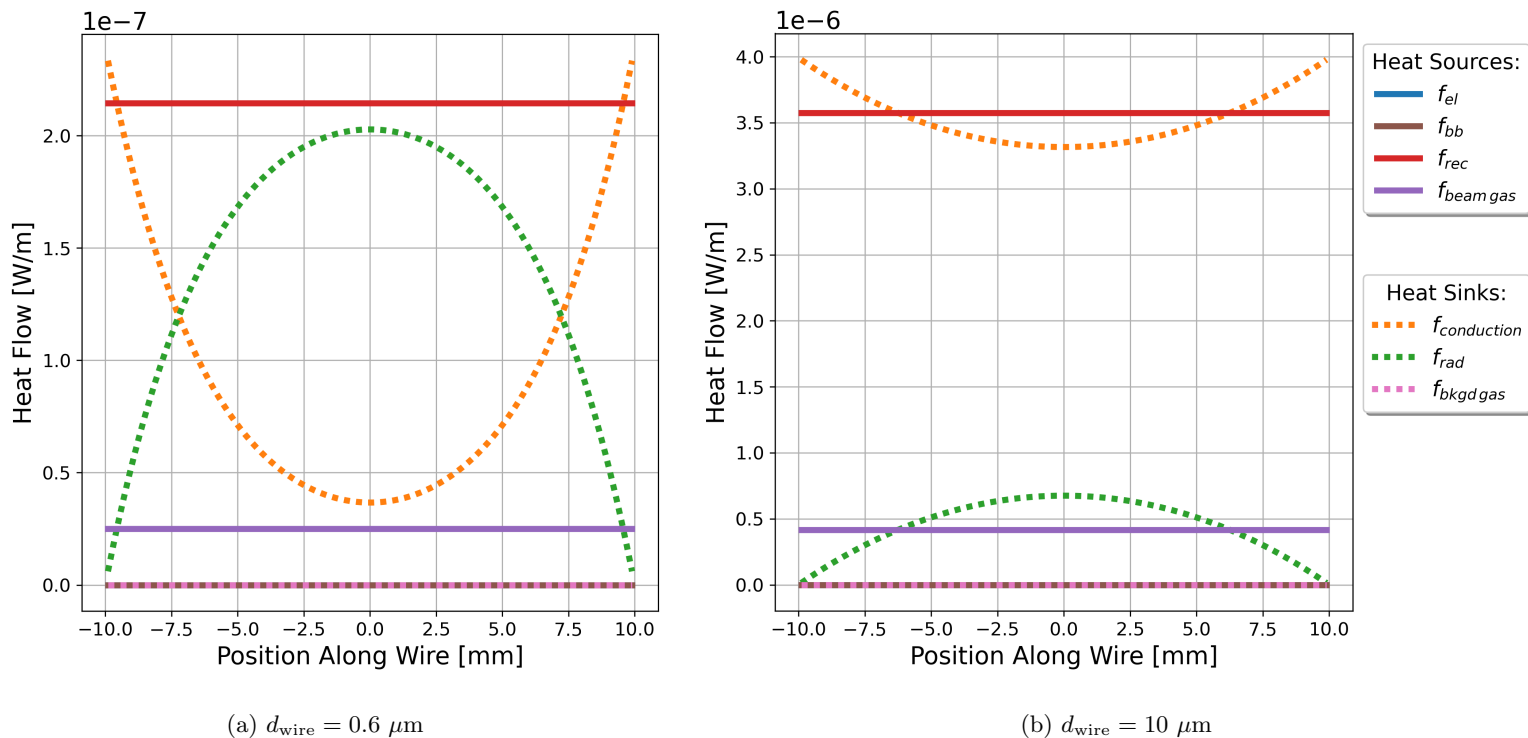


Figure 5.12: Heat flows in wires of different thicknesses for the same uniform beam intensity of 10^{16} atoms/(cm^2s). Sources which transfer heat into the wire are plotted with solid lines, while sinks that remove heat from the wire are drawn in dashed lines. Note that the heat sinks are subtracted in Eq. (5.10), and therefore cancel out a heat source of equal size in this plot. For the thin $0.6 \mu\text{m}$ wire on the left, radiative heat losses (f_{rad}) are of approximately equal importance as conductive heat losses (f_{cond}), while for the thicker $10 \mu\text{m}$ wire f_{rad} is just starting to be a non-negligible fraction of heat losses. f_{el} , f_{bb} and $f_{\text{bkgd gas}}$ are both set to 0 in this simulation for simplicity.

Additionally in Figure 5.13 we plot the relative signal size for a range of wire thicknesses and beam intensities. This shows that for a sufficiently intense beam the relative effect sizes for all beams flatten out and converge. This is because a heat source (not necessarily the beam itself but perhaps f_{bb} or f_{el}) can cause the wire temperatures to rise high enough that even for comparatively thick wires, f_{rad} becomes dominant due to its $\propto T^4$ scaling. At that point both the dominant heat loss mechanism (radiation) and the heat signal (recombination) scale equally with the surface area of the wire such that all wires behave similarly. The reduction in slope of the relative signal for wires in the radiation dominated regime is one reason why operating the wires at temperatures $> 500\text{K}$ is not generally useful.

For the laboratory measurements presented in this thesis, we chose to use $5 \mu\text{m}$ thick wire, as this was the minimum thickness of tungsten wire that was readily available for purchase. We have found offers for wires down to a thickness of $0.6 \mu\text{m}$ in platinum, but given the diminishing returns in relative signal with wire diameter we do not think it is necessary to pursue even thinner wires for a gain of perhaps a factor of 3 in relative signal. The potential effects of an accompanying change in material are discussed in Section 5.5.3 below.

Constructing detectors from very thin wires becomes progressively more difficult with

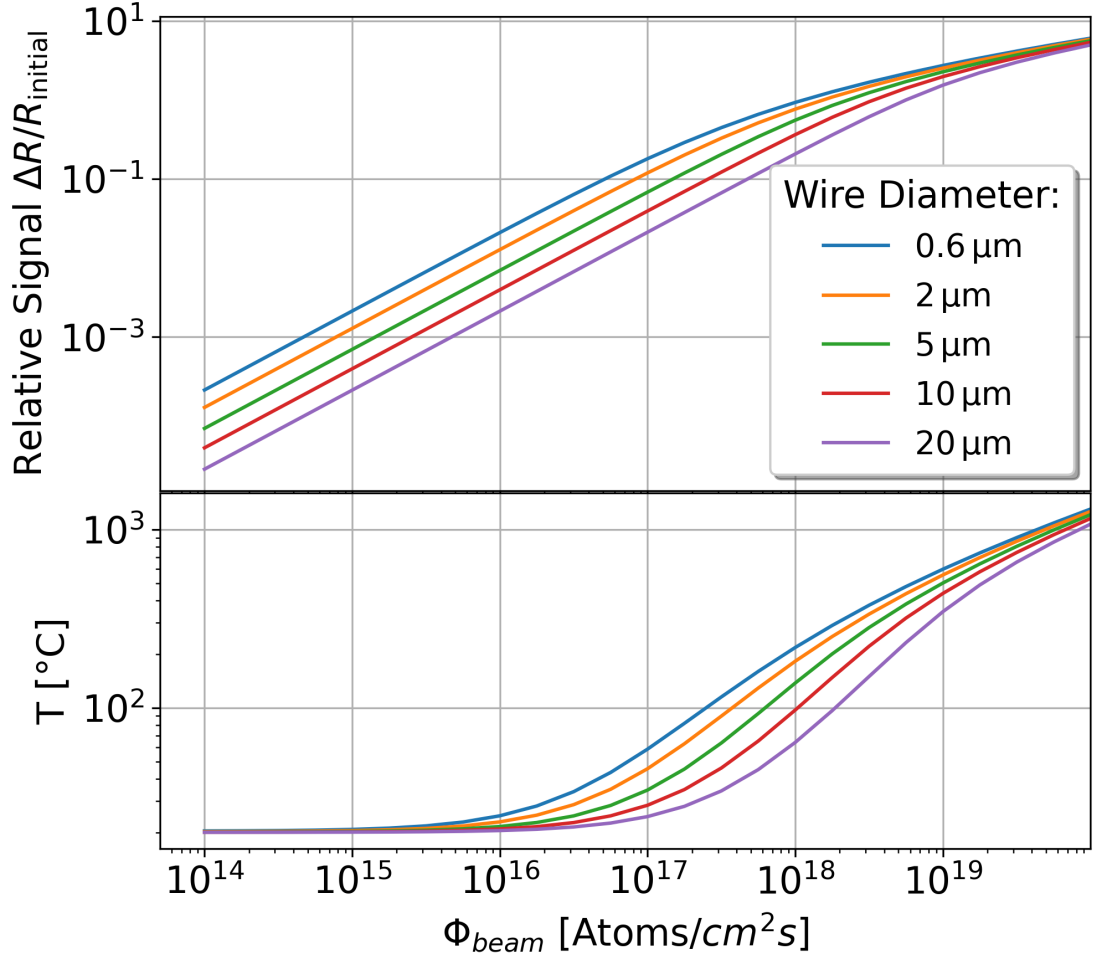


Figure 5.13: Simulated relative signal size plotted as a function of the beam intensity for a uniform density beam for wires of varying diameter. For low intensity beams and therefore low temperature wires, signal size increases linearly with beam intensity as expected. At high operating temperatures (T_{avg} as defined in Eq. (7.2)) the linearity breaks and all wires converge to an equal and shallower relative signal size increase. Thinner wires show generally higher relative signal, but the effect is much reduced at high operating temperatures.

decreasing wire thickness. The wires become increasingly difficult to see, and even more crucially, they become very easy to destroy by accident since the tensile strength decreases with $1/d_{\text{wire}}^2$. Using thinner wires may be possible but only with more sophisticated manufacturing methods and therefore cost. The cost factor is compounded, as thinner wires are also significantly more expensive, costing upwards of 1000€ for a single meter of 0.6 μm platinum wire.

If detectors with significantly shorter wire lengths than 2 cm are desired, then it may be required to overcome these challenges and go to thinner wires, to ensure conductive heat losses do not overly reduce the signal as shown in Figure 5.8.

5.5.3 Alternate wire material platinum as a case study for the calorimetric efficiency of the detector

For the investigation presented in this thesis, both simulation and laboratory measurements, we have used gold coated tungsten wire (W/Au) wire unless otherwise indicated. It has been suggested, that platinum (Pt) wires may also be a good or better candidate

for this work. This has been argued on the grounds of platinum’s catalytic properties, which are hoped to result in high recombination rates.

For illustration of what I ultimately deem to be at least a partial misconception I will recount the content of 3 sources as they relate to the calorimetric efficiency of the wire detector:

Recall from Section 5.3.1 that we define the calorimetric efficiency for recombination of atoms on a given surface as the fraction of the total available chemical energy in form of the difference in binding energy between atomic and molecular hydrogen that is ultimately transferred to the wire as heat. This fraction which we will call η_{rec} can be divided into multiplicative factors based describing sub-steps of the process. One possible division is

$$\eta_{rec} = \alpha_H \cdot \gamma_S \cdot \beta_{rec} \quad (5.48)$$

where α_H the likelihood of an atom, which hits the surface to stick to it, γ_S the likelihood of an atom adhered to the surface to recombine into H_2 , and β_{rec} is the fraction of the recombination energy that is deposited into the wire (rather than being carried away by the H_2).

Livshits et al. [44] claims that for sufficiently clean platinum $\gamma_S \approx 1$, and that this applies for many other metals independent of temperature so long as they are sufficiently clean. Livshits cites [45] for this claim. This is a PhD thesis I don’t have access to and therefore cannot further evaluate. He claims, that other experiments report γ_S to be between 0.05 and 0.3 because their surfaces were ”insufficiently cleaned”. As we can neither replicate their cleaning procedure, since we cannot access a description of them, nor verify their claims, we have to assume our surface will be ”insufficiently cleaned” and therefore we expect γ_{rec} to be smaller than 0.3, potentially significantly smaller. Livshits additionally assumes $\alpha_H = 0.2$ when evaluating data presented in the source. As this paper deals primarily with the net dissociation of H_2 this paper does not include any assumptions, measurements or references for β_H , since this parameter is only relevant for calorimetry based on recombination.

Nevertheless, Ugur et al [4] argues based on Livshits that their platinum calorimeter can be treated as having a ”recombination coefficient” $\gamma_{Ugur} = 1$ due to being degassed before use. They further effectively subsume all the sub-step parameters into γ_{Ugur} such that $\gamma_{Ugur} \equiv \eta_{rec}$ as defined above (though they do not state this explicitly). We point this out, because it is fairly common practice in literature on atomic hydrogen calorimetry to implicitly simplify η_{rec} by setting it to 1 to obtain ”measurements” of absolute H flux densities. While we do use this simplification for the wire simulations presented, we deem this an unrealistic simplification, which is why we will not present absolute flux measurements based on this simplification except as lower limits.

With differing symbol convention, Melin et al. [42, 46] presents measurements of the components of $\eta_{rec} = \gamma' \cdot \beta_H$ where effectively $\gamma' \equiv \alpha_H \cdot \gamma_S$. We reproduce their Table 1 measurements for various metals in our Table 2. While the values presented therein show very significant uncertainties, it seems clearly evident, that the product η_{rec} relevant for calorimetry of H recombination is far below 1 for any metal that was tested.

Based on Table 2 we cannot expect tungsten or platinum to have higher η_{rec} than the gold coated tungsten wires we use. Of course, as these are surface based parameters, different surface treatment may indeed result in different values. Livshits [44] suggests properly treating platinum may result in improved η_{rec} . Indeed platinum exists in untreated form with a thin surface layer of PtO_2 which may be removable by heating to beyond 500 °C in vacuum [47, 48]. But unless we can confirm a consistent way to prepare the surface to increase η_{rec} the assumption of such an improvement seems unwarranted

at present.

Metal	$\gamma' \equiv \alpha_H \cdot \gamma_S$	$\beta_H \equiv \beta_{rec}$
Ag	0.05 ± 0.02	0.87 ± 0.3
Au	0.03 ± 0.02	0.65 ± 0.2
Co	0.13 ± 0.05	0.28 ± 0.1
Cu	0.09 ± 0.04	0.43 ± 0.15
Fe	0.10 ± 0.04	0.08 ± 0.04
Ni	0.10 ± 0.04	0.11 ± 0.05
Pt	0.06 ± 0.03	0.15 ± 0.05
W	0.08 ± 0.03	0.20 ± 0.08

Table 2: Hydrogen recombination parameters by surface material reproduced from Table 1 in Melin et al. [43]. According to this data one would not expect $\eta_{rec} \approx 1$ for any of these materials, and indeed would expect a higher calorimetric efficiency for both gold and tungsten than for platinum.

While it may be worth investigating thorough and standardized surface cleaning methods, we do not expect a change to platinum wires alone to make a simplification to $\eta_{rec} \approx 1$ reasonable when reporting measured absolute atomic flux densities. Unless robust methods for measuring η_{rec} in-situ were to become available, we must treat it as a free parameter in our modeling. If absolute H flux were known from another measurement, a thusly calibrated beam could be used to measure η_{rec} (See Section 8.6), but this was not the case for results presented in this thesis.

While we cannot make definitive statements on the surface characteristics of platinum wires compared to gold coated tungsten, we can simulate the calorimetric properties of the wire that result from the bulk characteristics. The values used for comparing the simulations are listed in Table 3. Note that the surface characteristics η_{rec} and ε are deliberately set to equal values, that are not necessarily accurate for either material.

Symbol	Name	W	Pt	Unit
ρ_R	Specific resistance	0.052×10^{-6}	0.1058×10^{-6}	$\Omega\text{m}/\text{m}^2$
a	Temperature coefficient of resistivity (at 20 °C)	4.9×10^{-3}	3.92×10^{-3}	1/K
κ	Thermal conductivity (at 20 °C)	174	71.6	Km/W
C_V	specific heat capacity	133	133	J/(kgK)
ρ	density	19 300	21 450	kg/m ³
ε	Emissivity	0.3	0.3	[1]
η_{rec}	Recombination energy yield	1	1	[1]
	Melting Point	3695	2141.4	K
	Tensile Strength	550 to 1920	125 to 300	MPa

Table 3: Material properties used in the simulations. Melting point is not used during the simulation, but shows that both wire materials are easily capable of larger temperature operating windows than required. Note that the surface characteristics η_{rec} and ε are **deliberately set to equal values**, that are not necessarily accurate for either material.

The resulting simulated relative signal for platinum and tungsten wires of varying thickness both exposed to the same atomic H beam of uniform flux density 10^{16} atoms/(cm²s) is shown in Figure 5.14. As previously shown in Figure 5.11, we see that when heat flow is dominated by thermal conduction at large wire diameters both wires exhibit relative signals scaling with $1/d_{\text{wire}}$. In this regime the relative signal of a Pt wire is

about a factor of 2 larger than for W. This is chiefly due to the much lower thermal conductivity of Pt listed in Table 3. When transitioning to very thin wires where thermal radiation dominates, the relative signals approach each other and eventually W has a slightly higher relative signal. This is because we used the same surface emissivity ε for both wires, and therefore they have the same thermal emission behavior in our model. Once both wires behave essentially equally thermally, the slightly higher temperature coefficient of resistivity of tungsten causes it to produce a slightly higher relative signal.

In all wire diameters, platinum will have a higher absolute signal ΔR due to its specific resistance, which is about twice the size as that of tungsten. From the point of view of manufacturing the detector, we caution that the tensile strength of platinum is only about one quarter that of tungsten. Therefore, for equal ease of assembly, a platinum wire would have to be about twice as thick as the tungsten wire. This matters for manual assembly, as breaking tungsten wires at $5\ \mu\text{m}$ thickness is very common. For sufficiently advanced manufacturing, this may not be a large problem beyond additional cost.

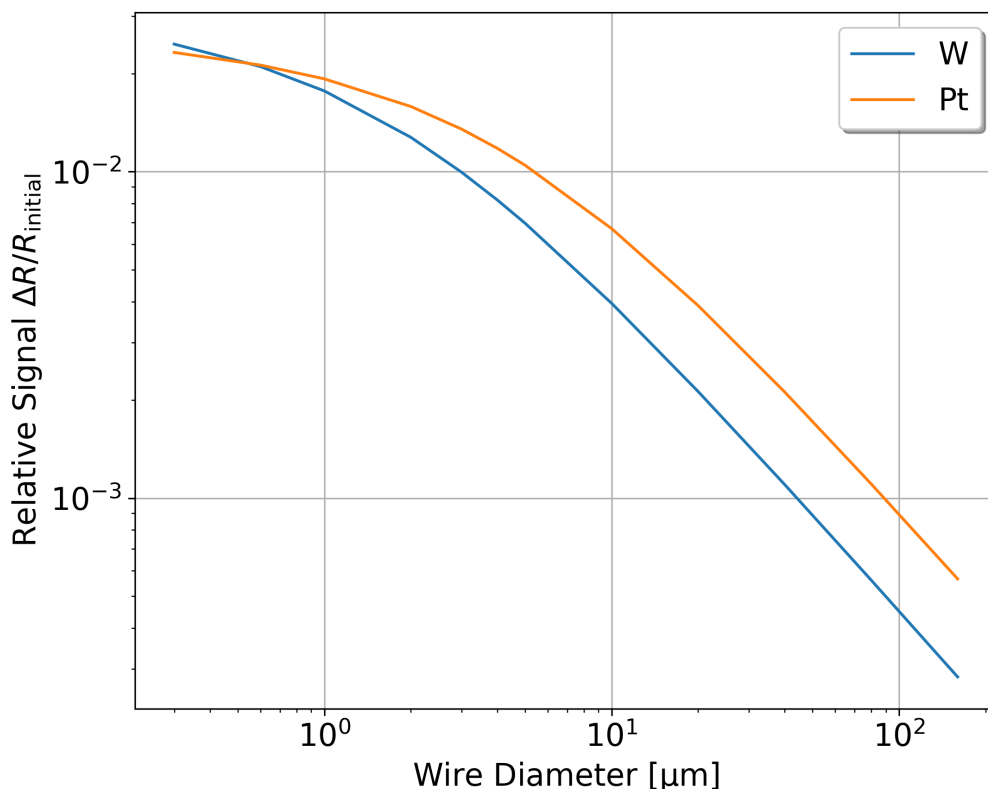


Figure 5.14: Simulated relative signal for wires of either tungsten or platinum of diameter, both illuminated with a uniform density beam of 10^{16} atoms/(cm^2s). Surface characteristics are set to be equal for both wires and only bulk properties are different (see Table 3). The platinum wire produces larger relative signals at large wire diameters by about a factor 2, with the gap narrowing below $10\ \mu\text{m}$ wire thickness.

Overall, use of monolithic platinum wires rather than gold coated tungsten wires may result in perhaps a factor of 2 in calorimetric efficiency based on purely the bulk properties of the material. In terms of surface characteristics, it is much harder to be certain. Work by Melin [43] suggests platinum would be less well suited than a gold surface, while

Livshits [44] claims properly treated platinum may be as much as 10 times as effective. In any case if surface properties alone are the goal, it is also possible to acquire platinum plated tungsten wires¹⁵. The question of optimal wire material is ultimately not resolved in this thesis. Work presented here will feature gold-coated tungsten wires primarily, and we will show that they are serviceable if perhaps not necessarily optimal.

5.6 Wire sensitivity

As we already saw in simulations presented in Section 5.5.1, the effect of heating power on wire resistance depends on where along the wire the power is applied. This is primarily due to the thermal insulation properties of the thin wire. For centrally located parts of the wire, the distance to the attachment points is maximized. This means that heat deposited here is less effectively conducted out of the wire, leading to a larger heating in place and in turn a larger change in wire resistance. In this section, we will quantify this effect by simulating a point heat source at all points along the wire and comparing the relative effect on wire resistance.

A test heating power can be applied to an arbitrary point of a simulated wire in thermal equilibrium. By calculating the total resistance of the wire with and without the test point source, the change in resistance due to the test source is determined. The position at which the test source is applied is then shifted along the wire, until a sample is generated at every segment of the simulated wire. This allows for determining the relative effect of a heating power based on the location at which it is applied to the wire. The absolute size of the simulated ΔR signal is deemed unreliable at worse than 10% accuracy, however the relative effect size should be much better than that.

In practice, a simulated $1 \mu\text{W}$ point source is applied along the wire and ΔR induced in the wire resistance is recorded. The values of ΔR are then normalized by the average value ΔR_{avg} yielding the relative wire sensitivity¹⁶

$$\eta_{\text{wire}}(x_i) = \frac{\Delta R(x_i)}{\Delta R_{avg}} \quad (5.49)$$

with x_i the position of the wire of segment i at which the simulated point heat source is applied.

Sensitivity is highest in the center of the wire with steepening decline to the ends of the wire. The change in local wire sensitivity is caused by the fact that the temperature profile is curved leading to places where (primarily) thermal conduction is more or less effective at carrying extra heat out of the wire. Figure 5.15 shows the value of the relative wire sensitivity along the wire.

When using the wire this means that the part of the beam hitting the center of the wire has a disproportionate effect. This is accounted for by interpolating over the $\eta_{\text{wire}}(x_i)$ of each segment and including the resulting function $\eta_{\text{wire}}(x)$ in the signal model given in Eq. (8.5).

The exact shape of the simulated wire sensitivity depends on the temperature distribution along the wire. For small amounts of heating the wire sensitivity is nearly parabolic in shape. For large amounts of heating $\gtrsim 100\mu\text{W}$ from any source, the wire temperature profile begins to flatten in the center as thermal radiation cooling (f_{rad}) becomes a more important contribution. This similarly affects the wire sensitivity profile.

The investigation into wire sensitivity distribution including attempts to measure it in situ, using a laser as a point heat source, rather than simulating it is covered in far

¹⁵For example from goodfellow.com

¹⁶Note that the wire sensitivity η_{wire} is **not** the same as the calorimetric efficiency η_{rec} they are separate factors which both influence the reported recombination signal multiplicatively.

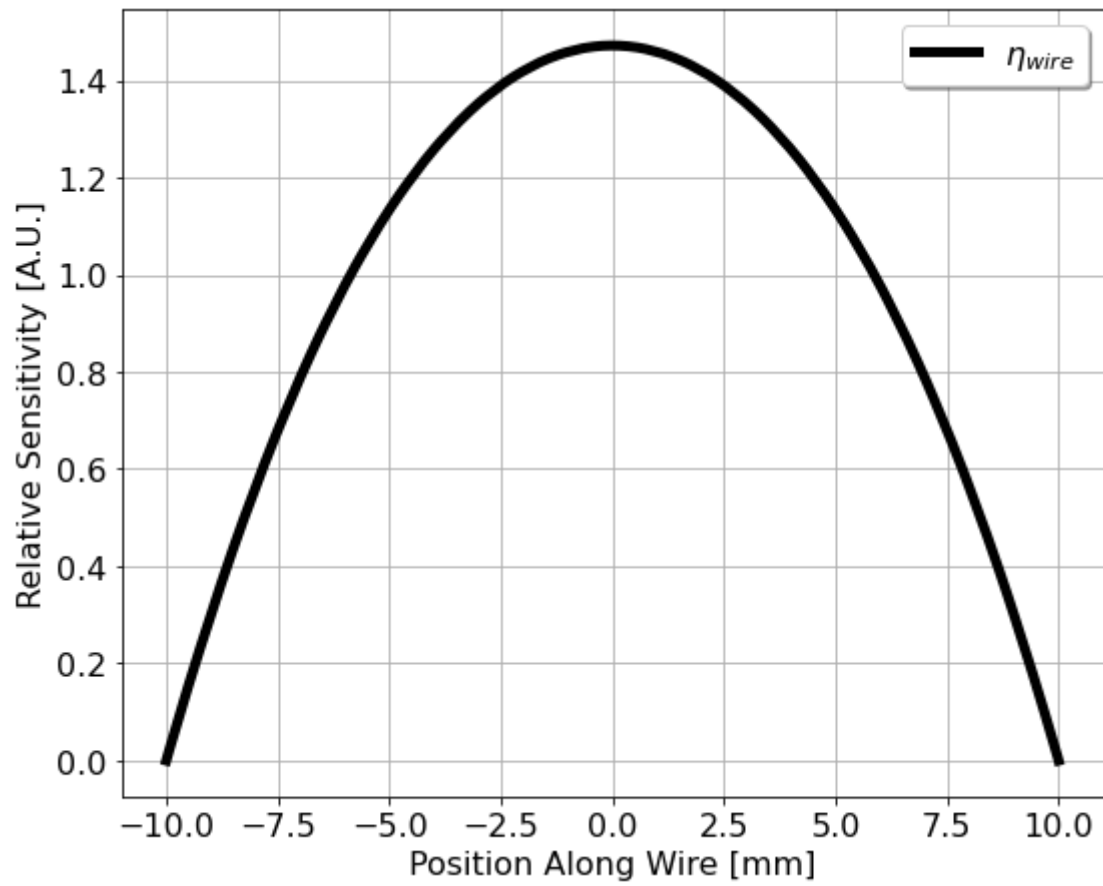


Figure 5.15: Normalized local wire sensitivity η_{wire} . A larger η indicates a larger resistance change for a given change in input power. Sensitivity is highest in the center of the wire with steepening decline to the ends of the wire.

greater detail in the bachelor thesis of Darius Fenner [49]. For the work presented in this thesis, we use the simulated wire sensitivity unless otherwise specified.

6 Design Iterations

This section will chronicle the history of changes made to the wire detector design. It serves as a reference for other sections such that it can be specified which data was taken with which version of the detector.

6.1 First realization (V1 Prototype)

The first prototype of the wire detector is pictured in Figure 6.1. It will be referred to as the Version 1 (V1) Wire detector when mentioned later in this document.

This prototype was realized by designing a simple PCB to hold the wire. Two 0.2 mm plated vias in the front of the board serve as solder spots to mount the wire. It was originally envisioned to thread the wire through the vias and to tension them by pulling from below. This was found to be infeasible and so the wire was simply laid across the vias and soldered to them. The solder connection therefore serves as both electrical and mechanical connection.

There is a large cutout in the PCB, separating the two wire mounting vias such that the wire is hanging freely. This is where the Hydrogen beam will pass through, and it also means the wire is hanging freely and not losing heat to the surrounding by conduction, except where it is attached to the board.

Each of the mounting points is connected with a trace to two 3 mm plated vias that act as current supply and voltage drop readout terminals. Figure 6.1 shows the assembled board with readout leads attached with ring terminals and the wire soldered in place.

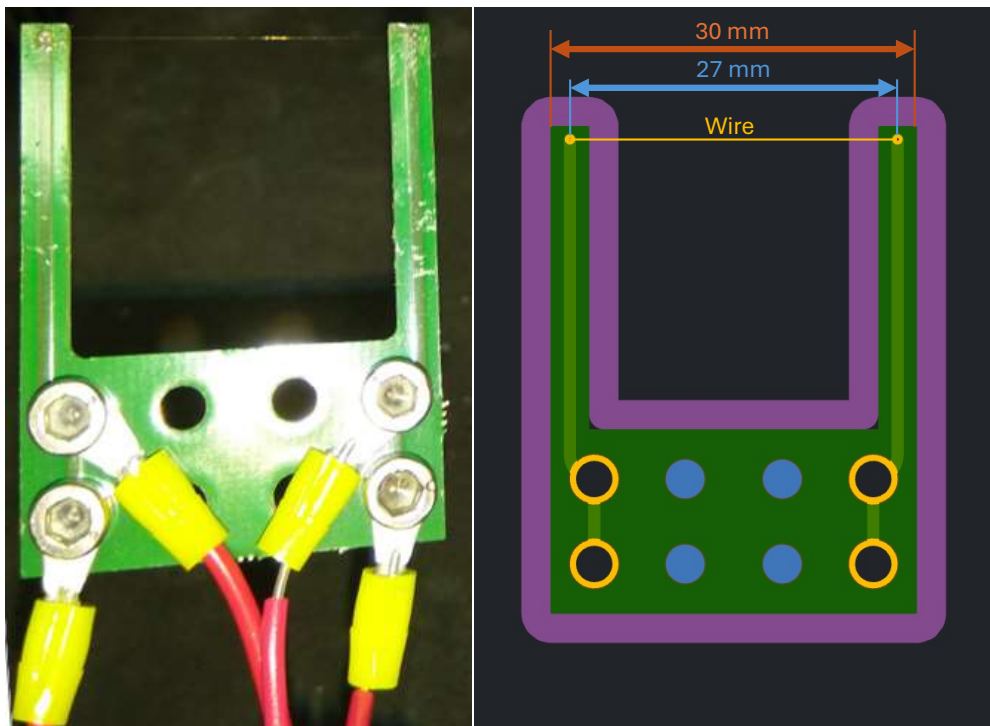


Figure 6.1: Version 1 of the assembled wire detector is pictured on the left. On the right the board schematic is displayed for clarification. The wire is soldered to the plated vias at the top of the board, such that it spans the cutout in the PCB. The length of the wire on this board is 27 mm. At the bottom of the board ring terminals are used to attach the wire leads for current supply and voltage measurement.

In this version of the detector the wire is $5\ \mu\text{m}$ thick and made of gold plated tungsten wire the gap between the mounting points and therefore the wire length is 2.7 cm. There is an additional 1.5 mm of PCB on each side of the mounting points leading to a free hanging wire length of 2.5 cm.

6.2 V2 outside via mounting

Version 2 of the wire detector pictured in Figure 6.2 differs from Version 1 only in features meant to facilitate easier assembly. As the wire is very difficult to see in lighting conditions and zoom that show the board well, the wire is additionally shown in a closeup in Figure 6.3.

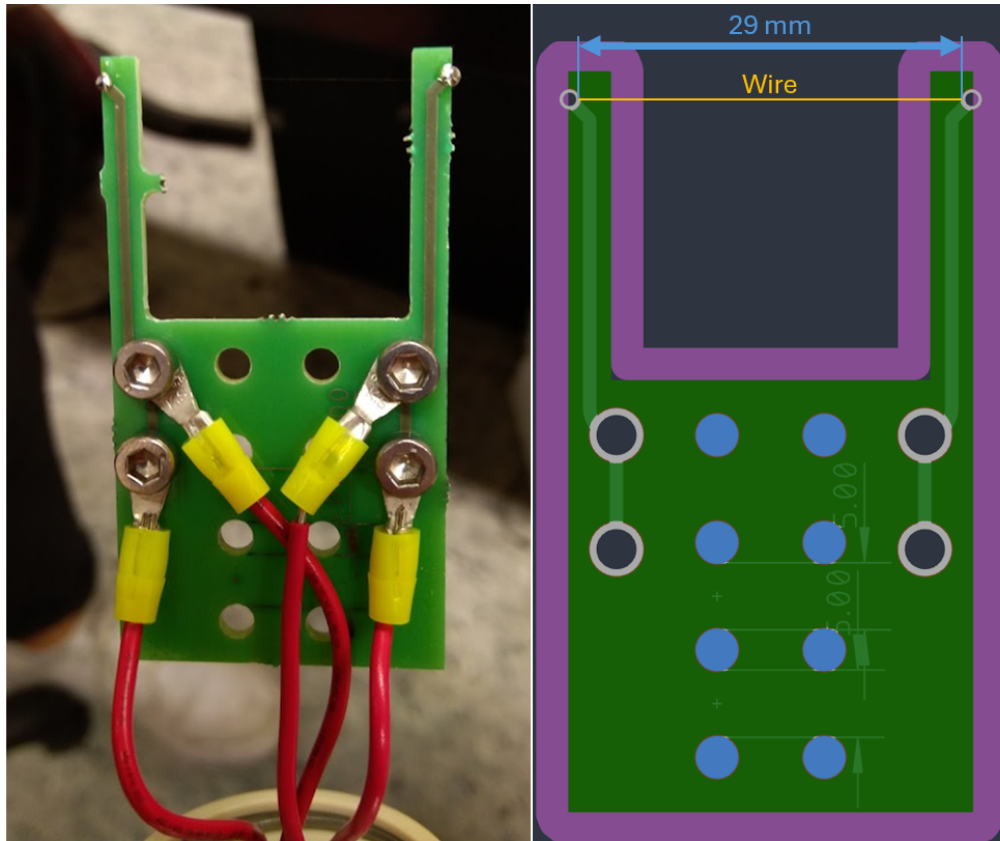


Figure 6.2: Version 2 of the assembled wire detector is pictured on the left. On the right the board schematic is displayed for clarification. The wire is soldered to the half open vias at the top of the board, such that it spans the cutout in the PCB. The length of the wire on this board is 29 mm. At the bottom of the board ring terminals are used to attach the wire leads for current supply and voltage measurement.

The vias for mounting the wire have been enlarged to 1 mm diameter and moved to the edges of the board. During production half the via is cut off leaving a conductive half cylinder for attaching the wire. This allows for laying the wire across both (half-)vias, and then weighting both ends with small tabs of tape. The indent formed by the open sided via then keeps the wire from sliding longitudinally along the board during assembly. Additionally, the weight of the tabs adds a small tension force keeping the wire as straight as possible during assembly. Moving the vias to the edge of the board has the additional effect, of slightly lengthening the wire to to 29mm and increasing the overlap with the PCB to 2.5 mm on either side.

The second change made to V2 is a lengthening of back end of the board to add 4 more 3mm mounting holes that are further away from the electrical terminals. This is required when attaching more substantial holding structures. In previous stages of testing the exact position of the board was not yet important so the PCB was simply held up by the AWG size 20 wires attached to the electrical terminals.

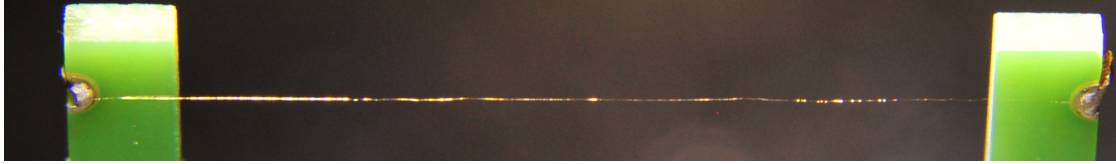


Figure 6.3: Closeup of the wire soldered to Version 2 of the wire detector board. There is about 2.5 mm of overlap of the wire with the PCB on either side.

6.3 V3 Multiple parallel wires

Version 3 of the Wire detector board is pictured in Figure 6.4.

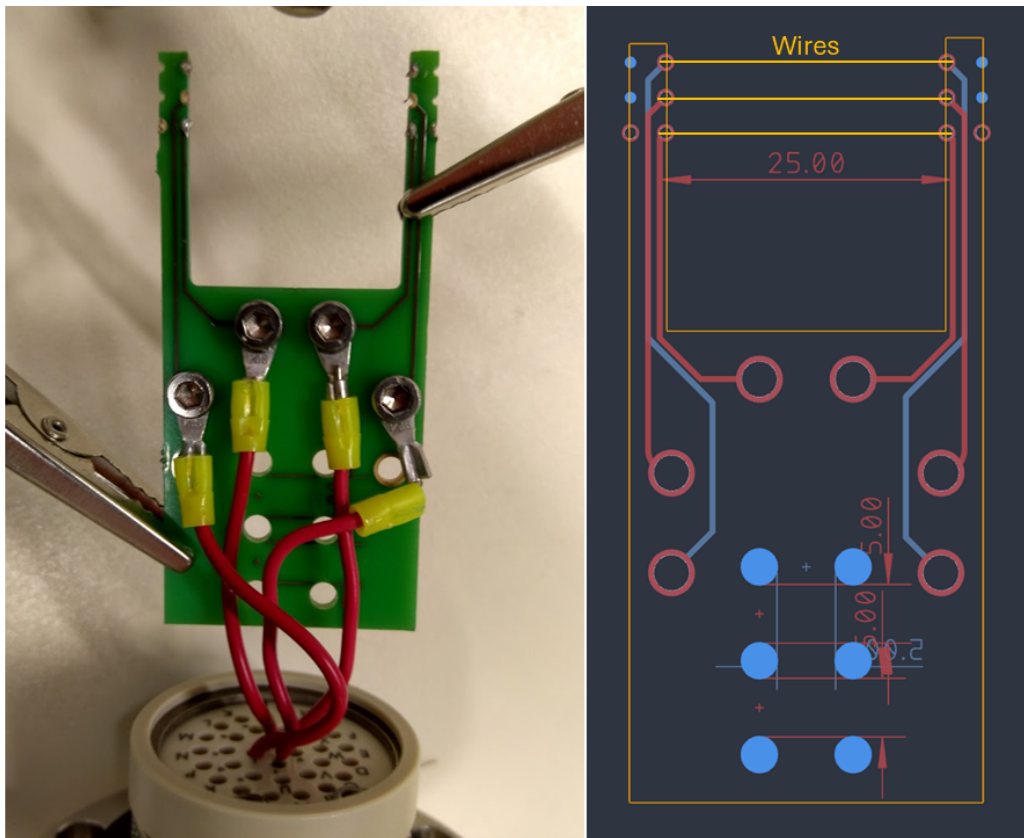


Figure 6.4: On the left is an image of Version 3 of the wire detector. This board has 3 sets of wire mounting pints and readout terminals. 2 of these readout terminals are pictured connected to ring terminals with wires running to the vacuum electrical feedthrough at the bottom edge of the image. On the right is a schematic of the PCB indicating the location the wires are to be mounted in and the way traces are run to the M3 terminals. Traces in red are run on the front side of the board, those in blue are on the back side.

The most important change in this version of the PCB is that it allows for attaching and reading 3 wires parallel to each other. This adds a degree of redundancy, as in the

case of a wire breaking, the same measurement can be done on one of the others. It also allows for checking whether separate wires act in similar ways without installing an entirely new detector board each time a consistency check is to be performed. Where required, the wires can also be read out simultaneously, to measure at multiple locations in the chamber and potentially across a beam at the same time. This was also envisioned to enable position reconstruction of a measured beam, by seeing how beam intensity evolves with wire position. However, the same goal was ultimately accomplished by moving the entire board by means of a z-translator.

Wires in close proximity to each other can also be used as a known radiative heat source by running a large current through one wire and measuring the effect on nearby wires.

In this version of the detector, the wires are soldered vias on the inside edge of the holding structure cutout. Contrary to version 2 this means there is no longer a section of the wire overlapping with the PCB. The length of the wires is now reduced to 25 mm all of which is suspended freely between the solder spots.

To keep the ease of assembly gained in Version 2, cutouts are retained on the outside edge of the board, inline with the wires. These once again allow for laying the wire across the now instrumented cutouts, and then weighting both ends with small tabs of tape. The cutouts then prevent the wire from sliding along the long side of the board during soldering. The bottom outside cutout had been accidentally left as a plated via, but a this is not connected to anything it functions the same as the simple drill holes.

Each wire is only connected via trace to has two rather than four M3 terminal locations in this version. The electrical readout on this board has therefore been reduced to a two-wire setup on the board to save space on the board and on the number of wires required to run inside the vacuum. However after running the wires out through the vacuum electrical feedthrough, a 4 wire measurement can of course be started from that location.

Due to space constraints, one of the traces leading from the M3 terminals to the wire attachment vias is run on the back of the PCB. This trace is colored blue in the Schematic in Figure 6.4.

6.4 V4 Ceramic PCB

Version 4 of the wire detector is pictured in Figure 6.5. It is the final version of the wire detector relevant to this thesis and was used for all measurements that feature atomic hydrogen. The main differences to Version 3 are:

- A change in material from plastic to ceramic (Aluminum Nitride)
- Change from using plated vias to pads as wire mounting points
- Width of "tongs" increased to 5mm
- Routing of all traces on the top of the PCB

The change in PCB material to Aluminum Nitride (AlN) ceramic was made to increase compatibility with ultra high vacuum as is present in some sections of our setup. Outgassing from ceramic is significantly lower than standard plastic PCB components [50], making it a requirement, at least in those parts of our vacuum chamber near to our mass spectrometer, where we aim to maintain pressures of $\approx 10^{-10}$ mbar.

Another advantage of using a ceramic PCB is that AlN has a very high thermal conductance of 170W/mK, as quoted by the manufacturer¹⁷, which is roughly 1000 times

¹⁷PCBs are manufactured by CERcuits: <https://cercuits.com/aluminum-nitride-pcb/>

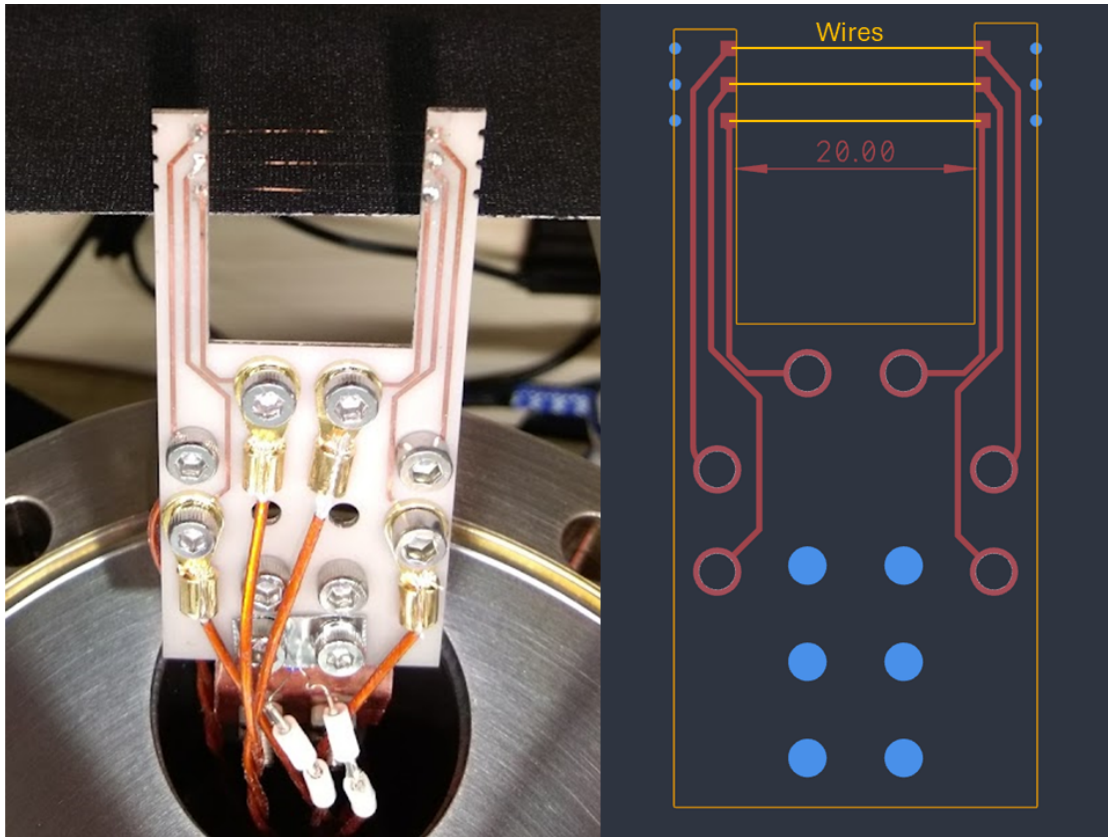


Figure 6.5: On the left is an image of Version 4 of the wire detector. This board is now made of Aluminum nitride ceramic and using pads rather than plated vias as solder points for attaching wires. 3 wires are attached and can be made out by their faint gold glint against the black background. On the right is a schematic of the PCB indicating the location the wires are to be mounted in and the way traces are run to the M3 terminals. All traces on this board are run on a single side.

higher than for plastic PCBs. This makes the ceramic substrate an excellent thermal sink for the attached wire detectors. This is desirable as we aim to do our calorimetry with known and stable temperatures for the attachment points of the sensor wire. A high thermal conductance guarantees that the detector board will not locally heat up and distort the results.

The increased chemical stability of AlN may also be relevant in an environment with significant quantities of highly reactive atomic hydrogen; however, it was not tested whether this would have constituted a real problem if using plastic PCBs.

In this version of the detector, we move to pads rather than vias for attaching our wires. This was changed because the initial use of plated half open vias was only used for ease of assembly of the Version 2 detectors, where the via would serve as both the attachment point, and the indent in board used to keep the wire from sliding during assembly. In both version 3 and 4 there are now separate indents cut in line with the wire mounting points to aid assembly. The larger surface area of the pads makes it slightly simpler to solder to.

The width of the detector "tongs" has been increased to 5 mm on each side in this version of the detector, as the manufacturer had concerns of the structural integrity of the ceramic for widths smaller than 5 mm during production. This reduces the width of the cutout in the PCB, and therefore the length of the wires to 20 mm. This increase in width also allows us to route all traces on the same side of the PCB. Which is now

important as we are using Pads which cannot be soldered to on either side of the PCB like the vias.

7 Beamless Wire detector measurements

In this section we will attempt to make measurements to either confirm or improve our understanding of the wire detector's behavior. In particular we will need to understand its response to heat. Since we do not have a well understood beam based heat source, we will present a number of measurements using the wire detector that do not involve any atomic or molecular beams. Instead we run current through the wire to heat it, since this is much simpler to control. By measuring both the voltage V over and the current I through the wire we measure both the heating power applied $P = V \cdot I$ and the wire's response in the form of its resistance $R = V/I$. Comparison to simulation will allow us to assess whether a particular aspect is well understood or not.

We will outline ways in which some of the parameters needed for describing the wire in simulation can be measured. However, we will ultimately conclude, that pursuing a perfectly adjusted simulation is not fruitful, and will instead chose to calibrate the wire's response to heat as directly as possible and use this instead when moving forward with beam based calorimetry.

7.1 Measuring zero current resistance

In this section we present measurements to determine the base resistance of the wire at the zero current limit. This is both a real world check on the parameters we used in simulation and is required for calculating the temperature that the wire actually has during operation. According to Eq. (5.1) the resistance of the wire is given by

$$R = \int_{\text{wire}} \frac{\rho_R}{A_{\text{cs}}} (1 + a \cdot (T(x) - T_{\text{ref}})) dx.$$

In the approximated case of a constant temperature coefficient of resistivity a this can be rewritten as

$$\begin{aligned} R &= \frac{\rho_R \cdot l_{\text{wire}}}{A_{\text{cs}}} \int_{\text{wire}} \frac{(1 + a \cdot (T(x) - T_{\text{ref}})) dx}{l_{\text{wire}}} \\ &= R_0(T_{\text{ref}}) \cdot \left(1 + a \cdot \left(\int_{\text{wire}} \frac{T(x) dx}{l_{\text{wire}}} \right) - a \cdot T_{\text{ref}} \right) \\ &= R_0(T_{\text{ref}}) \cdot (1 + a \cdot (T_{\text{avg}} - T_{\text{ref}})), \end{aligned} \quad (7.1)$$

where $R_0(T_{\text{ref}})$ is the base resistance of the wire when it is at a constant reference temperature T_{ref} and T_{avg} is the average temperature of the same wire when measured at a resistance R at some other time. Which results in a relation for calculating the average temperature of the wire from resistance measurement:

$$T_{\text{avg}} = \frac{R - R_0(T_{\text{ref}})}{a} + T_{\text{ref}}. \quad (7.2)$$

The simplification of using a constant a rather than one which changes with Temperature might cause systematic deviations in calculated and actual T_{avg} of up to 5% over the range of temperatures the wire is operated at if we adopt a literature formula for the electrical resistivity of tungsten R_W in $\text{n}\Omega\text{m}$ given by $R_W = 48.0(1 + 4.8297 \times 10^{-3}T + 1.663 \times 10^{-6}T^2)$ for T in $^\circ\text{C}$ based on page 2123 of [51]. We will retain the simplification of a constant a with temperature, since this is the only case in which there is a unique T_{avg} for every wire resistance R regardless of which of the infinite options for the underlying temperature distribution $T(x)$ that would result in R is the true one. The average wire temperature will be useful during later analysis such as in Section 8.1.1 and Appendix B.2.

The wire detector is operated using DC current and voltage measurements. Any resistance measurement based on DC current necessarily carries with it a power dissipated on the resistor of

$$P_{el} = I_{meas}^2 \cdot R \quad (7.3)$$

where I_{meas} is the current running through the resistor for measurement of the voltage drop

$$V = R \cdot I_{meas} \quad (7.4)$$

over it.

The very purpose of the calorimeter wire is to respond very sensitively to any power applied to it. The P_{el} applied to it by the measurement current therefore causes an increase in wire temperature and therefore resistance. For general operations we run the wire detector at a constant 1 mA measurement current, which leads to an average operating temperature of $\approx 60^\circ\text{C}$. This is a compromise between keeping the operating temperature low and increasing the precision on the measurement current which is discussed in Section 7.2.

We use our power supply¹⁸ to run a series of increasing currents through the wire and measure the voltage drop over the wire using a precision digital multimeter¹⁹. The tests are carried out with the V4 iteration of the wire detector (see Section 6.4) located in Chamber 1 (see Figure 4.1) with the HABS turned off such that chamber pressures are lower than 10^{-7} mbar, which essentially eliminates background gas cooling ($f_{\text{bkgd_gas}}$) as a factor.

Figure 7.1 shows measured wire resistance when currents between 0.01 mA to 1 mA are applied to the wire. For currents above 0.1 mA wire resistance is nearly perfectly linear in heating power applied due to the measurement current as per Eq. (7.3), but for very low measurement currents/powers, the calculated resistance falls off steeply. This may be attributable to an offset between the current the power supply reports and that which is actually applied to the wire, either because of a small leakage current or simply because of a miscalibration of the power supply in the current range used. Due to limitations with integrating the power supply²⁰, all measurements were taken with the same 10 mA current output range setting. In this range the datasheet of the Keithley SourceMeter 2400 reports an expected source accuracy of $0.045\% + 2 \mu\text{A}$ and a measurement accuracy of $0.035\% + 600 \text{ nA}$.

In the following analysis we will use 2 different methods to determine the zero-current wire resistance limit. Method 1 is an attempt to fit for the suspected current offset and subtract it from the raw data. Method 2 is simply dropping data at low currents and extrapolating from data above 0.1 mA where the effect of any current offset would be minimal.

¹⁸Keithley SourceMeter 2400

¹⁹Keysight 34461A

²⁰Multiple attempts were made but no permanent solution for stable fully automated operations of the power supply were achieved. See the Bachelor thesis of Maxim Astashov for more details [52]

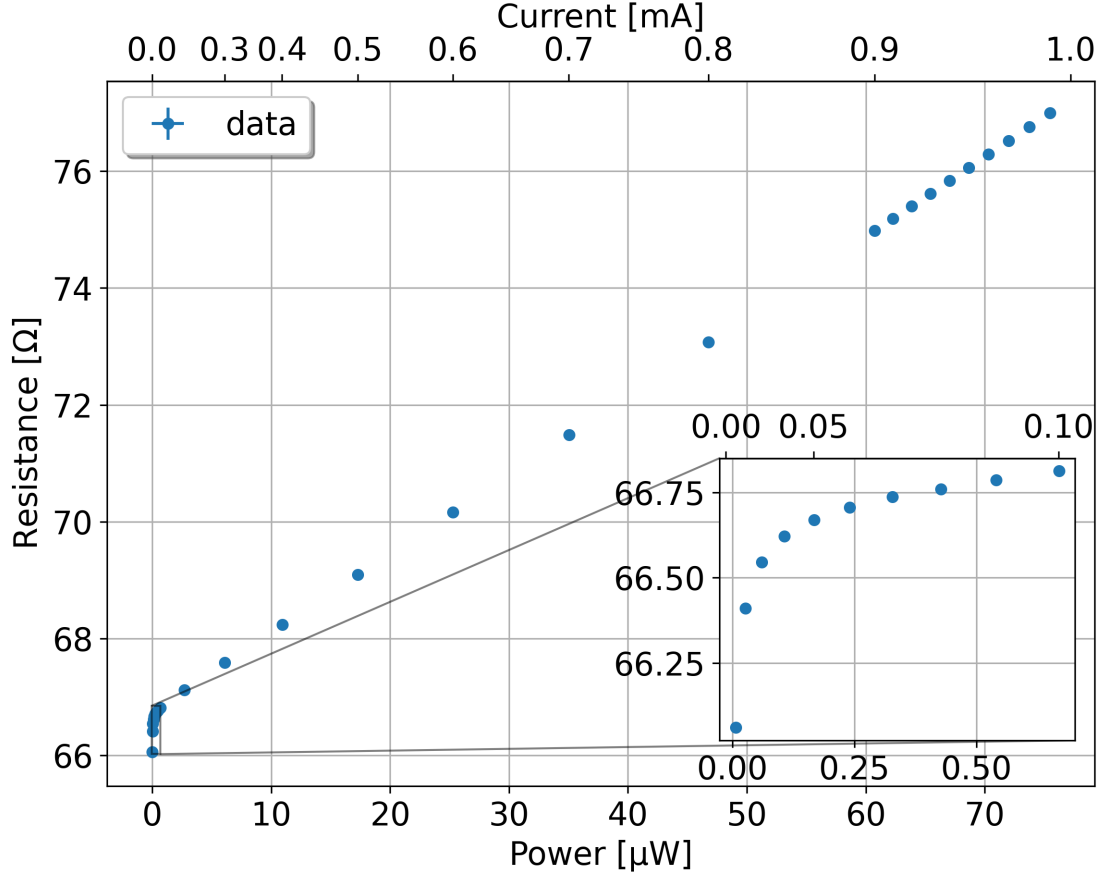


Figure 7.1: Measured wire resistance measured shown in response to applied electrical power. The inset in the lower right shows the non-linear "turn-on" behavior at low power below $0.25 \mu\text{W}$. Above this threshold the resistance response to additional power is essentially linear. The top axis shows the current supplied to the wire to produce the electrical heating power shown on the bottom axis.

7.1.1 Method 1: Low power current offset

For method 1 we want to perform a linear fit to $R(P_{el})$ after both R and P_{el} are linearized by removing the effect of the current offset I_{off}

$$R(P_{el}; m, R_0, I_{\text{off}}) = R_0 + m \cdot P_{el}(I + I_{\text{off}}, V) \quad (7.5)$$

$$= R_0 + m \cdot (I + I_{\text{off}}) \cdot V \quad (7.6)$$

where the fit parameters are: m the resistance increase per power applied, R_0 the base resistance, and I_{off} the current offset.

In order to linearize the axes we, we solve

$$V = R(P_{el}; m, R_0, I_{\text{off}}) \cdot (I + I_{\text{off}}) \quad (7.7)$$

$$= (R_0 + m \cdot (I + I_{\text{off}}) \cdot V) \cdot (I + I_{\text{off}}) \quad (7.8)$$

for V resulting in

$$V(I; m, R_0, I_{\text{off}}) = R_0 \left(\frac{I + I_{\text{off}}}{1 - m(I + I_{\text{off}})^2} \right) \quad (7.9)$$

after simplification. Resulting in a fit we can perform on the original raw current and voltage data. If the current offset assumption is good we can recalculate $R = V/(I + I_{\text{off}})$

and $P_{el} = V \cdot (I + I_{\text{off}})$ including the current offset and end up with linearized power and resistance axes.

Figure 7.2 shows this method applied to data taken at currents between 0.01 mA to 0.1 mA corresponding to the inset in Figure 7.1. The comparison shows that the curve at low powers/currents in the untreated data is mostly removed when including a rather small current offset of just 113 nA in this case. This is a far smaller offset than even the quoted accuracies for current source and measurement accuracy quoted by in the power supply's data sheet.

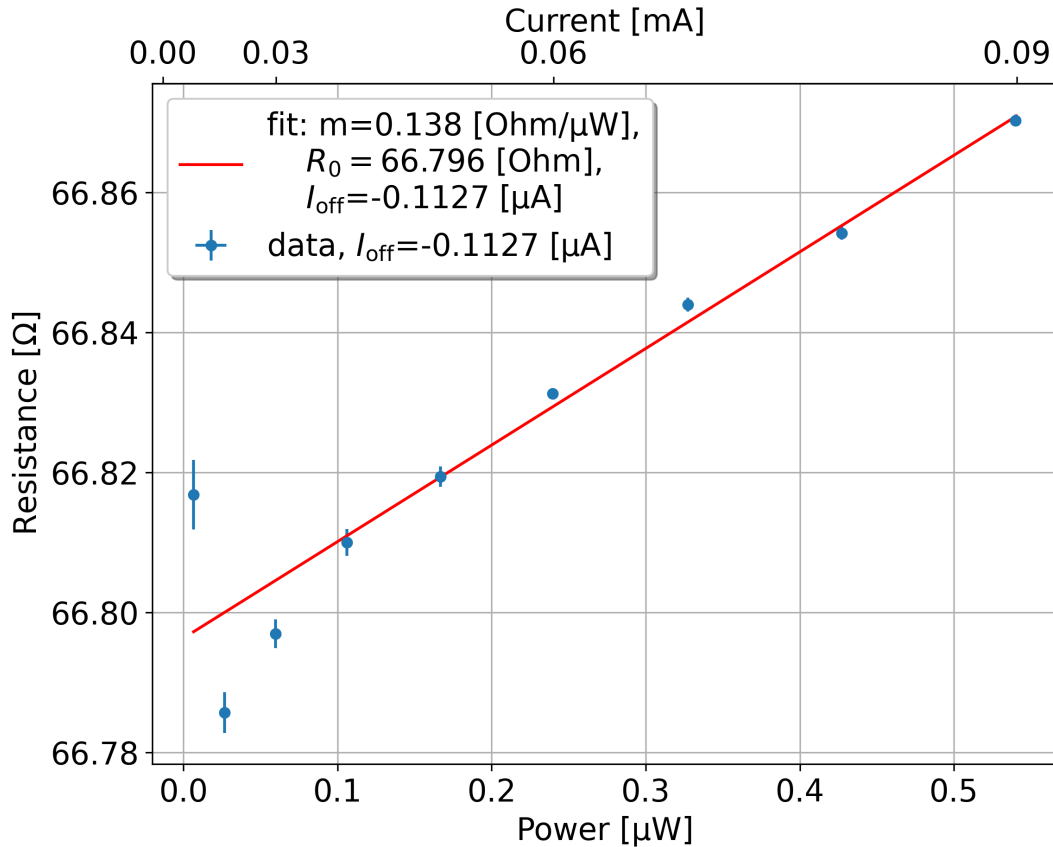


Figure 7.2: First order polynomial fit applied to data subset with currents below 0.1 mA heating current. We correct both the data and the fit by the offset current I_{off} in an attempt to remove the non-linear effects seen at low current/power in Figure 7.1.

The decent results of this method are not however proof that this is an accurate and full explanation of the underlying cause of the non-linearity in $R(P_{el})$ for low currents. As a repeatability check we performed the same analysis on 7 equivalent datasets. These produce a spread of $\bar{R}_0 = 66.78 \pm 0.10 \Omega$ and $I_{\text{off}} = -119 \pm 10 \text{ nA}$. Further we can use the Pt1000 temperature sensor located at the back end of the wire detector board (see Figure 6.5) to gauge whether there are any trends correlated with the temperature of the wire's surroundings.

Figure 7.3 indicates there may be a correlation I_{off} and the temperature reported by the Pt1000 sensor on the wire detector board. It seems likely, that this would be an indirect effect caused by a common higher room temperature which raises both the operating temperature of the power supply as well as the vacuum chamber and indirectly the wire detector board. This might be investigated by actively controlling the

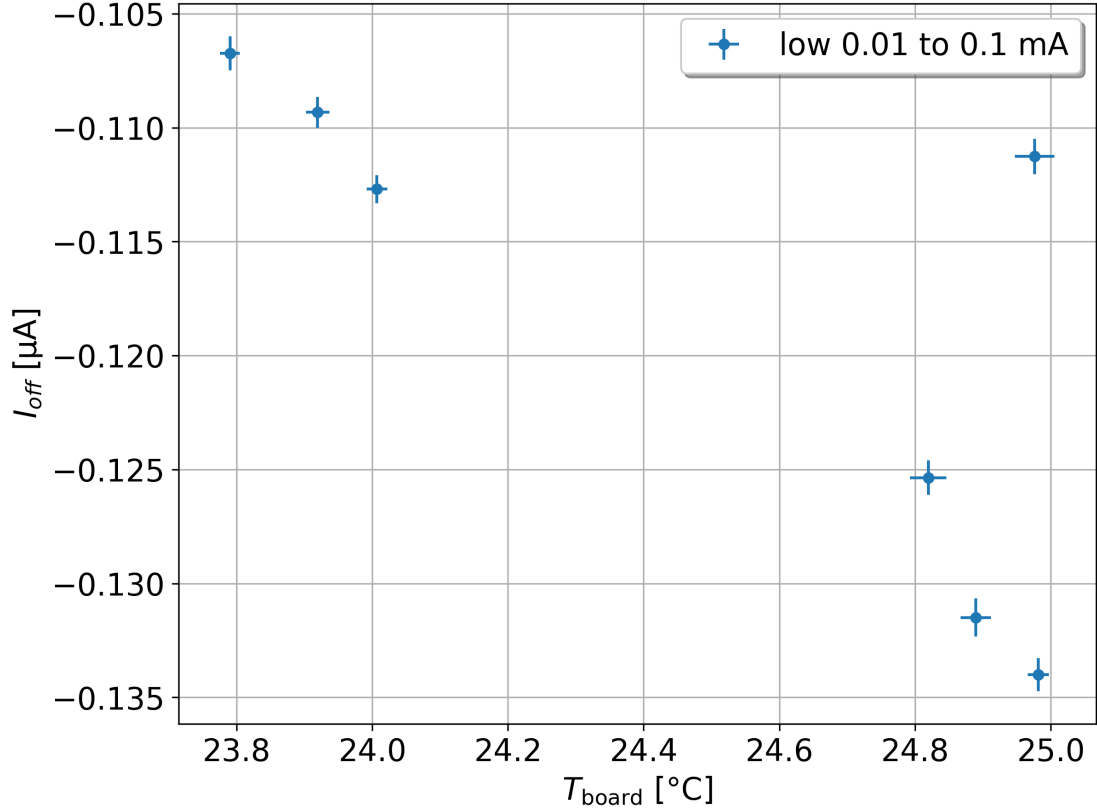


Figure 7.3: I_{off} extracted from fitting procedure shown over T_{board} , the PCB temperature as measured by the Pt 1000 sensor at the back of the wire detector board. With one outlier, there seems to be a strong correlation.

chamber temperature with the chamber bake-out heaters but such a measurement was not performed. The temperature seen here is caused entirely by passive temperature drifts not commanded by operators. There was no concurrent logged temperature monitoring of the laboratory air temperature at the time, so the hypothesis of a change in room temperature cannot be confirmed based on archival data.

7.1.2 Method 2: high power extrapolation

In method 2 we attempt to simply ignore any unexplained low current/power effects by using data taken at higher currents between 0.1 mA to 1.1 mA. We aim to make use of the largely linear relation between resistance and power in this range indicated in Figure 7.1. This time we simply apply a fit of the form of Eq. (7.5) directly to $R = V/I$ and $P_{el} = V \cdot I$ calculated without the consideration of a current offset.

Figure 7.4 shows the relevant high current data range without adjustments along with the linear fit. Despite using disjunct data ranges both methods produce similar values for R_0 and m . While resistance is superficially linear in power, there is a clear systematic deviation evident in the residual subplot. Given that we do expect there to be effects with nonlinear scaling in temperature such as thermal radiation this is not surprising. However the magnitude of the residuals, at a maximum relative deviation of $> 0.1\%$ is small enough to disregard for now. More accurate fit models will be considered for Calibration in Section 7.3.

We again apply this method to 7 equivalent datasets for consistency check. For method 2 the spread in base resistance is $\bar{R}_0 = 66.70 \pm 0.10 \Omega$. Plotting the results for

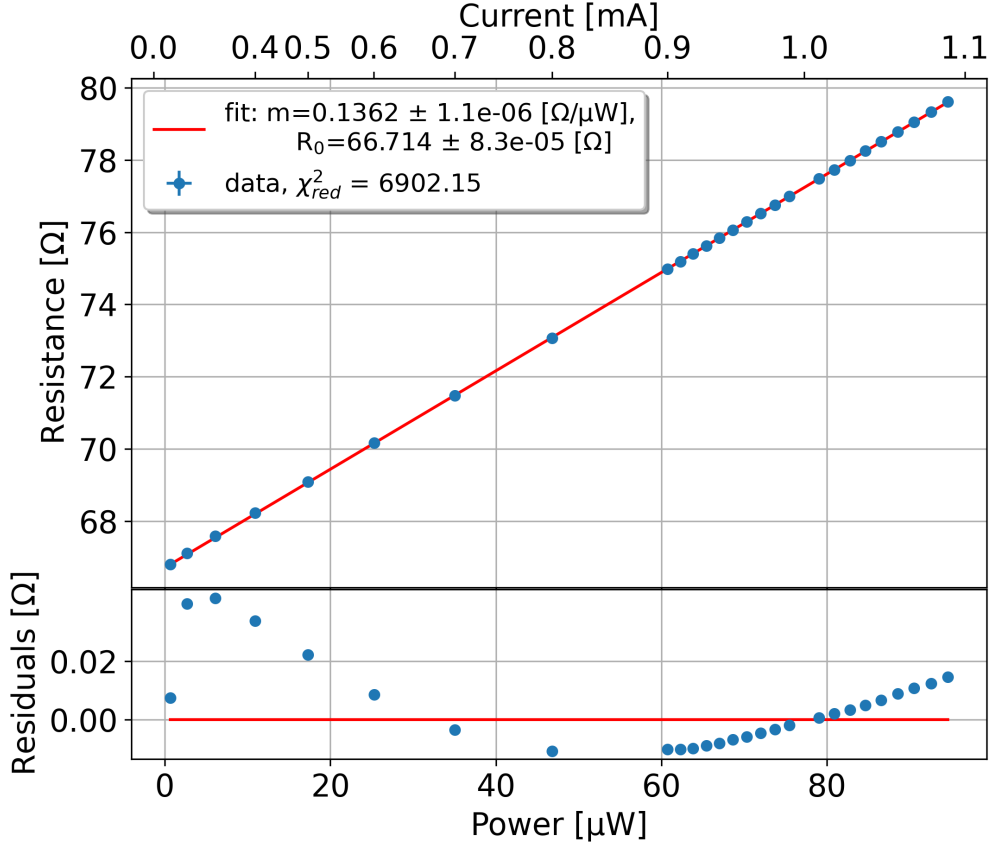


Figure 7.4: "High power" subset of the Resistance response to over heating power for heating currents above 0.1 mA. A linear fit without current offset to this subset is plotted alongside the data. The residuals to this fit shown in the lower subplot indicate systematic disagreement of the data with the fit, but only at very low magnitude of less than 0.04Ω which is less than 1 part in a thousand.

R_0 of both the low and high current methods over wire detector board temperature in Figure 7.5 shows that the approximately 0.08Ω deviation between the methods seen in the example fits in Figures 7.2 and 7.4 is in fact a systematic offset. Additionally, we see a monotonous yet inconsistent downward trend of the measured R_0 values with board temperature.

Since the temperature of the board is also the baseline temperature of the wire attachment points, it is not surprising to see a correlated change resistance as per Equations (5.1) and (5.3) to first order we may expect a change of

$$\Delta R_0 = R_0(T = 25^\circ\text{C}) \cdot (1 + a \cdot \Delta T) \quad (7.10)$$

if we approximate that a change in temperature of the wire detector board correlates with a uniform change in wire temperature ΔT along the entire length of the wire. This expected resistance change with temperature in first order approximation is plotted as in Figure 7.5 labeled as "Illustrative scaling" based on an arbitrary choice of $R_0(T = 25^\circ\text{C}) = 66.85 \Omega$ for the high current method and $R_0(T = 25^\circ\text{C}) = 66.78 \Omega$ for the low current method, as well as a temperature coefficient value of $a = 0.77 \cdot 4.9 \times 10^{-3} \text{ 1/K}$. Here $4.9 \times 10^{-3} \text{ 1/K}$ is the literature value for the temperature coefficient of resistivity at 25 K [51]²¹ and

²¹based on the formula for the electrical resistivity of tungsten R_W in $\text{n}\Omega\text{m}$ given by $R_W = 48.0(1 + 4.8297 \times 10^{-3}T + 1.663 \times 10^{-6}T^2)$ for T in $^\circ\text{C}$ based on page 2123 of [51]

0.77 is a purely empirical factor to produce better alignment. While this factor in this case yields a fit which describes only an arbitrary subset of the data shown in Figure 7.5, some preliminary analysis shown in Appendix B.3.1 suggests a similar deviation from the literature value for a is better able to describe the relationship between wire temperature and detector board temperature as measured by the Pt1000 temperature sensor. Whether this is actually due to a different temperature coefficient of resistivity, or just because the relation between wire temperature and board temperature is not one-to-one for any other reason is not obvious.

Based on only the data shown here, we cannot physically explain the discrepancy between the measured behavior of R_0 with temperature and what might naively be expected from the literature values for tungsten. Any proper judgment of this should be based on a dataset with a longer temperature baseline which is not available at this time. Such a dataset might be produced by deliberate heating using the chamber bake-out heater, which we suggest should be attempted as future follow up work to this thesis. Such a measurement could provide independent calibration of wire resistance and the temperature coefficient of resistivity, regardless of whether it is known how and why these values deviate from expected literature values.

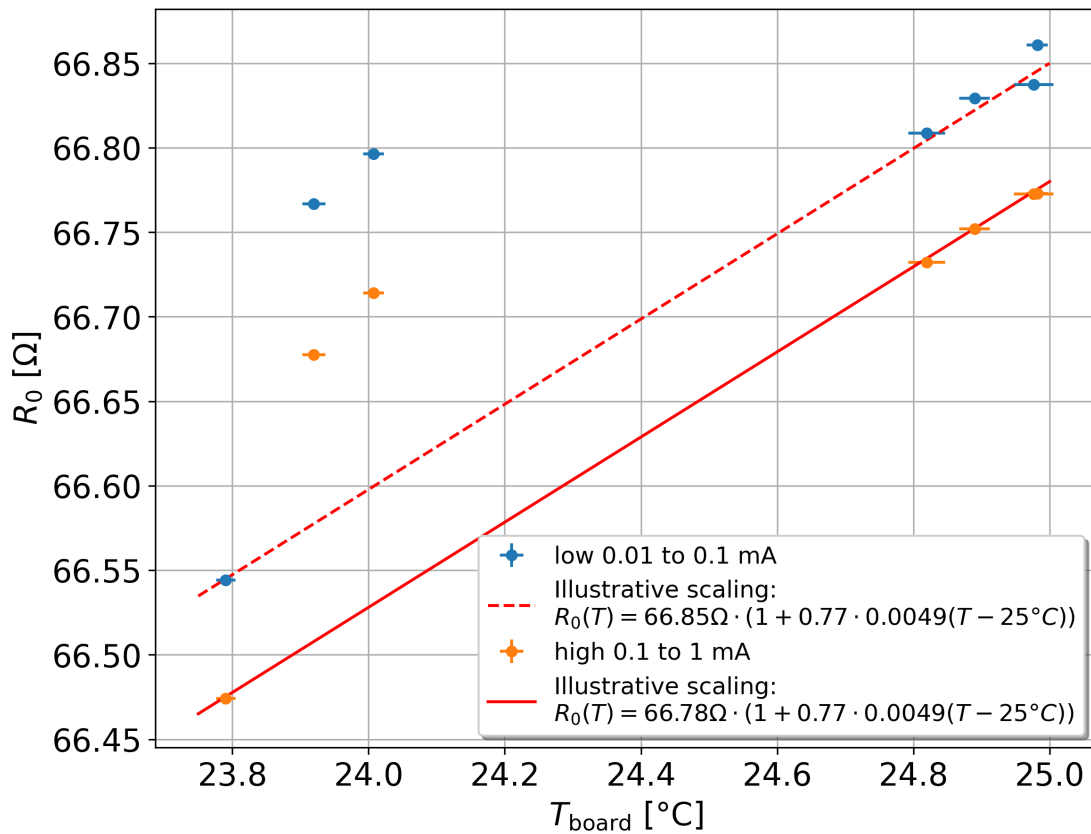


Figure 7.5: Extracted base resistance R_0 for the low and high power data subset methods plotted over the respective wire detector board temperatures T_{board} as measured by the attached Pt1000 sensor. The data suggests a portion of the variance in R_0 may be explicable by changing board or background temperatures, but the large outliers in the data presented here mean it is insufficient for a strong conclusion.

7.1.3 Conclusion

While very much imperfect, the base resistance measurement performed here does clearly put the value at roughly $66.7\ \Omega$. The most important result moving forward is actually that this disagrees markedly with the prediction from the resistance calculated by the simulation based on literature values which with $R = (\rho_R \cdot l_{\text{wire}}/A)$ and the value for specific resistance $\rho_R = 52 \times 10^{-9}\ \Omega\text{m}$ (at $20\ ^\circ\text{C}$) results in a resistance of $52.87\ \Omega$ for a wire with length 20 mm and diameter $5\ \mu\text{m}$ resulting in a mismatch of 26%.

This substantial disagreement must be explained by sizable errors in our values for wire length, diameter, specific resistance, and perhaps a small contribution by contact resistances. The wire is never perfectly tensioned and has small kinks and bends which will subtly increase its length. The magnitude of this could not be measured, and is difficult to estimate, but this will be a certain increase in resistance as there is no conceivable way in which the wire might be shorter than 20 mm. Potentially the most substantial part of the discrepancy, may be due to a smaller than advertised wire diameter. The manufacturer only guarantees wire diameter to $\pm 10\%$ precision. As the cross sectional area is quadratic in d_{wire} , if the wire diameter were indeed $4.5\ \mu\text{m}$ this on its own would immediately result in a 23% increase in resistance. Specific resistivity of tungsten varies in literature between $52 \times 10^{-9}\ \Omega\text{m}$ to $56 \times 10^{-9}\ \Omega\text{m}$ at room temperature [51], [53], and so can perhaps contribute 7% to the mismatch. And finally there may be a small $< 1\ \Omega$ contact resistance not due to the wire itself, but included in the measurement.

Discrepancies such as this as well as others that will be pointed out in following sections, ultimately lead us to forgo attempts to precisely tune all possible model parameters with the goal of using the simulation for direct reconstruction of measured wire detector signals. Here we will however offer some brief suggestions for how some of this parameter degeneracy might be resolved, but they were not performed during this thesis.

The effect of wire length inaccuracy and contact resistance, might be resolved by stringing up wires over gaps of varying lengths, to allow for calibration of the constant resistance offset due to contact resistance. Using sufficiently precise microscopy the wire diameter might be directly measured. With more complicated analysis of microscope images wire length deviation from gap span based on deviations of the wire from being perfectly straight might be determined. An attempt to measure bends in the wire was performed by Darius Fenner [49]. An image from this work is shown in Figure 7.6. Bends of less than 1 mm were regularly measured. Additionally, the wires are often strung at small angles away from perfectly perpendicular, which will add a small extra length to the wire. Ultimately, for the purposes of this work, wire length effects are deemed small enough that we proceed without treating them accounting for them explicitly. The trade-off in additional model complexity is not deemed worthwhile at this point.

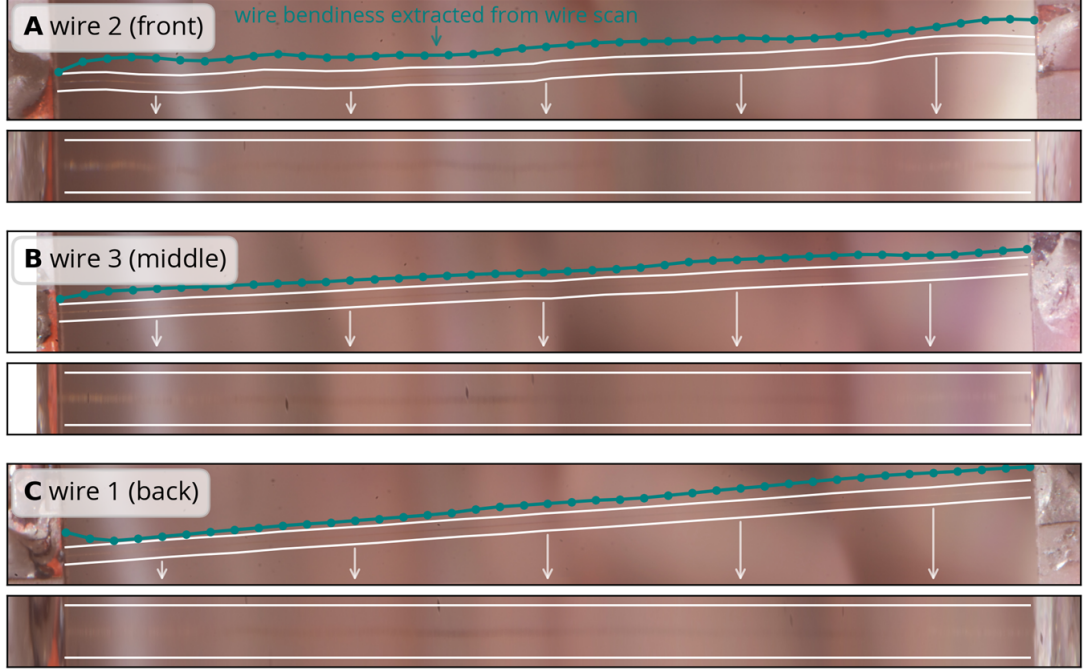


Figure 7.6: Three wires attached to a V4 detector board imaged in the vacuum chamber with a macro lens. The images here show an attempt at digitally map the bends in the wire is performed and used to digitally straighten the wire in the repeat image below each of the 3 wires. Work and image by D. Fenner, for details see Appendix A.7 in [49].

7.2 Detection threshold

We measure the resistance change of the wire calorimeter by DC measurements of both current and voltage. We pass a constant current over the wire and measure the voltage drop over the wire once every second. To ensure that measured effects are due to external inputs of power onto the wire, and not fluctuations of the measurement current, a highly stable power supply is required to provide the measurement current.

The precision with which the resistance change can be measured depends on both the precision in voltage V and the measurement current I . Since $R = U/I$ The uncertainty in measured in resistance σ_R can be expressed in terms of the uncertainties in voltage σ_V and current σ_I as

$$\sigma_R = \sqrt{\left(\sigma_V \cdot \frac{1}{I}\right)^2 + \left(\sigma_I \cdot \frac{V}{I^2}\right)^2} \quad (7.11)$$

With real power supplies and multimeters σ_V and σ_I are functions of V and I respectively. To find the optimal operating current, we supplied a range of currents to the wire using two different power supplies, and measured the statistical uncertainties σ_V , σ_I and σ_R . σ_R represents the smallest change in wire resistance that can be reliably resolved in a single measurement. Recall from Section 5.1 and Eq. (5.3) that the change in wire resistance ΔR in response to a power input is the signal we want to measure. The precision σ_R with which the resistance can be measured therefore directly limits the minimum resolvable power input on the wire.

Using the power to resistance change conversion factor $k = \frac{dP}{dR}$ introduced in Section 7.3 we can calculate the minimum resolvable power

$$\sigma_{P_{\text{meas}}} = k \cdot \sigma_R, \quad (7.12)$$

where P_{meas} is the measured heating power applied to the wire from any source. We plot this for every measurement current in Figure 7.7. We also display an atom flux density that would deliver an equivalent amount of recombination energy to the wire, given a flat distribution of atoms and perfect transfer efficiency of available chemical energy to the wire:

$$\sigma_{J_0} = \frac{E_{\text{rec}}}{2 \cdot A_{\text{wire}}} \cdot \sigma_{P_{\text{meas}}} , \quad (7.13)$$

See Eq. (5.19) in Section 5.3.1 for the derivation. As the assumptions made are for perfect energy transfer to the calorimeter, this can be treated as a lower floor for the atom flux density required to cause a signal measurable with a single measurement.

Note, that as these are statistical uncertainties and therefore better resolutions can still be obtained with the same power supply and beam by repeating the same measurement N times for an improvement of a factor $1/\sqrt{N}$ in resolution. We show such a procedure in Section 8.2.1.

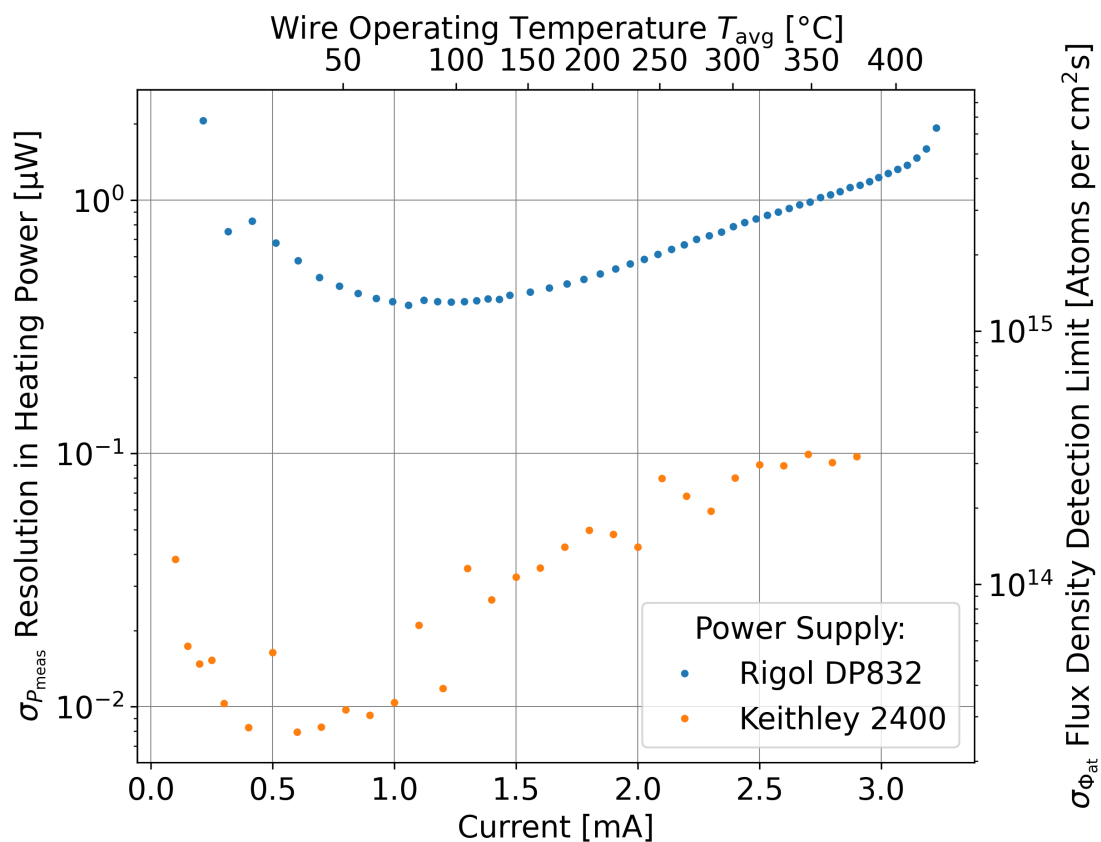


Figure 7.7: Resolution in heating power at various measurement currents. Measurement are shown for two power supplies of differing stability. We ultimately use the Keithley model due to its superior performance. An additional y-axis displays the density of a uniform beam that would result in such a heating power. An additional x-axis shows the average temperature along the wire when the corresponding current is applied to it.

The achievable power resolution has an optimum between 0.5 mA to 1.5 mA depending on the power supply that is used. At extremely low measurement currents, the relative precision of the Voltage measurement and current control both get worse which results in an increase in σ_R . On the other end of the current range, high measurement currents raise the operating temperature of the wire. This increases the relative effect of cooling by thermal radiation as per Eq. (5.37). This effect scales with T^4 and therefore much

more steeply with temperature than thermal conduction which is dominant at lower temperatures. This means that any further increase in temperature requires more power. A smaller change in temperature also results in a smaller signal ΔR as per Eq. (5.1). Even though the relative precision of the resistance measurement improves with high currents, this is more than outweighed by the "stiffening" of the temperature response of the wire such that the crucial resolution in input power gets worse.

Based on the data presented in Figure 7.7 we ultimately decided to use 1 mA as the default measurement current. We had already been using it, and it is close enough to the best power resolution for either of the power supplies used. Changing the power supply or multimeter used may move the optimal operating current, changing wire parameters such as wire thickness certainly does.

7.3 Calibration of resistance response to heating power

In order to convert between changes in wire resistance and the heating power causing them, a calibration of the detector is performed by running an increasing series of currents over the wire. Since input voltage (V) and current (I) through the wire are independently measured, both the resistance, as well as a direct measurement for the electrical power imparted to the wire via Joule heating ($P_{el} = V \cdot I$) is performed simultaneously.

To produce a calibration function, a 4th order polynomial function of resistance is fit to the calibration data as shown in Figure 7.8. A 4th order polynomial is chosen because the highest-ordered effect is that of thermal radiation (f_{rad} defined in Section 5), which scales with the 4th power in temperature, and because it empirically fits the data to about 1 part in one thousand over the resistance range used in our measurements. This means potential systematic calibration errors due to the parametrization of this fit are significantly smaller than the statistical errors on beam measurements of about 1% in the best case (see Figure 8.2).

The calibration function k can then be expressed as the derivative of the fit function

$$k(R') = \left. \frac{dP}{dR} \right|_{R'}, \quad (7.14)$$

such that

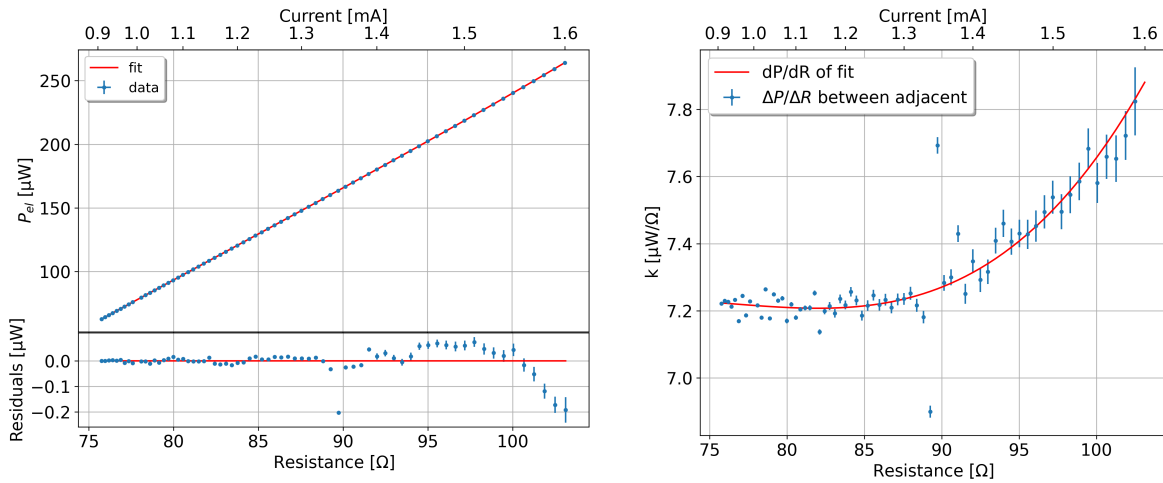
$$\Delta P_{calib}(R', \Delta R) = \left. \frac{dP}{dR} \right|_{R'} \cdot \Delta R, \quad (7.15)$$

where ΔP is the change in heating power supplied to the wire required to produce a small change in measured wire resistance ΔR away from an initial resistance R' . The choice of local calibration around an initial R' rather than a global calibration is taken, as the initial resistance is subject to changes due to background effects, for example due to a change in the temperature of the surrounding apparatus. In practice the changes in resistance due to the atomic beam are always small, so the implicit locally linear approximation made when using the local slope approximation is justifiable.

When taking data with an external heat source like the beam, we additionally need to account for the feedback Joule heating due to the measurement current.

$$P_{fb} = I^2 \cdot \Delta R. \quad (7.16)$$

With a constant measurement current I , an externally caused resistance change ΔR will result in additional electrical power draw and therefore heating of the wire, which needs to be subtracted to arrive at the measured external heating P_{meas}



(a) Electrical power supplied to the wire plotted over the resistance the wire reaches when heated with that power. The data is fitted with a 4th order polynomial. The data deviates from the fit function used towards the upper end of the range measured; however deviations are never more than 1.5 per thousand and so are accepted in the current analysis. The significant deviation in the data point at 90 Ω is unexplained, and we treat it as an aberration. It has no significant effect on the fit.

(b) Calibration function k extracted from the slope of the power-resistance curve. The local approximation of the slope $\Delta P/\Delta R$ is calculated between adjacent data points and shown to illustrate the scatter. The outlier at 90 Ω causes the local approximations to fluctuate significantly, but the fit curve which is used for further analysis suppresses this effect.

Figure 7.8: Calibration curve produced by varying electrical power supplied to the wire and measuring the resulting wire resistance. The measurement is realized by changing the current across the wire from 0.9 mA to 1.6 mA in 0.01 mA steps. The resulting range of wire resistances corresponds to the range observed when heating the wire with external sources, primarily the thermal radiation from the HABS when heated to 2200 K.

$$P_{meas} = \Delta P_{calib} - P_{fb} \quad (7.17)$$

$$= k(R') \cdot \Delta R - P_{fb} \quad (7.18)$$

$$= (k(R') - I^2) \cdot \Delta R. \quad (7.19)$$

With the typical operating current I of 1 mA this results in a correction of $-1 \mu\text{W}/\Omega$.

7.3.1 Correcting calibration for temperature distribution and resulting wire sensitivity

The calibration method initially assumes that the wire is heated equally in all places by the measurement current. This is incorrect, but a convenient approximation, because only the total resistance of the wire is measurable and therefore only an approximation for its average temperature can be derived.

A better approximation can be obtained, by simulating the wire behavior. The finite elements simulation results in a prediction for the wire temperature profile in response to the heating due to the measurement current, shown in Figure 5.3. The maximum of the wire temperature is reached in the center of the wire at just over 50 $^{\circ}\text{C}$. There is a roughly 30 $^{\circ}\text{C}$ temperature difference to the edges of the wire.

Of course the real calibration measurement already includes these effects. What remains for us is to correct the assumption, that k as calculated above is the average conversion factor for ΔR to power. As calculated, it is actually already the conversion

factor weighted for the unequally distributed heating power. To get back to the average conversion factor for a flat input power the effect of the additional central heating needs to be removed.

The difference in global calibration factor based on the real input power distribution and a flat input power can be interpreted as a correction factor c , the quotient of the integrals over the power distribution weighted by η_{wire} along the wire

$$c = \frac{\int_{wire} I^2 R_{dens}(T(x)) \cdot \eta_{wire}(x) dx}{\int_{wire} I^2 \frac{R_{tot}}{l_{wire}} \cdot \eta_{wire}(x) dx}, \quad (7.20)$$

which simplifies to

$$c = \frac{\int_{wire} R_{dens}(T(x)) \cdot \eta_{wire}(x) dx}{\frac{R_{tot}}{l_{wire}} \int_{wire} \eta_{wire}(x) dx}. \quad (7.21)$$

and finally

$$c = \frac{\int_{wire} (1 + a \cdot \Delta T(x)) \cdot \eta_{wire}(x) dx}{\int_{wire} \eta_{wire}(x) dx}, \quad (7.22)$$

where a is the temperature coefficient of resistivity and $\Delta T = T(x) - T_{avg}$. T_{avg} being the average wire temperature that would result in it having a total resistance of R_{tot} . The correction resulting from a simulation at 1 mA is $c = 1.023$, meaning that the calculated $k_{eff} = c \cdot k$ is too high by this factor compared to the equally distributed heating power assumption. The accuracy of this correction depends on the accuracy of the simulation, but since it is a fairly small correction, even large inaccuracies in the simulation on the order of 10% would only translate into part per thousand level changes to the calibration factor k .

8 Beam measurements

In this Section we present measurements of beams produced by the HABS which is described in Section 4.1. First in Section 8.1, we will develop a model for calculating the expected heat load due to a beam on the wire in this location. In Section 8.2, we will then describe the method by which we extract the beam signal from raw measurements and then further how to extract the signal component due to heating due to H recombination. We will then present scans of H₂ beams with varied wire position in Section 8.3 and finally scans of composite H and H₂ with varied wire position in Section 8.4, with the aim to determine the shape of the distribution with which the H component is emitted from the source.

Measurements presented in this section are all taken with the version 4 wire detector placed in the source chamber directly below the HABS as illustrated in Figure 4.1. While some measurements were taken with the wire detector located below the mass spectrometer in chamber 3, these all failed to detect a signal that could be attributed to the beam, and they are therefore not presented here.

8.1 Beam model

This section will show that a given model for the beam shape such as j_{HABS} from Eq.(4.1) could be integrated to predict the absolute expected heating power received by the wire. However, due to some poorly-known parameters we only carry out part of the integration and leave the overall heat scaling as a free parameter.

The recombination intensity I_{rec} is the power density per unit solid angle [W/sr] from recombination heating on a surface exposed to an atomic hydrogen beam. It can be expressed as

$$I_{\text{rec}} = \Phi_{\text{in}} \cdot 2\alpha_{\text{dissoc}} \cdot j_{\text{HABS}}(\theta; l_{\text{eff}}) \cdot \eta_{\text{rec}} \cdot \frac{E_{\text{rec}}}{2}, \quad (8.1)$$

where Φ_{in} is the flow of molecules per second into the source, and α_{dissoc} is the fraction of these which are dissociated into atoms in the source. η_{rec} is the calorimetric efficiency of the wire surface (See Eq. (5.48)), and E_{rec} is the total energy released when two hydrogen atoms recombine into a molecule.

The values of α_{dissoc} and η_{rec} are both initially unknown. They are difficult to disentangle with currently available data. Some values for the recombination parameters in η_{rec} are available from literature [42], but with large uncertainties, and it is unclear if they are directly applicable. Due to the degeneracy caused by including all three as separate parameters, for the purposes of a fit model, all such purely multiplicative parameters will be combined into a single scaling parameter

$$A = \Phi_{\text{in}} \cdot 2\alpha_{\text{dissoc}} \cdot \eta_{\text{rec}} \cdot \frac{E_{\text{rec}}}{2}. \quad (8.2)$$

A is then implicitly a complicated function of gas flow, source and wire temperature, as well as wire surface properties. However, as long as these are constant for the dataset to which a fit is applied, the complexities will be absorbed into the fit parameter.

The recombination intensity can be expressed using A as

$$I_{\text{rec}} = A \cdot j_{\text{HABS}}(\theta; l_{\text{eff}}). \quad (8.3)$$

Using the definition for beam intensity given in the equation above, a parametric model for the heating power due to recombination measured by the wire calorimeter can

be defined. This takes the form of integrating I_{rec} over the surface of the wire:

$$P_{\text{rec}}(z_{\text{pos}}; l_{\text{eff}}, A) = A \left(\iint_{\text{wire}} dz dx j_{\text{HABS}}(\theta(x, z); l_{\text{eff}}) \cdot \eta_{\text{wire}}(x) \cdot \frac{\cos^3(\theta(x, z))}{y_0^2} \right), \quad (8.4)$$

which can be simplified under the assumption of a wire aligned with the x-axis and with a very small extent in z-direction of $\Delta z = d_{\text{wire}}$ as well as neglecting any effects due to the curvature of the wire surface. Neglecting wire surface curvature is justified, because any effect would just modify η_{rec} , which is already a free parameter of the model and because tests of other metal surfaces [54] indicate that sticking coefficients of atomic hydrogen are not generally strongly dependent on angle of incidence, though the source does not specifically measure this for the case of an untreated gold surface. The simplified integral over wire area projected along the y-axis is:

$$P_{\text{rec}}(z_{\text{pos}}; l_{\text{eff}}, A) = A \left(\int_{\text{wire}} dx d_{\text{wire}} \cdot j_{\text{HABS}}(\theta(x, z_{\text{pos}}); l_{\text{eff}}) \cdot \eta_{\text{wire}}(x) \cdot \frac{\cos^3(\theta(x, z_{\text{pos}}))}{y_0^2} \right), \quad (8.5)$$

where η_{wire} is the relative sensitivity of the wire to heat depending on location (see Section 5.6), and x is the position along the length of the wire over which the integration is performed. P_{rec} is evaluated as a function of z_{pos} , the position along the z-axis at which the wire is placed. θ can be calculated as a function of the Cartesian coordinates (x, z, y) per their definition shown in Appendix A. The multiplication with $\frac{\cos^3(\theta(x, z_{\text{pos}}))}{y_0^2}$, where y_0 is the distance from the capillary end face to the wire plane, results from the transformation between the spherical coordinates in which the beam is defined and the Cartesian coordinates defining the locations along the wire over which we integrate. The derivation is shown in Appendix A.1.

This yields a model for the signal expected on the wire detector, which can be fit to data as will be shown later. It has two principal parameters: the scaling parameter A and l_{eff} which describes the shape of the distribution.

8.1.1 Beam gas heating model

An analogous calculation can be done for the total heating power due to beam gas heating, based on the beam gas heating description $f_{\text{beam_gas}}$ Eq. (5.20) introduced in Section 5.3.2.

The intensity of beam gas heating due to atoms and molecules

$$I_{\text{beam_gas}} = I_{\text{at}} + I_{\text{mol}} \quad (8.6)$$

is the power density per unit solid angle [W/sr] from the kinetic energy incident on a surface exposed to a hydrogen beam. The components $I_{\text{at/mol}}$ can be expressed as

$$I_{\text{at/mol}} = \Phi_{\text{at/mol}} \cdot j_{\text{HABS}}(\theta; l_{\text{eff_at/mol}}) \cdot \alpha_{E_{\text{at/mol}}} \cdot \left(C_{V_{\text{at/mol}}}(T_{\text{at/mol}}) \cdot T_{\text{at/mol}} - C_{V_{\text{at/mol}}}(T(x)) \cdot T(x) \right) \quad (8.7)$$

where

$$\Phi_{\text{at}} = \Phi_{\text{in}} \cdot 2\alpha_{\text{dissoc}} \quad (8.8)$$

and

$$\Phi_{\text{mol}} = \Phi_{\text{in}} \cdot (1 - \alpha_{\text{dissoc}}) \quad (8.9)$$

where the $\Phi_{\text{at/mol}}$ is the respective flow out of the capillary, α_E is the energy accommodation coefficient of the gas on the wire, $C_{V_{\text{at/mol}}}$ ²² is the heat capacity per particle of atomic and molecular hydrogen respectively as a function of the temperature of the gas $T_{\text{at/mol}}$ and $T(x)$ is the temperature of the wire at position x . By selecting the appropriate subscript $_{\text{at/mol}}$ this equation yields the intensity of the atomic or molecular beam gas heating component.

For application to real data taken with our setup, we can generally apply a few simplifications to keep the number of free parameters in check. For any measurements which are taken at temperatures too low for any substantial dissociation of H_2 to occur ($< 1600 \text{ K}$) $\alpha_{\text{dissoc}} = 0$ can be assumed. When extrapolating the effect of beam gas heating into hotter temperatures where dissociation occurs (see Figure 8.3) we can choose to disregard a low fraction of dissociation as a first order approximation, since at temperatures 1500 K to 2500 K the heat capacity of 2 individual hydrogen atoms is within 10% of the heat capacity of molecular hydrogen, as shown in Figure 8.1. Since P_{rec} quickly becomes much larger than $P_{\text{beam_gas}}$ for any appreciable degree of dissociation $\alpha_{\text{dissoc}} \gtrsim 10\%$ the error in total modeled power due to this simplification is strictly less than 5% and usually much less. This means we can forego the significant challenges to determine α_{dissoc} or a separate $\alpha_{E_{\text{at}}}$ for the kinetic energy accommodation of atomic hydrogen for the purposes of modeling $I_{\text{beam_gas}}$.

As an additional simplification, we approximate the wires temperature $T(x)$ as a constant average temperature along the wire, which is acceptable whenever $T_{\text{at/mol}}$ is significantly greater than the temperature range along the wire of $\approx 40 \text{ K}$. Under these assumptions we can simplify Equation 8.6 to

$$I_{\text{beam_gas}} \approx \Phi_{\text{mol}} \cdot j_{\text{HABS}}(\theta; l_{\text{eff_mol}}) \cdot \alpha_{E_{\text{mol}}} \cdot (C_{V_{\text{mol}}}(T_{\text{mol}}) \cdot T_{\text{mol}} - C_{V_{\text{mol}}}(T_{\text{avg}}) \cdot T_{\text{avg}}) \quad (8.10)$$

where T_{avg} is the average temperature of the calorimeter wire. The average wire temperature can be approximately calculated from its resistance as derived in Section 7.1. Φ_{mol} is measured at the mass flow controller that lets gas into the HABS capillary, and $C_{V_{\text{H}_2}}(T)$ is taken from literature [55]. This means that $I_{\text{beam_gas}}$ can be well approximated as a simple function of temperature with unknowns in the form of the energy accommodation coefficient α_E and the beam shape j_{HABS} . The determination of both is subject of Section 8.3 where we model the total beam gas heating power using

$$P_{\text{beam_gas}}(z_{\text{pos}}; l_{\text{eff}}, A_{\text{bg}}) = A_{\text{bg}} \left(\int_{\text{wire}} dx d_{\text{wire}} \cdot j_{\text{HABS}}(\theta(x, z_{\text{pos}}); l_{\text{eff}}) \cdot \eta_{\text{wire}}(x) \cdot \frac{\cos^3(\theta(x, z_{\text{pos}}))}{y_0^2} \right), \quad (8.11)$$

where the scaling factor A_{bg} is now

$$A_{\text{bg}} = \Phi_{\text{mol}} \cdot \alpha_{E_{\text{mol}}} \cdot (C_{V_{\text{mol}}}(T_{\text{mol}}) \cdot T_{\text{mol}} - C_{V_{\text{mol}}}(T_{\text{avg}}) \cdot T_{\text{avg}}). \quad (8.12)$$

²²NIST [55] $C_{V_{\text{H}_2}}(T)$: <https://webbook.nist.gov/cgi/cbook.cgi?ID=C1333740&Type=JANAFG&Table=on#JANAFG>, $C_{V_{\text{H}}}(T)$: <https://webbook.nist.gov/cgi/cbook.cgi?ID=C12385136&Mask=1>

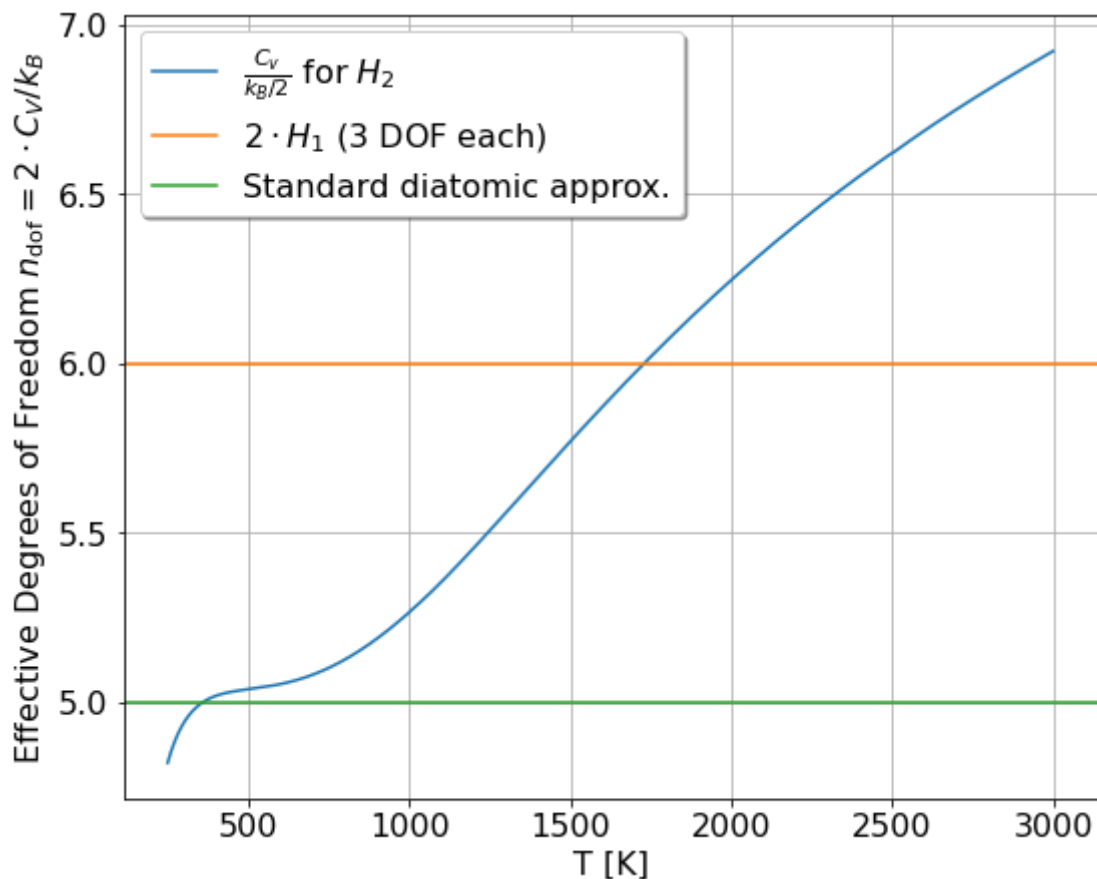


Figure 8.1: The heat capacity of hydrogen is plotted in terms of multiples of half the Boltzmann constant. This way the relationship to the effective degrees of freedom is highlighted. At room temperature molecular hydrogen is well approximated by the standard diatomic approximation of 5 degrees of freedom, increasing by up to 30% over the temperature range of interest. Data from NIST [55].

8.2 Signal extraction

8.2.1 Primary signal extraction

The beam heating effects on the wire ($P_{\text{beam.gas}}$ and P_{rec}) can be quite small, on the order of $10^{-9} - 10^{-6}$ W. Since the wire is subject to external temperature drifts, signals are extracted as a relative measurement by periodic switching between the “beam on” and “beam off” states, to allow for constant comparison against the drifting background. An example of this is shown in Figure 8.2. Here a typical 1 sccm hydrogen beam is cycled on and off every 5 minutes. To get a relatively fast equilibration of flow to the nominal setpoint of the mass flow controller, we first let gas flow through the mass flow controller and hydrogen purifier for at least 1 hour before starting the flow cycling scheme. Flow through the purifier can take hours to equilibrate at low flows if it is not saturated with the correct amount of hydrogen for steady state operation. We therefore open and close a pneumatic valve downstream of the hydrogen purifier in time with the 5 minute switching interval of the mass flow controller. This way the pressure of hydrogen in the mass flow controller gets “locked in” and flow can resume quickly. See Appendix B.2 for more details on flow equilibration.

For each 5 minute section only a segment of data from 2.5 to 4.15 minutes after flow switching is used to allow for equilibration of flow as well as wire temperature

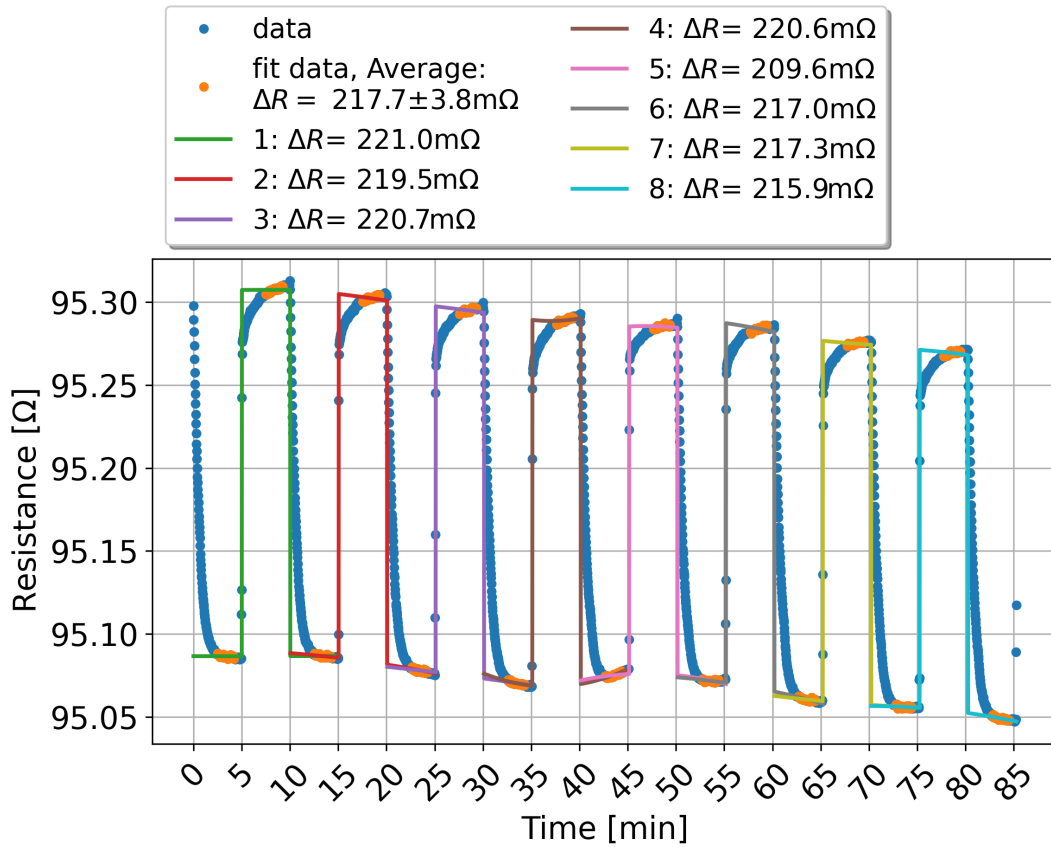


Figure 8.2: Example of signal extraction for the wire positioned centrally in the beam at $z = 1.5\text{mm}$, with the HABS at $\approx 2200\text{K}$ and a flow of 1 sccm . The flow is cycled on and off 8 times. For each cycle the difference in resistance when the flow is on is extracted using a fit to a subset of the data after equilibration, marked in orange. Fits are applied individually to every set of three 5 minute segments in an beam off-on-off pattern.

and to avoid potential issues with slight de-synchronization at the end of the segment. This data is marked orange in the plot. Then three 5 minute sections are combined in an “off”-“on”-“off” pattern. The two “off” sections allow for fitting the background trends and then determining the average difference ΔR when the beam is “on” in the central 5 minute section. A quadratic function is fit to the data as a basic model of local background temperature drift, with an additional ΔR offset factor only applied to the “beam on” data, which represents the extracted beam signal.

$$R_{\text{fit}}(t) = \begin{cases} c_0 + c_1t + c_2t^2 & \text{if “beam off”} \\ c_0 + c_1t + c_2t^2 + \Delta R & \text{if “beam on”} \end{cases}, \quad (8.13)$$

Tracking the change in resistance in the “beam off” state, as the flow switching method does, practically eliminates any slow-changing background effects. The measurement turns into a comparison of two values, where the only variable is hydrogen flow through the HABS. This eliminates the need to model effects which are not affected by hydrogen flow directly, such as $P_{\text{el}}, P_{\text{bb}}$, with great precision in order to extract the much smaller beam-related effects.

We do not attempt to model the equilibration process of each cycle, as it is a potentially complex superposition of thermalization processes of various components (wire, detector board, vacuum chamber), as well as the equilibration of gas flow after switching, all of which take place over different time scales. From the simulation (e.g.

Figure 5.5) and measurements (see P. Kern’s Bachelor Thesis [56]), it is known that the wire temperature equilibrates on the scale of a few seconds, while the detector PCB temperature has been measured to take tens of minutes to reach full equilibrium. The 5 minute cycle is a compromise in letting the fast processes that affect the wire directly equilibrate, while not waiting for all components to fully thermalize over e.g. one hour, because the ability to background-subtract unintended external temperature drifts would be lost. The partial inclusion of background temperature equilibration is undesired but not easily avoidable. Competing systematic errors caused by equilibration processes in pressure and temperature are discussed in Appendix B.

Since our model in Eq. (8.5) includes a scaling parameter A , for the purposes of this thesis any proportional systematic will simply be absorbed by A . This is yet another reason why an absolute calibration is difficult to achieve, but the effects on measuring the beam shape in terms of relative flux, as shown in Section 8.4, should be minor.

The flow switching method enables checking for repeatability and stacking of multiple measurements to increase SNR. With 8 such repetitions, signals as small as $\Delta R = 2 \text{ m}\Omega$ (equivalent to $P_{\text{meas}} \approx 13 \text{ nW}$, or $\approx 10^{14}$ atoms/(cm^2s)) have been resolved with an SNR of $\frac{\mu\Delta R}{\sigma\Delta R} \approx 4$. See Figure D.1a the appendix for extracted data of a 0.002 sccm beam at $\approx 2200 \text{ K}$ which produces signals of approximately such a size and precision.

After ΔR is extracted, we use Eq. (7.19) to calculate P_{meas} , the net heating power responsible for the resistance change.

8.2.2 Secondary signal extraction

The result of primary signal extraction is the net heating power as derived from the net change in resistance. In a second extraction step, the atomic hydrogen recombination heating P_{rec} must be extracted from the net heating power.

The assumption is made that the components remaining in the signal are

$$P_{\text{meas}} = P_{\text{rec}} + P_{\text{beam_gas}} - P_{\text{bkgd_gas}}. \quad (8.14)$$

The other components listed in Eq. (5.10) ought to be eliminated by the flow switching scheme of the primary signal extraction.

With the HABS actively putting gas into the vacuum chamber, the background pressure is typically $\simeq 2 \times 10^{-5} \text{ mbar}$ at the 1 sccm flow that is used for measurements presented in this section. Assuming that the background gas component is in thermal equilibrium with the walls and has no atoms in it due to the recombination and thermalization on the chamber walls, it will provide a constant cooling effect. The hot molecules in the beam, in contrast, will deposit power increasing with temperature. One source of non-linearity that needs to be accounted for is the non-trivial scaling of the heat capacity of molecular hydrogen with temperature²³ $C_{V,\text{H}_2}(T)$.

To extract just the power due to recombination, equivalent measurements are taken at three HABS temperature setpoints $T_{\text{low}}, T_{\text{mid}}, T_{\text{high}}$. T_{low} is chosen as room temperature, T_{mid} at $\approx 1277 \text{ K}$, high enough to see the effects of $P_{\text{beam_gas}}$ but low enough that no atomic hydrogen will be produced, and T_{high} is chosen to be $\approx 2211 \text{ K}$, the highest reliably reachable temperature with the hardware employed. The precise numerical values of the temperatures seem arbitrary, because they are the conversion of flat thermocouple voltages which are used for stabilization. While the stabilization is quite good, the absolute conversion should be taken as no more than 5% accurate, as precise calibration of capillary temperature measurements remains a challenge.

²³NIST [55] <https://webbook.nist.gov/cgi/cbook.cgi?ID=C1333740&Type=JANAFG&Table=on#JANAFG>

The measurements at T_{low} and T_{mid} are the minimum number of points required to scale the heating and cooling effects of molecular hydrogen P_{H_2} to what they should be at T_{high} .

$$P_{H_2} = P_{beam_gas} - P_{bkgd_gas} = (a \cdot C_{V,H_2}(T) \cdot T + b). \quad (8.15)$$

a and b are determined by fitting to data at T_{low} and T_{mid} . The scaled effect is subtracted from the raw measurement to obtain the extracted recombination heating power

$$P_{rec}(T_{high}) = P_{meas}(T_{high}) - (a \cdot C_{V,H_2}(T_{high}) \cdot T_{high} + b), \quad (8.16)$$

Figure 8.3 illustrates such a fit using a dataset with higher resolution in HABS temperature at a single wire z-position. The temperature scan is performed twice at each temperature, once scanning up in temperature once going down. In the example, Eq. (8.15) is applied to the data below a temperature cutoff of 1600 K to ensure none of the measured power is due to atomic H. The model describes the data below the cutoff well, but with discrepancies not fully explainable by statistic fluctuation. These may be partially the a result of imperfect calibration of the temperature axis. Work on improved temperature determination is ongoing, but not presented in this thesis.²⁴ Beyond that, Eq. (8.15) may not fully capture all temperature dependencies if further parameters in Eq. (5.20) carry significant temperature dependence. For example, in Section 8.3.3 we attempt to determine the temperature dependence of $\alpha_{E_{mol}}$ and find that while we cannot determine it with high precision, as much as a 10% change in $\alpha_{E_{mol}}$ over our temperature range is consistent with the data. For the extraction process we will treat it as constant for simplicity, incurring a potential systematic error. This would carry forward to derived quantities which are discussed in following sections such as the accommodation coefficient α_E , as well as more indirectly the measured atom flow and the beam shape parameter l_{eff} .

A choice of only three representative temperature points is made to minimize total required data taking time. Since full z-scans of with 40 z-points as presented in Figure 8.4 require 80 hours of data taking per temperature, using high resolution in temperature as well quickly becomes operationally prohibitive. Based on the dataset presented in Figure 8.3 we estimate the three temperature point method introduces roughly an additional 5% uncertainty on the extracted P_{rec} compared to doing a full resolution fit when the baseline between the chosen T_{low} and T_{mid} is at least 500 K.

Eq. (8.16) describes the procedure by which measurements at multiple temperatures can be combined to extract only the heating due to hydrogen recombination. This recombination heating is used in this work to trace the relative flux density of atomic hydrogen. Therefore the preceding section has described the prescription for using a wire calorimeter as a detector for atomic hydrogen, so long as the assumptions that were made are valid.

²⁴See an upcoming PhD thesis by Brunilda Muçogllava focused on source temperature determination.

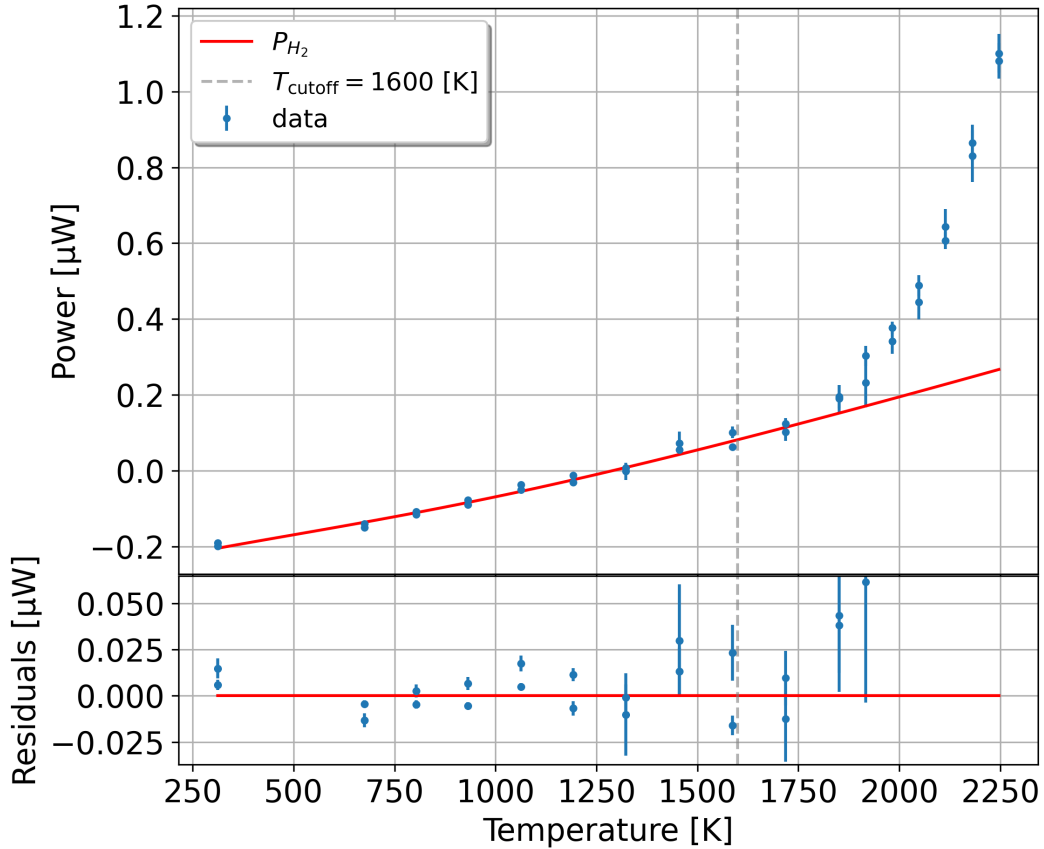


Figure 8.3: Power detected on the wire after primary extraction (P_{meas}) at 1 sccm for a fixed z-position over a range of temperatures. The temperature scan is performed twice in this dataset for each temperature position, once scanning up in temperature and once down. A fit based on Eq. (8.15) is applied to data points below the temperature cutoff $T_{\text{cutoff}} = 1600$ K. Below this temperature no dissociation of hydrogen is expected, and therefore no contribution of atomic hydrogen to the heat detected on the wire.

8.3 Molecular beam shape scans

In this section we focus on use of the wire detector for detecting beams of (warm) molecular hydrogen below the dissociation threshold. We will scan the wire detector through beams at various temperatures to determine beam shapes as well as an estimation of α_E , the energy accommodation coefficient of H_2 on the wire surface. The reduced number of unknowns due to using a beam of pure H_2 composition will in effect allow us to perform an absolute calibration of the sensitivity of the wire detector to such beams. This is in contrast to atomic H beams covered in Section 8.4, where our inability to produce a pure H beam means we are always dealing with a mixture of H and H_2 and the additional free parameter in the form of α_{dissoc} will preclude an absolute calibration and we will merely be able to present limits in Section 8.6.

We will be using data taken at a flow rate of 1 sccm shown in Figure 8.4. Of the data sets shown we will use the five taken at temperatures below 1600 K such that no relevant amounts of dissociation occur and the beam can be modeled as a pure H_2 beam.

Each scan is taken by performing the flow “off”-“on”-“off” switching method shown in Figure 8.2 for 2 hours at each position. We usually take measurements at about 40 positions per scan taking the average of 8 flow cycles for each position. The translation stage on which the wire detector is mounted is then moved along the z-axis, positioning

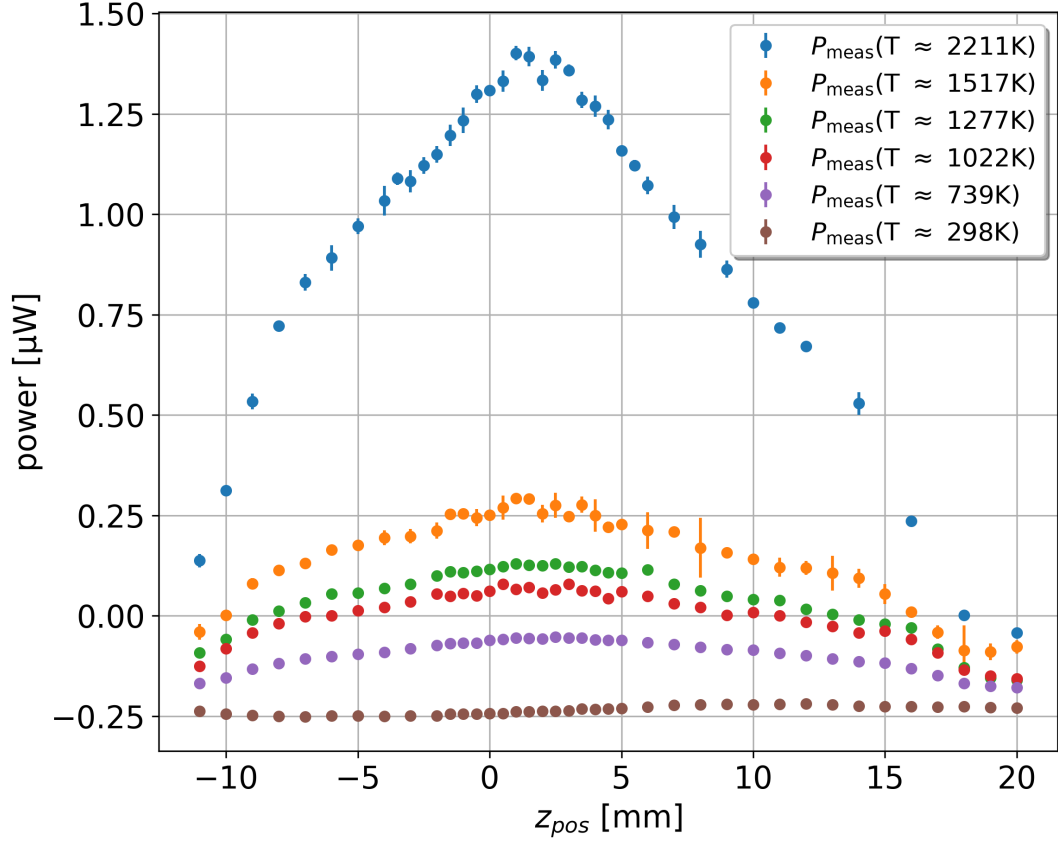


Figure 8.4: Power detected on the wire after primary extraction (P_{meas}) at 1 sccm for an extended range of source temperatures. All datasets below 1600 K are below the dissociation threshold and measure a pure H_2 beam. These data sets are then used in the secondary extraction procedure, to yield the effect of recombining atoms on the surface. Negative detected powers indicate a net cooling of the wire, which is identified with the convection cooling due to gas pressure in the detector chamber ($f_{\text{bkgd.gas}}$).

the wire at a new angle θ with respect to the capillary. As an attempt to reduce systematic effects of potential temperature drifts, the z-positions are measured in a non-sequential order.

8.3.1 Secondary signal extraction for fully molecular beams

The result of primary signal extraction is the net heating power as derived from the net change in resistance. In the case of HABS temperatures below 1600 K that we are concerned with in this section, the assumption is made that the components remaining in the signal are

$$P_{\text{meas}} = P_{\text{beam.gas}} - P_{\text{bkgd.gas}}. \quad (8.17)$$

No contribution is made by P_{rec} in this case since no atomic H is produced. The other heating and cooling components listed in Eq. (5.10) ought to be eliminated by the flow switching scheme of the primary signal extraction.

To extract just the power due to the thermal energy of particles in the beam hitting the wire, which we call “beam gas” heating, we can proceed in a simplified manner to the one described for extracting recombination heating in Section 8.2.2. In this case we only require a minimum of 2 temperature points T_{low} and T_{mid} , both below the dissociation

threshold temperature. However, in this case since we do not need to extrapolate to higher temperatures, we forego a fit for P_{H_2} such as described by Equation (8.15). We can simply identify our room temperature data set at $T_{low} \approx 298$ K as a proxy for $P_{\text{bgd_gas}} \approx P_{\text{meas}}(T \approx 298 \text{ K})$ and subtract it from any of the T_{mid} datasets between 700 K to 1600 K. Our measurement for $P_{\text{beam_gas}}$ at following from Eq. (8.17) is thus extracted by applying

$$P_{\text{beam_gas}}(T_{mid}) = P_{\text{meas}}(T_{mid}) - P_{\text{meas}}(T_{low} \approx 298 \text{ K}) \quad (8.18)$$

to any of the intermediate temperature datasets. This procedure is applied for every z_{pos} for which data was taken at both T_{low} and T_{mid} .

8.3.2 Molecular beam fit model

We fit a function based on the model described in Section 8.1.1 to the extracted $P_{\text{beam_gas}}$ values. For this we adapt Eq. (8.11) by adding two setup geometry parameters z_0 and d_{ch} as well as a power offset P_0 resulting in the fit function

$$\begin{aligned} &P_{\text{beam_gas}}(z_{\text{pos}} + z_0; l_{\text{eff}}, A_{\text{bg}}, P_0, d_{\text{ch}}) = \\ &A_{\text{bg}} \left(\int_{\text{wire}} dx d_{\text{wire}} j_{\text{HABS}}(\theta(x, z_{\text{pos}} + z_0; l_{\text{eff}}, d_{\text{ch}})) \cdot \eta_{\text{wire}}(x) \frac{\cos^3(\theta(x, z_{\text{pos}} + z_0))}{y_0^2} \right) \\ &+ P_0 \quad . \end{aligned} \quad (8.19)$$

z_0 is a simple offset to the wire position, which is required, since the calibration of the z-position used by when addressing the z-translator is not perfectly aligned with the center of the beam. d_{ch} is the distance between the HABS capillary end face and the HABS shroud opening as is further explained in Section 4.1.2. Its primary effect is to determine the cutoff angle at which the capillary is shaded by the HABS shroud, which results in a sharp drop in beam intensity at those angles.

The addition of P_0 represents a parameter without a determined physical explanation. If our model included all relevant effects, and the extraction scheme perfectly isolated them, then P_0 should be compatible with 0. However, in practice to attain reasonable fits it is required. This does indicate some level of model deficiency, which we will not be able to address in this work and will only briefly mention possibilities here: Our beam model does not anticipate any portion of the beam to hit the wire once the capillary is fully occluded by the HABS shroud. However, gas trapped in the HABS shroud does eventually leave it, presumably as a diffuse beam of intermediate temperature. We have not robustly quantified whether this is a significant effect. Another possibility is, that our assumption implicitly made for $P_{\text{bgd_gas}}$ in Section 5.3.7 that the gas introduced into the chamber by the source quickly accommodates to the temperature of the chamber is not entirely correct. If background gas retained on average 5% of its initial temperature difference to the chamber (100 K hotter than chamber temperature for a source at 2300 K) this would make background gas and the wire have approximately equal temperatures at high source temperatures, resulting in $P_{\text{bgd_gas}} \approx 0$. This would be consistent with some but not all out of beam data presented in Figure C.1 and be of an effect size large enough to explain P_0 under some circumstances.

In Figure 8.5 we show the four intermediate temperature data presented in Figure 8.4 after extracting $P_{\text{beam_gas}}$ as described in Section 8.3.1 and apply a fit with the model defined in Equation (8.19).

The fit model is generally able to describe the data fairly well with only few data points that are statistically incompatible with the fits. An exception is the 1022 K

dataset in Figure 8.5b which shows larger than usual scatter around the fit function, especially in relation to the estimated errors. The scatter seems to be stochastically scattered though, with no obvious additional systematic deviations.

The only clear systematic deviation seems to be in the inner edge of the penumbra region between 21° to 23° where all datasets show the data points above the fit model. This may indicate additional subtle effects caused by the HABS shroud shadowing that are not fully described by the g_{visible} model.

It should be noted, that since z_0 and d_{ch} are geometric parameters, they should in principle be fixed for all measurements presented here. They therefore allow the models some additional flexibility that it should not have. Short of precision measurements of these values in-situ, this could be addressed with a combined fit of multiple datasets with a single global value for geometric parameters such as z_0 and d_{ch} . For the data presented here z_0 and d_{ch} show only small variations beyond the parameter error estimates indicating no large disagreements about underlying geometry and we will not carry out the combined fits here.

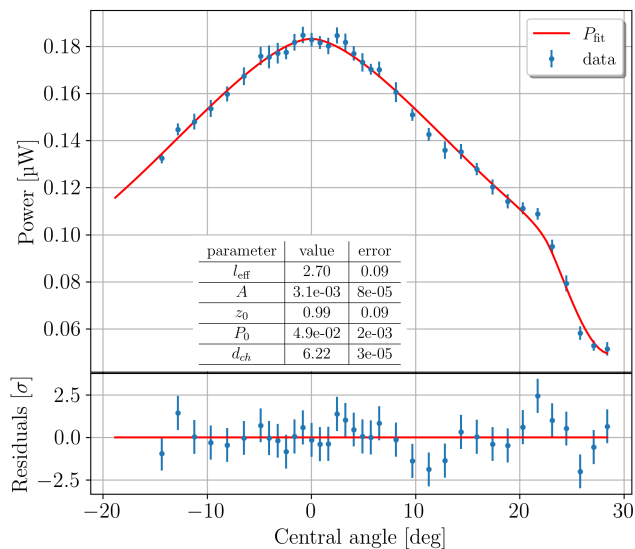
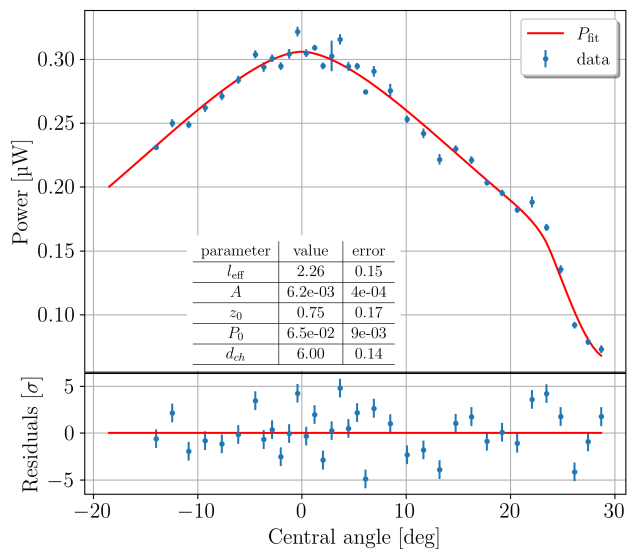
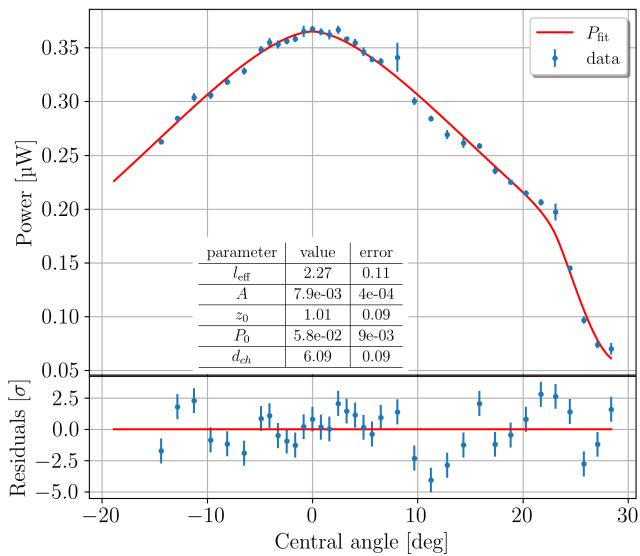
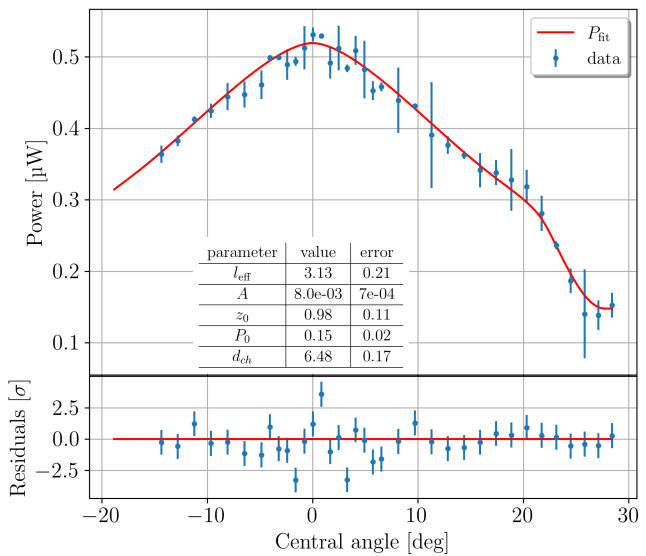
(a) $T \approx 739$ K(b) $T \approx 1022$ K(c) $T \approx 1277$ K(d) $T \approx 1517$ K

Figure 8.5: The sub-figures show the extracted measurements for $P_{\text{beam_gas}}$ for scans of the wire detector along the z -axis across pure H_2 beams at the indicated source temperatures. In each case the total flow of H_2 as measured by the mass flow controller is 1 sccm. Fits using the model defined in Equation (8.19) are plotted alongside the data, and the best fit parameters are listed in the inset table.

8.3.3 Accommodation coefficient and implications for absolute calibration

Having determined the beam shape in the previous section, we can now use Equation (8.12) to calculate the accommodation coefficient α_E ; the fraction of the kinetic energy available in the hot H_2 that hits the wire that is transferred to the wire. Solving Equation (8.12) for α_E yields

$$\alpha_{E_{\text{mol}}} = \frac{A_{\text{bg}}}{\Phi_{\text{mol}} \cdot (C_{V_{\text{mol}}}(T_{\text{mol}}) \cdot T_{\text{mol}} - C_{V_{\text{mol}}}(T_{\text{avg}}) \cdot T_{\text{avg}})}. \quad (8.20)$$

Inputting the fits values we can calculate values for α_E that would explain the observations under the model described in Equation (8.19). The resulting values are plotted in Figure 8.6. The plot is quite sparse with only 4 data points since these measurements were not prioritized during data taking. The 5 datasets required for this analysis took a combined 20 days of runtime. Given the size of the error bars it is therefore difficult to draw any firm conclusions beyond saying that available data suggests a value of $\alpha_E = \mu_{\alpha_E} \pm \sigma_{\alpha_E} \approx 0.47 \pm 0.07$ within the covered range of temperatures.

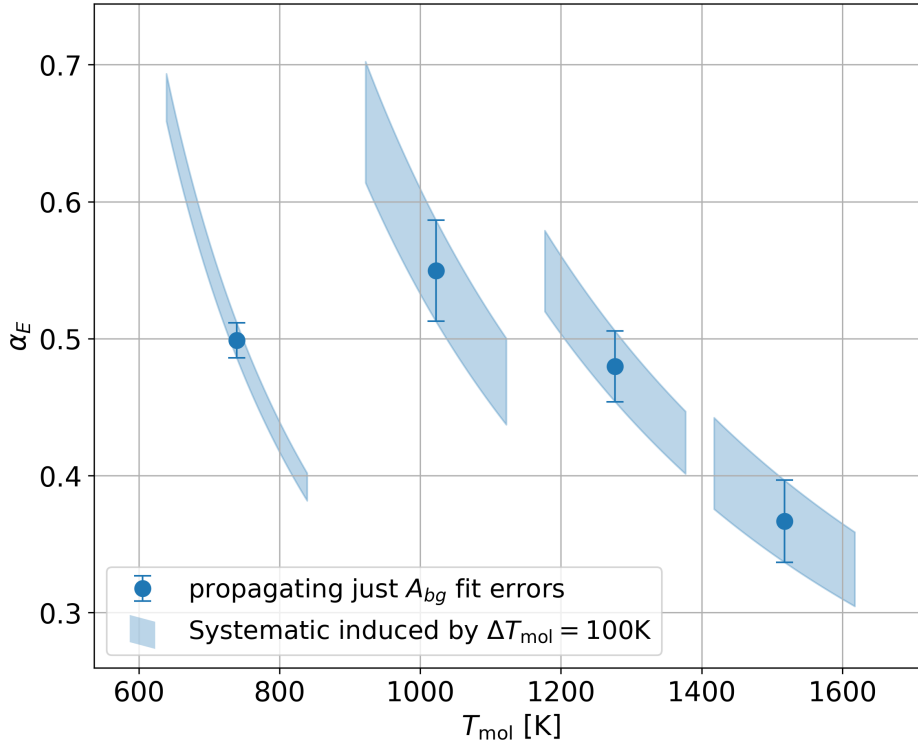


Figure 8.6: Plot of the values for α_E calculated from Eq. (8.20) based on the fit values presented in Figure 8.5 at 4 temperature setpoints. We include error bars based only on fit parameter error estimates. We additionally shade a region corresponding to a systematic offset in T_{mol} of 100 K either side of the nominal value after propagation through Eq. (8.20). The value of ΔT_{mol} is chosen for illustration purposes only, actual temperature errors may be different and likewise the induced systematic error.²⁵

²⁵The value of $\Delta T_{\text{mol}} = 100$ K is chosen according to an internal writeup by Larisa Thorne and Maximilian Hüneborn (Analysis Note: HABS temperature measurements, v2 <https://www.overleaf.com/project/64a69c57f63487ca657993cf>), and is not a precise determination. More detailed measurements of the source temperature are currently being undertaken as part of the PhD thesis of B. Muçogllava. We encourage referring to these when available. We do not cover problems related to uncertainty in T in detail in this thesis.

Our base assumption was, that α_E does not scale strongly with temperature. This was required for our extrapolation approach to secondary extraction of atomic H data described in Section 8.2.2. Given the errors, this assumption is still roughly compatible with the measured values. However, both the quality and number of data points are insufficient to say this definitively. By disregarding a single data point one might easily claim no measured trend with temperature if disregarding the 1517 K datapoint, or a strong downward trend with temperature if disregarding the 739 K. Measurements at additional temperatures in the range 400 K to 1600 K as well as repeat measurements to establish more reliable error estimates and potentially better understanding of systematics in T_{mol} would be necessary for a more definitive conclusion.

For atomic H heating power extraction in this work we stick to the assumption of an α_E that is constant with temperature. Since we have to extrapolate to temperatures where H_2 dissociates, we must make some assumption for the functional behavior with temperature. The assumption of constant α_E is the simplest and current data presented in figure 8.6 is not clear enough to recommend a different approach.

This simplified approach could induce a significant systematic error in P_{H_2} as reconstructed by extraction fits according to Equation (8.17) (pessimistically as much as $\approx 30\%$ judging from Figure 8.6). Since the P_{rec} is significantly larger than $P_{\text{beam_gas}}$ in all atomic H datasets we present in this thesis, the systematic error this would carry forward in the extracted P_{rec} can at least be expected to be smaller in relative terms than the error in the $P_{\text{beam_gas}}$ reconstruction.

An accurate measurement of $\alpha_E(T)$ would constitute an absolute calibration of the wire detector in the sense that one could directly relate the flow of H_2 in the beam Φ_{mol} to the signal measured on the wire detector, at least within the context of the model described here. This would allow in principle for measuring the flux of H_2 from a source with unknown flux. We mention this because, while measuring the total flux of H_2 is easily accomplished in the testing setup, the analogous problem for atomic H is non-trivial though it would be very useful.

The corresponding absolute calibration for mixed H and H_2 is not currently possible. There are two hurdles to such an absolute calibration. Firstly, we have no source of a pure H on which to calibrate the absolute calorimetric efficiency η_{rec} of the detector in this case. Secondly, in the case of the mixed beams as we produce them, there is a degeneracy between the dissociation fraction α_{dissoc} and calorimetric efficiency of recombination heating ($\eta_{\text{rec}} = \gamma'\beta_{\text{rec}}$ described in Section 5.5.3). Both are included as factors in the model for recombination heating (I_{rec} Equation (8.6)) and cannot be independently measured by any measurement of the kind presented in this thesis. A calibration measurement with a beam where α_{dissoc} can be separately determined would in principle allow for measuring η_{rec} at least for that particular gas temperature and atom flux density. If η_{rec} could be shown to be well approximated as a constant in the relevant parameter space this would constitute a global absolute calibration for the wire detector that would allow for directly measuring the absolute flux density of H from an unknown beam. We explore absolute H flux determination and current limitations further in Section 8.6.

8.4 Atomic Beam shape scans

8.4.1 3-temperature-point method at 1scm

In this section we measure the shape of the atomic hydrogen component of a hot beam using the 3-temperature-point (3-T-P) extraction procedure described in Section 8.2.

Figure 8.7 shows data taken when flowing 1 sccm (4.48×10^{17} molecules/s) of hydrogen

through the HABS at three capillary temperatures $T_{low} \sim 298 K$, $T_{mid} \sim 1277 K$ and $T_{high} \sim 2211 K$. The beam distribution is measured by sweeping across the hydrogen beam with the wire detector by means of the translation stage on which it is mounted. The range of z-positions represents the full range available in the limited space of the vacuum chamber. To avoid an impact of time-dependent effects over the measurement period of many hours, data at the different positions are acquired in non-consecutive order.

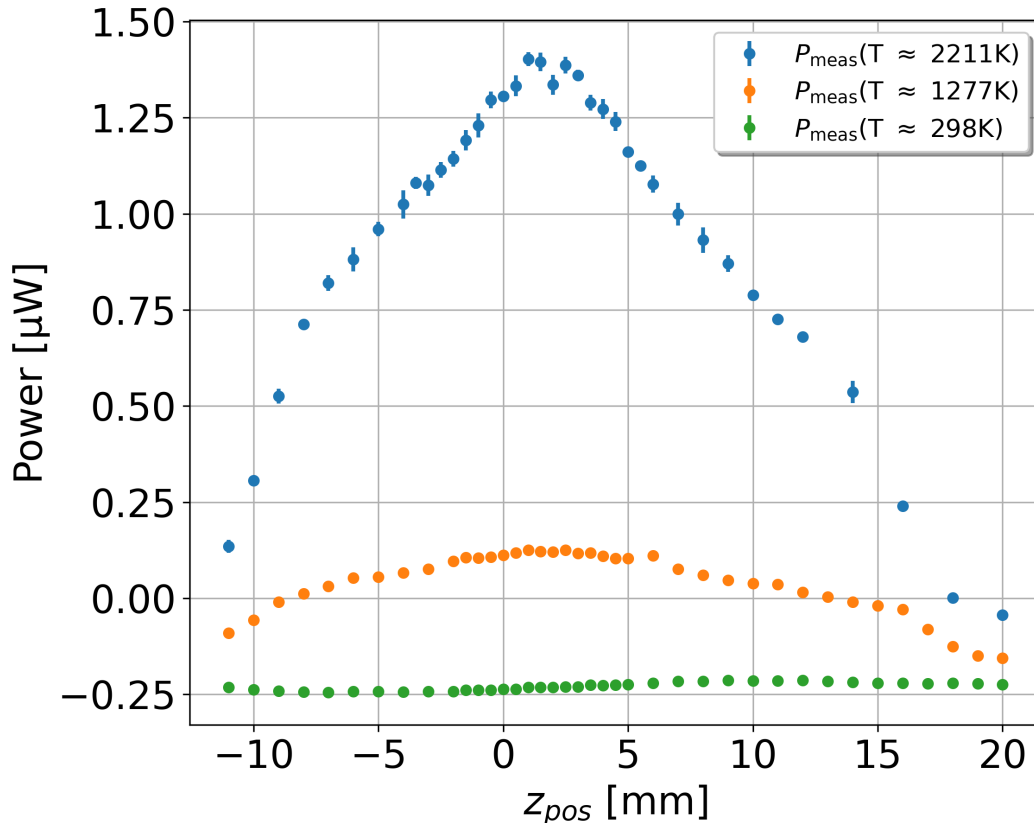


Figure 8.7: Power detected on the wire after primary extraction (P_{meas}) at 1 sccm for room temperature, a non-dissociating medium temperature, and a high temperature where atom production is expected. These data sets are then used in the secondary extraction procedure, to yield the effect of recombining atoms on the surface. Negative detected powers indicate a net cooling of the wire, which is identified with the cooling due to gas pressure increase in the detector chamber induced by gas flow from the source. (f_{bgd_gas}).

As seen in Figure 8.7, room temperature measurements initially yield a negative net heating power. This is because at this low temperature the beam imparts no significant heating to the wire, but it still fills the vacuum chamber with gas such that the pressure rises. This room temperature background gas cools the wire, since the wire reaches $\approx 70^\circ C$ in the center due to being heated by the measurement current. Both effects are described in Section 5.

At medium temperatures (1277 K in Figure 8.7) there is a slight heating on the order of 300 nW which can be seen to be higher when the wire is centered under the source ($z_{pos} \approx 1.5$ mm). This can be accounted for by a beam of hot molecular H_2 which transfers some of its thermal energy to the wire when hitting it (f_{beam_gas}).

Finally at high temperatures (2211 K in Figure 8.7) larger than the dissociation

threshold temperature, the beam contains a fraction of atomic hydrogen. This is the primary signal we are looking for, and can account for the much larger μW -scale peaked signal in the high temperature power data plotted in blue. The high temperature dataset shows a larger signal than can be explained by the increased thermal “beam gas” heating indicating the detection of recombination heating due to atomic hydrogen.

These three data sets are combined using the procedure described in Section 8.2.2 using Eq. (8.16) to determine the heating power due to recombination heating alone. The resulting extracted values are plotted in Figure 8.8.

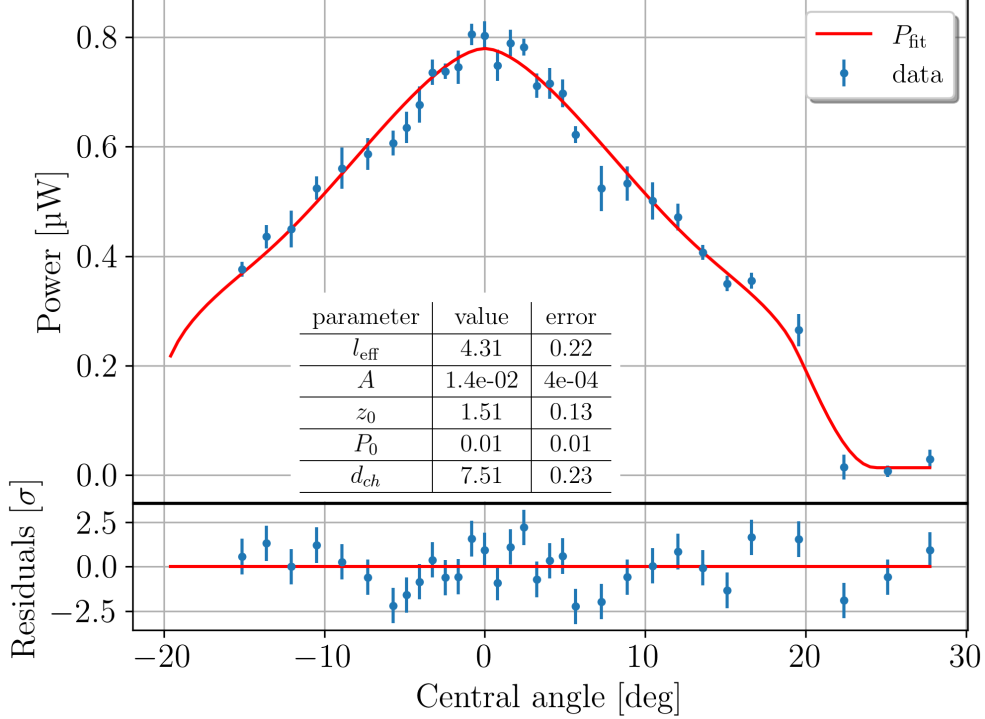


Figure 8.8: Extracted heating power attributed to recombination (P_{rec}) for a flow of 1 sccm at 2211 K source temperature, shown over the range of positions the wire was placed at. The optimized beam shape model is plotted alongside the data and the values of the best fit parameters are shown in the inset table.

The model from Eq. (8.5) is then adapted for fitting to the extracted recombination power data. An offset power P_0 , to account for a residual background, as well as a positional offset z_0 are introduced. The necessity of this can be seen in Figure 8.7, where the zero of the z -axis does not initially line up with the center of the beam. The resulting final fit function is given by

$$\begin{aligned}
 P_{\text{rec}}(z_{\text{pos}} + z_0; l_{\text{eff}}, A, P_0, d_{\text{ch}}) = & \\
 A \left(\int_{\text{wire}} dx d_{\text{wire}} j_{\text{HABS}}(\theta(x, z_{\text{pos}} + z_0); l_{\text{eff}}, d_{\text{ch}}) \cdot \eta_{\text{wire}}(x) \frac{\cos^3(\theta(x, z_{\text{pos}} + z_0))}{y_0^2} \right) & \\
 + P_0 \quad . & \quad (8.21)
 \end{aligned}$$

Figure 8.8 shows the fit applied to the final extracted data. As previously described, the parameter A is effectively just a vertical scaling parameter, while P_0 and z_0 translate the fit in the direction of the y and x plot axes respectively. l_{eff} determines the shape of the beam’s distribution as described in Section 4.1.1, and d_{ch} determines the angles at

which the beam is cut off by the HABS shroud as described in Section 4.1.2. The units of the fit parameters as they are reported in the figure and the rest of this thesis are given in Table 4.

Symbol	Description	Unit
A	Scaling parameter	W
P_0	Offset power	μW
z_0	z-axis position offset	mm
l_{eff}	Capillary effective length	$\frac{[\text{length of free molecular flow}]}{[\text{capillary diameter}]} = \frac{\text{mm}}{\text{mm}}$
d_{ch}	Distance: capillary to HABS shroud	mm

Table 4: Fit parameters and the units in which they are reported throughout this thesis, and in particular in the insets of plots showing fits.

This fit yields a value for the shape parameter l_{eff} , which allows us to reconstruct the beam intensity profile at the exit of the HABS. The resulting j_{HABS} as per Eq. (4.1) is shown in Figure 8.9 alongside an error band. The error band results from calculating $j_{\text{HABS}}(l_{\text{eff}})$ for the values l_{eff} shifted up and down by the fit error on l_{eff} . The error band deviation is zero at the center and at the edges by construction of the model, since it only shows relative flux. Any changes in flux scaling (errors in A) and background offset (errors in P_0) are external to this model. They would be important for a measurement of absolute flux, but not relative flux as is presented in this work. This example demonstrates that the procedure presented allows for measuring the shape of the original beam to better than 5% precision, relative to the central intensity, at any point along the distribution.

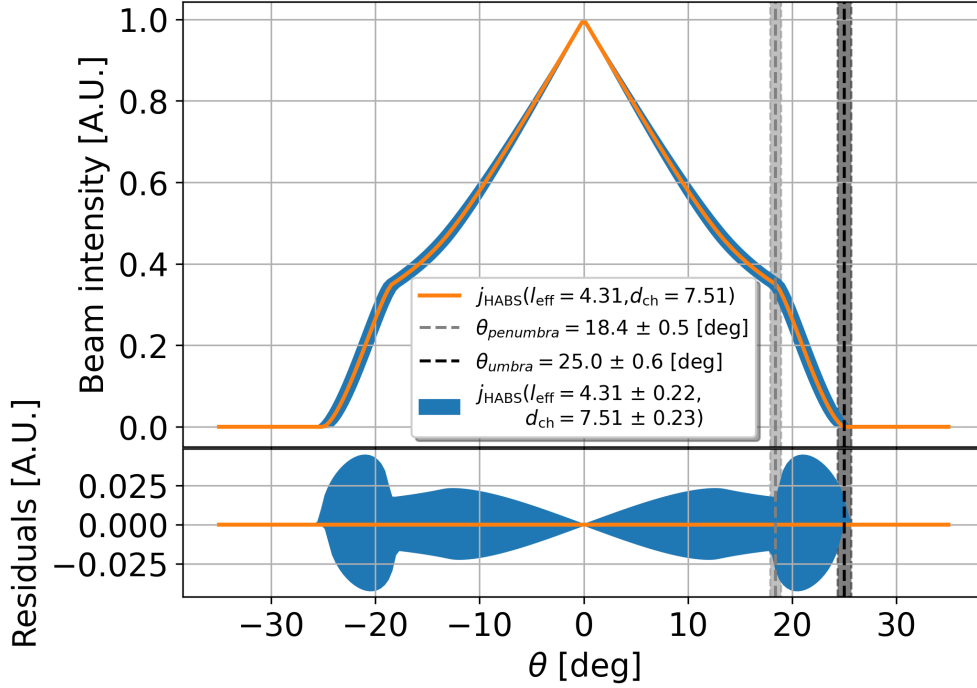


Figure 8.9: Reconstruction of the underlying beam shape model j_{HABS} , including both the effects of the theoretical beam shape emitted from a long tube, as well as the truncation of the edges due to shadowing of the beam by the source shroud, both as described in Section 4.1. The uncertainty on the extracted beam model is illustrated by propagating the fit errors the beam parameters l_{eff} and d_{ch} through the model in maximally correlated form. This illustrates a reconstruction of the beam as it exits the HABS to better than 5% precision, relative to the central intensity, at any point along the distribution.

8.4.2 Systematic errors from temperature selection

For the 1 sccm flow setting we took additional z-scans at additional intermediate temperatures below the dissociation threshold. Additional scans were not taken for every flow setting due to time constraints in the availability of the setup. Each of the z-scans with 38 positions requires about 80 hours to measure with the procedure presented in Figure 8.2, such that the 6 datasets in Figure 8.4 represent over 20 days of runtime alone. The three-temperature-point method presented in this thesis is a deliberate minimum of runtime, to make it possible to search in other parts of the parameter space, such as flow.

We use the additional z-scans to gauge possible systematic deviation in fit parameters due to the arbitrary choice of temperatures below the dissociation threshold we used to fit Eq. 8.15. The secondary extraction procedure (Section 8.2.2) is performed using all possible combinations (containing between 2-5) of the non-dissociating temperature setpoints (the set 1518 K, 1277 K, 1022 K, 739 K, 298 K). The sole dissociating temperature setpoint 2211 K must of course always be included as T_{high} . The resulting extracted powers are then fit with Eq. 8.21. The resulting l_{eff} fit parameter of all 26 combinations is shown as a histogram in Figure 8.10. The result of the three-point-method (3-T-P) as used in this thesis is shown in green along with its error band. Similarly the result of the extraction and fit based on all 6 available datasets at once (6-T-P) is shown in blue. The extracted recombination power and its fit are shown in Figure 8.11. The value of $l_{\text{eff}} = 4.62 \pm 0.38$ is statistically compatible with the three-point-method result previously discussed.

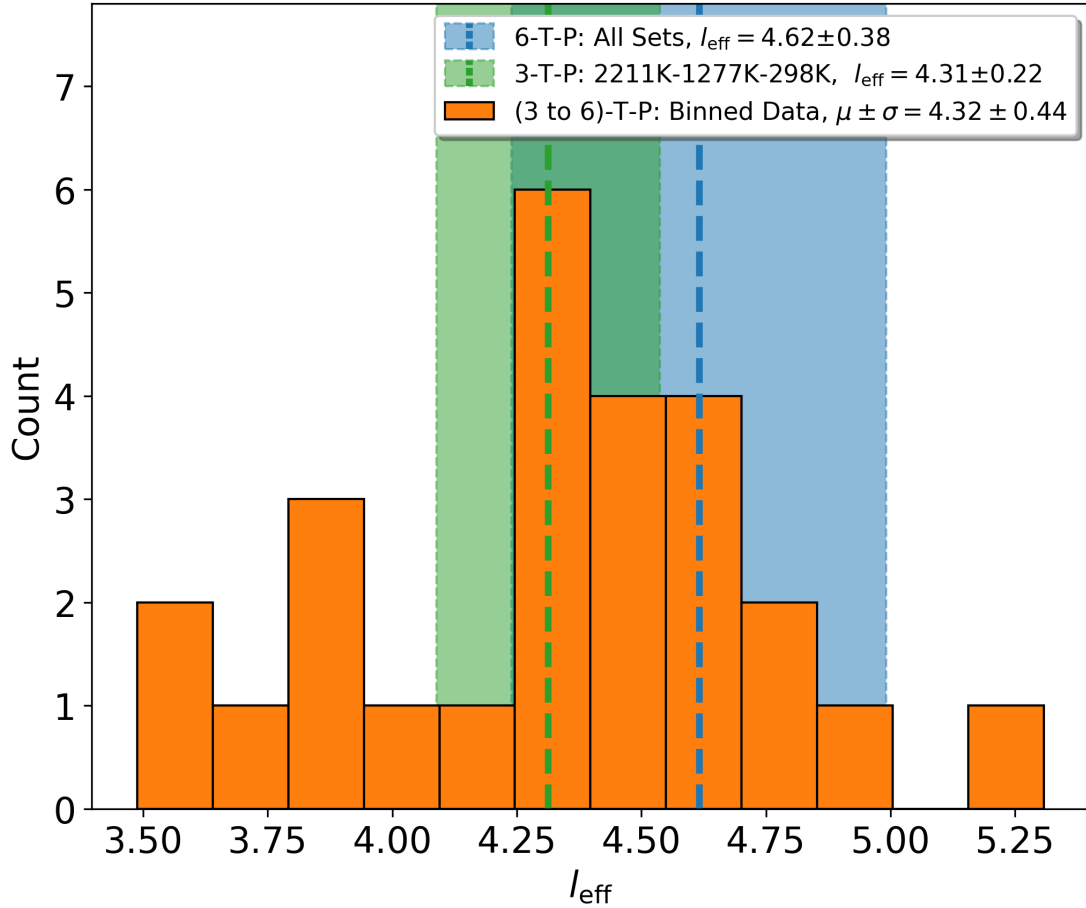


Figure 8.10: Histogram of fit parameter l_{eff} when using all possible combinations of the sub-dissociation datasets to fit P_{H_2} (Eq. (8.15)). These use between 3 and 6 total data sets when including the high temperature 2200 K dataset. The results of the fits using data sets at all 6 available temperature points (6-T-P) at once (Figure 8.11) and one example of three-temperature-method (3-T-P) as presented in Section 8.4.1 (Figure 8.8) are displayed with error bands.

This histogram is an imperfect proxy for systematic error due to temperature setpoint selection. The entries are clearly not entirely statistically independent as only 6 independent datasets exist. It is therefore unsurprising that the histogram does not approximate a normal distribution well. Nevertheless it illustrates that three-point-method using the 2211 K , 1277 K and 298 K datasets presented in this work is a reasonable expedient. For the systematic error bar displayed in Figure 8.14 we use the span of all results for l_{eff} after excluding the outlier at 5.31. This outlier is produced when extrapolating from the 1277 K and 1022 K datasets. It is perhaps unsurprising, that using datasets that are adjacent in temperature are more prone to large variation due to their shorter temperature baseline. The resulting span of values for l_{eff} is 3.48 to 4.91, which leaves the three-point-method result of $l_{\text{eff}} = 4.31 \pm 0.22$ well centered within. This span is plotted in orange as a systematic error bar in Figure 8.14.

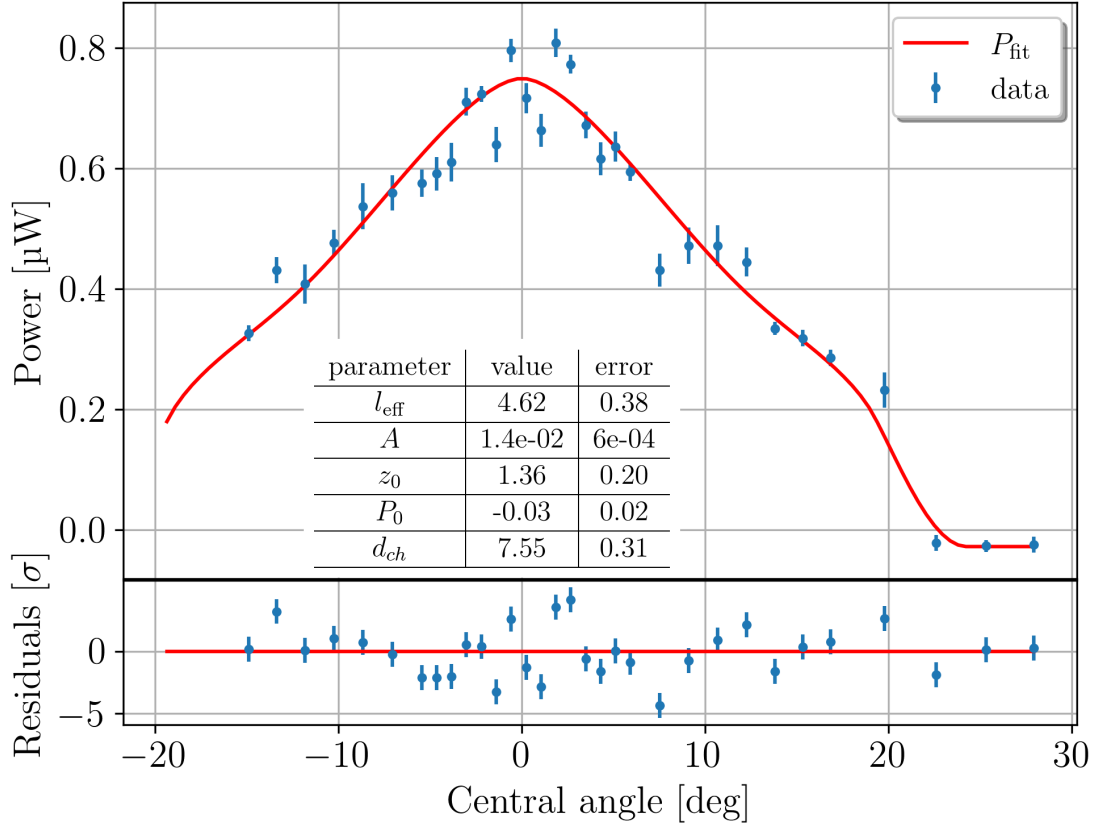


Figure 8.11: Extracted heating power attributed to recombination (P_{rec}) for a flow of 1 sccm at 2211 K source temperature, shown over the range of positions the wire was placed at. The optimized beam shape model is plotted alongside. P_{H_2} (Eq. (8.15)) was determined using all available z-scans below the dissociation threshold: 1518 K, 1277 K, 1022 K, 739 K and 298 K.

8.4.3 Additional lower flows

This section contains the results of the three-temperature-point method applied to data taken at flows of 0.2 sccm and 0.05 sccm along with fits. The data after primary extraction used for this analysis can be found in Appendix C in Figures C.1d and C.1c respectively. The method is equivalent to the procedure demonstrated for a flow of 1 sccm in Section 8.4.1. The resulting values for l_{eff} are included in Figure 8.14.

In Figure 8.12 we show the results of the beam model applied to P_{rec} extracted from data taken with a flow of 0.2 sccm. There is good compatibility between the model and data in this case. As expected l_{eff} and A change with flow compared to the 1 sccm fit. It is worth highlighting the small but significant deviation of P_0 from 0 W for which we have no firm physical explanation as previously previously discussed in Section 8.3.2.

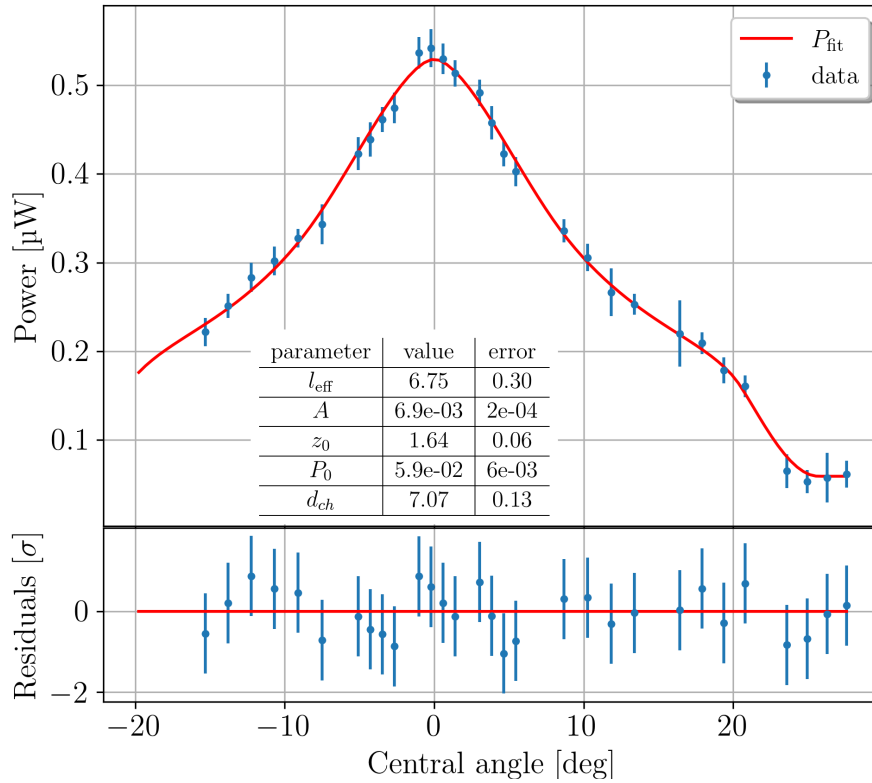


Figure 8.12: Extracted heating power attributed to recombination (P_{rec}) for a flow of 0.2 sccm at 2211 K source temperature, shown over the range of positions the wire was placed at. The optimized beam shape model is plotted alongside. P_{H_2} (Eq. (8.15)) was determined using z-scans 1277 K and 298 K.

In Figure 8.13 we show equivalently analyzed results for a flow of 0.05 sccm. This time the fit residuals are not as evenly distributed around the model. For example, there is a cluster of 7 negative residuals for measurements taken at angles of $0^\circ < \theta < 8^\circ$ followed immediately by a cluster of 9 positive residuals between $8^\circ < \theta < 21^\circ$. Collectively, this suggests that there is a small but statistically significant systematic effect we have not accounted for affecting this data set. If such an effect persisted when repeating this measurement, it may be worth following up on.

We have taken data from other flow settings, but do not have enough temperature setpoints, or data of sufficient quality to apply the three-temperature-point method. See Appendix C and D for this data and more rudimentary analysis methods applied to it.

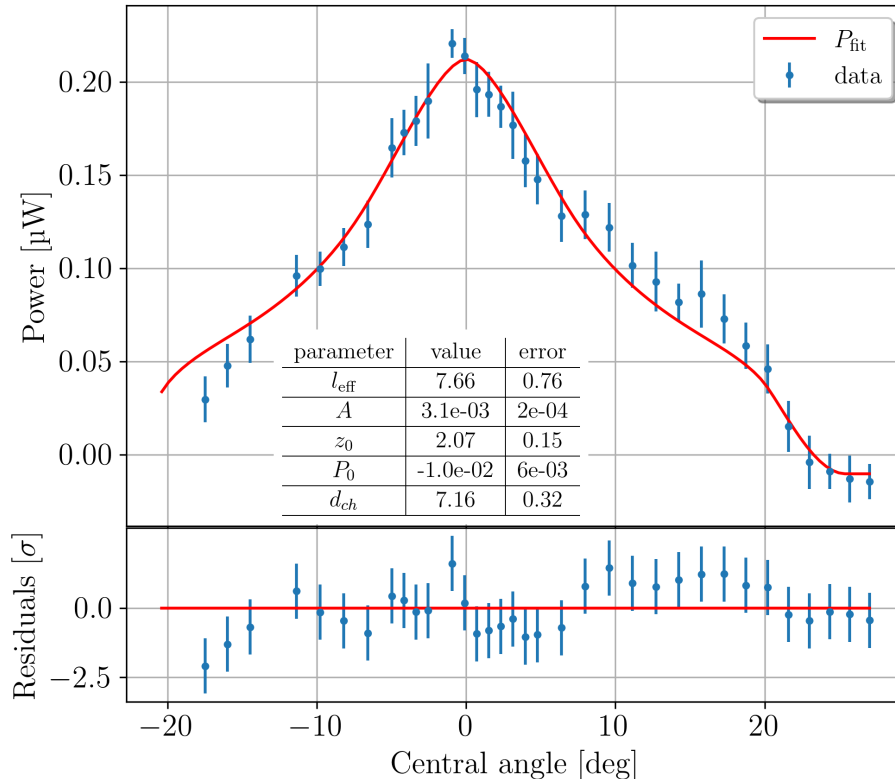


Figure 8.13: Extracted heating power attributed to recombination (P_{rec}) for a flow of 0.05 sccm at 2211 K source temperature, shown over the range of positions the wire was placed at. The optimized beam shape model is plotted alongside. P_{H_2} (Eq. (8.15)) was determined using z-scans 1277 K and 298 K.

8.5 Effective length over flow

The same three temperature scan procedure as illustrated in Section 8.4.1 has been performed for beams at 0.05 sccm and 0.2 sccm flow. This provides overlap with the lower flow regimes probed by Tschersich et al. [40]. Values for l_{eff} listed in Table I of that work are compared to the ones produced by this work in Figure 8.14. Extending the range of flows measured with the wire detector is the subject of ongoing work.

The two works provide values that are roughly compatible. In either case, the effective length of transparent flow is measured to increase with lower flows, which matches expectations, as lower flows correspond to lower densities in the capillary. Tschersich et al. [40] do not quote errors on their l_{eff} values. Additionally, while their source is very similar to the source used in this work (Section 4.1) and indeed is a prototype of the same, it is not exactly equivalent, especially in the precise geometry of its housing. They also operate their source at higher temperatures, although we do not expect this to have a significant direct effect on l_{eff} .

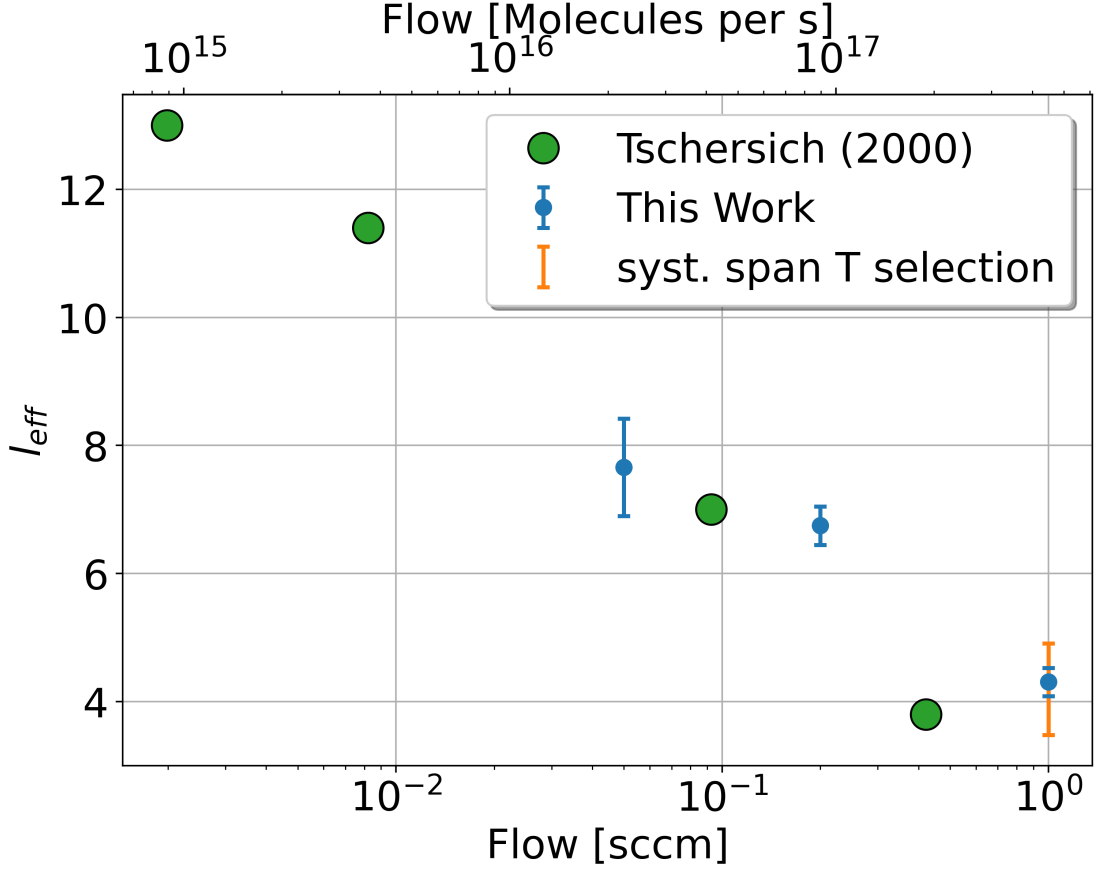


Figure 8.14: Comparison of fit parameter l_{eff} for the atomic hydrogen portion of the beam at three different flows using the methods described in this work to values from Table I in Tschersich et al. (2000) [40]. No error estimation is available for the sourced l_{eff} values. Plots showing fits in this work for 0.05 sccm and 0.2 sccm are available in Section 8.4.3. The orange error bar is the span of l_{eff} when datasets at different temperatures are used to determine P_{H_2} (see Section 8.4.2 for details).

8.6 Absolute atom count limits

Solving Eq. (8.2) for the unknowns, we get

$$\alpha_{\text{dissoc}} \cdot \eta_{\text{rec}} = \frac{A}{\Phi_{\text{in}} \cdot E_{\text{rec}}}. \quad (8.22)$$

Of these A is determined by fit, Φ_{in} is controlled and measured by the mass flow controller, and E_{rec} is known from literature. This leaves an ambiguity between α_{dissoc} and η_{rec} both of which must be values between 0 and 1. We can therefore determine lower limits for either α_{dissoc} or η_{rec} by setting the other to its maximum possible value of 1, i.e.:

$$\alpha_{\text{dissoc}} \geq \frac{A}{\Phi_{\text{in}} \cdot E_{\text{rec}}}. \quad (8.23)$$

The resulting lower limits, based on the 3-temperature-point datasets at 0.05 sccm, 0.2 sccm and 1 sccm presented in previous sections, are plotted in Figure 8.15 along with the results of values for α_{dissoc} determined using other methods and data taken with mass spectrometers. The mass spectrometer methods carry different systematic uncertainties, which are not accounted for in the displayed error bars.

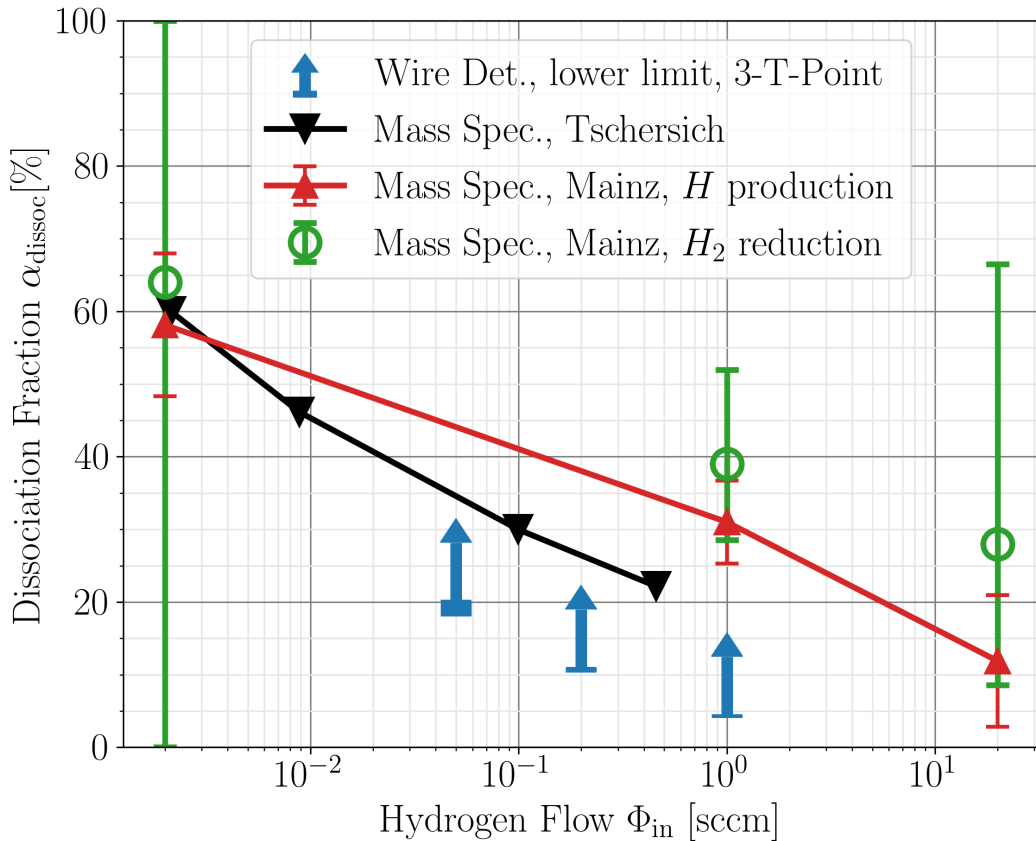


Figure 8.15: Values of the dissociation fraction α_{dissoc} determined for the HABS using 4 different methods. The lower limit values based on wire detector measurements presented in this thesis are shown as blue arrows, where the height of the horizontal bar at the bottom is the statistical error on the limit value, while the arrow indicates the fact that it is a lower limit with the true value anywhere between it and 1. The black downward triangles indicate mass spectrometer based values taken from Fig. 6 in Tschersich et al. [40] at 2200 K and include no error bars. The red upward triangles and green circles two different mass spectrometer based measurements performed in Mainz reproduced from A. Lindman’s PhD thesis (Section 45, [57]).

We reproduce the “Mainz”, mass spectrometer values for α_{dissoc} from the PhD thesis of Alec Lindman (Section 45, [57])²⁶, we will describe the methods used only very briefly and refer the reader there for additional details. Both the “Tschersich” and the “Mainz, H production” datasets measure the relative intensity of atomic H flux by counting the number of particles the mass spectrometer measures with a mass-to-charge-ratio of 1. They measure this at various temperatures between 300 K to 2600 K and then compare to a theoretical model to extract α_{dissoc} .

The “Mainz, H_2 reduction” measurements are instead calculated by measuring the reduction in H_2 counts measured by the mass spec as a result of the dissociation of molecules into atoms. While this method is conceptually simple, accounting for the background change in counts at a mass-to-charge-ratio of 2 as a function of source temperature regardless of dissociation has proven to be rather challenging. While this is not the focus of this thesis and the analysis presented here, we will point out, that this is likely to cause systematic uncertainties potentially in excess of displayed error bars.

²⁶A. Lindman’s thesis also contains values for α_{dissoc} based on the same wire detector measurements, but based on outdated analysis. The values presented here can be considered more rigorous.

Once again refer to Section 45 of A. Lindman’s thesis [57], for the details on the mass spectrometer based results as presented here.

“Mass Spec., Tschersich” data is read from Figure 6 in [40] at 2211 K. It is worth noting that wire detector data is taken at an estimated temperature of 2211 K, and the “Mainz” mass spec data has an estimated reference temperature of 2230 K. Referring again to [40] this range of temperatures may result in as much as a 5% relative change in α_{dissoc} . In addition, these reported temperatures all carry potentially significant calibration differences. We do not account for or display these systematics in Figure 8.15. While temperature differences are unlikely to explain the differences in reported α_{dissoc} on their own, it is a notable contribution to the difficulty of reliable comparison between methods.

We can conclude however, that values of α_{dissoc} based on wire detector measurements are compatible with previous measurements of a similar source using different methods. Given that we conservatively only report lower limits and therefore include a wide range of possible values for α_{dissoc} between this limit and 1, this is perhaps not especially impressive. Nevertheless, as the goals of our source development for Project 8 are primarily to produce as many hydrogen atoms as possible, a lower limit can still be used to determine with certainty whether a given source produces a sufficient number of atoms so long as the lower limit is already above the required number.

In Figure 8.16 we present the total atom flux as calculated from the α_{dissoc} values presented above using the Equation:

$$\Phi_{\text{at}} = 2 \cdot \alpha_{\text{dissoc}} \cdot \Phi_{\text{in}} \quad (8.24)$$

where Φ_{in} is the total flow of molecules through into the source. This calculation assumes, that α_{dissoc} is a good estimate for the average dissociation fraction across the entire beam distribution. In the case of wire detector measurements, this is a well founded assumption, since measurements are taken spanning the entire beam. Data from Tschersich equivalently spans the entire beam geometry. However the mass spectrometer measurements at Mainz were only performed on axis, and therefore carry additional uncertainty. Judging from both wire detector data presented here and Tschersich data we do not expect α_{dissoc} to change significantly over the beam distribution, at least for the relatively high flows presented here.

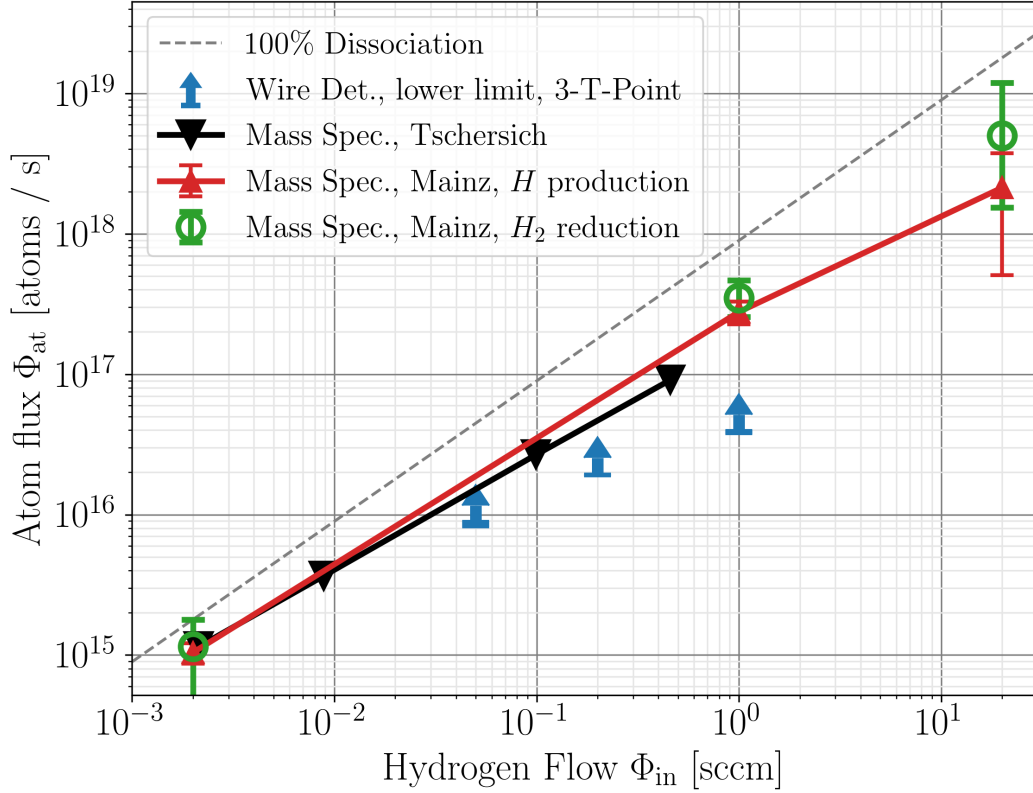


Figure 8.16: Total atom flux calculated from α_{dissoc} values as presented in Figure 8.15 using Eq. (8.24). The dashed line indicates the number of atoms that would be produced at a dissociation rate of 100%. The height of the horizontal bar at the bottom of the blue wire detector arrows indicates the statistical error on the lower limit, while the arrow indicates the fact that it is a lower limit with the true value anywhere between it and the dashed line. Includes data reproduced from Tschersich et. al. [40] and A. Lindman (Section 45, [57]).

In combination, the analysis of wire detector measurements presented in Figures 8.15 and 8.16 show that in agreement with previous studies, the dissociation fraction α_{dissoc} decreases as flow is increased, but slowly enough, that the total number of hydrogen atoms produced still increases with increased flow. With our conservative lower limit approach we can say with confidence, that using the HABS we can produce at least 4×10^{16} atoms/s at a flow of 1 sccm into the source.

9 Known issues and Suggestions

In the following section we will present some unfinished concepts, for potential improvements to the detector and analysis methods, that we recommend evaluating, but that were not deeply investigated during the time available for this thesis.

9.1 Suggested detector changes

9.1.1 Installation of an aperture

The interpretation of wire detector measurements is made significantly more difficult by the fact that it is an extended detector. Any resistance change in the wire must be interpreted as a convolution of the heat source with the wire sensitivity integrated over the length of the wire. For illustration of the problem recall Equation (8.5) for recombination heating on the wire:

$$P_{\text{rec}}(z_{\text{pos}}; l_{\text{eff}}, A) = A \left(\int_{\text{wire}} dx d_{\text{wire}} \cdot j_{HABS}(\theta(x, z_{\text{pos}}); l_{\text{eff}}) \cdot \eta_{\text{wire}}(x) \cdot \frac{\cos^3(\theta(x, z_{\text{pos}}))}{y_0^2} \right).$$

Here in order to determine the beam distribution j_{HABS} we must have both a parametrized model for the beam shape itself, as well as a model for the sensitivity of the wire at any point η_{wire} . If we could instead use a point detector, the integral would be reduced to a simple multiplication of the local beam intensity with a single, rather than a position-dependent detector sensitivity. A true point detector is infeasible, since it would have to measure an infinitesimal heating power. However, an approximation might be made with the installation of a small e.g. 2 mm wide aperture to mask all but the central portion of the calorimeter wire as illustrated in Figure 9.1.

Such a setup would reduce the effect of the convolution integral in Equation (8.5) enough, that with reasonable approximation one could measure arbitrary beam shapes directly, i.e. one could treat the relative intensity of the beam as measured by the wire detector covered by an aperture as the relative beam intensity at the exact center of the wire with only very minor distortion.

In addition the wire sensitivity η_{wire} would be essentially equal for all exposed parts of the wire. As shown in Figure 5.15 the convex nature of $\eta_{\text{wire}}(x)$ makes this approximation particularly good in the center of the wire. η_{wire} could be treated as a single constant, further reducing model dependence of the reconstruction and enabling, if desired, for it to be absorbed into the fit parameter A along with the other calibration constants.

The chief downside of placing an aperture over the wire detector would be the interruption of the beam. One of the primary drivers of the wire detector project, was the idea that it could be used as a minimally disruptive to the beam disturbing less than a thousandth of the particles in the beam. This disadvantage only matters if the beam is used downstream of the wire detector such as in an on-line configuration of the final Project 8 experiment. However, so long as the wire detector is used for development work only and not in conjunction with further detectors downstream, this disadvantage is irrelevant.

A secondary disadvantage of an aperture would be a reduction in signal, since some atoms would be blocked from reaching the wire reducing the heating power on the wire. However, since the wire detector is maximally sensitive in the center at a factor of more than 2 times the average sensitivity a reduction of the effective wire length to 10% of the total wire length (2 mm aperture size on a 20 mm wire) would still result in more than

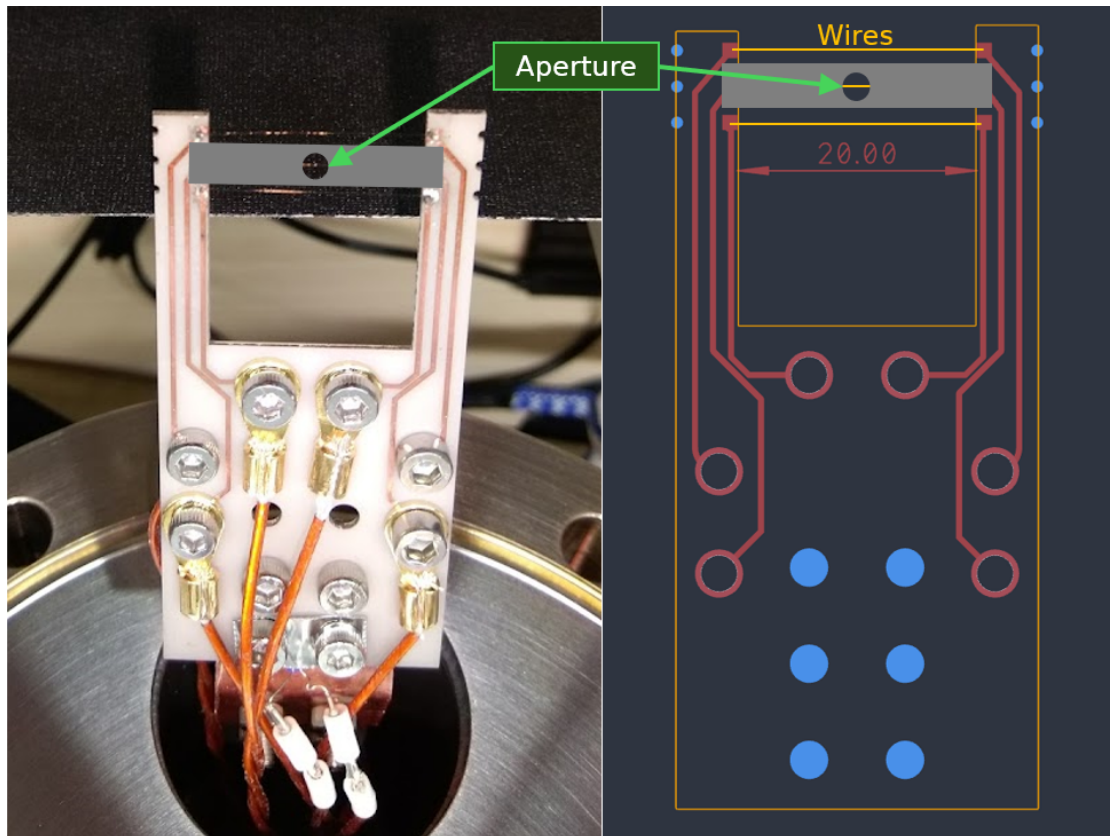


Figure 9.1: Sketch of a hypothetical aperture, which if mounted above the wire would reduce the active portion of the calorimeter wire to just the central 2 mm.

20% of the heating signal. If we factor in, that the beam is also centrally concentrated, the peak wire signal with the wire centered in the beam can be more than 30% the signal size for the same beam and a fully exposed wire.

9.1.2 Increase detector travel range

In its current configuration the wire detector mounted to the z-translation stage can be moved by 31 mm which equates to roughly 30° in the positive direction and -15° in the negative direction. This range is just barely sufficient for reaching an out-of-beam placement of the wire in the positive direction and is insufficient to do the same in the negative direction, as can be seen on any of the beam fit plots such as Figure 8.8. This means it is never possible to establish whether the beam is fully symmetric or whether a stable background is measurable on either side of the travel outside of the beam.

This is not an inherent shortcoming of the detector itself, but the way it is mounted. As shown in Figure 5.1 the wire detector board is currently mounted at an angle in order to get it to fit underneath the HABS in the current source chamber configuration. Travel is restricted on the inward side by the board colliding with the HABS on the inward side and with the chamber wall on the outward side.

On future iterations of the detector, we recommend enabling a larger range of angles relative to the source to be sampled with the wire detector if measuring beam shape is a priority. This could be enabled with existing equipment, by moving the HABS up a few centimeters to allow for the wire detector board to be laid flat such that traversing the full 10 cm of travel available with the z-translator is possible without colliding with either the chamber or the source. The tradeoff would be marginally reduced beam intensity in

downstream chambers of the setup, most importantly at the mass spectrometer. This should not be more than a 30% percent effect, if moving the HABS upwards by no more than 3 cm.

9.2 Issues with flow switching

In its current form, measuring the heating due to the beam requires filtering out larger background heat sources. As presented above, we currently use an off-on-off flow switching pattern to extract just the heating due to beam related sources. Requiring this flow switching sadly precludes the wire detector from serving as a true online detector for changes in a nominally stable beam. There are a few ways we may get back some of this utility at the cost of other trade offs.

The first method would be the use of a motorized beam shutter to switch illumination of the wire on or off without switching the source itself on or off. This would fulfill a similar function as the currently employed switching, with the difference, that it would also shutter any heating due to thermal radiation from the source (P_{bb} in Eq. (5.10)) which is usually very substantial. This means in analysis we would need at minimum a reference measurement at equivalent source temperature but no flow, to quantify the magnitude of P_{bb} at every wire position and temperature. Naively it should be sufficient to do this once at zero flow and then the same reference could be subtracted out when comparing to any higher flow.

A downside of this method would be an unavoidable disturbance of the beam at the frequency of the shutter, resulting in a pulsed beam downstream. Depending on the precise layout of the shutter, it may not have to obscure the entire beam, or do so for only very short periods of time, to enable a high duty cycle for the beam. Nevertheless it still means the wire detector cannot operate with precision without disturbing the beam substantially.

A less precise, but truly online solution might be, to use temperature sensors placed on the wire detector PCB as reference thermometers for drifts in background temperature. The current detector board has a Pt1000 resistive temperature sensor mounted to the back edge (see Figure 5.1). Tentative efforts with existing data have shown that with an appropriate calibration factor, changes in PCB temperature can be subtracted from changes in wire temperature, to subtract out slow background temperature trends. It is unclear what level of precision might be achievable with such a scheme, but it is currently our only idea for using the wire detector without relying on a pulsed signal for constant background trend subtraction. Since background trends in wire temperature are generally much larger than signals, not eliminating them with one scheme or another is not an option.

9.3 Suggestions elsewhere in the text

- Using temperature sensors other than the wire to subtract out background temperature effects. See Appendix B.2.
- Using bakeout controllers to heat wire detector to known temperatures for calibration of R_0 and a as proposed in 7.1.
- Fitting geometric parameters such as d_{ch} and z_0 globally over all datasets rather than for every individual dataset. See Section 4.1.2.

10 Conclusion

The Project 8 collaboration seeks to measure the beta decay spectrum of atomic tritium with sufficient precision to measure the effective neutrino mass m_β or through non-detection to establish a new best lower limit of 40 meV. Reaching such a lower limit would definitively establish that neutrino mass hierarchy must be normally ordered.

To reach this goal, Project 8 pioneers the use of cyclotron radiation emission spectroscopy (CRES) of beta decay electrons produced by tritium decay. The required statistical precision requires overcoming the low fraction of decays which occurs close to the endpoint energy, where only $\approx 3 \times 10^{-13}$ of the decays occurs within 1 eV of the endpoint, by observing a sufficient number of tritium decays. Furthermore, it requires eliminating the smearing effect caused by the final state distribution of the decay of tritium bound in T_2 molecules by instead using unbound atomic T.

Project 8 will need fill a magnetic trap with a sufficient number of tritium atoms to observe the required number of CRES events required for the targeted neutrino mass sensitivity. To this end, we must develop an atomic tritium source of intensities on the order of 10×10^{19} atoms/s.

The Mainz Atomic Test Setup (MATS) used in this thesis is part of this effort. In this thesis, we describe the use of this setup to develop a calorimetric wire detector capable of characterizing and monitoring atomic tritium beams. This detector, as described in the preceding text, can in the future be used to evaluate changes made to atomic tritium sources in the pursuit of developing a suitable source for use with the final experiment. We also anticipate using it as a minimally invasive probe to monitor the beam during operations of this final experiment.

As part of the design work on the detector, we simulate the thermal behavior of the wire detector in response to arbitrary atomic beams. This simulation can be used as a guide when aiming to improve the sensitivity of the wire detector.

The performance of the wire detector as built, was demonstrated by measuring the relative intensity profile of the beam produced by the HABS which is undergoing testing in the MATS. It is possible to reconstruct the underlying shape of the hydrogen beam emitted from a capillary based on a theoretical model, showing that remaining uncertainties are reasonably constrained. Good agreement with the theoretical model for the relative distribution of the beam was demonstrated. This constitutes an independent confirmation of this model. The beam shape parameters determined with the method described in this work are compared to those measured for a similar source using a QMS by another group [40] and are found to be compatible.

We cannot perform fully calibrated absolute intensity measurements, due to an undetermined proportionality factor for the fraction of available energy from recombination that is transferred into the wire. However, it has been possible to place lower limits on the measured atomic hydrogen flux, demonstrating that the calorimetric wire detector can be used to measure hydrogen beams with densities on the order of 10^{16} atoms/(cm²s) with significant SNR $\left(\frac{\mu_{\Delta R}}{\sigma_{\Delta R}} \approx 50\right)$.

We have therefore demonstrated the preliminary suitability of the calorimetric wire detector for characterizing hydrogen beam sources during further development as part of Project 8. This thesis has revealed a number of areas in which the performance of the wire detector might be further improved, and we encourage follow-up on the cataloged suggestions in future work.

Abbreviations

CMB cosmic microwave background. 6

CRES cyclotron radiation emission spectroscopy. ii, 13–16, 104

FSD final state distribution. 10, 11, 14

HABS Hydrogen Atomic Beam Source. ii, 17–19, 23–25, 33, 34, 46, 47, 75, 77, 83–85, 91, 98, 100, 102–104, 114, 116, 134

IMO inverted mass-ordering. 4, 7, 9

MAC-E Magnetic–Adiabatic Collimation — Electrostatic. 10, 12

MATS Mainz Atomic Test Setup. 17, 104

MECB magnetic evaporative cooling beamline. 15

NMO normal mass-ordering. 4, 7

PCB printed circuit board. 26, 56–61, 66, 103, 116

sccm standard cubic centimeters per minute. 18

SNR Signal-to-Noise Ratio. 80, 104, 128, 132

References

- [1] Project 8 Collaboration, A. A. Esfahani et al., [The project 8 neutrino mass experiment](#) (2022). doi:10.48550/ARXIV.2203.07349.
URL <https://arxiv.org/abs/2203.07349>
- [2] A. Vassiliev, Online monitor of the hydrogen (deuterium) atomic beam. the, "online" (Nov 1996).
- [3] V. A. Trofimov, A. A. Vasil'ev, A. I. Kovalev, P. A. Kravtsov, [A two-coordinate detector for a beam of atomic hydrogen or deuterium](#), Instruments and Experimental Techniques 48 (1) (2005) 122–126. doi:10.1007/s10786-005-0024-z.
URL <http://dx.doi.org/10.1007/s10786-005-0024-z>
- [4] D. Ugur, A. J. Storm, R. Verberk, J. C. Brouwer, W. G. Sloof, [Quantification of the atomic hydrogen flux as a function of filament temperature and h2 flow rate](#), Journal of Vacuum Science & Technology A: Vacuum, Surfaces, and Films 30 (3) (Apr. 2012). doi:10.1116/1.3700231.
URL <http://dx.doi.org/10.1116/1.3700231>
- [5] H.-L. Schumacher, Detector for atomic hydrogen, Bachelor Thesis, JGU Mainz (2019).
- [6] G. Schwendler, Messungen am atomaren wasserstoffstrahl, Bachelor Thesis, JGU Mainz (2019).
- [7] B. Tscharn, Measurements on the cryogenic hydrogen beam, Bachelor Thesis, JGU Mainz (2020).
- [8] A. Winkler, [Interaction of atomic hydrogen with metal surfaces](#), Applied Physics A: Materials Science & Processing 67 (6) (1998) 637–644. doi:10.1007/s003390050835.
URL <http://dx.doi.org/10.1007/s003390050835>
- [9] C.-F. Cheng, J. Hussels, M. Niu, H. Bethlem, K. Eikema, E. Salumbides, W. Ubachs, M. Beyer, N. Hölsch, J. Agner, F. Merkt, L.-G. Tao, S.-M. Hu, C. Jungen, [Dissociation energy of the hydrogen molecule at 1e-9 accuracy](#), Physical Review Letters 121 (1) (Jul. 2018). doi:10.1103/physrevlett.121.013001.
URL <http://dx.doi.org/10.1103/PhysRevLett.121.013001>
- [10] S. U. A. H. Syed, S. Maher, S. Taylor, [Quadrupole mass filter operation under the influence of magnetic field](#), Journal of Mass Spectrometry 48 (12) (2013) 1325–1339. doi:10.1002/jms.3293.
URL <http://dx.doi.org/10.1002/jms.3293>
- [11] J. A. Formaggio, A. L. C. De Gouvêa, R. H. Robertson, [Direct measurements of neutrino mass](#), Physics Reports 914 (2021) 1–54. doi:10.1016/j.physrep.2021.02.002.
URL <https://linkinghub.elsevier.com/retrieve/pii/S0370157321000636>
- [12] Particle Data Group, P. A. Zyla et al., [Review of Particle Physics](#), Progress of Theoretical and Experimental Physics 2020 (8) (2020) 083C01. doi:10.1093/ptep/ptaa104.
URL <https://academic.oup.com/ptep/article/doi/10.1093/ptep/ptaa104/5891211>

- [13] W. Pauli, [Letter to tübingen conference participants](#), web document. English translation also in [2, page 27] (1930).
URL <http://www.math.utah.edu/~beebe/talks/2015/qtm/pdf/pauli-1930-ltc.pdf>.
- [14] J. N. Bahcall, M. H. Pinsonneault, S. Basu, [Solar Models: Current Epoch and Time Dependences, Neutrinos, and Helioseismological Properties](#), *The Astrophysical Journal* 555 (2) (2001) 990–1012. doi:10.1086/321493.
URL <https://iopscience.iop.org/article/10.1086/321493>
- [15] B. T. Cleveland, T. Daily, R. Davis, Jr., J. R. Distel, K. Lande, C. K. Lee, P. S. Wildenhain, J. Ullman, [Measurement of the Solar Electron Neutrino Flux with the Homestake Chlorine Detector](#), *The Astrophysical Journal* 496 (1) (1998) 505–526. doi:10.1086/305343.
URL <https://iopscience.iop.org/article/10.1086/305343>
- [16] SNO Collaboration, Q. R. Ahmad et al., [Direct Evidence for Neutrino Flavor Transformation from Neutral-Current Interactions in the Sudbury Neutrino Observatory](#), *Physical Review Letters* 89 (1) (2002) 011301. doi:10.1103/PhysRevLett.89.011301.
URL <https://link.aps.org/doi/10.1103/PhysRevLett.89.011301>
- [17] T. S.-K. Collaboration, [Solar 8B and hep Neutrino Measurements from 1258 Days of Super-Kamiokande Data](#), arXiv:hep-ex/0103032 (Mar. 2001). doi:10.48550/arXiv.hep-ex/0103032.
URL <http://arxiv.org/abs/hep-ex/0103032>
- [18] The Super-Kamiokande Collaboration, Y. Fukuda et al., [Evidence for oscillation of atmospheric neutrinos](#), arXiv:hep-ex/9807003 (Aug. 1998). doi:10.48550/arXiv.hep-ex/9807003.
URL <http://arxiv.org/abs/hep-ex/9807003>
- [19] I. Esteban, M. Gonzalez-Garcia, M. Maltoni, T. Schwetz, A. Zhou, [The fate of hints: updated global analysis of three-flavor neutrino oscillations](#), *Journal of High Energy Physics* 2020 (9) (2020) 178. doi:10.1007/JHEP09(2020)178.
URL [https://link.springer.com/10.1007/JHEP09\(2020\)178](https://link.springer.com/10.1007/JHEP09(2020)178)
- [20] A. de Gouvea et al., [Neutrinos](#), arXiv:1310.4340 (Oct. 2013). doi:10.48550/arXiv.1310.4340.
URL <http://arxiv.org/abs/1310.4340>
- [21] M. Agostini, G. Benato, J. A. Detwiler, [Discovery probability of next-generation neutrinoless double- beta decay experiments](#), *Physical Review D* 96 (5) (2017) 053001. doi:10.1103/PhysRevD.96.053001.
URL <https://link.aps.org/doi/10.1103/PhysRevD.96.053001>
- [22] B. J. P. Jones, [The Physics of Neutrinoless Double Beta Decay: A Primer](#), arXiv:2108.09364 (Feb. 2022). doi:10.48550/arXiv.2108.09364.
URL <http://arxiv.org/abs/2108.09364>
- [23] KamLAND-Zen Collaboration, S. Abe et al., [Search for Majorana Neutrinos with the Complete KamLAND-Zen Dataset](#), arXiv:2406.11438 (Jun. 2024). doi:10.48550/arXiv.2406.11438.
URL <http://arxiv.org/abs/2406.11438>

- [24] DESI Collaboration, A. G. Adame et al., [DESI 2024 VI: Cosmological Constraints from the Measurements of Baryon Acoustic Oscillations](#), arXiv:2404.03002 (Nov. 2024). doi:10.48550/arXiv.2404.03002.
URL <http://arxiv.org/abs/2404.03002>
- [25] KATRIN collaboration, M. Aker et al., [Direct neutrino-mass measurement based on 259 days of KATRIN data](#), arXiv:2406.13516 (Jun. 2024). doi:10.48550/arXiv.2406.13516.
URL <http://arxiv.org/abs/2406.13516>
- [26] T. J. Loredo, D. Q. Lamb, [Bayesian analysis of neutrinos observed from supernova SN 1987A](#), Physical Review D 65 (6) (2002) 063002. doi:10.1103/PhysRevD.65.063002.
URL <https://link.aps.org/doi/10.1103/PhysRevD.65.063002>
- [27] JUNO Collaboration, F. An et al., [Neutrino physics with JUNO](#), Journal of Physics G: Nuclear and Particle Physics 43 (3) (2016) 030401. doi:10.1088/0954-3899/43/3/030401.
URL <https://iopscience.iop.org/article/10.1088/0954-3899/43/3/030401>
- [28] Hyper-Kamiokande Proto-Collaboration, K. Abe et al., [Hyper-Kamiokande Design Report](#), arXiv:1805.04163 (Nov. 2018). doi:10.48550/arXiv.1805.04163.
URL <http://arxiv.org/abs/1805.04163>
- [29] Y. A. Akulov, B. A. Mamyrin, [Half-life and \$t_{1/2}\$ value for the bare triton](#), Physics Letters B 610 (1) (2005) 45–49. doi:10.1016/j.physletb.2005.01.094.
URL <https://www.sciencedirect.com/science/article/pii/S0370269305001784>
- [30] M. Kleesiek, J. Behrens, G. Drexlin, K. Eitel, M. Erhard, J. A. Formaggio, F. Glück, S. Groh, M. Hötzel, S. Mertens, A. W. P. Poon, C. Weinheimer, K. Valerius, [Beta-Decay Spectrum, Response Function and Statistical Model for Neutrino Mass Measurements with the KATRIN Experiment](#), arXiv:1806.00369 (Jun. 2018). doi:10.48550/arXiv.1806.00369.
URL <http://arxiv.org/abs/1806.00369>
- [31] S. Schneidewind, J. Schürmann, A. Lokhov, C. Weinheimer, A. Saenz, [Improved treatment of the \$T_2\$ molecular final-states uncertainties for the KATRIN neutrino-mass measurement \(2023\)](#). doi:10.48550/ARXIV.2310.12634.
URL <https://arxiv.org/abs/2310.12634>
- [32] KATRIN collaboration, M. Aker et al., [The Design, Construction, and Commissioning of the KATRIN Experiment](#), arXiv:2103.04755 (Jun. 2021). doi:10.48550/arXiv.2103.04755.
URL <http://arxiv.org/abs/2103.04755>
- [33] KATRIN collaboration, M. Arenz et al., [Commissioning of the vacuum system of the KATRIN Main Spectrometer](#), arXiv:1603.01014 (Mar. 2016). doi:10.48550/arXiv.1603.01014.
URL <http://arxiv.org/abs/1603.01014>
- [34] L. I. Bodine, D. S. Parno, R. G. H. Robertson, [Assessment of molecular effects on neutrino mass measurements from tritium beta decay](#), arXiv:1502.03497 (Feb. 2015). doi:10.48550/arXiv.1502.03497.
URL <http://arxiv.org/abs/1502.03497>

- [35] A. Saenz, S. Jonsell, P. Froelich, Improved Molecular Final-State Distribution of HeT⁺ for the β -Decay Process of T 2, *Physical Review Letters* 84 (2) (2000) 242–245. doi:10.1103/PhysRevLett.84.242. URL <https://link.aps.org/doi/10.1103/PhysRevLett.84.242>
- [36] Project 8 Collaboration, D. M. Asner et al., Single-Electron Detection and Spectroscopy via Relativistic Cyclotron Radiation, *Physical Review Letters* 114 (16) (2015) 162501. doi:10.1103/PhysRevLett.114.162501. URL <https://link.aps.org/doi/10.1103/PhysRevLett.114.162501>
- [37] E. W. Otten, C. Weinheimer, Neutrino mass limit from tritium beta decay, arXiv:0909.2104 (Sep. 2009). doi:10.48550/arXiv.0909.2104. URL <http://arxiv.org/abs/0909.2104>
- [38] Project 8 Collaboration, B. J. P. Jones et al., Dynamics of Magnetic Evaporative Beamline Cooling for Preparation of Cold Atomic Beams, arXiv:2502.00188 (Jan. 2025). doi:10.48550/arXiv.2502.00188. URL <http://arxiv.org/abs/2502.00188>
- [39] K. G. Tschersich, J. P. Fleischhauer, H. Schuler, Design and characterization of a thermal hydrogen atom source, *Journal of Applied Physics* 104 (3) (Aug. 2008). doi:10.1063/1.2963956. URL <http://dx.doi.org/10.1063/1.2963956>
- [40] K. G. Tschersich, Intensity of a source of atomic hydrogen based on a hot capillary, *Journal of Applied Physics* 87 (5) (2000) 2565–2573. doi:10.1063/1.372220. URL <http://dx.doi.org/10.1063/1.372220>
- [41] K. G. Tschersich, V. von Bonin, Formation of an atomic hydrogen beam by a hot capillary, *Journal of Applied Physics* 84 (8) (1998) 4065–4070. doi:10.1063/1.368619. URL <http://dx.doi.org/10.1063/1.368619>
- [42] G. A. Melin, R. J. Madix, Energy accommodation during oxygen atom recombination on metal surfaces, *Trans. Faraday Soc.* 67 (1971) 198–211. doi:10.1039/TF9716700198. URL <http://dx.doi.org/10.1039/TF9716700198>
- [43] G. A. Melin, R. J. Madix, Energy accommodation during hydrogen atom recombination on metal surfaces, *Transactions of the Faraday Society* 67 (0) (1971) 2711–2719. doi:10.1039/TF9716702711. URL <https://pubs.rsc.org/en/content/articlelanding/1971/tf/tf9716702711>
- [44] A. I. Livshits, F. E. Balghiti, M. Bacal, Dissociation of hydrogen molecules on metal filaments in H⁺ ion sources, *Plasma Sources Science and Technology* 3 (4) (1994) 465–472. doi:10.1088/0963-0252/3/4/003. URL <https://iopscience.iop.org/article/10.1088/0963-0252/3/4/003>
- [45] G. A. Beitel, Recombination of atomic hydrogen on metal surfaces in ultra high vacuum., Ph. D. Thesis (1969). URL <https://search.library.wisc.edu/catalog/999872957802121>

- [46] G. A. Melin, R. J. Madix, [Energy accommodation during oxygen atom recombination on metal surfaces](#), Transactions of the Faraday Society 67 (1971) 198. doi:10.1039/tf9716700198.
URL <https://xlink.rsc.org/?DOI=tf9716700198>
- [47] L. Brewer, [Thermodynamic Properties of the Oxides and their Vaporization Processes.](#), Chemical Reviews 52 (1) (1953) 1–75. doi:10.1021/cr60161a001.
URL <https://pubs.acs.org/doi/abs/10.1021/cr60161a001>
- [48] B. J. C. Chaston, [Reaction of Oxygen with the Platinum Metals: I—The Oxidation of Platinum](#), Platinum Metals Review 8 (2) (1964) 50–54. doi:10.1595/003214064X825054.
URL <https://technology.matthey.com/content/journals/10.1595/003214064X825054>
- [49] D. A. Fenner, Sensitivity of project 8's atomic hydrogen wire detector, Bachelor Thesis, JGU Mainz (2024).
- [50] G. Lee, [Materials for ultra-high vacuum](#), Tech. Rep. FNAL-TM-1615, 6985168, Fermi National Accelerator Laboratory (Aug. 1989). doi:10.2172/6985168.
URL <http://www.osti.gov/servlets/purl/6985168-EkBmta/>
- [51] David R. Lide ed., CRC handbook of chemistry and physics: a ready reference book of chemical and physical data, 86th Edition, CRC Press, Boca Raton, 2005, p. 2123.
- [52] M. Astaschov, [Evaluierung des amqp-basierten-netzwerkprotokolls dripline 3 im kontext eines teststandes zur erzeugung atomaren tritiums](#), Bachelor Thesis, JGU Mainz (2023).
- [53] R. A. Serway, Principles of physics, 2nd Edition, Saunders golden sunburst series, Saunders College Pub, Fort Worth, 1998, p. 602.
- [54] A. Winkler, [Interaction of atomic hydrogen with metal surfaces](#), Applied Physics A: Materials Science & Processing 67 (6) (1998) 637–644. doi:10.1007/s003390050835.
URL <http://link.springer.com/10.1007/s003390050835>
- [55] J. Chase, M.W., [NIST-JANAF Thermochemical Tables](#), fourth edition Edition, J. Phys. Chem. Ref. Data, Monograph 9, 1998.
URL <https://webbook.nist.gov/cgi/cbook.cgi?ID=C1333740&Type=JANAFG&Table=on#ref-1>
- [56] P. J. Kern, Calibration measurement of a wire detector for atomic hydrogen, Bachelor Thesis, JGU Mainz (2022).
- [57] A. Lindman, Atomic tritium technology: Production, cooling, and trapping, PhD Thesis, JGU Mainz (2025).
- [58] Y. Kalambet, [Reconstruction of exponentially modified functions](#), ResearchGate (2019). doi:10.13140/RG.2.2.12482.84160.
URL <http://rgdoi.net/10.13140/RG.2.2.12482.84160>

A Coordinate definitions

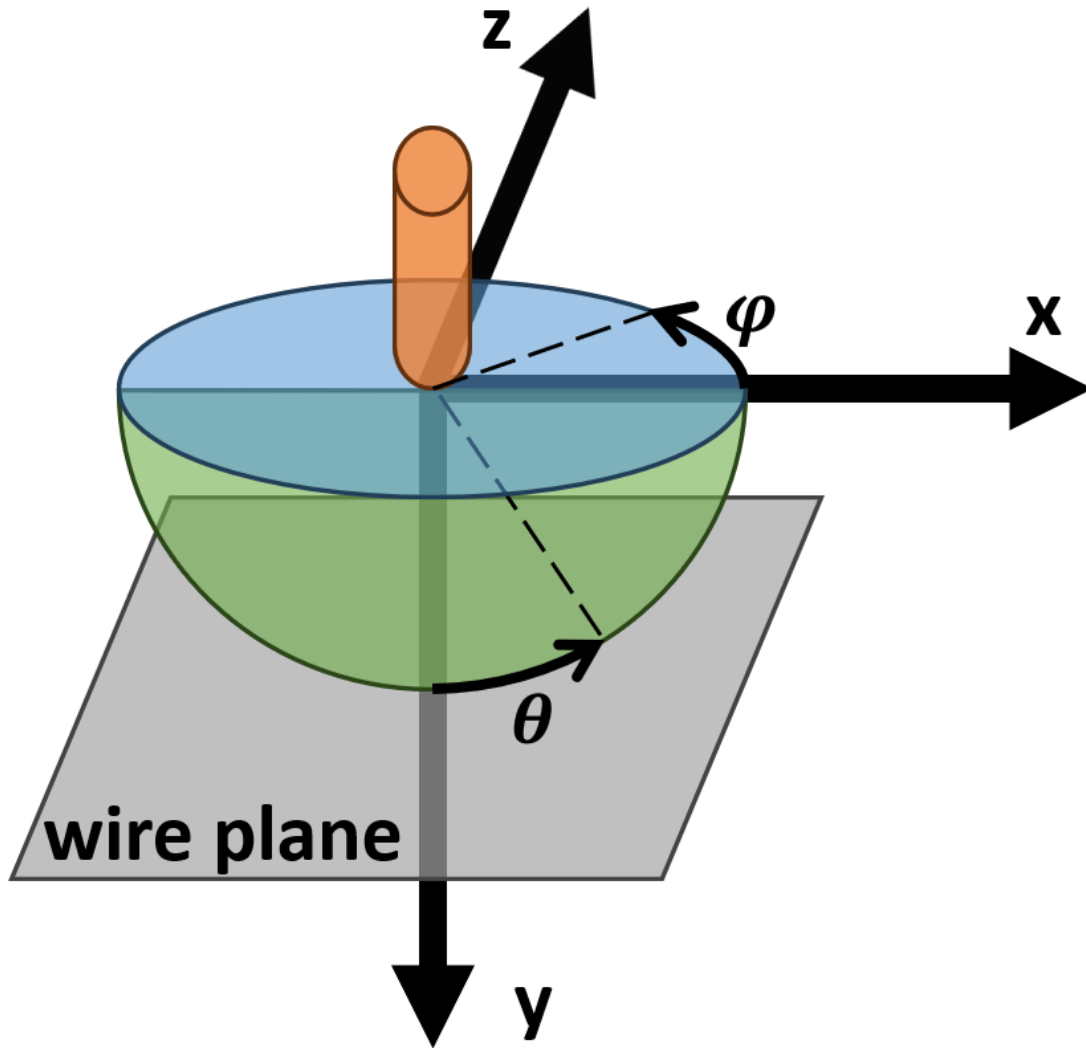


Figure A.1: Half-sphere axes definitions. The HABS capillary is indicated by the orange tube. The wire is oriented parallel to the x-axis in the wire plane. It can be moved in the z-direction by a translation stage. The distance to the capillary in the y-direction is fixed.

Following the diagram in Figure A.1 the relationship between cartesian coordinates (x, z, y) and spherical coordinates r, θ, φ is given by

$$\begin{pmatrix} x \\ z \\ y \end{pmatrix} = \begin{pmatrix} r \sin \theta \cos \varphi \\ r \sin \theta \sin \varphi \\ r \cos \theta \end{pmatrix} \quad (\text{A.1})$$

Note that z and y axis are deliberately switched from the standard definition of the spherical coordinates. This is because internal working group usage had already been calling the z-axis by that name because the translation stage ("z-translator") that the wire detector is mounted to is operating along this axis. Because this device is marketed as a "z-translator" it was simpler at the time to retain this name for the axis. I do recognize that in other contexts such as this one this arbitrary choice is instead more confusing.

An additional difference to convention is that y-axis points downwards beam is emitted in the positive y-direction, even though this is the "down" direction.

The inverse transformation from (x, y, z) to (r, θ, φ) is given by

$$\vec{r} = \begin{pmatrix} r \\ \theta \\ \varphi \end{pmatrix} = \begin{pmatrix} \sqrt{x^2 + z^2 + y^2} \\ \arccos\left(\frac{y}{\sqrt{x^2 + z^2 + y^2}}\right) \\ \arctan\left(\frac{z}{x}\right) \end{pmatrix}. \quad (\text{A.2})$$

In the lower half sphere $y > 0$ this is equivalent to:

$$\begin{pmatrix} r \\ \theta \\ \varphi \end{pmatrix} = \begin{pmatrix} \sqrt{x^2 + z^2 + y^2} \\ \arctan\left(\frac{\sqrt{x^2 + z^2}}{y}\right) \\ \arctan\left(\frac{z}{x}\right) \end{pmatrix} \quad (\text{A.3})$$

which we will be using since it is more convenient for calculating θ in the wire-plane for constant $y = y_0$.

A.1 Coordinate transform to the wire plane

For determining the fraction of a beam which hits the calorimeter wire we will need to integrate in the xz -plane in which the wire lies. Since the source intensity j_{norm} (Eq. (4.5)) is defined in terms of solid angles we will therefore need to derive an relation for projecting any solid angle onto the surface of the xz -plane where the beam intersects the wire. Based on the geometry sketched out in Figure A.1 and our axes definitions given in Eq. (A.2) we can define the *wire-plane-coordinates* as an xz -plane at constant $y = y_0$ in terms of the variables y_0, θ, φ :

$$\vec{r} = \begin{pmatrix} x \\ z \\ y \end{pmatrix} = \begin{pmatrix} y_0 \tan \theta \cos \varphi \\ y_0 \tan \theta \sin \varphi \\ y_0 \end{pmatrix}. \quad (\text{A.4})$$

The surface element of the wire-plane (the xz -plane at the location of constant $y = y_0$) is described by

$$dx dz = dS_{y_0} = \left\| \frac{\partial \vec{r}}{\partial \theta} \times \frac{\partial \vec{r}}{\partial \varphi} \right\| d\theta d\varphi. \quad (\text{A.5})$$

Calculating the partial derivatives, we obtain

$$\frac{\partial \vec{r}}{\partial \theta} = y_0 \begin{pmatrix} \frac{\cos \varphi}{\cos^2 \theta} \\ \frac{\sin \varphi}{\cos^2 \theta} \\ 0 \end{pmatrix}, \quad \frac{\partial \vec{r}}{\partial \varphi} = y_0 \begin{pmatrix} -\tan \theta \sin \varphi \\ \tan \theta \cos \varphi \\ 0 \end{pmatrix}. \quad (\text{A.6})$$

And when plugging this into Eq. (A.5) and solving the cross product we obtain

$$dx dz = dS_{y_0} \quad (\text{A.7})$$

$$= y_0^2 \frac{\tan \theta}{\cos^2 \theta} d\theta d\varphi \quad (\text{A.8})$$

$$= y_0^2 \frac{\sin \theta}{\cos^3 \theta} d\theta d\varphi \quad (\text{A.9})$$

which we can solve for an equivalence between differential solid angle $d\Omega$ and a surface in the projected xz -plane

$$d\Omega = \sin\theta d\theta d\varphi = \left(\frac{\cos^3\theta(x, z, y_0)}{y_0^2} \right) dx dz. \quad (\text{A.10})$$

This equation tells us the size of surface area in the projected xz -plane that a unit of solid angle is projected onto as a function of θ . We can substitute this expression into any integral over θ, φ in the half-sphere to return an integral over x, z in the plane into which it projects. For example, we can use it to write the normalization condition of the beam profile j_{norm} from Eq. (4.6) as

$$1 = \int_0^{\frac{\pi}{2}} \int_0^{2\pi} j_{\text{norm}}(\theta, l_{\text{eff}}) d\Omega \quad (\text{A.11})$$

$$= \int_0^{\frac{\pi}{2}} \int_0^{2\pi} j_{\text{norm}}(\theta, l_{\text{eff}}) \sin\theta d\theta d\varphi \quad (\text{A.12})$$

$$= \int_{-\infty}^{\infty} \int_{-\infty}^{\infty} j_{\text{norm}}(\theta, l_{\text{eff}}) \left(\frac{\cos^3\theta(x, z, y_0)}{y_0^2} \right) dx dz. \quad (\text{A.13})$$

Since we chose a rotationally symmetric j_{norm} model, neither the beam model nor dS_{y_0} is dependent on φ . Thus we only have to define θ in terms of the model parameters and cartesian coordinates to carry out the integration over the plane. We use the definition from Eq. (A.3):

$$\theta = \arctan \left(\frac{\sqrt{x^2 + z^2}}{y_0} \right) \quad (\text{A.14})$$

$$= \arctan \left(\frac{\sqrt{x^2 + (z_{\text{pos}} - z_0)^2}}{y_0} \right) \quad (\text{A.15})$$

with $z = z_{\text{pos}} - z_0$ defining the z coordinate in terms of the position of the z -translator z_{pos} and z_0 the offset of the z -translator zero from the beam/coordinate centerline. Thus we have defined an integral in terms of measurable quantities that we can actually carry out over the area spanned by the calorimeter wire. In Section 8.1 we use integrals of this type to calculate the fraction of particles from the beam that hit the wire, and thereby obtain the heating power we can expect to measure.

B Primary extraction equilibration and systematics

In this section, we discuss how we chose the parameters of the extraction scheme discussed in Section 8.2.1. The goals are to minimize the runtime required and the impact of systematic errors due to partial equilibration of gas flow and pressure as well as system and wire detector board temperatures.

B.1 Gas flow and pressure

In our extraction process we repeatedly switch the flow through the source on and off. This does not occur instantaneously, so we must allow for enough time for flow through the HABS to equilibrate. Knowing the flow through the source is made more difficult by the fact, that there are components of the gas system between the mass flow controller and the source. The gas system is shown in simplified form in figure 4.3. Most importantly as discussed in Section 4.1 the purifier downstream of the mass flow controller act as a capacitor for the flow of hydrogen, and must be saturated before it passes on the proper flow. For this reason, any measurement must be preceded by at least a few minutes and usually hours at the lower flows of uninterrupted flow through the hydrogen purifier, in order to fully equilibrate it. We do not show this equilibration phase, but all data shown in this thesis is preceded by a long period of flow through the source at the desired target flow. During the flow switching scheme, we then close both the mass flow controller in front of and the pneumatically actuated valve behind the purifier at the same time. This isolates the purifier at operating pressure, ensuring a swift return to full flow. Nevertheless, there is still a non-negligible time for full flow through the source to be established after switching.

To measure the flow through the source we cannot trust the flow as measured at the flow controller for the reasons above. Instead we must rely on a downstream measurement. We use a pressure gauge (PG60²⁷) attached to the source chamber, which also contains the wire detector as illustrated in Figure 4.1. Since pressure in the source chamber is a lagging indicator for the flow through the source, if pressure is equilibrated, flow must necessarily already be equilibrated as well.

In Figure B.1 we show the pressure response when switching a 1 sccm flow on and off for 10 minutes at a time. This is deliberately a longer time than the 5 minute interval we use during regular measurements, to clarify, that chamber pressure and therefore flow is fully equilibrated by the time we sample the wire detector. The sample window used for extraction is shown as an orange region in Figure B.1. We also calculate the average pressure in this window for numerical comparison to later measurements with faster switching intervals.

²⁷This is a Pfeiffer HPT 200 Gauge

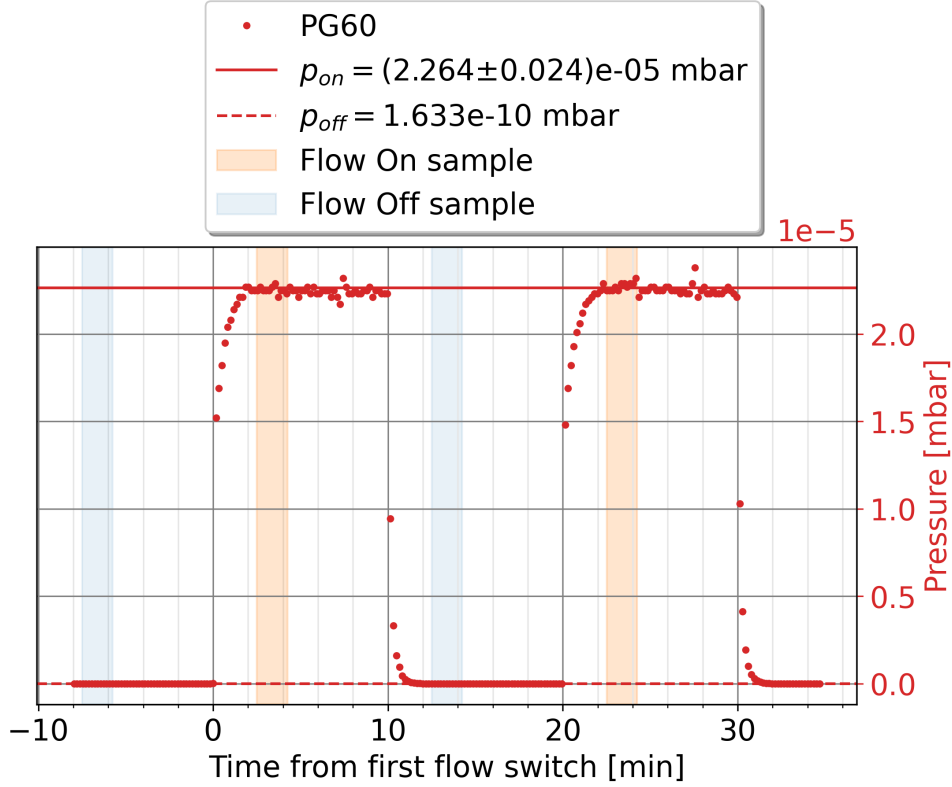


Figure B.1: Pressure in the source chamber as measured by PG60 during flow switching tests. A flow of 1 sccm of Hydrogen is turned on at 0 and 20 minutes and turned off at 10 and 30 minutes. The pressure reaches equilibrium roughly 2 minutes after being turned on and reaches a negligible relative pressure slightly faster after being turned off. The region shaded in orange indicates a window from 2.5 to 4.25 minutes after flow is switched on, and the regions shaded in blue are the equivalent time frame after flow is switched off. These are the sample window we use during normal operations as for extraction of the wire resistance change. The average of the flow on windows is marked with a red horizontal line, and the average of the flow off windows with a similar dashed line.

Faster switching intervals are desired for reducing measurement time, but also for suppressing the effect of changes in background temperature, which will be discussed in Section B.2 below. In Figure B.2 we show pressure measurements during flow switching operation using the 5 min intervals used during regular extraction for flows of 1 sccm and 0.01 sccm. Pressure was recorded in 10 second intervals and the pressure usually jumps from its baseline to about 85% of its equilibrated pressure with flow on within the time of the first 10 second polling interval after flow switching. These examples show that a 5 minute interval is sufficient to get pressure (and therefore flow) equilibration to within approximately 1% of final values within the sample windows for the flow range used in this thesis. Repeatability of the pressures reached is also approximately 1% in these examples, and is never worse than 5% in any dataset we have analyzed.

An additional conclusion from the comparison of 1 sccm and 0.01 sccm data shown here is that, after subtracting the flow off background pressure, pressure in the chamber scales linearly with flow to within 1% precision. This corroborates that the pressure measurement is a reasonable proxy for the actual flow through the source.

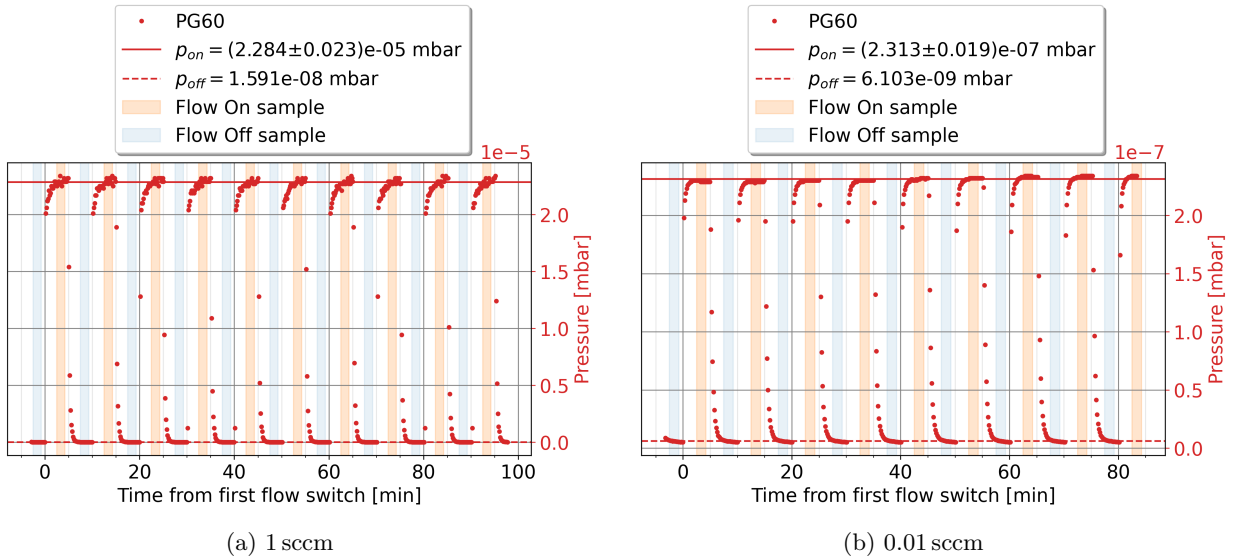


Figure B.2: Pressure plots equivalent to Figure B.1 but this time for flow switching intervals of 5 minutes at 2 different flows. Pressure data was recorded every 10 seconds. A comparison shows, that a 5 minute interval is sufficient for reproducing equilibrated pressures at 1% precision in these cases. On the right we show that at the much lower flow of 0.01 sccm reproducibility is still of similar quality and when subtracting the flow off background pressure the pressure also scales with flow to within 1%. Both these datasets are taken with the wire detector positioned fully outside of the beam at $z=20$ mm.

B.2 Detector board temperature equilibration

In this Section we will discuss efforts to mitigate indirect effects on the wire detector signal from temperature drifts in its surroundings. These are not accounted for explicitly in the net heat flow on the wire as described in Section 5.3. They are included as various background temperatures: T_{chamber} the temperature of the chamber and by simplification the gas within it, T_{board} the temperature of the wire detector PCB, and T_{HABS} the temperature of the source. In the simulated model all background temperatures (i.e. except for the wire temperature itself) are always treated as constant throughout a single simulation. Effects of feedback, such as a potential heating or cooling effect of a gas loading on the chamber and detector board are not included.

In the following we will show that reducing the flow switching interval reduces systematic errors due to inclusion of periodic background temperature changes due to gas flow. We will also propose potential ways in which one might subtract out measured background temperature changes in future analysis.

B.2.1 Detector board temperature oscillations

In Figure B.3 we once again show data from the same 1 sccm, 10 min switching interval measurement as in Figure B.1, but here we show simultaneous measurements with the wire detector, and the Pt1000 temperature sensor located on the detector board (See Figure 5.1). The wire detector positioned outside of the beam ($z_{\text{pos}} = 20$ mm) and the HABS is not heated and is therefore at approximately room temperature. We plot the resistances of both the detector wire and the Pt1000. Since both of these are used to detect changes in temperature by means of measuring their resistance, we can convert both into a measure of their temperature, which we plot as a secondary axis. For the wire, we use the average temperature as previously defined by Eq. (7.2), while for the

Pt1000 we use a standard conversion formula²⁸ to convert between R_{Pt1000} and T_{board} .

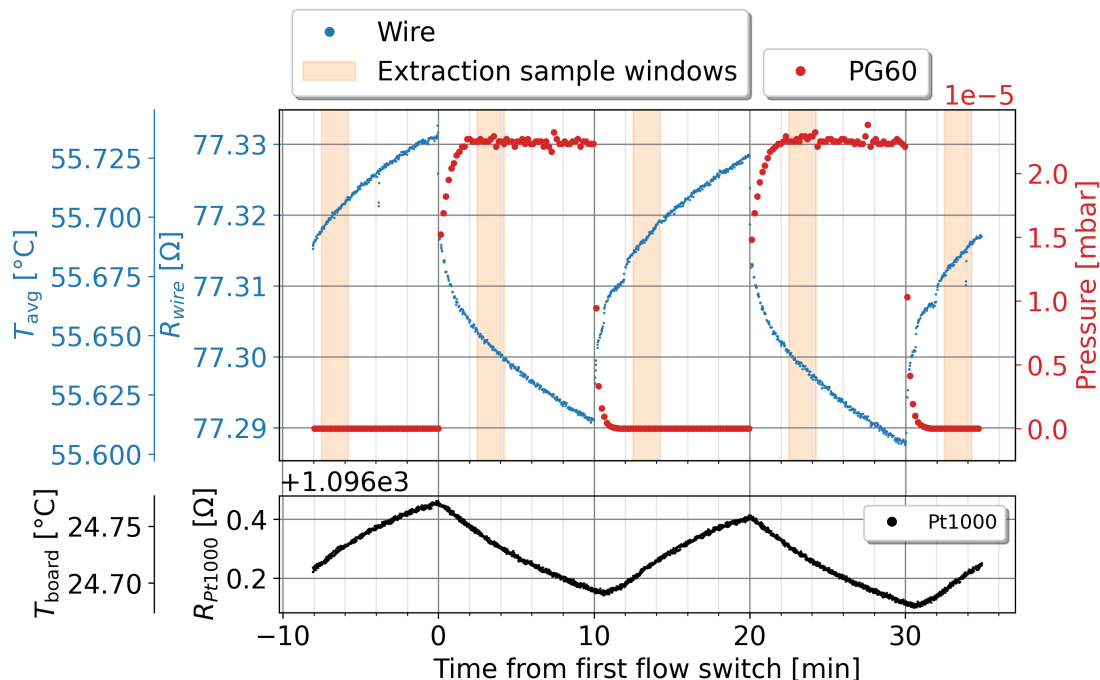


Figure B.3: Wire detector response to flow switching in 10 minute intervals at 1 sccm and the source at room temperature. Wire resistance and equivalent temperature T_{avg} as defined in 7.2 plotted with the source chamber pressure as a proxy for gas flow. In the lower third we show an additional axis showing the temperature of the wire detector PCB T_{board} as measured by a Pt1000 sensor. The key observation is, that the wire and board temperatures continue changing in phase with each other long after a stable chamber pressure is established.

In this situation, our model expects the only direct effect of turning the beam on should be an increase in background pressure, which in turn linearly increases cooling due to $P_{\text{bkgd.gas}}$ (See Eq. 5.43), lowering the wire temperature. In Figure B.3 we see this anti-correlation of pressure and wire resistance, which causes an initial fast change in wire temperature when flow is switched.

However, we also see an additional slower long term trend of both wire and Pt1000 resistance which persists the full 10 minute interval beyond the equilibration of chamber pressure. We interpret this as cooling effects either due to or at least correlated with the gas pressure, which do not directly affect the wire, but instead its surroundings such as the detector board as measured by the Pt1000 and potentially also the chamber walls, the temperature of which is not measured here. In any case the changes in T_{board} occur much slower than the direct effects on the wire, with equilibration not reached within the 10 minute intervals. Changes in the temperature of the wire's surroundings, would in turn change the equilibrium temperature of the wire due to the effects of $P_{\text{conduction}}$, P_{rad} and $P_{\text{bkgd.gas}}$, that are in various ways related to the temperatures of the wire's surroundings (see Section 5.3).

Simply waiting for full equilibration of T_{board} potentially for as much as an hour per measurement is not a good option for a number of reasons. Firstly, including long term equilibration, which is evidently not correlated with gas flow as measured by the chamber

²⁸According to IEC 751: For the range -200°C to 0°C : $R(T) = R_0[1 + A \cdot T + B \cdot T^2 + C(T - 100^{\circ}\text{C})T^3]$ and for the range 0°C to 850°C : $R(T) = R_0[1 + A \cdot T + B \cdot T^2]$ with $A = 3.9083 \cdot 10^{-3} (^{\circ}\text{C})^{-1}$, $B = -5.775 \cdot 10^{-7} (^{\circ}\text{C})^{-2}$, $C = -4.183 \cdot 10^{-12} (^{\circ}\text{C})^{-4}$, and $R_0 = 1000 \Omega$ the Resistance at $T = 0^{\circ}\text{C}$

pressure, is not the goal of our measurement. We care principally only about the effect of the beam on the wire; everything else is a nuisance effect which we aim to removed. Secondly, since we want to use the extraction process to remove non-periodic background temperature changes as well, waiting for full equilibration of T_{board} means unrelated changes in background temperature which regularly cause changes far in excess of the periodic ≈ 0.08 K changes seen in Figure B.3 are much harder to account for. Finally waiting for full equilibration stretches measurements to prohibitive lengths, meaning fewer measurements can be performed with the same setup.

B.2.2 Shorter 5 minute intervals at 1 sccm

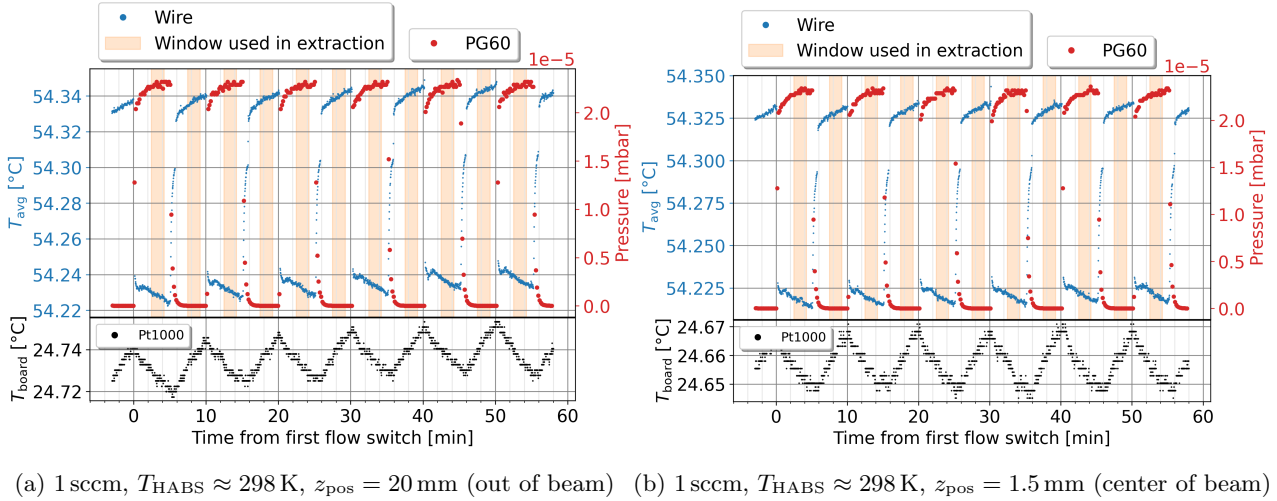


Figure B.4: Flow switching in 5 min intervals at 1 sccm and the source at room temperature K with the detector placed at 2 different z -positions. The plots show simultaneous measurements of wire and board temperatures and chamber pressure as a proxy for gas flow.

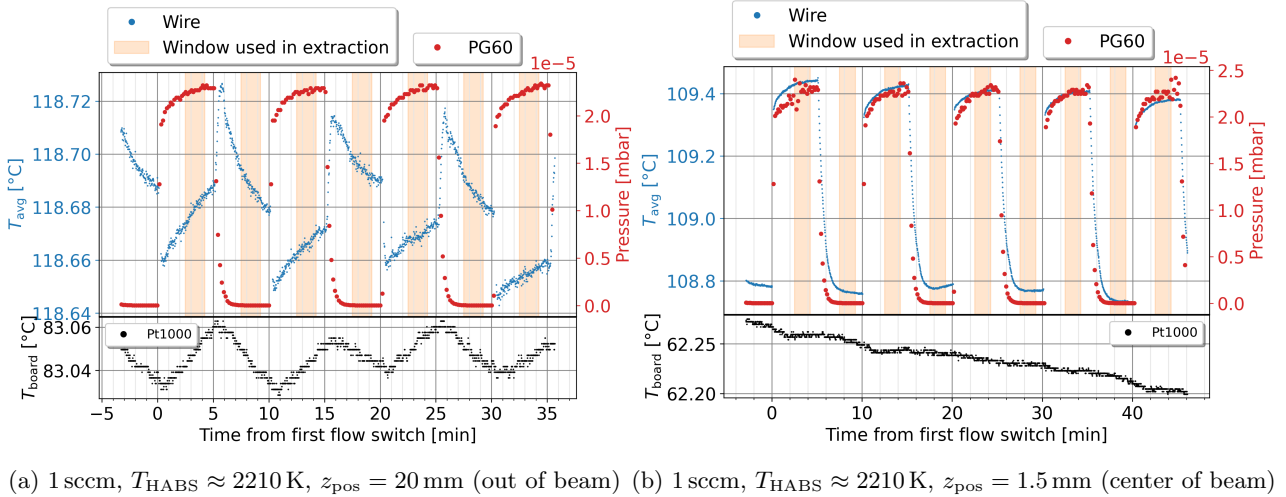


Figure B.5: Flow switching in 5 min intervals at 1 sccm and the source at 2210 K with the detector placed at 2 different z -positions. The plots show simultaneous measurements of wire and board temperatures and chamber pressure as a proxy for gas flow.

Figure B.4 shows changes in both wire and board both for 1 sccm flow switching with

a room temperature source. Of these Figure B.4a shows entirely equivalent settings as shown in Figure B.3 except that the flow switching interval is shortened to 5 minutes. Shortening the flow switching reduces the oscillations in board temperature. For equivalent settings of 1 sccm of flow with the source at room temperature and the wire positioned out of the beam ($z = 20$ mm), oscillations in T_{board} are reduced from ≈ 80 mK for 10 minute switching intervals to ≈ 20 mK for 5 minute switching, corresponding to an induced change in wire resistance ΔR_{wire} of ≈ 23 m Ω and ≈ 6 m Ω respectively. Using the calibration function $k = \frac{dP}{dR} \approx 7.2$ [$\mu\text{W}/\Omega$] as determined in Section 7.3 we can also express this systematic error in terms of the heating power measured by the wire of ≈ 170 nW Ω and ≈ 40 nW Ω respectively.

The change in magnitude of the board temperature oscillations suggests a super-linear scaling of the oscillations with flow switching interval length. This is consistent with a thermal equilibration process, as for such an exponential process, the rate of temperature change is larger, when the target equilibrium is further away. A longer switching interval gives more time for the system temperature to change, such that upon switching the flow back the target equilibrium is then a larger temperature change away, which increases the rate of change in temperature. Multiplying a faster rate of change, with a longer time for temperature change results in a superlinear increase in the amplitude of the temperature oscillations. Keeping the flow switching intervals as short as possible is therefore an effective way of suppressing this systematic error. In fact it may be reasonable to shorten the interval even beyond the 5 minutes we currently use in future if this effect is deemed to be of a relevant size.

A comparison to the extracted measured powers for 1 sccm shown in Figure C.1e shows that the maximum measured powers are ≈ 1.3 μW when the wire is located centrally under the source at 2210 K. This means the induced equivalent heating effect of ≈ 40 nW Ω due to the board temperature changes are approximately 3% of the maximum signal. For the derived quantities such as the absolute flow limit the effect size compared to the maximum value is the relevant quantity.

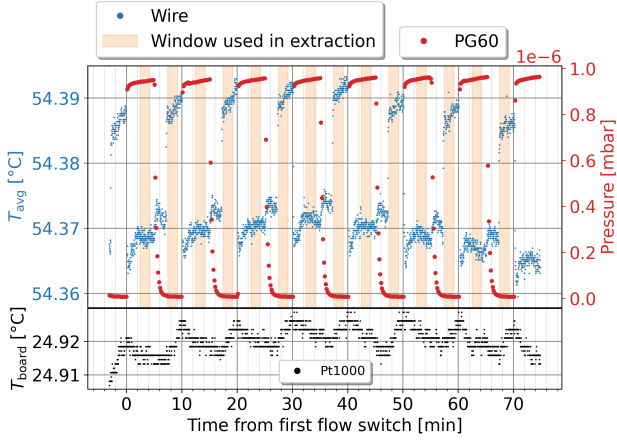
For the individual extracted powers, the relative effect can of course be much larger for those data points, where only small or no net heating is otherwise measured. See for example Figure B.5a, where the temperature drifts induced by the board temperature changes are of equivalent size to the nearly instantaneous change in wire temperature when flow switching. Note also, that in this case with the source at 2210 K the oscillation in board temperature is actually phase shifted by half a period compared to the measurements with the source at room temperature. The flow on / high pressure segments now have increasing board temperature rather than decreasing ones. While we cannot establish this with certainty, this may be caused by the additional heat transported into the chamber and to the board by the hot and partially dissociated beam. The measurement at $z_{\text{pos}} = 20$ mm puts the wire outside of the line of sight of the source capillary, however the detector board is actually fully inserted in this position, receiving the maximum heating from the source. This is also the reason, why the baseline temperatures of both the wire and the board are highest here (at 118.7 K and 83.05 K respectively). Figure B.5b shows an equivalent measurement with the source hot and the wire centered under the source ($z_{\text{pos}} = 1.5$ mm). Here we see, that the previous board temperature oscillations of ≈ 20 mK are small compared to the maximum heating signals of ≈ 600 mK $\hat{=} 220$ m Ω $\hat{=} 1.3$ μW produced by the 1 sccm beam acting on a centered wire. The T_{board} measurements in this particular case are also not dominated by periodic oscillations, but by a longer term background trend of ≈ 70 mK over the time range shown. The oscillations in this case are also at most ≈ 10 mK. It is not unusual for background trends to be larger than periodic oscillations, however non-periodic trends are well accounted for by the extraction process

which fits the background with a quadratic function. The previous examples shown here were deliberately selected from the available datasets, for conditions, where the periodic flow induced oscillations are dominant. Examples shown in following sections are often more dominated by non-periodic background trends.

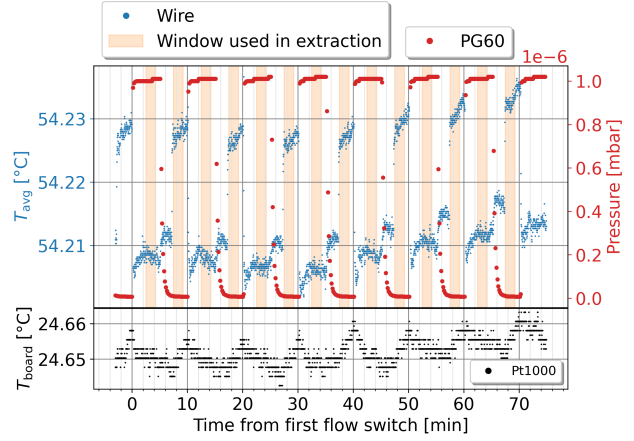
For the extraction process as presented in Section 8.2.1 we simply accept the $\approx 3\%$ systematic error on extracted heating power as small enough to be neglected for the conclusions we draw in this thesis. However in the following sections we briefly outline ways in which this systematic might be further suppressed in future investigation.

B.2.3 Equivalent sample measurements at lower flows

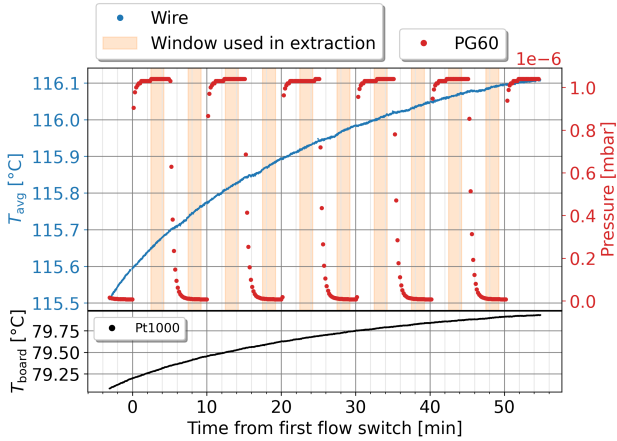
In this section we show raw data with equivalent settings as in the previous section, except at lower flows. This is to show, that periodic oscillations decrease in magnitude for lower flows, but slower than linearly with flow. The 0.05 sccm examples in Figure B.6 still show oscillations in T_{board} with an amplitude of ≈ 5 mK and the 0.2 sccm examples in Figure B.7 show oscillations with amplitudes of up to 20 mK. At this point we do not attempt to explain this relationship, but we encourage follow up investigations in this regard if suppressing this systematic becomes a priority.



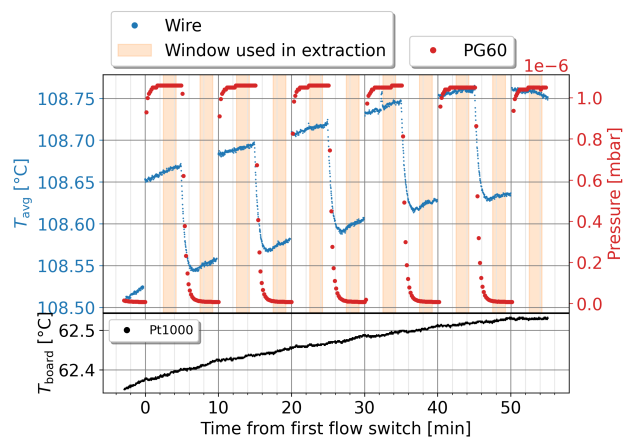
(a) 0.05 sccm, $T_{\text{HABS}} \approx 298 \text{ K}$, $z_{\text{pos}} = 20 \text{ mm}$ (out of beam)



(b) 0.05 sccm, $T_{\text{HABS}} \approx 298 \text{ K}$, $z_{\text{pos}} = 1.5 \text{ mm}$ (center of beam)

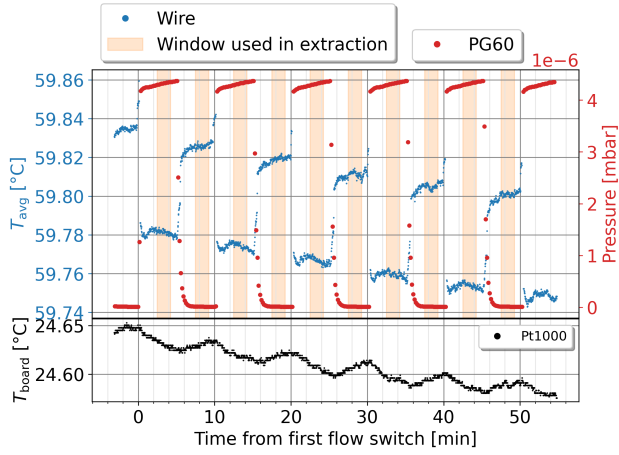


(c) 0.05 sccm, $T_{\text{HABS}} \approx 2210 \text{ K}$, $z_{\text{pos}} = 20 \text{ mm}$ (out of beam)

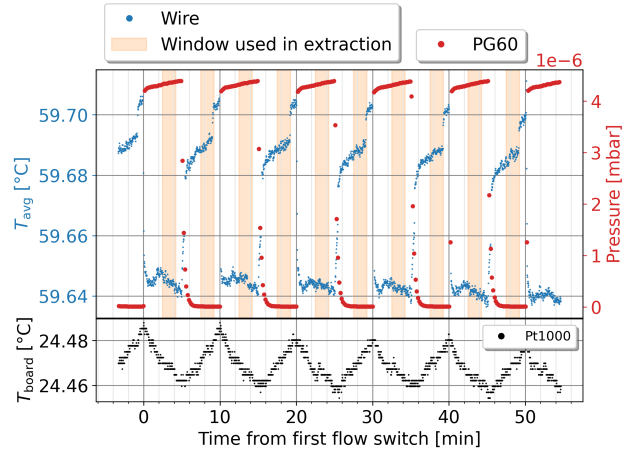


(d) 0.05 sccm, $T_{\text{HABS}} \approx 2210 \text{ K}$, $z_{\text{pos}} = 1.5 \text{ mm}$ (center of beam)

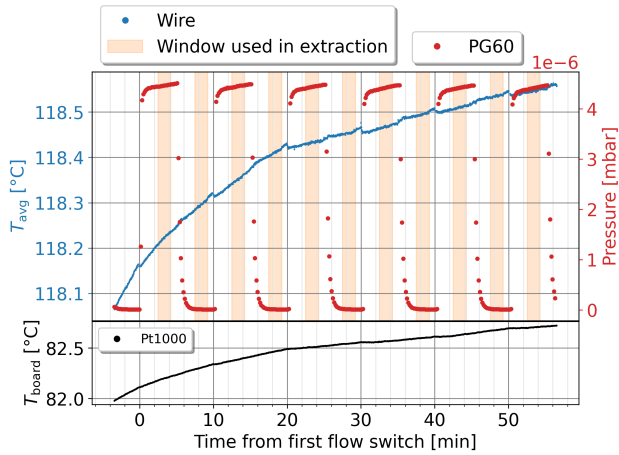
Figure B.6: Results of flow switching in 5 min intervals at 0.05 sccm. The plots show simultaneous measurements wire and board temperatures and chamber pressure as a proxy for gas flow.



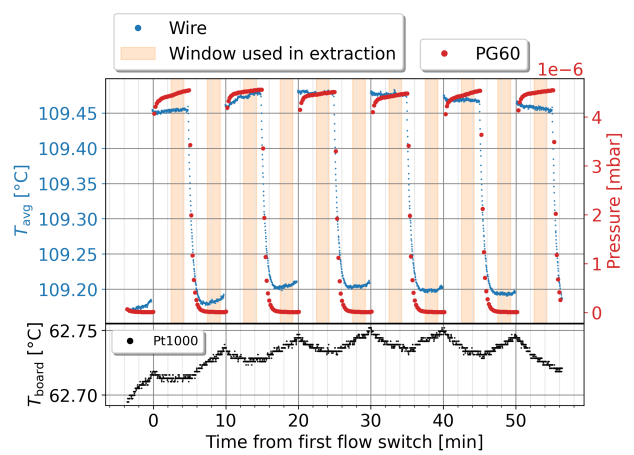
(a) 0.2 sccm, $T_{\text{HABS}} \approx 298 \text{ K}$, $z_{\text{pos}} = 20 \text{ mm}$ (out of beam)



(b) 0.2 sccm, $T_{\text{HABS}} \approx 298 \text{ K}$, $z_{\text{pos}} = 1.5 \text{ mm}$ (center of beam)



(c) 0.2 sccm, $T_{\text{HABS}} \approx 2210 \text{ K}$, $z_{\text{pos}} = 20 \text{ mm}$ (out of beam)



(d) 0.2 sccm, $T_{\text{HABS}} \approx 2210 \text{ K}$, $z_{\text{pos}} = 1.5 \text{ mm}$ (center of beam)

Figure B.7: Results of flow switching in 5 min intervals at 0.2 sccm. The plots show simultaneous measurements wire and board temperatures and chamber pressure as a proxy for gas flow.

B.3 Further Background temperature change mitigation strategies

In this Section we briefly discuss potential mitigation strategies for the effects of background temperature changes (as measured by T_{board}) on the wire. The showcase below should be treated as exploratory rather than fully rigorous. We do not adopt any of these for the analysis in this thesis, but invite future work to explore them further if required.

B.3.1 Subtraction schemes

A possible way to eliminate the effect of board temperature changes on the wire detector might be to simply subtract T_{board} from the wire temperature T_{avg} . Such a scheme requires, that both temperatures are accurately calculated, and that changes in T_{board} are a good proxy for all external temperatures, i.e. both T_{chamber} and T_{board} in our model, as we do not have an independent record of T_{chamber} for the measurements presented. Under the assumption that all external temperatures change by a small amount ($\lesssim 1$ K) we would expect the wire temperature to change by the same amount.

It turns out however, that a simple subtraction of T_{board} does not yield best results, and instead

$$\Delta T = T_{\text{avg}} - C \cdot T_{\text{board}}, \quad (\text{B.1})$$

with a parameter value of $C = 0.77$ yields best results in terms of producing a quantity that changes in proportion to the pressure in the source chamber. In Figure B.8 we once again show this with the same 10 minute flow cycling example at 10 sccm and the source at room temperature. Since the source and chamber are cold compared to the wire, a higher pressure leads to a lower wire temperature, but otherwise this partial subtraction of T_{board} produces excellent (anti-)correlation between ΔT and source chamber pressure, with flat plateaus in regions of stable pressure.

The proportionality factor of $C = 0.77$ has been previously empirically seen in Figure 7.5 for the base resistance of the wire in relation to T_{board} . It is plausible, both could be explained by the same underlying physical cause, as in both cases R and T are connected via the same relation given by Eq. (7.10):

$$\Delta R_0 = R_0(T = 25^\circ\text{C}) \cdot (1 + a \cdot \Delta T),$$

where altering either the temperature coefficient of resistivity a or the presumed wire temperature T by a factor $C = 0.77$ would make the equation mathematically compatible with the observations. We do not however have a reliable physical explanation for why this might be appropriate.

In Figure B.9 we show an example of the subtraction method applied to data taken with the source at ≈ 2200 K switching with our minimum reachable flow of 0.002 sccm. This example illustrates that under favorable conditions, the subtraction method can be used to remove background trends many times larger than the signal we are looking to resolve. In this case the beam switching signal is less than 10 mK, while the board temperature changes by more than 250 mK. It should be noted that the extraction scheme as presented in Section 8.2.1 is also able to remove the non-periodic temperature background trend to extract a resolvable signal. Indeed, the result of this extraction based on the same raw data as shown here is presented in Figure C.1a. However the subtraction method as presented here has the advantage, that it could be applied in an on-line fashion to data as it is collected, rather than as a post data taking analysis step. This would be useful as instant feedback when working with the atomic beam in the lab.

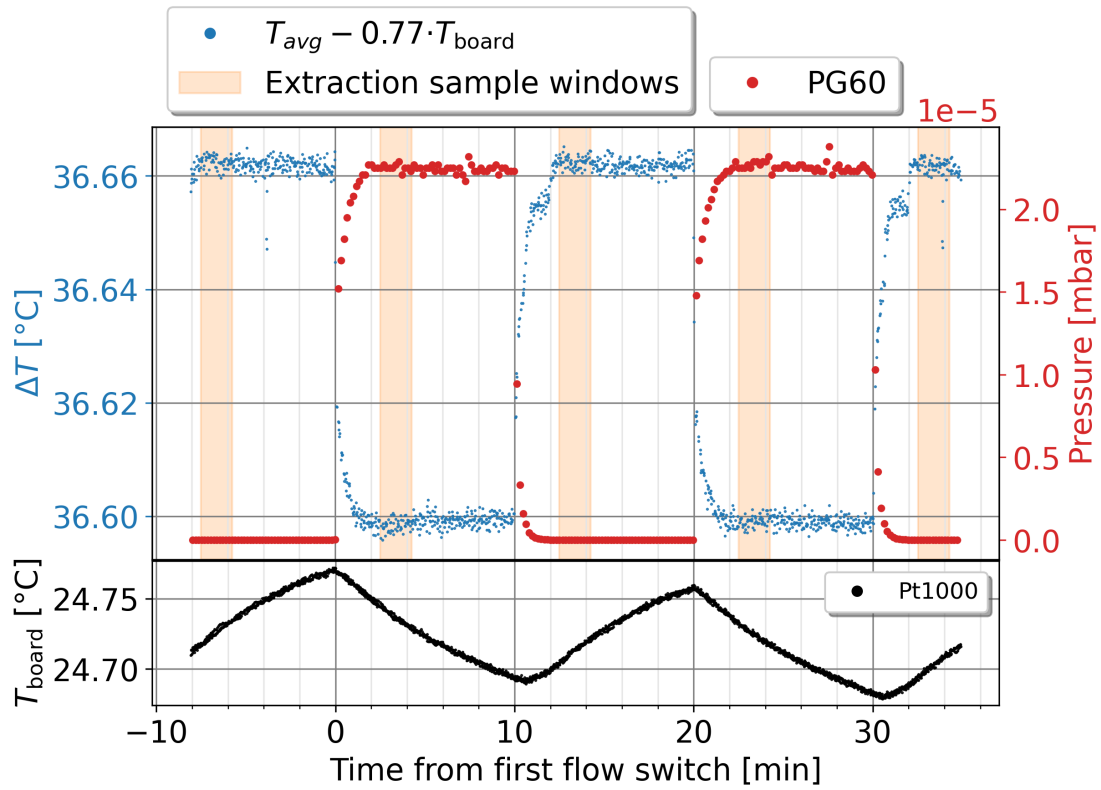


Figure B.8: Wire detector response to flow switching in 10 minute intervals at 1 sccm and the source at room temperature. The wire response is expressed in terms of the difference to the detector board temperature as defined in Eq. (B.1). In the lower third we show an additional axis showing the temperature of the wire detector PCB T_{board} as measured by a Pt1000 sensor. After subtracting out the board temperature modified by a factor of 0.77 the wire detector response mirrors the pressure data as expected, with stable plateaus where the pressure is also stable.

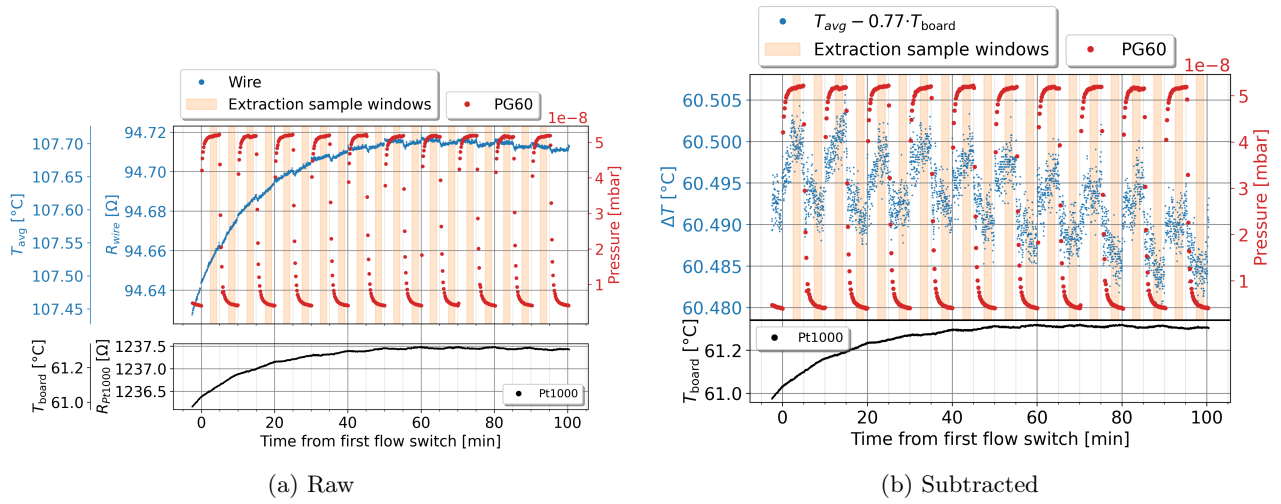


Figure B.9: Wire detector response to flow switching in 5 minute intervals at 0.002 sccm, $T_{HABS} \approx 2200$ K, $z_{pos} = 0$ mm. On the left we present the raw data and on the right the modified temperature difference after subtraction of the detector board temperature as defined in Eq. (B.1). This example illustrates that very small periodic beam signals can be isolated by subtracting out much larger trends in the background temperature as measured on the board.

Not all effects are equally well subtracted out however. It seems, that slow processes are well removed by the subtraction scheme, but fast changes in T_{board} are usually not entirely removed when subtracting from the wire temperature T_{avg} .

An example for 1 sccm flow switching with a hot source is shown in Figure B.10. Around the 10 minute mark there is a sharp increase in both board and wire temperatures, and even after subtraction, the baseline temperature in ΔT remains bumpy. A plausible explanation for this is, that fast changes in the thermal environment of the vacuum chamber affect the wire faster than the board and attached Pt1000. This would make sense given the much smaller thermal mass of the wire and simulated wire thermalization time constant of $\tau \approx 0.475$ s (See Section 5.4.1). By contrast we never see the T_{board} make any temperature changes that are completed less than 5 minutes. We propose a possible solution to this problem in the next section.

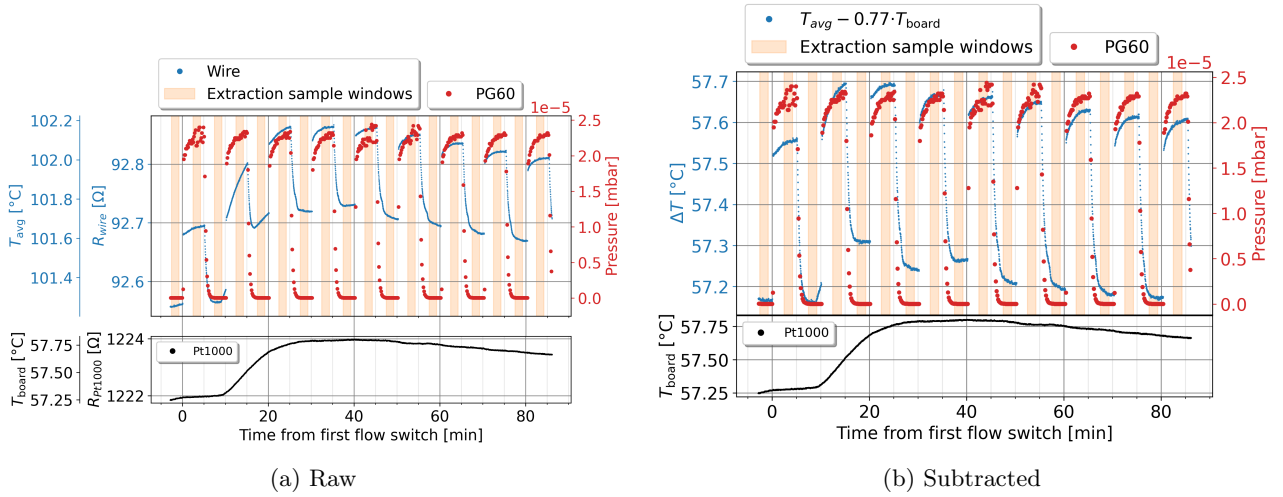


Figure B.10: Wire detector response to flow switching in 5 minute intervals at 1 sccm, $T_{\text{HABS}} \approx 2210 \text{ K}$, $z_{\text{pos}} = -6 \text{ mm}$. On the left we present the raw data and on the right the modified temperature difference after subtraction of the detector board temperature as defined in Eq. (B.1). This example illustrates that fast changes in temperature cannot always be cleanly removed by this subtraction process.

B.3.2 Deconvolution Subtraction

Newtons law of cooling results in thermal equilibration processes which can be described as exponential approaches to a target temperature with a time constant τ . This suggests, that the observation that fast temperature changes seem to be smeared out in T_{board} in comparison to the concurrent effect on the wire temperature, may be explainable by that fact that they are both approaching a new equilibrium in response to the same stimulus, but with differing time constants.

The smoothing of functions with exponential filters is a common problem in signal analysis. Thankfully this means that existing literature contains solutions we can adopt. The modification of a function with an exponential filter is in fact exactly reversible if the time constant τ is known. Kalabet 2019 [58] shows a proof, that any function $F(t)$ convoluted with the exponential function $E(t) = \{e^{-t/\tau} | t \geq 0, E(t) = 0 | t < 0\}$ can be fully recovered from the convoluted form $F(t) * E(t)$ by adding the derivative multiplied with the time constant:

$$F(t) = F(t) * E(t) + \tau \cdot \frac{d}{dt}(F(t) * E(t)). \quad (\text{B.2})$$

In our case we can identify $F(t) * E(t) = T_{\text{board}}(t)$ as the time series of board temperature measurements, where $E(t)$ is the natural smoothing due to the thermalization time constant and $F(t) = T_{\text{board, deconv}}(t)$ is the time series of board temperatures, if it instantly responded to the external temperature change (i.e. $\tau \rightarrow 0$).

We calculate the wire temperature time series after subtraction of the deconvoluted board temperature time series as:

$$\begin{aligned} \Delta T_{\text{deconv}} &= T_{\text{avg}} - F(t) \\ &= T_{\text{avg}} - T_{\text{board, deconv}}(t) \\ &= T_{\text{avg}} - \left(T_{\text{board}}(t) + \tau_{\text{board}} \cdot \frac{dT_{\text{board}}(t)}{dt} \right) \end{aligned} \quad (\text{B.3})$$

The challenges remaining for the deconvolution is then, that the time constant of the board as sampled by the Pt1000 is unknown a priori. This means we are trading one

free parameter in the form of C for another in the form of τ . In principle this might be measured by deliberately applying a known heat source in a future experiment. For the results presented here we have chosen $\tau_{\text{board}} = 1.7$ min based purely on the visual stability of the baseline wire temperature after subtraction of the deconvoluted board temperature signal. We implicitly treat the wire detector as having instant temperature $\tau_{\text{wire}} = 0$, which is a reasonable approximation, since τ_{wire} as determined via simulation Section 5.4.1 is at least 100 times shorter than τ_{board} and also shorter than the sampling time interval of 1 s.

The deconvolution requires the calculation of a local derivative, this process is extremely sensitive to noise on the $T_{\text{board}}(t)$ time series. The noise penalty is acceptable for large signals as they are produced by intense beams such as 1 sccm, but it is often prohibitive for less intense beams of fluxes below 0.05 sccm for current data quality provided by the Pt1000 measurement.

In Figure B.11b We show an example of the deconvolution subtraction applied to the same 1 sccm dataset which yielded unsatisfactory results in the direct subtraction in the previous section.

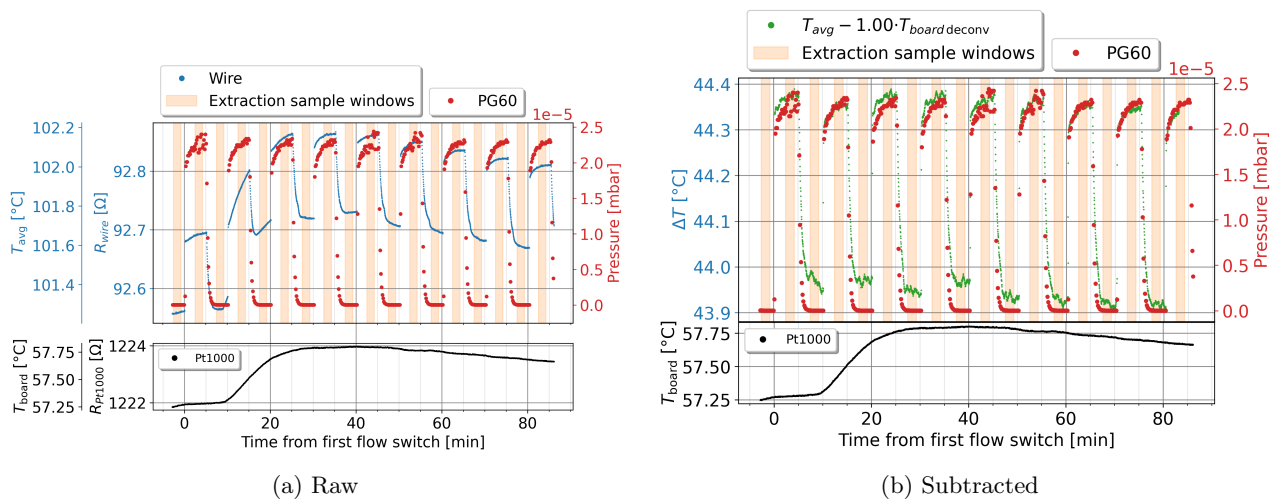


Figure B.11: Wire detector response to flow switching in 5 minute intervals at 1 sccm, $T_{\text{HABS}} \approx 2210$ K, $z_{\text{pos}} = -6$ mm. On the left we present the raw data and on the right the modified temperature difference after deconvolution based subtraction of the detector board temperature as defined in Eq. (B.3). This example illustrates that fast changes in temperature can be more effectively removed when subtracting the deconvoluted board temperature time series.

In this example a rapid change of T_{board} of comparable size to the beam signal at about 600 mK each is subtracted in deconvoluted from the wire temperature time series. The result is a ΔT signal in which the change in which the large temperature change at the 10 minute mark is essentially invisible, and in which the baseline temperature has a residual drifts of less than 50 mK over more than 80 minutes of measurement.

While not every dataset we tested with this method showed equally impressive results, we nevertheless recommend further investigation into deconvoluted subtraction in future analysis campaigns. Results might potentially be further improved if time series of chamber temperature sensors were also available and incorporated.

C Extracted data for all flows

This section compiles the measured heating power after primary extraction (Section 8.2.1) for all available datasets. Z-scan measurements were taken for the following flows: 0.002 sccm, 0.01 sccm, 0.05 sccm, 0.2 sccm, 1 sccm, and 10 sccm. For all of these flows a dataset was taken at the highest regularly achievable source temperature $T \approx 2200$ K. Additional lower temperature datasets at $T \approx 1250$ K and $T \approx 300$ K were taken at 0.05 sccm, 0.2 sccm, 1 sccm, and 10 sccm, and another 3 datasets were taken at 1 sccm at intermediate temperatures.

C.1 data

In Figure C.1 we plot the neat heating power measured after primary extraction for all available z-scans across the beam. In general beams at lower flows produce smaller heating effects and are more centrally concentrated. At 0.002 sccm and 2200 K we measure only a 30 nW difference between a centered measurement at $z_{pos} = 1.5$ mm and the minima at the edges, while at 10 sccm the same difference just over $5 \mu\text{W}$. In the case of the lowest 2 flows, we did not prioritize getting follow up measurements at non-dissociating beam temperatures due to the low Signal-to-Noise Ratio (SNR) of the raw data at these flows. Where available however there we can see a systematic offset between the $T \approx 298$ K room temperature baseline measurement and the nominally out-of-beam background measurements at $z_{pos} = 20$ mm at 2200 K. The model we use does not predict such an offset in a region where there should not be any direct beam effects. We can therefore not properly account for this trend. In the range observed 0.05 sccm to 10 sccm there is generally an offset between $P_{\text{meas}}(z_{pos} = 20 \text{ mm}, T \approx 2200\text{K})$ and $P_{\text{meas}}(z_{pos} = 20 \text{ mm}, T \approx 298\text{K})$ that is roughly one fifth of the difference between the centered maximum and the edge at 2200 K, or expressed as an equation:

$$\begin{aligned} & P_{\text{meas}}(z_{pos} = 20 \text{ mm}, T \approx 2200\text{K}) - P_{\text{meas}}(z_{pos} = 20 \text{ mm}, T \approx 298\text{K}) \\ & \approx \frac{1}{5} (P_{\text{meas}}(z_{pos} = 1.5 \text{ mm}, T \approx 2200\text{K}) - P_{\text{meas}}(z_{pos} = 20 \text{ mm}, T \approx 2200\text{K})). \end{aligned} \quad (\text{C.1})$$

While none of the datasets is perfectly symmetrical, it is worth highlighting that the 10 sccm dataset at 2200 K is by far the worst example. In part due to this asymmetry, it does not agree well with the beam shape model used in this thesis as can be seen in Figure D.1f. Additionally the 10 sccm dataset at 1277 K anomalously reports larger heating than the 2200 K dataset at around $z_{pos} \approx 15$ mm. This is difficult to explain within the paradigms set out in this thesis. We must therefore concede, that within the scope of this thesis we have not managed to model beam effects at flows larger than 1 sccm. This may be a real effect, insofar that the model we adapted from Tschersich [41] in Section 4.1 breaks down, if the gas flow in the capillary does not become transparent for a significant length at the end of the capillary. As we have been unable to resolve these issues, we have not included the 10 sccm datasets in the 3-temperature-point analysis shown in the main portion of this thesis. Additional measurements would be required to say anything with great certainty in this high flow regime.

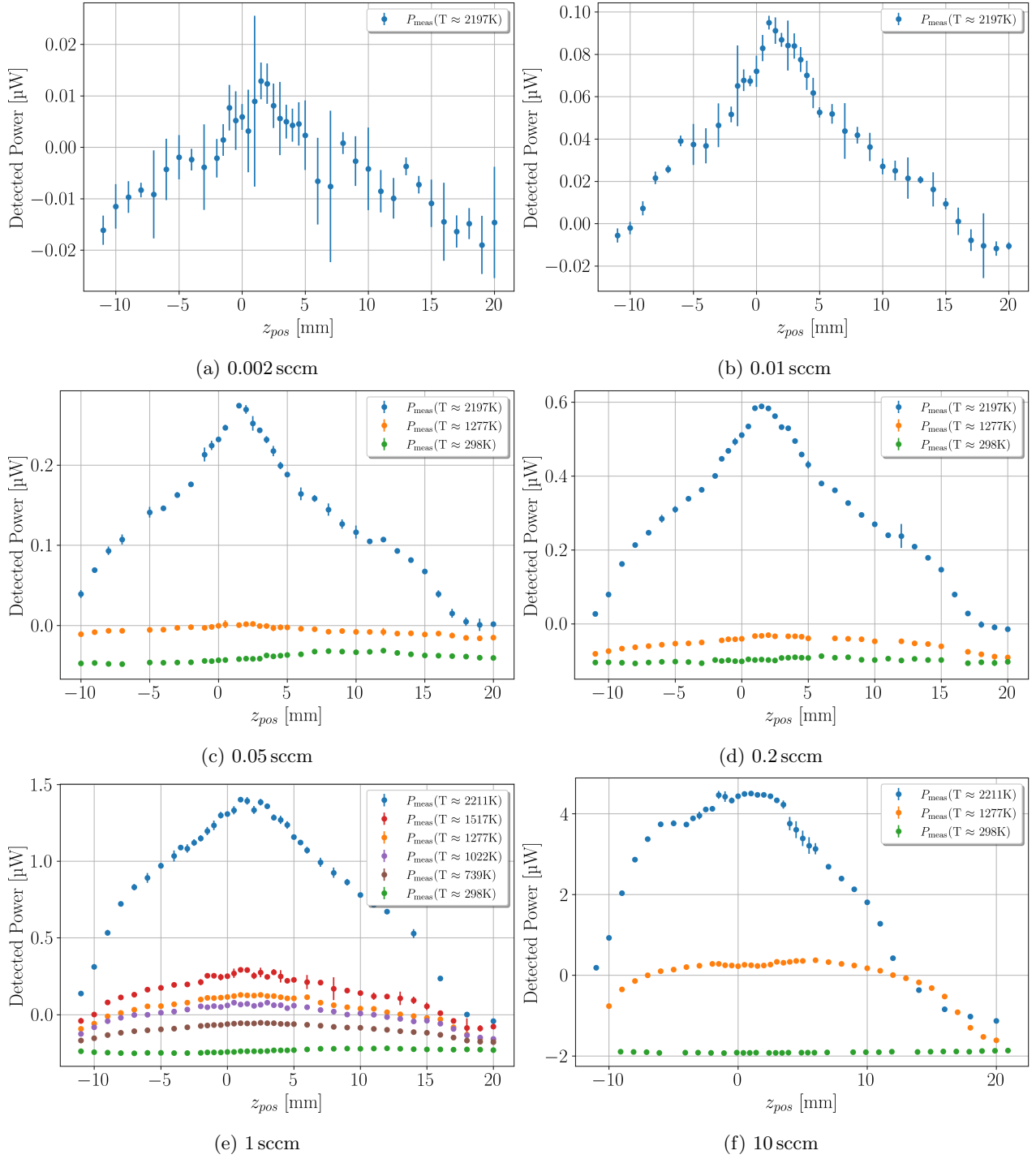


Figure C.1: Power detected on the wire after primary extraction (P_{meas}) at multiple flows as indicated by the sub-captions for a range of source temperatures. All datasets below 1600 K are below the dissociation threshold and measure a pure H_2 beam. These data sets are then used in the secondary extraction procedure, to yield the effect of recombining atoms on the surface. Negative detected powers indicate a net cooling of the wire, which is identified with the convection cooling due to gas pressure in the detector chamber ($f_{\text{bkgd.gas}}$).

D 1-temperature-point method for beam analysis

In this section we will introduce the *1-temperature-point* (1-T-P for short) method for beam shape analysis as an alternative to the 3-temperature-point (3-T-P) method we use as the mainline method in this thesis (see Section 8.4.1). As the name suggests in this method we need just a single z-scan at a single temperature setpoint to perform beam shape analysis. This is done by simply skipping the secondary extraction step described in Section 8.2.2 and applying beam model fits directly to the data after primary extraction.

The benefit of this method is chiefly, that we can apply it where we either could not spend the time on setup to acquire multiple datasets, or where data quality or deficiencies in data compliance with model assumptions make secondary extraction behave poorly. The tradeoff is, that without secondary extraction, we are assured that the signal we are fitting is not entirely caused by heating due to recombination of atomic hydrogen (P_{rec} and still contains contributions due to the kinetic energy the atoms and molecules impart to the wire due to their temperature ($P_{\text{beam-gas}}$ and P_{bkgd}). This problem is proportionally larger for beams with a low atom fraction, as P_{rec} is then a smaller portion of the primary signal. As evident from Figure 8.15 this means measurements at large flows are especially untrustworthy when conducted in this manner.

Our primary motivation for performing this analysis is to extend the range of flows for which we have sufficient data to perform analysis on α_{dissoc} and l_{eff} over flow, such as was shown in Figures 8.15 and 8.14 using the 3-T-P method. Of course we caution that any conclusions based on this analysis must be dampened by the fact, that skipping secondary extraction makes the fitted model inherently deficient.

In Figure D.1 we show the fits to 1-T-P data when always using the highest available temperature datasets shown in Figure C.1. Then in Section D.1 we discuss the extended trends in l_{eff} and in Section D.2 we do the same for the atom count lower limits derived from the 1-T-P method.

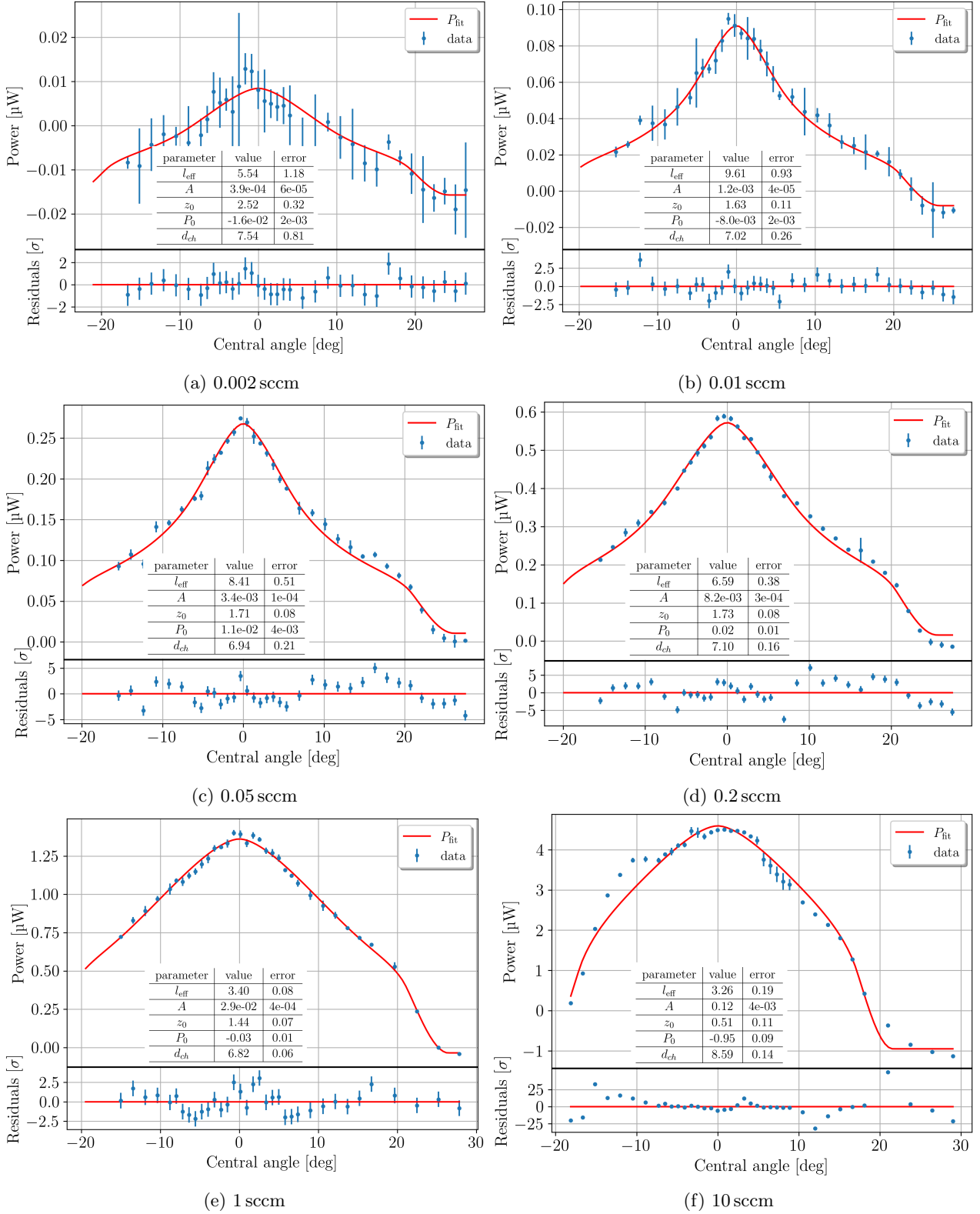


Figure D.1: Fits using the 1-T method to the 2200 K datasets at 6 different flows as indicated by the sub-captions. The power values displayed are the result of primary extraction. No secondary extraction for P_{rec} was performed, and therefore we know that the model is insufficient.

D.1 Effective length

In Figure D.2 we repeat an equivalent plot from Section 8.5, but this time with the inclusion of the 1-T-P fit results shown in Figure D.1. For data points where both sets of analyses are available results are similar, though not equivalent. No 3-T-P results for 10 sccm are shown, as the data has proved incompatible with the model, due to asymmetry and stronger than expected heating due to hot non-dissociated H_2 at large angles. The 0.002 sccm datapoint is the strongest outlier from the trend of increasing l_{eff} with decreasing flow. We believe this is likely to be due to the low SNR of this dataset, which means a wide range of parameters can describe the dataset with similar fit goodness. In fact with earlier less sophisticated models that did not include the "penumbra" shadowing effects described in Section 4.1.2 this datafit was often alternatively yielding values of $l_{\text{eff}} \approx 12$.

The 1-T-P method is only meant to showcase the best we can do with the more limited datasets we acquired in the high and low flow regimes. We encourage follow up studies at these flows taking more data to enable three or more temperature dataset analyses. No firm conclusions should be drawn on the basis of the 1-T-P analysis.

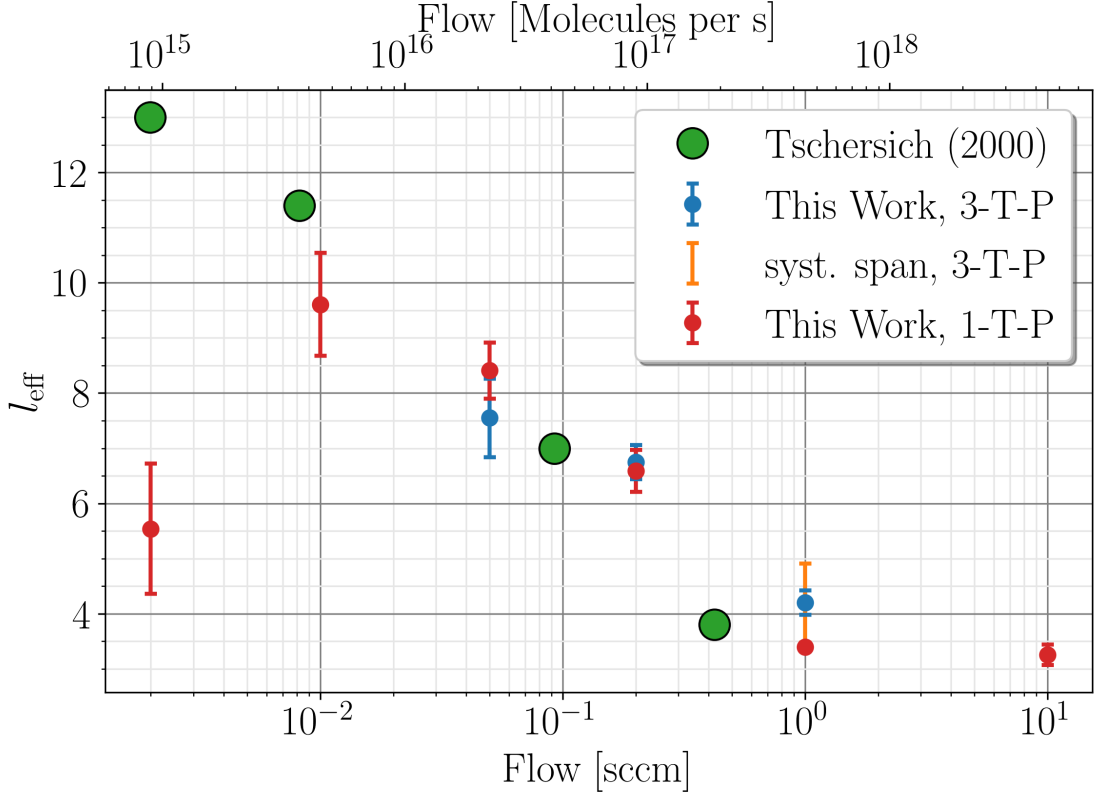


Figure D.2: Fit parameter l_{eff} for the atomic hydrogen portion of the beam at various flows using both the three- and one-temperature-point methods described in this work compared to values from Table I in Tschersich et al. (2000) [40]. No error estimation is available for the sourced l_{eff} values. Plots showing fits in this work for 0.05 sccm and 0.2 sccm are available in Section 8.4.3. The orange error bar is the span of l_{eff} when datasets at different temperatures are used to determine P_{H_2} (see Section 8.4.2) for details). The red data points use the 1-T-P simplified analysis method using just the ≈ 2200 K dataset for each flow.

D.2 Absolute atom count limits based on the 1-T-P method

This section shows identical plots of α_{dissoc} and atom count over flow as Section 8.6, with the addition of a comparison to results obtained with the 1-T-P method. Most importantly we point out, that the 1-T-P method produces larger dissociation fractions and atom counts than the 3-T-P method where available. This fits expectations perfectly, since the difference between the methods is skipping secondary extraction, which has the primary purpose of subtracting out the heating effect of leftover hot molecular gas $P_{\text{beam_gas}}$ on the wire. The primary extracted power is therefore universally higher than the secondary extracted power. The 3-T-P method fulfills its purpose of yielding a conservative lower limit for the value of the dissociation fraction.

Since $P_{\text{beam_gas}}$ is proportionally higher at low dissociation fractions, we expect the difference between the 1-T-P and 3-T-P methods to be larger at higher flows. Within the limited scope of the 3 flow point comparison at 0.05 sccm, 0.2 sccm, and 1 sccm this expectation is confirmed. We may therefore carefully assume that the two low points at 0.01 sccm and 0.002 sccm have lower systematic deviations due to the erroneous inclusion of $P_{\text{beam_gas}}$.

Of course we recommend following up with more multi-temperature datasets to confirm the trends for α_{dissoc} suggested by the 1-T-P method in Figures D.3 and D.4.

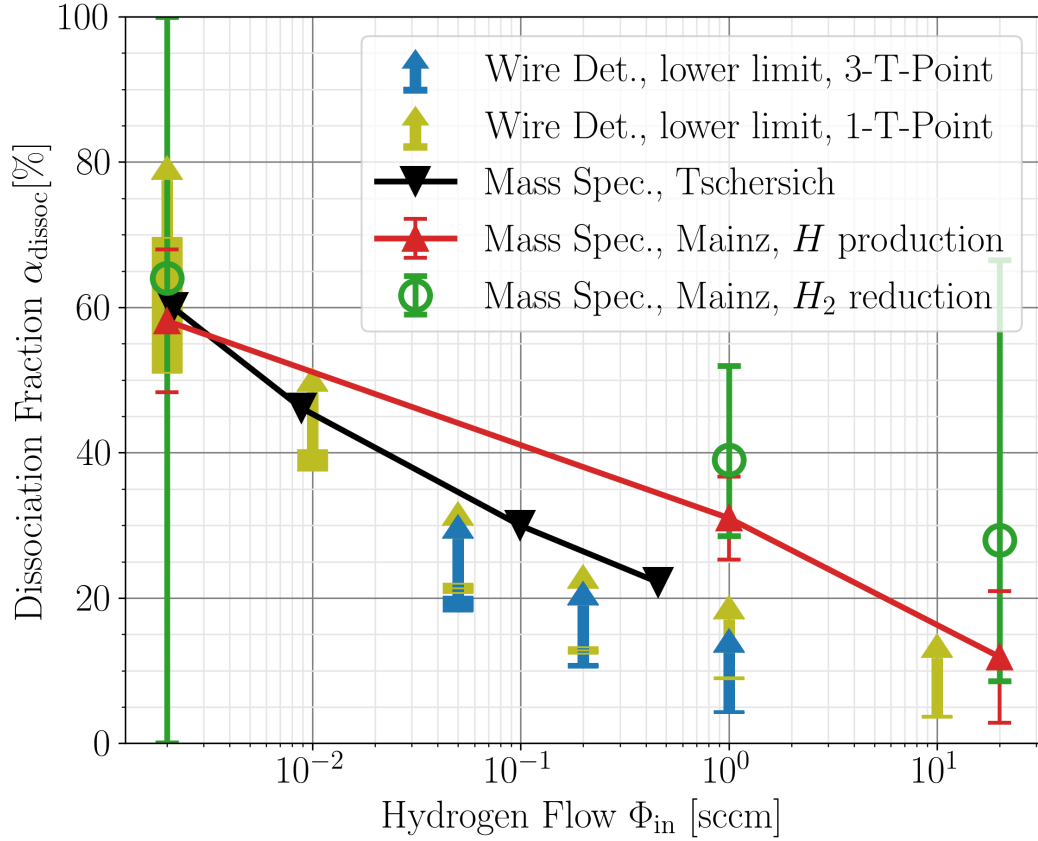


Figure D.3: Values of the dissociation fraction α_{dissoc} determined for the HABS using 4 different methods. The lower limit values based on wire detector measurements presented in this thesis are shown as blue arrows, where the height of the horizontal bar at the bottom is the statistical error on the limit value, while the arrow indicates the fact that it is a lower limit with the true value anywhere between it and 1. The equivalent analysis value based on the 1-T-P method is shown as yellow arrows. The black downward triangles indicate mass spectrometer based values taken from Fig. 6 in Tschersich et al. [40] at 2200 K and include no error bars. The red upward triangles and green circles two different mass spectrometer based measurements performed in Mainz reproduced from A. Lindman's PhD thesis (Section 45, [57]). Compare to 3-T Method Figure 8.15 in the main body of the thesis.

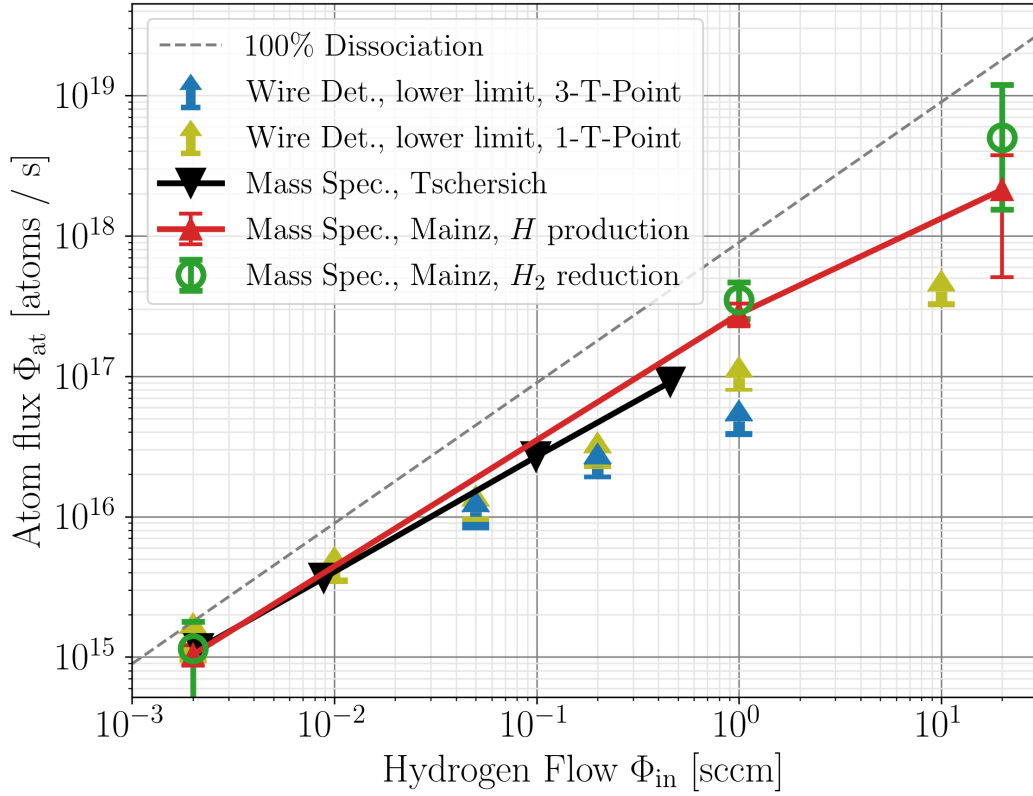


Figure D.4: Total atom flux calculated from α_{dissoc} values as presented in Figure 8.15 using Eq. (8.24), now including 1-T-P method results in yellow. The dashed line indicates the number of atoms that would be produced at a dissociation rate of 100%. The height of the horizontal bar at the bottom of the blue wire detector arrows indicates the statistical error on the lower limit, while the arrow indicates the fact that it is a lower limit with the true value anywhere between it and the dashed line. Includes data reproduced from Tschersich et. al. [40] and A. Lindman (Section 45, [57]). Compare to Figure 8.16 in the main body of the thesis.

Christian Matthé

Curriculum vitae

Binger Straße 6
55116 Mainz
Germany

☎ +49175 5597869

✉ christian.matthe.ger@gmail.com

Born 14 June 1996, Mainz, Germany



Employment History

- since 10/2020 **Scientific Employee, PhD student Physics,**
Institute for Physics (JGU Mainz) – Experimental Particle and Astroparticle Physics,
Collaborator on Project 8: an experiment for the determination of the neutrino mass. Developed a calorimetric wire detector for atomic hydrogen, to aid in the development of an atomic tritium source. Wrote a finite elements thermal simulation of the calorimeter wire using python. Designing, sourcing parts for and assembly of the final detector intended to work in ultra-high vacuum conditions. Assembly and rebuilding of the relevant vacuum chamber parts required for installation of the detector. Supervision of bachelor students and interns in working on parts of this project. .
- 04/2017–06/2017 **Student research assistant (part time),**
Institute for Physics (JGU Mainz) – Experimental Particle and Astroparticle Physics,
Development of a control system for the automation of an experimental setup, using LabVIEW, for testing optical elements for a potential upgrade of the IceCube Neutrino Observatory.
- 05/2015–07/2020 **Auxiliary student operator at the particle accelerator MAMI (part time),**
Institute for Nuclear Physics (JGU Mainz),
Running of routine operations of the particle accelerator on weekend and night shifts..

Publications

Astaschov M et al., *Calorimetric wire detector for measurement of atomic hydrogen beams.* *Eur Phys J D* **2025;79:60.** <https://doi.org/10.1140/epjd/s10053-025-00987-y>., *Primary author of text and content*, Paper covering part of PhD thesis topic, published with the Project 8 collaboration.

Education

- 04/2017–08/2020 **Master of Science – Physics,**
University of Heidelberg,
Specialisation: Astrophysics,
Master Thesis: “Evaluation of wobble for extracting radial velocities from CARMENES data“(Grade: 1.0).
Average Grade: 1.2 (German Scale 1-5, 1 being the best.)
- 04/2014–03/2017 **Bachelor of Science – Physics,**
University of Mainz,
Bachelor Thesis: “Development and Application of a Control System for the Wavelength-shifting Optical Module Tube Tester“(Grade: 1.0).
Average Grade: 1.7 (German scale)

08/2011–03/2014 **Allgemeine Hochschulreife**,
Gymnasium am Kurfürstlichen Schloss, Mainz.
Average Grade: 1.4 (German Scale)

08/2009–06/2011 **High School**,
International Academy, Bloomfield Hills, USA.

Programming and Software Experience

Python Data analysis for coursework as well as for my master thesis work extracting radial velocity information from stellar spectra. Data visualisation with *Matplotlib*. For my PhD thesis project I wrote a finite-elements simulation of heat flow along a wire calorimeter and performed analysis of data taken with the same.

Mathematica Data analysis and visualization, as well as symbolic computation for university courses, labs and bachelor thesis

LabVIEW Automation of an experimental setup as part of my bachelor thesis

Autodesk Inventor CAD modelling of parts of a calorimetric wire detector for manufacture by institute workshops as well as outside companies. Modelling of Vacuum chambers for planning of assembly of the aforementioned detector within.

Autodesk Eagle Design of printed circuit boards for manufacture in aluminum nitride for vacuum compatibility.

Languages

German Native language

English Fluent *4 years living and attending school in the United States, as well as daily use as a working language*

Teaching

05/2024–07/2024 **Tutor Experimental Physics 1**, Bachelor level course,
Prof. Dr. Jochen Walz.

05/2023–07/2023 **Tutor "Statistic, Data Analysis and Simulation"**, Master level course,
Prof. Dr. Sebastian Böser.

10/2021–02/2020 **Tutor Programming for Physicists**, Bachelor level course,
Prof. Dr. Sebastian Böser.

05/2020–07/2020 **Tutor Experimental Physics 4**, Bachelor level course,
Prof. Dr. Kurt Aulenbacher.

08/2017–10/2017 **Tutor *Mathematica* vacation block course.**



Christian Matthé
Mainz, September 17, 2025